amU
Aix Marseille Université

NNT : 0000AIXM0000

THÈSE DE DOCTORAT

Soutenue à Aix-Marseille Université
le 22 mai 2025 par

Anassya RAAD

Investigation of faceted solid-liquid interface behavior during the directional solidification of salol

Discipline
Physique et Sciences de la Matière

Spécialité
Matière Condensée et Nanosciences

École doctorale
ED 352

Laboratoire/Partenaires de recherche
IM2NP UMR 7334 CNRS

Composition du jury

Sabine BOTTIN- ROUSSEAU INSP, Sorbonne Université	Rapporteuse
Sylvain DEVILLE ILM, Université Lyon 1	Rapporteur
Laszlo STURZ Access e.V, RWTH Aachen University	Examinateur
Marc GEORGELIN IRPHE, Aix-Marseille Université	Président du jury
Nathalie MANGELINCK-NOEL IM2NP, Aix-Marseille Université	Directrice de thèse
Fatima MOTA IM2NP, Aix-Marseille Université	Co-directrice de thèse
Nathalie Bergeon IM2NP, Aix-Marseille Université	Membre invitée

im2np

cnrs

Affidavit

I, undersigned, Anassya RAAD, hereby declare that the work presented in this manuscript is my own work, carried out under the scientific supervision of Nathalie MANGELINCK-NOEL, Fatima MOTA and Nathalie BERGEON, in accordance with the principles of honesty, integrity and responsibility inherent to the research mission. The research work and the writing of this manuscript have been carried out in compliance with both the French national charter for Research Integrity and the Aix-Marseille University charter on the fight against plagiarism.

This work has not been submitted previously either in this country or in another country in the same or in a similar version to any other examination body.

Marseille, France , on 22 of May 2025.

Anassya RAAD



Cette œuvre est mise à disposition selon les termes de la Licence Creative Commons Attribution - Pas d'Utilisation Commerciale - Pas de Modification 4.0 International.

Publication list

[1] A. Raad, N. Bergeon, N. Mangelinck-Noël, F.L. Mota, Defect dynamics during the faceted growth of salol, Materialia 40 (2025) 102405.

Résumé

Lors de la solidification à partir du bain fondu, la morphologie de l'interface solide-liquide dépend des paramètres physiques du matériau et des conditions de traitement. Il est crucial de caractériser cette interface, car elle influence les propriétés finales du matériau. La solidification dirigée permet un contrôle précis des paramètres du processus. Les interfaces facettées à l'échelle macroscopique sont une morphologie caractéristique générée lors de la solidification de matériaux, tels que les semi-conducteurs, les quasi-cristaux, etc… Dans ce cas, l'attachement anisotrope et lent des atomes à l'interface a une influence dominante sur la croissance, et les cristaux présentent des surfaces lisses à l'échelle atomique. Toutefois, comprendre la dynamique des facettes nécessite des observations in situ et en temps réel. Ces données sont fondamentales pour optimiser les outils de simulation prédictive des processus d'élaboration des matériaux stratégiques. Cette thèse explore les mécanismes régissant la croissance des interfaces facettées, à travers des expériences de solidification dirigée sur un matériau organique transparent. Les résultats obtenus avec du salol pur, dont la structure orthorhombique se développe à partir de son bain fondu, révèlent une interface facettée marquée, en raison de son degré élevé d'anisotropie. Les expériences sont réalisées avec le dispositif ECODIS, combinant un four de type Bridgman et un microscope optique à lumière polarisée. Une série d'expériences est conduite sous différents gradients thermiques et vitesses de tirage, mettant systématiquement en évidence une interface solide-liquide très facettée. La dynamique complexe de l'interface révèle plusieurs défauts, comme les bulles, les macro-marches de croissance, les divisions et distorsions des facettes, ainsi que les joints des macles. Les observations in situ montrent que les bulles sont très probablement dues à l'inclusion d'azote dans le liquide, et que le déplacement des dislocations, ainsi que la désorientation des cristaux, favorisent la formation de défauts. Différentes conditions expérimentales sont appliquées afin de caractériser la formation des réseaux. Une augmentation de la vitesse de tirage donne des facettes plus nettes, tandis qu'une diminution du gradient thermique favorise la croissance des pointes facettées dans la direction du gradient thermique. Les données quantitatives sur le mouvement de l'interface, la taille des facettes et les angles interplanaires sont analysées, notamment en ce qui concerne la relation entre la vitesse de la facette, leur nature cristallographique et le sous-refroidissement.

Mots clés : solidification, systèmes facettés, structure de l'interface, observation in situ.

Abstract

During solidification from the melt, the solid-liquid interface morphology depends on the material physical parameters and the processing parameters. It is all the more important to characterize this interface as it plays a critical role in defining the final material properties. Directional solidification allows for precise control of processing parameters. Faceted interfaces at the macroscopic scale are a typical interface morphology generated during solidification of materials like semiconductors, quasicrystals, etc… In this case, the anisotropic and slow attachment of atoms from the liquid to the interface has a dominant effect on growth, and the crystals exhibit smooth surfaces at the atomic scale. A clear understanding of the faceted morphology dynamics requires in situ and real time observations of the process. This benchmark information is fundamental for optimizing predictive simulation tools for the elaboration processes of strategic materials. This thesis explores the mechanisms governing the growth of faceted interfaces through directional solidification experiments on an organic transparent material. The results obtained with pure salol, whose orthorhombic structure grows from its melt with a marked faceted interface dur to its high degree of anisotropy. The experiments are carried out using the ECODIS device, which combines a Bridgman-type furnace and an optical microscope with polarized light. Series of experiments are performed under different thermal gradients and pulling velocities, which all display a highly faceted solid-liquid interface. The complex dynamics of the interface reveals several defects, such as bubbles, growth striations, facet splits and distortions, as well as twin boundaries. In situ observations show that the bubbles are most likely due to the nitrogen inclusion in melt, and that the stress-induced dislocation movement, as well as crystal misorientation, promote defect formation. Various experimental conditions are applied to characterize the pattern formation. Increasing the pulling velocity results in sharper facets, while reducing the thermal gradient favors faceted tips in the direction of the thermal gradient. Quantitative data on the interface movement, facet size, and interplanar angles are analyzed, particularly concerning the relationship between facet velocity, its crystallographic nature and the undercooling.

Keywords: solidification, faceted systems, interface structure, in situ observation.

RÉSUMÉ ÉTENDU

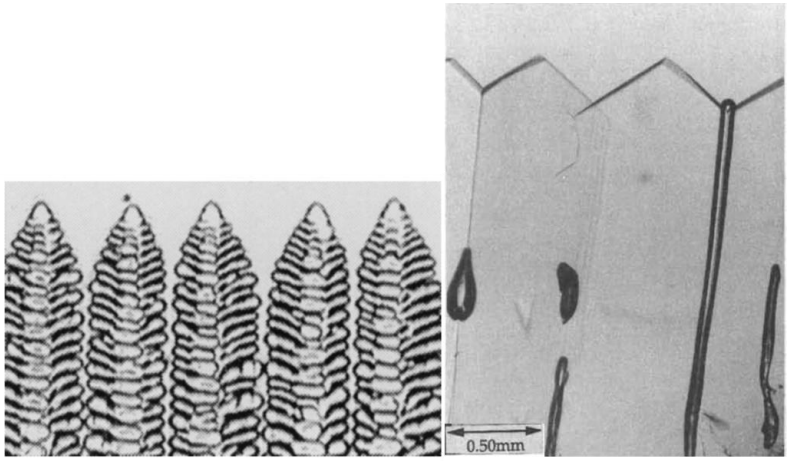
Introduction :

La solidification, passage de l'état liquide à l'état solide, joue un rôle fondamental dans les domaines industriels et scientifiques. L'étude et le contrôle de la morphologie des microstructures formées à l'interface solide-liquide lors de la solidification est importante pour améliorer les propriétés finales des matériaux et leurs qualités. Cette thèse vise à approfondir la compréhension des mécanismes de croissance des interfaces facettées par des expériences de solidification dirigée du salol qui est matériau organique transparent. Les expériences sont menées dans le dispositif ECODIS (Experimental Setup for COnfined DIrectional Solidification) développé au laboratoire. La thèse explicite le comportement dynamique des interfaces solide-liquide facettées qui est d'un grand intérêt en science des matériaux, en particulier à cause de son rôle dans la croissance des semi-conducteurs et des oxydes [1-5], et les facteurs influençant leur croissance. Ce travail est mené au sein de l'équipe MCA *(Microstructures de Croissance Autoorganisées)* de l'IM2NP (*Institut des Matériaux Microélectronique et Nanosciences de Provence*) dans le cadre du projet MATHIFA (Mechanism Analysis during THIck samples solidification of FAceted systems), financé par l'ANR (*Agence National pour la Recherche*).

Résumé du Chapitre 1 : État de l'Art

La solidification dirigée est une technique essentielle pour l'étude des microstructures car elle permet de contrôler indépendamment les paramètres expérimentaux qui régissent leur formation : la composition des alliages (concentration solutale C_0), le gradient thermique (G), et la vitesse de solidification (V_p). Lors de la solidification, l'interface solide-liquide peut présenter des microstructures différentes en fonction des conditions expérimentales de la solidification mais également des caractéristiques du matériau. En particulier, l'interface solide-liquide peut être rugueuse [6] ou facettée [7] (Figure 1).

L'interface rugueuse est caractéristique des matériaux présentant une faible anisotropie de la tension de la surface. L'interface est rugueuse à l'échelle atomique, ce qui facilite l'attachement des atomes pendant la croissance, et induit une cinétique d'attachement rapide [8]. La microstructure la plus typique associée à ce type de matériaux dans les procédés métallurgiques est la microstructure dendritique, illustrée en Figure 1a. L'interface facettée (Figure 1b) est caractéristique des matériaux présentant une forte anisotropie de la tension de surface. L'interface est lisse à l'échelle atomique, et le passage de l'état liquide à solide se fait couche par couche. Il s'accompagne d'une forte entropie de fusion. L'attachement est plus difficile et la croissance est plus lente que pour une interface rugueuse [9, 10].



(a) (b)

Figure 1 – Images de l'interface solide-liquide lors de la solidification dirigée : (a) interface rugueuse constitué d'un réseau de dendrites dans un alliage succinonitrile-coumarine [6], et (b) interface facettée du salol [7].

Le caractère rugueux ou facetté d'une interface cristalline peut être évalué par le critère de Jackson, établi par une analyse thermodynamique de l'attachement de nouveaux atomes au niveau de l'interface [11, 12]. Le paramètre de rugosité α_J proposé par Jackson dépend de la cristallographie de la surface et de l'entropie de fusion. Si $\alpha_J > 2$, l'interface est facettée et si $\alpha_J < 2$, l'interface est rugueuse. Le paramètre de rugosité α_J est exprimé comme suit dans l'équation 1:

$$\alpha_J = \frac{\eta}{Z}\frac{\Delta H_m}{R_g T_M} \qquad \textit{Eq. 1}$$

Avec η est le nombre de sites de voisins les plus proches adjacents à un atome dans le plan de l'interface, Z le nombre total de voisins les plus proches d'un atome dans le cristal, ΔH_m représente la chaleur latente de fusion, T_M est la température de fusion, et R_g la constante universelle des gaz.

Les caractéristiques de la cinétique d'attachement se manifestent par l'existence d'un sous-refroidissement cinétique ΔT_k, qui dépend du type et de la vitesse de croissance V_f. Il est typiquement négligeable en croissance rugueuse mais prend toute son importance en croissance facettée pour laquelle son amplitude dépend des mécanismes d'extension des facettes. Des lois $V_f = f(\Delta T_k)$ différentes sont obtenues pour la croissance continue, latérale, par nucléation bidimensionnelle ou en présence de dislocations vis [13].

La formation des microstructures est un phénomène dynamique qui évolue tout le long du processus de solidification. L'observation in situ en temps réel de l'interface est donc un outil majeur pour ce type d'études. Les matériaux organiques transparents sont utilisés comme modèles expérimentaux pour

suivre l'évolution de l'interface solide-liquide durant la solidification. Outre leur transparence à la lumière visible, ces matériaux ont un faible point de fusion généralement inférieur à 100°C [11, 14]. Ils sont très largement utilisés dans l'étude de la croissance des matériaux métalliques, d'interfaces rugueuses, depuis leur première mise en œuvre par Jackson et Hunt [11]. La croissance des matériaux présentant une interface facettée reste moins étudiée bien que plusieurs systèmes organiques transparents présentent ce type d'interface. Parmi eux, le salol, de facteur de Jackson de 7, a donné lieu à plusieurs études [13, 15].

Pendant la solidification des matériaux facettés se forment de nombreux défauts qui interagissent avec la microstructure et influencent la qualité du solide final [16]. L'observation in situ et en temps réel permet de suivre et caractériser ces défauts. Les défauts incluent les bulles, les macro-marches de croissances, la division des facettes, des distorsions du cristal, ainsi que les joints des macles. L'apparition de ces défauts peut être attribuée à de nombreux facteurs : ils peuvent provenir du germe cristallin initial, être liés à la pureté du matériau ou se développer sous l'effet de variations du champ thermique ou de contraintes internes.

Résumé du Chapitre 2 : Dispositif Expérimental et Procédures

Dans cette thèse, la croissance facettée est étudiée en solidification dirigée, en utilisant des analogues organiques transparents. L'observation et le suivi de l'interface *in situ* et en temps réel se fait dans le dispositif expérimental « Experimental setup for Confined Directional Solidification » (ECODIS) développé au laboratoire. Il est composé d'un four à gradient de type Bridgman formé de deux zones thermiques régulées, séparées par une zone non régulée. Les échantillons sont insérés dans ce four sur une platine qui permet le tirage de l'échantillon à travers le four, de la zone chaude vers la zone froide pour induire la solidification. Les températures des zones thermiques sont contrôlées pour que l'interface solide-liquide se situe dans la zone thermique non régulée. Un microscope optique accompagné d'une caméra numérique haute résolution placé au-dessus de la zone non régulée permet l'observation de l'interface (Figure 2).

Les creusets contenant les matériaux sont formés de deux plaques de verre séparées par des cales qui fixent l'épaisseur de l'échantillon à 50µm. Ces creusets sont remplis dans une boite à gants sous atmosphère inerte puis scellés.

Pour réaliser les expériences de solidification dirigée, nous avons préparé des creusets de trois systèmes organiques transparents différents : le salol pur, le système Succinonitrile-bornéol (SCN-BN) et le système Succinonitrile-vanilline (SCN-VAN). Cependant, les résultats présentés dans la thèse sont focalisés sur l'étude de l'interface facettée du salol. Des perspectives sont données en ce qui concerne l'étude des autres systèmes.

- Le salol (phényl salicylate), de formule chimique $C_{13}H_{10}O_3$, est un matériau organique transparent de point de fusion T_M = 41.5°C [17, 18]. Il possède une structure cristallographique orthorhombique avec des paramètres de maille : a = 23.40 Å, b = 11.26 Å et c = 7.96 Å [19]. Il est biréfringent, ce qui permet la mise en évidence des grains et des champs de contrainte à l'aide de la lumière polarisée [20]. En outre, le salol a un critère de Jackson $\alpha_J \approx 7$ caractéristique d'une interface hautement facettée [12].
- Le système Succinonitrile-bornéol (SCN-BN) présente un diagramme de phase de type eutectique. Le SCN est non-facetté alors que le bornéol est facetté en dessous de sa transition polymorphique (72°C). Pour des concentrations entre 3.3wt% et environ 11 wt% de BN dans le SCN, le facteur $\alpha_J \approx 2{,}4$ indique une interface facettée attendue [21].
- Le système Succinonitrile-vanilline (SCN-VAN) présente aussi un diagramme de phase de type eutectique. La vanilline adopte un comportement facetté à des températures modérées [22] avec un facteur de Jackson α_J égal à 2,6 pour 25 wt% et 35 wt% de la vanilline dans le succinonitrile.

Avant de préparer les alliages et le remplissage des creusets, les matériaux sont purifiés : par distillation pour le salol et le SCN , par sublimation pour le bornéol et par recristallisation pour la vanilline.

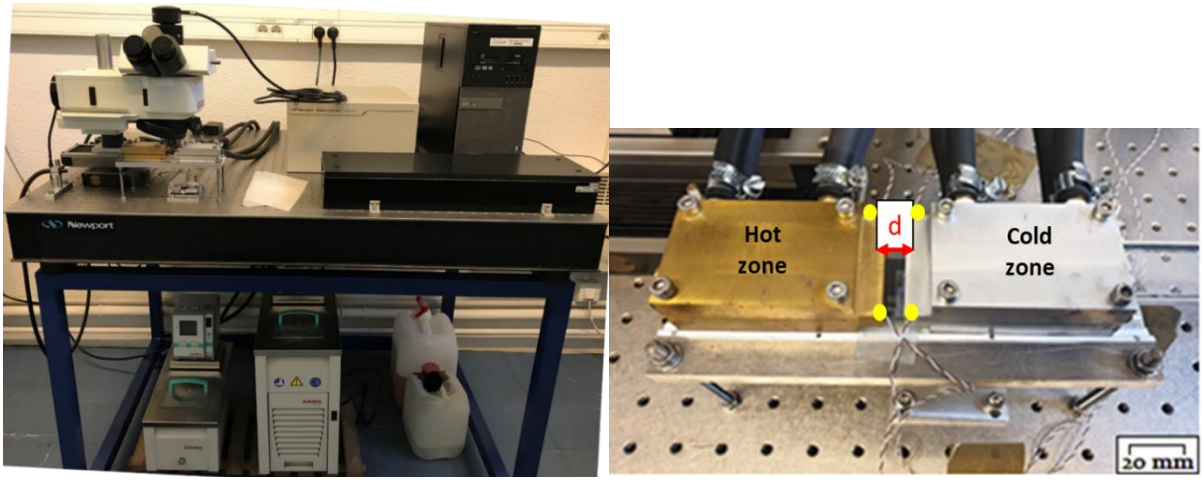


Figure 2 – Photographie du dispositif ECODIS (Experimental setup for COnfined DIrectional Solidification) utilisé pour l'observation in situ de la solidification dirigée (gauche). Four de type Bridgman avec les zone chaude et froide (droite).

Dans ces matériaux, la morphologie interfaciale dépend de l'orientation cristallographique. Une procédure spécifique est donc mise en œuvre dans le four pour former un talon solide monocristallin. Cette étape de germination est suivie d'une stabilisation du talon pendant 12 heures. Le tirage commence ensuite en déplaçant l'échantillon de la zone chaude vers la zone froide à vitesse contrôlée. Plusieurs

expériences sont menées en faisant varier les conditions expérimentales (gradient thermique et vitesse de tirage) afin d'étudier le comportement de l'interface facettée et l'influence des différents paramètres de contrôle sur celui-ci, de caractériser et indexer les facettes, d'analyser les défauts et leurs origines et d'établir des lois cinétiques.

Résumé du Chapitre 3 : Analyse phénoménologique du comportement des facettes et des défauts lors de la solidification directionnelle du salol

Dans ce chapitre, nous analysons la formation et l'évolution des facettes ainsi que la dynamique des défauts qui apparaissent au cours de la solidification et leurs interactions.

Les expériences de solidification dirigée du salol sont faites avec deux gradients thermiques différents et trois vitesses de tirage. L'analyse des facettes a montré que quand la vitesse de tirage augmente, les facettes sont stationnaires. A basse vitesse de tirage, l'interface a une dynamique très importante avec des éliminations de facettes plus fréquentes. Et quand le gradient est faible, les pointes des facettes poussent dans une direction presque alignée avec le gradient thermique.

L'évolution dynamique et complexe de l'interface facettée révèle plusieurs types de défauts tels que des bulles, des macro-marches de croissance, des divisions de facettes associées à de la compétition, des distorsions cristallines et des formations de macles. Les différents défauts sont présentés dans la Figure 3.

Les bulles, présentes dans toutes les expériences, sont des défauts volumiques [16]. La formation des bulles est essentiellement attribuée aux impuretés gazeuses résiduelles dans le liquide. Leur nucléation se produit dans les sillons entre les facettes [23-27]. Les bulles se forment avec une forme arrondie lorsqu'elles sont libres. Puis, elles peuvent croitre et être piégées dans le solide, s'allongent, bifurquent ou se déforment en fonction de l'environnement de la croissance, de la compétition entre facettes, et de leur migration et piégeage dans le solide. Dans la thèse, plusieurs mécanismes sont décrits. Malgré quelques tendances observées, nous n'avons pas identifié de relation directe entre l'apparition des bulles et la variation de la vitesse de croissance des facettes.

Nous avons observé des macro-marches de croissance qui apparaissent parallèlement aux facettes. Plusieurs hypothèses peuvent être données sur la nature de ces marches de croissance. Les stries de croissance sont des couches visibles ou des zones d'irrégularité qui peuvent se former durant la croissance des cristaux [16, 24, 28, 29] ; elles apparaissent sous forme de lignes parallèles à la surface ou bien à l'intérieur du cristal. Ces marches peuvent également être la trace de plans de glissement de dislocations. Les plans de glissement sont généralement des plans de haute densité. Pour le salol, les plans les plus denses sont les plans cristallographiques de type {111}.

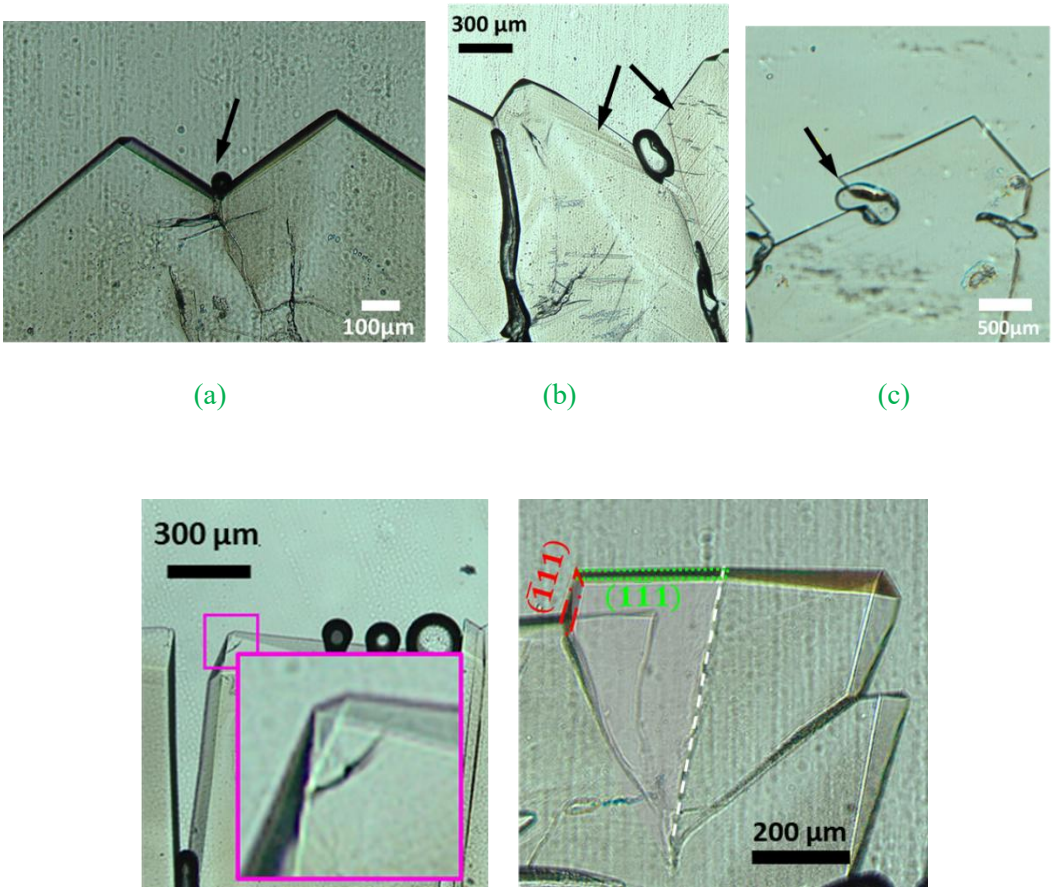


Figure 3 – Différents types de défauts observés lors de la solidification dirigée du salol, (a) les bulles, (b) les macro-marches de croissances, (c) la division d'une facette, (d) une zone de distorsion cristalline, et (e) un joint de macle.

La division des facettes se produit lorsque la taille de la facette devient instable, quand une bulle entre en contact avec la facette, ou encore quand un autre défaut favorise la division. Ces défauts influencent la vitesse de croissance des facettes.

Nous avons également observé des distorsions du cristal qui peuvent apparaitre suite à une accumulation des contraintes thermiques ou mécaniques durant le processus de solidification.

Le dernier défaut majeur observé est la formation de joints de macles, défaut cristallographique plan. Les instabilités thermiques, les impuretés et les dislocations peuvent être l'origine de ces défauts [1-3, 16, 28, 30-35]. L'analyse des macles observées dans nos expériences nous a permis d'identifier le plan de maclage, de type {111}, et les caractéristiques de la macle, de type Σ3.

Résumé du Chapitre 4 : Analyse Quantitative de la Croissance des Facettes lors de la Solidification Directionnelle du Salol

Ce chapitre présente une étude quantitative de la croissance des facettes du salol au cours de la solidification dirigée. Plusieurs caractéristiques de croissance sont analysées : le mouvement de l'interface solide-liquide, la taille des facettes, l'angle interplanaires entre les facettes formant des pointes, la vitesse de croissance des facettes et la relation entre celle-ci et le sous-refroidissement de la facette afin d'établir des lois cinétiques.

La position de l'interface solide-liquide dans le champ thermique est mesurée au cours du temps. Au début du tirage, l'interface recule (régime transitoire) avant de se stabiliser à une position – et donc une température - stationnaire. La mesure du recul total de l'interface permet de remonter au sous-refroidissement de l'interface, qui dépend de la vitesse de tirage et des mécanismes de croissance.

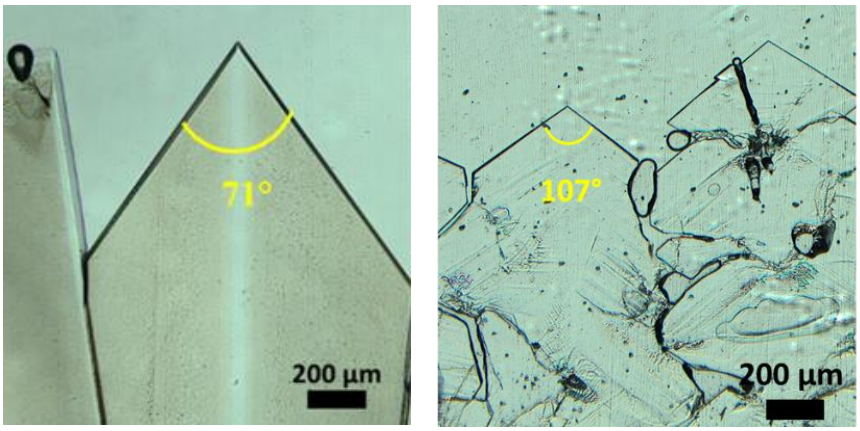
Les facettes correspondent à des surfaces planes du cristal en croissance. Leur taille est influencée par plusieurs paramètres incluant la vitesse de tirage, le gradient thermique, l'orientation cristallographique et les défauts [36, 37]. Nos résultats montrent une forte hétérogénéité des tailles de facettes. Lorsqu'une facette se divise, sa taille diminue drastiquement avant de recommencer à croître. Nous avons observé que les tailles moyennes de facettes diminuent avec l'augmentation de la vitesse de tirage et la diminution du gradient thermique.

Les angles interplanaires, qui correspondent aux angles entre deux facettes voisines, ont été caractérisés. Ces angles interplanaires permettent de déterminer l'orientation cristallographique des facettes [38, 39]. Nos mesures montrent que la majorité des facettes appartiennent à la famille du plan cristallographique {111}, et que des angles entre 65° et 75° sont observés à une vitesse de tirage égale à 10 µm/s, alors qu'à basse vitesse de tirage (2.5 µm/s), ces angles se situent entre 105° et 110° : Figure 4.

Au cours de la solidification, on peut définir pour chaque facette sa vitesse de croissance propre dans la direction normale à la facette. En régime stationnaire de croissance, cette vitesse de facette, notée V_f [40], correspond à la projection de la vitesse de tirage dans la direction normale à la facette. Pour vérifier le caractère stationnaire de la croissance, nous avons représenté les vitesses des facettes en fonction de leurs orientations et constaté que les données s'alignent avec les prédictions théoriques. Certaines déviations sont observées qui peuvent être liés à des évènements et à des défauts qui perturbent la croissance de la facette, entrainant ainsi un écart par rapport à des valeurs théoriques attendues. Ces mesures sont également utilisées pour analyser l'orientation des joints de grains [41].

Enfin, différents auteurs ont caractérisé la cinétique de croissance du salol et proposé des lois cinétiques reliant la vitesse de croissance et le sous-refroidissement [20, 42-49]. En se basant sur ces lois, nos mesures révèlent que les facettes {111} suivent potentiellement une croissance par dislocation vis ou

par germination bidimensionnelle. Et que le régime de croissance peut passer à une croissance continue à fort sous-refroidissement. Une analyse plus approfondie sera nécessaire pour mieux explorer les régimes de croissance et confirmer cette hypothèse.



(a) (b)

Figure 4 – L'interface du salol avec des angles interplanaires notés, à (a) V_p = 10 µm/s, G= 2.4 K/mm et (b) V_p = 2.5 µm/ s, G = 1.1 K/mm.

Conclusion

Ce travail a permis d'explorer la compréhension de la croissance de l'interface facettée lors de la solidification dirigée du salol. Les études expérimentales ont révélé une dynamique riche et complexe de l'interface, qui est influencée par la vitesse de tirage, le gradient thermique et l'orientation cristallographique. L'analyse et l'étude des défauts, tels que les bulles, les macro-marches de croissance, la division des facettes, les joints des macles et les des distorsions du cristal, ont mis en évidence leur impact sur la croissance des facettes. Les mesures quantitatives ont confirmé que les facettes correspondent à la famille des plans cristallographique {111}, et ont confirmé des lois de croissance cinétique de ces facettes en lien avec leur sous-refroidissement. Nos résultats apportent de nouvelles perspectives pour le contrôle des microstructures dans les matériaux facettés. Des études complémentaires seront essentielles et indispensables pour mieux comprendre la croissance facettée et valider les hypothèses sur les régimes de croissances.

Bibliographie

[1] K. Fujiwara, L. C. Chuang, and K. Maeda, « Dynamics at crystal/melt interface during solidification of multicrystalline silicon », High Temperature Materials and Processes, vol. 41, p. 31- 47, 2022.

[2] T. Riberi-Beridot, M. G. Tsoutsouva, G. Regula, G. Reinhart, F. Guittonneau, L. Barrallier, and N. Mangelinck-Noel, « Strain building and correlation with grain nucleation during silicon growth », Acta Materialia, vol.177, p. 141 -150, 2019.

[3] M. G. Tsoutsouva, T. Riberi-Beridot, G. Regula, G. Reinhart, J. Baruchel, F. Guittonneau, L. Barrallier, and N. Mangelinck-Noel, « In situ investigation of the structural defect generation and evolution during the directional solidification of < 110 > seeded growth Si », Acta Materialia, vol.115, p. 210-223, 2016.

[4] S. Deville, « Ice-templating, freeze casting: Beyond materials processing », Journal of Materials Research, vol. 28, p. 2202 - 2219, 2013.

[5] A. Lenart, Z. Samardžija, M. Godec, B. Mirtič, and S. Šturm, « Twin-boundary formation in Japan-law twinned quartz crystals », European Journal of Mineralogy, vol. 24, p. 509-517, 2012.

[6] W. Losert, B. Q. Shi, and H. Z. Cummins, « Evolution of Dendritic Patterns during Alloy Solidification: Onset of the Initial Instability », Proceedings of the National Academy of Sciences of the United States of America, vol. 95, p. 431- 438, 1998.

[7] N. Dey and J. A. Sekhar, « Interface configurations during the directional growth of Salol—I. Morphology », Acta Metallurgica et Materialia, vol. 41, p. 409-424, 1993.

[8] D. A. Porter, and K. E. Easterling, « Phase Transformations in Metals and Alloys », Springer, New York, 1992.

[9] S. A. Norris, S. H. Davis, S. J. Watson, and P. W. Voorhees, « Faceted interfaces in directional solidification », J. Cryst. Growth, vol. 310, p. 414-427, 2008.

[10] A. K. Boukellal, A. K. Sidi Elvalli, and J. M. Debierre, « Equilibrium and growth facetted shapes in isothermal solidification of silicon: 3D phase-field simulations », J. Cryst. Growth, vol. 522, p. 37- 44, 2019.

[11] K. A. Jackson, and J. D. Hunt, « Transparent compounds that freeze like metals », Acta Metallurgica, vol. 13, p.1212 -1215, 1965.

[12] K. A. Jackson, « Mechanism of growth in: Liquid metals and solidification, Asm, Cleveland, p. 174–186, 1958.

[13] M. C. Flemings, « Solidification processing », New-York: McGraw-Hill, 1974.

[14] W.D. Huang and L.L. Wang, « Solidification researches using transparent model materials — A review », Sci. China Technol. Sci., vol. 55, no 2, p. 377-386, 2012.

[15] Y. D. Bensah, « Morphological growth criterion for faceted to non-faceted transition in pure materials », Results in Physics, vol. 48, p. 106418, 2023.

[16] T. Kobayashi, K. Sato, M. Kobayashi, H. Kappler, « Organic Crystals I: Characterization », 1 ed., Springer Berlin Heidelberg, 1991.

[17] G. Kuriakose, and N. Nagaraju, « Selective synthesis of phenyl salicylate (salol) by esterification reaction over solid acid catalysts », Journal of Molecular Catalysis A: Chemical, vol. 223, p. 155-159, 2004.

[18] NIST Chemistry WebBook, [Online]. Available: https://webbook.nist.gov/chemistry/,

[19] J. H. Bilgram, U. Dürig, M. Wächter, and P. Seiler, « Zone refining and structure determination of salol crystals », J. Cryst. Growth, vol. 57, p. 1-5, 1982.

[20] H. G. Riveros, « Growth of salol crystals », J. Cryst. Growth, vol. 2, p. 173-177, 1968.

[21] D. J. Fisher, and W. Kurz, « The growth mechanism of faceted/non-faceted eutectics ». Proc. Int. Conf. on the Solidification and Casting of Metals vol. 3, p. 59, 1977.

[22] J. Singh, P. Gupta, S. S. Das, and N. B. Singh, « Phase Diagram Study of Succinonitrile-Vanillin Organic Alloy System », Molecular Crystals and Liquid Crystals, vol. 605, p. 240-258, 2014.

[23] S. Akamatsu, and G. Faivre, «Residual-Impurity Effects in Directional Solidification: LongLasting Recoil of the Front and Nucleation-Growth of Gas Bubbles», Journal de Physique I, vol. 6, p. 503-527, 1996.

[24] Th. Scheffen-Lauenroth, H. Klapper, and R. A. Becker, « Growth and perfection of organic crystals from undercooled melt », J. Cryst. Growth, vol. 55, p. 557-570, 1981.

[25] T. Werner, M. Becker, J. Baumann, C. Pickmann, L. Sturz, and F. Kargl, « In situ observation of the impact of hydrogen bubbles in Al–Cu melt on directional dendritic solidification », J Mater Sci, vol. 56, p. 8225-8242, 2021.

[26] K. Yoshimura, T. Inada, and S. Koyama, « Growth of Spherical and Cylindrical Oxygen Bubbles at an Ice−Water Interface », Crystal Growth & Design, vol. 8, p. 2108-2115, 2008.

[27] H. Jamgotchian, R. Trivedi, and B. Billia, « Interface dynamics and coupled growth in directional solidification in presence of bubbles », J. Cryst. Growth, vol. 134, p. 181-195, 1993.

[28] M. Li, C. Zhang, M. Li, F. Liu, L. Zhou, Z. Gao, J. Sun, D. Han, and J. Gong, « Growth defects of organic crystals: A review », Chemical Engineering Journal, vol. 429, p. 132450, 2022.

[29] H. Klapper, « Defects in non-metal crystals. In Characterization of Crystal Growth Defects by X-ray Methods », Boston, MA: Springer US, 1980.

[30] I. A. Olson, A. G. Shtukenberg, B. Kahr, and M. D. Ward, « Dislocations in molecular crystals », Rep Prog Phys, vol. 81, p. 096501, 2018.

[31] G. Dhanaraj, K. Byrappa, V. Prasad, and M. Dudley, « Crystal growth techniques and characterization: an overview. Springer Handbook of Crystal Growth, 2010.

[32] K. Fujiwara, R. Maeda, K. Maeda, and H. Morito, « In situ observation of twin boundary formation at grain-boundary groove during directional solidification of Si », Scripta Materialia, vol. 133, p. 65-69, 2017.

[33] D. Hull, and D. J. Bacon, « Introduction to Dislocations (Fifth Edition) », Butterworth-Heinemann, Oxford, 2011.

[34] L. Priester, « Les joints de grains, De la théorie à l'ingénierie », 1ère édition, 2006.

[35] F. Yang, L. C. Chuang, K. Maeda, J. Nozawa, H. Morito, K. Fujiwara, and T. Duffar, « Dislocation interaction with vicinally faceted groove at grain boundary in multi-crystalline silicon », J. Cryst. Growth, vol. 639, p. 127722, 2024.

[36] V. V. PODOLINSKI, « Investigation of structural formation and growth kinetics of organic crystals », J. Cryst. Growth, vol. 46, p. 511 - 522, 1979.

[37] V. Stamelou, M. G. Tsoutsouva, T. Riberi-Béridot, G. Reinhart, G. Regula, J. Baruchel, and N. Mangelinck-Noël, « {1 1 1} facet growth laws and grain competition during silicon crystallization », J. Cryst. Growth, vol. 479, p. 1 - 8, 2017.

[38] C. Malgrange, C. Ricolleau, and F. Lefaucheux, « Symétrie et propriétés physiques des cristaux », EDP sciences, 2011.

[39] N. Millot, and J.-C. Nièpce, « Cristallographie géométrique: Cours, exercices et problèmes corrigés », Lavoisier, 2014.

[40] J. G. Dash, V. A. Hodgkin, and J. S. Wettlaufer, « Dynamics of Faceted Grain Boundary Grooves », Journal of Statistical Physics, vol. 95, p. 1311 - 1322, 1999.

[41] T. Duffar, and A. Nadri, « The grain–grain–liquid triple phase line during solidification of multi-crystalline silicon, Comptes Rendus Physique, vol. 14, p.185-191, 2013.

[42] V. Danilov and V. Malkin, « Experimental Verification of the Theory of Crystal Growth and the Relation between the Equilibrium Forms and the Growth Forms », Z. Fiz. Khim, vol. 27, p. 1837, 1954.

[43] V. I. Malkin, « On the Rate of Crystal Growth of Salol in the Glassy State », Z. Fiz. Khim vol. 28, p1966-1968, 1954.

[44] J. W. Cahn, W. B. Hillig, and G. W. Sears, « The molecular mechanism of solidification ». Acta Metallurgica, vol. 12, p.1421 -1439, 1964.

[45] H. Pollatschek, « The Determination of the Temperature at the Solid-Liquid Boundary During the Crystallization of Undercooled Melts », Z. Phys. Chem. A , vol. 142, p. 289-300, 1929.

[46] K. Neumann, and G. Micus, « The Linear Crystallization Rate of Salol in Thin Layers », Z. Phys. Chem. vol. 2, p. 25-39, 1954.

[47] J. W. Cahn, « Theory of crystal growth and interface motion in crystalline materials », Acta Metall, vol.8, p. 554-562, 1960.

[48] K. A. Jackson, D. R. Uhlmann, and J. D. Hunt, « On the nature of crystal growth from the melt », J. Cryst. Growth, vol. 1, p. 1 - 36, 1967.

[49] W. Q. Jin, J. Lin, and H. Komatsu, « Experimental studies on growth kinetics of salol crystals from the melt », J. Cryst. growth, vol. 99, p. 128- 133, 1990.

Acknowledgement

These three years of research have been an adventure filled with challenges, discoveries, and invaluable learning experiences, and the journey has come to an end. For this, I would like to express my gratitude to the people from whom I was inspired and received generous support.

This work was carried out at Institut Matériaux Microélectronique et Nanosciences de Provence laboratory (IM2NP) UMR CNRS 7334, associated with Aix-Marseille University (AMU). I would like to thank every member of the team Microstructure of Self-organized Growth (MCA) in which I carried out this thesis work. And I am grateful to the French National Research Agency (ANR) for its financial support of my thesis as part of MATHIFA (Mechanism Analysis during THIck samples solidification of FAceted systems) project.

I would like to express my deepest appreciation to my research supervisors Nathalie Mangelinck Noël, Fatima Lisboa-Mota and Nathalie Bergeon. Their expertise in the field has been a valuable source of inspiration and learning for me. Their encouragement has been essential throughout this work. As well, their continuous support, insightful advice, and unwavering encouragement have been instrumental in overcoming challenges and pushing this work forward. I am grateful for their patience, and commitment, which have played a crucial role in my scientific growth.

I would like to thank also the members of my monitoring committee, Fabienne MICHELINI and Miha ZALOŽNIK for their constructive feedback, and enriching discussions that have significantly contributed to the progress of my research.

I am deeply thankful for the members of my thesis jury, Marc GEORGELIN, Sabine BOTTIN-ROUSSEAU, Sylvain Deville, and Laszlo STURZ for accepting to evaluate my work over these three years.

I would like to thank as well my friends in Lebanon (Shams, Hadi, Hala, Diana and Carole) and in France (Terkia, Mehdi, Melissa, Nay, Leen, Ahmad C., Elie, Soufiane, Marie Rose, Mahmoud Y., Mahmoud C., Théo, Amira, Sirine, Moiz, Sara, Lara, Nawal, Valentin, and Jérémy) for their support and encouragement, sharing valuable moments with them made this thesis memorable.

I would like to express my deepest gratitude to my fiancé Ahmad for his unwavering support, patience, love and encouragement throughout this journey. His belief in me, even during the most challenging moments, has been a constant source of strength and motivation. Through

every success and setback, he has been my greatest cheerleader, reminding me of my capabilities when I doubted myself. His understanding, and presence have made this experience meaningful, and I am truly grateful to have him by my side.

To my beloved family, mom and dad, Adonis and Hamza, Marwa and Amal, Abbas, Hussein and Ali, this achievement is as much yours as it is mine. I would not be here without your unconditional love, sacrifices, and unwavering support. Through every challenge, you have been my strength, my foundation, and my greatest source of encouragement. Every late night, every moment of doubt, and every step forward was made possible because of you. I hope this accomplishment makes you proud of me. From the bottom of my heart, thank you for everything.

Finally, a heartfelt thank you to all those who, in one way or another, have contributed to this scientific and human adventure.

This thesis is the result of collective effort, and I am deeply grateful to everyone who made this journey possible.

Glossary

Latin

3D	three-dimensional
BN	Borneol
C_E	eutectic concentration
C_L	equilibrium solute concentration in the liquid phase
C_P	heat capacity of the liquid
C_S	equilibrium solute concentration in the solid phase
C_0	initial composition
C_α	concentration of phase α at the eutectic
C_β	concentration of phase β at the eutectic
d_0	capillary length
D_L	solute diffusion coefficient in the liquid
D_{LM}	liquid diffusion coefficient at the melting temperature
ECODIS	Experimental setup for COnfined DIrectional Solidification
FoV	field-of-view
G	thermal gradient
L	solidified length
k	partition coefficient
K	local interface curvature
m	*liquidus* slope
PET	Polyethylene terephthalate
r	radius of the solid spherical nucleus
r^*	critical radius
R_g	universal gas constant
SCN	succinonitrile
t	time
T	actual temperature of the liquid

TC	thermocouple
T_E	eutectic temperature
T_M	melting temperature of pure material
V	interface velocity
VAN	vanillin
V_f	facet velocity
V_p	pulling velocity
VPT	Vapor Pressure Temperature
Z	total number of nearest neighbors of an atom in the crystal

Greek

α_J	Jackson roughness criterion
β	thermal expansion coefficient
γ	interplanar angle between two neighboring facets
Γ	Gibbs-Thomson coefficient
δ	sample thickness
δ_c	solute boundary layer thickness
∂	wetting angle of the crystal formed on the substrate
ΔG_{het}	Gibbs' free energy of heterogeneous nucleation
ΔG_{hom}	Gibbs' free energy of homogeneous nucleation
ΔG_v	free energy change per unit volume
ΔG^*	critical free energy
ΔH_m	latent heat of melting
ΔS_m	entropy of melting
ΔT	undercooling
ΔT_0	equilibrium freezing range of the alloy
ΔT_c	constitutional undercooling
ΔT_k	kinetic undercooling
ΔT_r	curvature undercooling
ΔT_t	thermal undercooling

η	number of nearest neighbor sites adjacent to an atom in the plane of the interface
θ	angle between the interface normal and the reference axis
θ_f	facet orientation relatively to the pulling direction
θ_r	angle between two bottomed facets
μ_1	kinetic coefficient
μ_2	constant function of diffuseness, lattice geometry and dislocation density
σ_{LS}	solid-liquid surface tension
$\sigma_{S\text{-}Sub}$	solid-substrate surface tension
$\sigma_{L\text{-}Sub}$	liquid-substrate surface tension
$\sigma(\theta)$	surface stiffness
φ	boundary orientation

Table of Contents

INTRODUCTION.....1

CHAPTER 1: STATE OF THE ART 6

1.1 Generalities on solidification 6

1.1.1 Directional solidification 6

1.1.2 Classical nucleation theory 7

1.1.3 Solid-liquid interface morphology 8

1.1.4 Surface roughness criterion 12

1.1.5 Undercooling during growth 13

1.1.6 Growth types 14

1.1.6.1 Continuous growth 15

1.1.6.2 Lateral growth 15

1.2 Solidification of transparent organic materials 17

1.2.1 Types of microstructures in an interface with rough morphology 18

1.2.2 Faceted morphology 20

1.3 Defects in crystals and during solidification 22

1.3.1 Bubbles 23

1.3.2 Growth striations 25

1.3.3 Dislocations 28

1.3.4 Grain boundaries 30

1.3.5 Stresses 32

1.4 The kinetics of the growth of salol 34

1.5 Bibliography 37

Chapter 2: EXPERIMENTAL APPARATUS AND PROCEDURES 46

2.1 The materials 46

2.1.1 Salol 47

2.1.2 Succinonitrile-borneol 47

2.1.3 Succinonitrile-vanillin 48

2.2 Purification of materials 49

2.2.1 Distillation 49

2.2.1.1 The distillation unit 49

2.2.1.2 The distillation process 51

2.2.1.3 Troubleshooting and Key Observations in Distillation 53

2.2.2 Sublimation 54

2.2.2.1 The sublimation unit 54

2.2.2.2 The sublimation process 55

2.2.2.3 Troubleshooting and key observations in sublimation 55

2.2.3 Recrystallization 56

2.2.3.1 The recrystallization unit 56

2.2.3.2 The recrystallization process 57

2.3 Thin samples preparation 58

2.3.1 Preparation of alloys 58

2.3.2 Preparation of the crucible 59

2.3.3 Sample filling 60

2.4 Experimental solidification device 63

2.4.1 Thermal control 64

2.4.1.1 Thermal gradient measurement 65

2.4.1.2 Thermal field characterization 67

2.4.2 Optical system 69

2.4.3 Movement system 70

2.5 Initial solid seed preparation 70

2.6 Experiments 74

2.7 Vesta software 75

2.8 Bibliography 76

CHAPTER 3: PHENOMENOLOGICAL ANALYSIS OF FACET AND DEFECT BEHAVIOR DURING DIRECTIONAL SOLIDIFICATION OF SALOL 80

3.1. Pattern formation 80

3.2. Comparison of the solid-liquid interface morphologies in different experiments..... 85

3.3 Investigation of defects observed during growth 87

3.3.1 Bubbles 87

3.3.2 Growth striations 99

3.3.3 Facet splitting 107

3.3.4 Crystal distortion 113

3.3.5 Twin crystals 118

3.4 Conclusions 121

3.5 Bibliography 122

CHAPTER 4: QUANTITATIVE ANALYSIS OF THE FACET GROWTH DURING THE DIRECTIONAL SOLIDIFICATION OF SALOL 128

4.1 Solid-liquid interface movement 128

4.2 Facet size 130

4.3 Interplanar angle 134

4.4 Faceted tip velocity 140

4.5 Facet velocity 144

4.6 Relationship between facet velocity and undercooling 156

4.7 Conclusions 158

4.7 Bibliography 159

CONCLUSIONS AND FUTURE WORK 162

INTRODUCTION

Solidification, the phase transition from a liquid to a solid state, is a common phenomenon in nature. During this transition, the physical properties and atomic arrangement of the material change significantly. One of the most familiar examples is the freezing of water into ice. Moreover, the process of casting metals is deeply related to human history, to the point where early eras are named after metals humanity mastered—such as the Bronze Age and the Iron Age. In modern times, many human activities rely on cast metals, welded materials, and the growth of semiconductors from the melt. Examples include turbine blades used in power-plants and jet engines, lightweight metallic foams for vehicle impact absorption, ultra-strong "super-metals" for electronics, high performance magnets, medical implants, fine metallic powders for catalyzing chemical reactions, and the manufacture of silicon-based solar panels, among numerous other applications. Solidification process plays such an important role in the production of materials in the field of metallurgy that research and development in the field is still very active.

During solidification from the melt, the morphology of the solid-liquid interface depends on both material properties and processing parameters. Characterizing this interface is crucial, as it directly influences the final material properties, especially the mechanical ones. Directional solidification provides precise control over process parameters, making it a powerful tool for studying the interface dynamics [1-3]. However, a comprehensive understanding remains challenging and requires key information concerning the dynamics of the interface structuration and of the formation of structural defects that can only be brought by *in situ* and real time observation of the process. In light of this, transparent organic materials have been and are still extensively used [4, 5]. They behave like materials of interest (metallic alloys, semiconductors) regarding solidification but are transparent to visible light so that optical techniques are sufficient for their observation. Such experiments serve as benchmark data to investigate complex mechanisms that control material growth, to better understand the formation of the interface morphology, and to validate numerical models.

Faceted interfaces at the macroscopic scale are a typical interface morphology generated during solidification of many materials, like semiconductors, quasicrystals, etc. [6-10]. In this case, the atom attachment from the liquid at the interface is anisotropic and slow, and its effect is dominant during growth. Crystals then exhibit atomically smooth surfaces. A clear understanding of the faceted interface implying a thorough investigation of the dynamics and

behavior of facets is required and such information can be attained using *in situ* and in real time observation experiments of the solidification process.

In this thesis, focusing on achieving advances in the analysis of mechanisms involved during faceted interface growth, directional solidification experiments of an organic transparent material are performed. We report results obtained with pure salol (phenyl salicylate) that is orthorhombic in structure [11] and grows from its melt with a marked macroscopic faceted interface because of its high degree of anisotropy [12]. This material presents a low melting temperature (41.5°C) [13], and is birefringent [14]. The experiments are conducted using the Experimental setup for COnfined DIrectional Solidification (ECODIS) device, which is dedicated to study solidification in thin rectangular samples from 25 µm to 1 cm of thickness. It is constituted of a Bridgman-type furnace equipped with an optical microscope to observe the solid-liquid interface dynamics *in situ* and real time. A series of experiments are performed with different thermal gradients and pulling velocities, which all display a highly faceted solid-liquid interface.

The organic crystals contain the same types of defects as inorganic materials [15-17], with the advantage that they can be observed by *in situ* investigations. In this thesis, the rich and complex dynamics of the faceted solid-liquid interface of salol during growth highlight the formation and evolution of several defects at different scales, namely: bubbles, growth striations, facet splits, crystal distortions, and also twin boundaries. The appearance of the defects at the solid-liquid interface relies on different factors, such as inherited defects from the crystal seed, the thermal conditions, the material purity, or internal stresses. Stresses may arise from variations in the thermal field, chemical compositions and crystal distortions [15-20].

The work presented in this manuscript has been conducted in the MCA (*Microstructures de Croissance Autoorganisées*) team of the IM2NP (*Institut des Matériaux Microélectronique et Nanosciences de Provence*) laboratory within the MATHIFA (Mechanism Analysis during THIck samples solidification of FAceted systems) project that is funded by the ANR (*Agence National pour la Recherche*). It represents three years of experimental and analytical studies seeking to understand the dynamical behavior of a faceted solid-liquid interface and the factors that can influence its growth. A combination of bibliographic research, sample preparation, experimental techniques, and advanced analysis are employed in order to achieve a comprehensive acknowledgment that fills some gaps in the understanding of the behavior and characteristic of facetted solid-liquid interfaces, and the formation of defects during solidification.

The manuscript is divided into four chapters which are presented in the following:

- **Chapter 1** introduces the state of the art and the basic principles related to the solidification process, with a focus on the directional solidification. Interface patterns are described together with the mechanisms and conditions of their formation. The chapter also highlights the growth behavior of transparent organic materials which are model systems for studying materials technologically important. Particular attention is given to the materials presenting a faceted interface during growth. The origin and implications of growth-in defects at the interface are discussed, emphasizing their impact on the material properties.
- **Chapter 2** provides a detailed description of the materials, the purification methods, and the experimental device used to achieve the directional solidification experiments. The samples preparation and filling are also carefully described. Additionally, the initial seed preparation, in order to try to achieve a well-controlled solidification and monocrystalline growth, is discussed.
- **Chapter 3** presents a detailed examination of salol solid-liquid interface evolution, and the various defects observed during solidification. The influence of the control parameters on the dynamic behavior of the facet and its morphology is discussed. This chapter brings special attention to the investigation of the various defects observed at the interface for different experimental conditions. These defects include: the nucleation and evolution of bubbles; growth striations that can be either growth striations, or indirect signs of dislocations or gliding planes; facet splitting and crystal distortion; and the formation of twin boundaries. Their formation mechanisms and their impact on facet growth is studied and analyzed.
- **Chapter 4** gives an in-depth quantitative analysis of the dynamical growth of the salol facets during directional solidification. First, the solid-liquid interface movement, which involves transient and steady-state phases, is analyzed since it is directly related to the interface and facet undercooling. After the indexation of the facets, the relationship between the facet velocity and the undercooling is explored, in order to establish kinetic growth laws and to determine the type of growth.

This manuscript ends with a general conclusion and statement of pending issues and perspectives deriving from the current studies.

Bibliography

[1] M. C. Flemings, « Solidification processing », New-York: McGraw-Hill, 1974.

[2] W. Kurz, and D. J. Fisher, « Fundamentals of Solidification », Trans. Tech. Publications., p. 353, 1998.

[3] J. A. Dantzig, and M. Rappaz, « Solidification », EPFL Press, Switzerland, 2009.

[4] K. A. Jackson, and J. D. Hunt, « Transparent compounds that freeze like metals », Acta Metallurgica, vol. 13, p.1212-1215,1965.

[5] W. D. Huang, and L. L. Wang, « Solidification researches using transparent model materials — A review », Sci. China Technol. Sci., vol. 55, p. 377-386, 2012.

[6] K. Fujiwara, L. C. Chuang, and K. Maeda, « Dynamics at crystal/melt interface during solidification of multicrystalline silicon », High Temperature Materials and Processes, vol. 41, p. 31-47, 2022.

[7] T. Riberi-Beridot, M. G. Tsoutsouva, G. Regula, G. Reinhart, F. Guittonneau, L. Barrallier, and N. Mangelinck-Noel, « Strain building and correlation with grain nucleation during silicon growth », Acta Materialia, vol.177, p. 141-150, 2019.

[8] M. G. Tsoutsouva, T. Riberi-Beridot, G. Regula, G. Reinhart, J. Baruchel, F. Guittonneau, L. Barrallier, and N. Mangelinck-Noel, « In situ investigation of the structural defect generation and evolution during the directional solidification of < 110 > seeded growth Si », Acta Materialia, vol.115, p. 210-223, 2016.

[9] S. Deville, « Ice-templating, freeze casting: Beyond materials processing », Journal of Materials Research, vol. 28, p. 2202-2219, 2013.

[10] A. Lenart, Z. Samardžija, M. Godec, B. Mirtič, and S. Šturm, « Twin-boundary formation in Japan-law twinned quartz crystals », European Journal of Mineralogy, vol. 24, p. 509-517, 2012.

[11] J. H. Bilgram, U. Dürig, M. Wächter, and P. Seiler, « Zone refining and structure determination of salol crystals », J. Cryst. Growth, vol. 57, p. 1-5, 1982.

[12] K.A. Jackson, « Liquid metals and solidification », American Society for Metals, Cleveland, 1958.

[13] NIST Chemistry WebBook, [Online]. Available: https://webbook.nist.gov/chemistry/,

[14] H. G. Riveros, « Growth of salol crystals », J. Cryst. Growth, vol. 2, p. 173-177, 1968.

[15] T. Kobayashi, K. Sato, M. Kobayashi, and H. Kappler, « Organic Crystals I: Characterization », 1 ed., Springer Berlin Heidelberg, 1991.

[16] M. Li, C. Zhang, M. Li, F. Liu, L. Zhou, Z. Gao, J. Sun, D. Han, and J. Gong, « Growth defects of organic crystals: A review », Chemical Engineering Journal, vol. 429, p. 132450, 2022.

[17] N. B. Ming, and C. Z. Ge, « Direct observation of defects in transparent crystals by optical microscopy », J. Cryst. Growth, vol. 99, p. 1309-1314, 1990.

[18] H. J. Scheel, and T. Fukuda, « Crystal Growth Technology », Willey, 2003.

[19] B. Cockayne, « Developments in melt-grown oxide crystals », J. Cryst. Growth, vol. 3-4, p. 60-70, 1968.

[20] I. A. Olson, A. G. Shtukenberg, B. Kahr, and M. D. Ward, « Dislocations in molecular crystals », Rep Prog Phys, vol. 81, p. 096501, 2018.

CHAPTER 1: SATE OF THE ART

1.1 Generalities on solidification

Solidification is the process when a liquid turns into solid as observed in the formation of ice, the freezing of solder in electrical circuits and the metal casting in industrial manufacturing. Solidification has always been of interest to humans since the Bronze Age and in the Modern era for researchers and industrials. One of the main subjects of solidification research is devoted to the understanding and control of the microstructure that forms at solid-liquid interfaces during the solidification process in order to optimize the final properties of the material and to have a high-quality product. Structural defects formed in the crystal during solidification have also a direct influence on the final properties and as such, constitute a related important subject of solidification research.

1.1.1 Directional solidification

Directional solidification is an important technique for investigating the fundamental aspects of the solidification process. Figure 1.1 presents the concept of directional solidification using a Bridgman-type furnace. The sample of initial composition C_0 is placed in a thermal gradient G imposed by the furnace so that one extremity of the sample is in the liquid state while the other is in solid state, creating a solid-liquid interface. Solidification occurs when the sample is pulled from the hot zone of the furnace at a controlled pulling velocity V_p toward the cold zone. The Bridgman solidification technique is useful to study interface morphology resulting from the solidification process, because it allows to independently control the three experimental parameters (C_0, G and V_p).

The thermodynamic approach reveals that crystallization passes through two fundamental stages: nucleation, which consists in the appearance in the melt of critical nuclei from which crystallization is triggered; and growth, which is the evolution of these nuclei into crystals/grains.

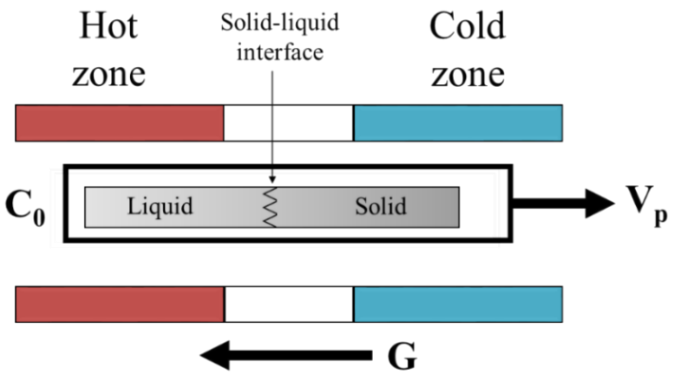


Figure 1.1 – Schematic illustration of the directional solidification in the Bridgman-type furnace.

1.1.2 Classical nucleation theory

Nucleation is a process in which a solid cluster forms with a critical size and acts as the initial nucleus of the crystal [1, 2]. Two types of nucleation mechanisms can be distinguished.

i) Homogeneous nucleation:

Homogeneous nucleation takes place when a solid cluster of critical size forms from the liquid. In fact, simply being below the melting temperature is not a sufficient condition for the formation of a solid nucleus, as there is an energy term related to the surface tension between the crystal and the liquid σ_{LS} that can delay the formation of the first solid. The variation of the Gibbs' free energy of homogeneous nucleation ΔG_{hom} of a solid aggregate is given by:

$$\Delta G_{hom} = \frac{4}{3}\pi r^3 \Delta G_v + 4\pi r^2 \sigma_{LS} \qquad \textit{Eq. 1.1}$$

with ΔG_v is the free energy change per unit volume, and r is the radius of the solid spherical nucleus and σ_{LS} is the solid-liquid surface tension. Once the system temperature is lower than the melting temperature of the material, the variation of the free energy becomes negative, whereas the formation of the solid-liquid interface results in a positive value for the second term. Therefore, during the formation of a solid nucleus the signs of the two terms in *Eq. 1.1* have opposite signs. The critical free energy ΔG^* corresponds to a critical radius r^* that should be surpassed in order to have solidification by homogeneous nucleation:

$$r^* = -2\,\frac{\sigma_{LS}}{\Delta G_v} \qquad \textit{Eq. 1.2}$$

ii) Heterogeneous nucleation:

When a substrate pre-exists in the liquid, besides the presence of the solid and the liquid, heterogeneous nucleation may take place. Heterogeneous substrates can be found in the liquid when impurities are present or when refining particles are added on purpose. Heterogeneous nucleation can also be initiated on crucibles when the solidification is done in a crucible. In these cases, the substrate helps in promoting the nucleation and reduces the nucleation undercooling needed for the formation of a new crystal. Practically, the heterogeneous nucleation is more frequent than the homogeneous due to the presence of nucleation sites leading to an energy advantage. In the heterogeneous nucleation, the different surface tensions must be taken into consideration: solid-liquid σ_{LS}, solid-substrate $\sigma_{S\text{-}Sub}$, and liquid-substrate $\sigma_{L\text{-}Sub}$. If the solid phase (crystal) formed is modeled by a spherical cap, the variation of the free energy of heterogeneous nucleation ΔG_{het} can be related to that of homogeneous nucleation by the relation:

$$\Delta G_{het} = \Delta G_{hom}\, f(\partial) \qquad \text{with} \qquad f(\partial) = \frac{(2+\cos\partial)\,(1-\cos\partial)^2}{4} \qquad \textit{Eq. 1.3}$$

where ∂ is the wetting angle of the crystal formed on the substrate. In the case of heterogeneous nucleation, the critical radius r^* is not changed when compared to homogeneous nucleation, whereas the critical number of structural units is decreased by the factor $f(\partial)$. As a result, the solid volume required to form a critical nucleus decreases significantly. The same applies to the critical free energy [1, 2].

1.1.3 Solid-liquid interface morphology

During solidification, the solid-liquid interface exhibits a spatial structuration which has a major influence on the final material properties. Depending on processes parameters and on materials characteristics, the growth can be columnar or equiaxed, and various types of morphology can develop. For example, during directional solidification of a single phase material, the interface can present cellular structures at low pulling speeds and dendritic structures at high pulling speeds (Figure 1.2a) [3], or faceted (Figure 1.2b) [4].

Once the nucleus has formed after homogenous or heterogeneous nucleation, growth can begin, and is mainly determined by three key factors:

- Heat and solute diffusion in the liquid.
- Capillarity.
- Kinetics of atomic attachment to the interface.

The relative importance of each of these factors depends on the material under consideration and on the solidification parameters.

In the case of a pure material, the origin of the destabilization of the interface is solely thermal, the growth is controlled by the latent heat removal and its kinetics governed by the thermal diffusion [1]. In the case of alloys, the thermal diffusion is faster than the solute diffusion. Thermal diffusivity varies from 10^{-3} cm^2/s for organics to 10^{-1} cm^2/s for metals, which is several orders of magnitude larger than the solute diffusivity (about 10^{-5} cm^2/s). Thus, slow solute diffusion is often the limiting physical process. Considering a binary alloy of solute concentration C_0, whose solute solubility in the solid phase is different than the one in the liquid phase. The partition coefficient k is defined by the relation C_S/C_L, with C_S and C_L the equilibrium solute concentrations, respectively, in the solid and liquid phases. If $k < 1$, solute is rejected from the solid upon solidification and accumulated in the melt in front of the interface. Consequently, a solute boundary layer of thickness δ_c will progressively build up. This layer is characterized by the solute diffusion in the liquid D_L and the interface velocity V:

$$\delta_C = D_L/V \qquad \textit{Eq. 1.4}$$

Curvature appears with non-planar microstructures forming at the solid-liquid interface. In addition to the solute and thermal diffusion lengths, this interface curvature introduces a third length scale, the capillary length d_0:

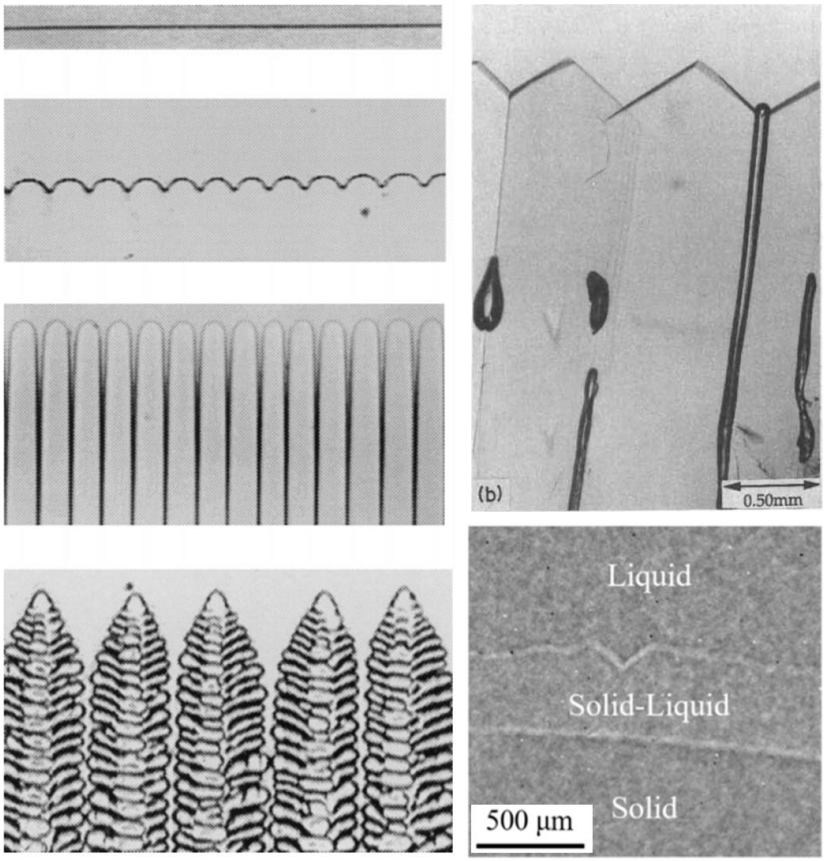
$$d_0 = \Gamma/\Delta T_0 \quad \text{for an alloy} \qquad \textit{Eq. 1.5}$$

$$d_0 = \Gamma\, C_P/\Delta H_m \quad \text{for a pure material} \qquad \textit{Eq. 1.6}$$

with $\Gamma \left(= T_M \sigma_{LS}/\Delta H_m\right)$ the Gibbs-Thomson coefficient function of the solid-liquid surface tension σ_{LS}, T_M the melting temperature of pure material, ΔH_m the latent heat of melting; ΔT_0 $(= mC_0(k-1)/k)$ is the equilibrium freezing range of the alloy, m is the *liquidus* slope, and C_P is the heat capacity of the liquid. The capillary length represents the characteristic length scale below which capillary effects prevail. When the interface radius of curvature reduces, the capillary effects make the equilibrium temperature to reduce. Mullins and Sekerka [5] investigated the incorporation of the capillarity into the analysis of the interface stability during solidification. Beyond an absolute stability threshold, the capillary effects are opposite to the curvature and re-stabilize the system. They act then in the selection of characteristic sizes of structures [6]. For an anisotropic surface tension, σ_{LS} is replaced in the capillary constant Γ by the surface stiffness $\sigma(\theta)$ which is written as [7]:

$$\sigma(\theta) = \sigma_{LS}(\theta) + \frac{\partial^2 \sigma_{LS}(\theta)}{\partial \theta^2} \qquad \textit{Eq. 1.7}$$

θ being the angle between the interface normal and the reference axis. The capillary forces are least effective at smoothing out protrusions of the solid–liquid interface in directions where the stiffness is minimum.



(a) (b)

Figure 1.2 – (a) Steady-state patterns formed during directional solidification of a succinonitrile-coumarin alloy: planar interface, cellular interface, deep cells and dendritic array [3]; (b) Faceted interface during directional growth of salol [4] (top) and silicon [8] (bottom).

Based on physical and experimental conditions two types of solid-liquid interface can be described: rough or faceted interfaces.

(a) Rough solid-liquid interface

Rough solid-liquid interface is created when the transition from liquid to solid phase takes place across multiple atomic layers and the ordering of atoms increases progressively from the highly ordered solid phase to the disorganized liquid phase (Figure 1.3a). The atomic layers within the interface undergo a slow transition whereby their thermodynamic properties gradually change from those of a liquid to those of a solid. Because most lattice locations are suitable for atom deposition, this configuration makes the growth of the interface easier and faster compared to faceted growth. This is known as continuous or normal growth. Usually, this kind of growth is seen in metallic alloys at low solidifications rates (Figure 1.2a) [9].

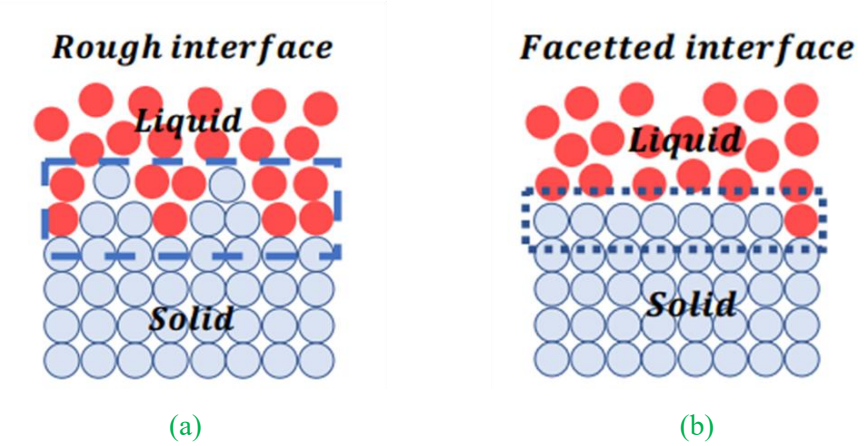


Figure 1.3 – Schematic illustration of (a) rough and (b) faceted interfaces.

(b) Faceted solid-liquid interface

Facets are defined as flat, planar surfaces that can limit the crystal during solidification. These surfaces result from a specific alignment of the crystal lattice, which leads to a highly anisotropic surface energy distribution. This anisotropy in surface energy causes the crystal to grow preferentially along certain crystallographic directions, forming smooth, flat faces, or facets (Figure 1.2b) [10]. Facets are a characteristic feature of crystals with strong anisotropic attachment kinetics and play a significant role in the morphological stability and dynamics of the solidification front. These facets can vary in size, shape, and orientation, depending on factors such as the type of solid material, the nature of the liquid, and the conditions under which the interface is formed. Both anisotropies of the solid-liquid surface energy and of the kinetic attachment coefficient need to be taken into account to model facets in crystals [11].

Conversely from the rough interface, faceted interface is characterized by a sharp transition from the liquid to the solid phase, resulting across a single atomic layer (Figure 1.3b). In such interface, the ordering of atoms increases suddenly from the liquid to the solid state, occurring with a high entropy of fusion. In this case, the growth is slower than in rough interface due to the difficulty of liquid atoms to be adsorbed on the planar interface and occurs in materials with solid-liquid interface more ordered and smoother. The presence of favorable sites, such as steps or defects, eases the attachment of atoms. In the case of steps, it leads to lateral growth.

Faceted morphology remains underexplored in materials science, as the facets are considered as a complex behavior of the solid-liquid interface. However, faceted interfaces are of high interest because they correspond to the growth behavior of semiconductors, for example silicon used in photovoltaic applications (Figure 1.2b). Understanding facet growth also provides valuable insight into crystallographic properties and into the formation of structural defects contributing to the development of models and simulations of crystal growth.

1.1.4 Surface roughness criterion

By evaluating the attachment rate of atoms at the interface (which depends on the diffusion of atoms in the liquid) and the detachment rate (which depends on the number of neighbors linking the atom to the interface), Jackson [12] determined a roughness criterion α_J [13] which allows to predict the faceted or rough character of the solid-liquid interface during growth:

$$\alpha_J = \frac{\eta}{Z}\frac{\Delta H_m}{R_g T_M} \qquad \textit{Eq. 1.8}$$

Here η is the number of nearest neighbor sites adjacent to an atom in the plane of the interface, Z the total number of nearest neighbors of an atom in the crystal, ΔH_m represents the latent heat of melting, T_M is the melting temperature, and R_g is the universal gas constant. The factor η/Z is always lower than 1. The criterion for determining the interface morphology is: $\alpha_J > 2$ faceted morphology; $\alpha_J < 2$ non-faceted morphology. A list of different materials with the corresponding value of the coefficient α_J as well as their growth morphology from different phases is given in Table 1.1.

The Jackson criterion has some limitations. First, the solid-liquid interface of materials having Jackson factor α_J between 2 and 3 can grow with faceted and/or non-faceted morphology depending on the crystallographic orientation [14, 15] . It does not address a sharp transition

between faceted and non-faceted morphologies. In addition, the Jackson criterion is qualitative and does not provide information about the size of the interface or the number of the atomic layers at the solid liquid interface. However, in the solidification of pure materials, the Jackson criterion has demonstrated notable effectiveness and a robust correlation with the experimental results [16].

Table 1.1 – Growth morphologies and Jackson factor.

Jackson Factor α_J	Material	Phase	Morphology
≈ 1	Metals	Molten bath	Non-faceted
≈ 1	Plastic crystals	Molten bath	Non-faceted
2-3	Semiconductors	Solution	Non-faceted / faceted
2-3	Semimetals	Solution	Non-faceted/ faceted
≈ 6	Molecular crystals	Solution	faceted
≈ 10	Metals	Vapor	faceted
≈ 20	Complex molecules	Molten bath	faceted
≈ 100	Polymers	Molten bath	faceted

1.1.5 Undercooling during growth

Growth kinetics and interface stability during solidification are linked to the phenomenon of undercooling, which occurs when a material remains in its liquid state even below its equilibrium melting point, T_M. The undercooling ΔT, given by the difference between T_M and the actual temperature of the liquid T, is a critical factor in the solidification process and is always present to some degree. As a result of undercooling, the actual position of the solid-liquid interface within the sample does not align with the melting (or *liquidus*) isotherm. Instead, it is influenced by different factors contributing to the undercooling of the interface, including the thermal gradient G, the pulling velocity V_p, the nature of the material and the presence of impurities. Understanding the nature of the undercooling is essential for predicting and controlling the microstructure of the solidified material, as it can influence, the solid-liquid interface structuration, the grain nucleation size, morphology, and defect formation. The total solid-liquid interface undercooling ΔT can be written theoretically as [17, 18]:

$$\Delta T = \Delta T_t + \Delta T_c + \Delta T_r + \Delta T_k \qquad \textit{Eq. 1.9}$$

with ΔT_t, ΔT_c, ΔT_r and ΔT_k respectively the thermal, constitutional, curvature and kinetic undercoolings.

Thermal undercooling ΔT_t occurs due to the release of latent heat at the solid-liquid interface during the transition from the liquid to the solid phase. Thermal undercooling is important during the solidification because the latent heat can slow down the growth and vary the local thermal gradient at the interface [1]. Constitutional undercooling ΔT_c takes place when the system that is solidifying is an alloy or when impurities are present. Rutter and Chalmers [19] introduced the notion of the constitutional undercooling from purely thermodynamics to explain, in the case of alloys and under a positive thermal gradient, the morphological instability of the interface. This instability leads to the formation of cellular and dendritic microstructures. If the interface is adjacent to a thermodynamically unstable liquid, the interface itself may become unstable when the imposed temperature is lower than the equilibrium temperature.

Curvature undercooling ΔT_r is defined as $\Delta T_r = \Gamma K$, with K the local interface curvature. The capillarity constant Γ (Gibbs-Thomson) parameter is given by $\Gamma = {\sigma_{LS}}/{\Delta S_m}$, σ_{LS} being the interface energy and ΔS_m the entropy of melting. When the radius of curvature reduces, it reduces the melting temperature of the crystal.

The dependence on the kinetic attachment of the atoms is characterized by the kinetic undercooling ΔT_k. The kinetic attachment depends on the local crystallographic orientation and allows kinetic attachment anisotropy to be considered. The relationship between the kinetic undercooling and the local normal velocity V_f of the solid-liquid interface depends on the type of growth of the crystal [2].

1.1.6 Growth types

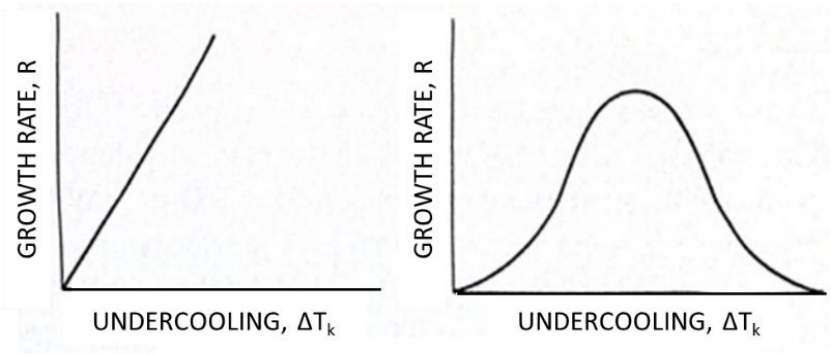
Growth in the concept of crystallization is the process by which molecules or atoms are added to a solid surface, leading to the growth and to the expansion of the crystal. The mechanism driving this growth can vary depending on the nature of the structure of the interface and on the thermodynamic parameters.

1.1.6.1 Continuous growth

When atoms or molecules are continuously added to the interface, it advances uniformly and experiences continuous growth. The interface can continue to grow in a steady state because the process occurs without the need to overcome a substantial energy barrier. The growth rate under continuous growth is related to the kinetic undercooling ΔT_k by [2]:

$$V_f = \mu_1 \frac{D_L(T)}{D_{LM}} \Delta T_k \qquad \textit{Eq. 1.10}$$

with μ_1 the kinetic coefficient, a constant that takes into consideration the probability of atoms to be incorporated at the interface, the lattice geometric factors of the crystal and the latent heat of solidification, $D_L(T)$ the liquid diffusion coefficient and D_{LM} the liquid diffusion coefficient at the melting temperature. If $D_L(T)$ and D_{LM} are similar, as in metals for example, the relationship simplifies to $V_f = \mu_1 \Delta T_k$ (Figure 1.4a). When D_L varies strongly with temperature, as in oxide glasses and polymers, the relationship can be more complicated (Figure 1.4b).



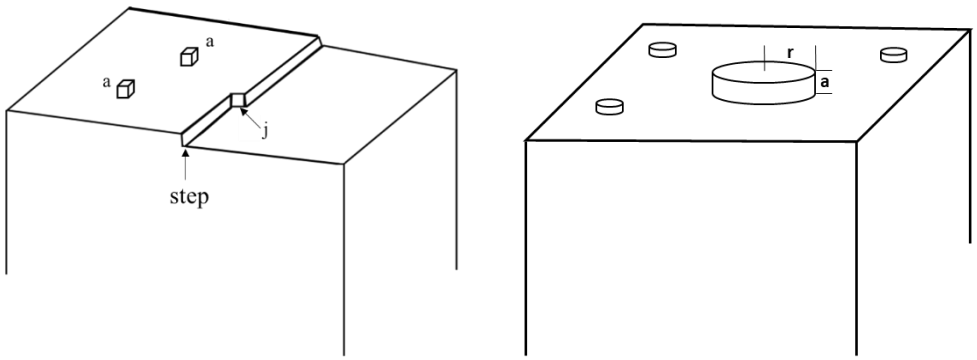
(a) (b)

Figure 1.4 – Characteristic continuous growth curves for (a) non viscous liquids, such as metals, and (b) oxide or organic polymers [2].

1.1.6.2 Lateral growth

Materials with high entropy of melting most likely adopt atomically flat interfaces. In such interfaces, if a single atom leaves the liquid and attaches itself to the flat solid interface, the number of broken bonds associated with the interface, i.e. the interfacial energy, is increased. There is therefore little probability for the atom to remain attached to the solid and it is likely to jump back into the liquid. However, if the interface contains steps, liquid atoms tend to attach at the steps with a much lower resulting increase in the interfacial energy. Jogs are other

irregularities in the interface, they are small displacements in the steps as shown in Figure 1.5a. If the step contains a jog (j), atoms from the liquid attach to the solid without any increase in the number of broken bonds and the interfacial energy remains unchanged. Consequently, the probability of an atom remaining attached to the solid at these positions is much greater than for an atom joining a flat facet. Smooth solid-liquid interfaces can therefore be expected to advance by the lateral growth of steps. Since the steps and jogs are non-equilibrium features of the interface, growth is very dependent of how the steps and jogs can be formed.



(a) (b)

Figure 1.5 – (a) Atomically flat interface with a step, a jog in the step (at j) and two adsorbed atoms (at a). (b) Two-dimensional clusters on a flat close packed surface [2].

(a) Growth by two-dimensional nucleation

Two-dimensional nucleation type of growth occurs when critical nuclei form on the surface of a crystal and afterward expands to create a new layer (Figure 1.5b). In this type of growth, the free energy barrier is necessitating a critical amount of undercooling to initiate the nucleation. When the nuclei form, they grow fast until they cover the entire interface. The kinetics of this growth can depend on the undercooling with exceptional high nucleation rates producing growth patterns similar to those observed in continuous growth [2]. The relationship between the growth rate V_f and the kinetic undercooling in this case is given by:

$$V_f = B \exp\left(-\frac{A}{\Delta T_k}\right) \qquad \textit{Eq. 1.11}$$

with A and B are constants. B depends on the lattice geometric factors and on the nucleation rate, A also depends on geometric factors and on the surface tension at the interface.

(b) Growth by screw dislocations

A screw dislocation emerging at the solid-liquid interface creates a step on the crystal surface (Figure 1.6) allowing a continuous growth without the need for two-dimensional nucleation. This step is self-perpetuating which means that no matter how many layers of atoms are deposited on the face, the step will persist. This mechanism allows growth at much lower undercoolings than by the two-dimensional nucleation [20]. For a single screw dislocation, a spiral staircase structure is created on the crystal surface by continuously depositing atoms at the exposed step. The step therefore rotates continuously about the point where the dislocation emerges. Since one end of the step is fixed, the step rapidly winds itself up (Figure 1.6). The relation between the growth rate V_f and the kinetic undercooling in the case of a single dislocation is given by [2]:

$$V_f = \mu_2 \Delta T_k^2 \qquad \textit{Eq. 1.12}$$

with μ_2 is a constant that depends on the diffuseness parameter, on lattice geometric factors and on the dislocation density.

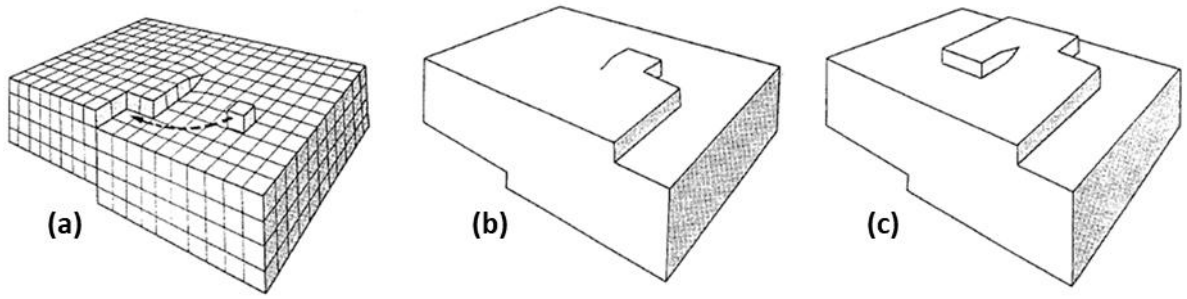


Figure 1.6 – Schematic drawing showing the point of emergence of a screw dislocation emerging at the surface of a cubic solid, and the development of a growth spiral when growth occurs on this surface [21].

1.2 Solidification of transparent organic materials

Both researchers and engineers look for model experiments that capture the key aspects of the materials microstructures and defect formation during solidification. The main advantages of transparent organic materials are the transparency to the visible light and their low melting point that is usually below 100°C. Their transparency allows direct observation of the interface morphology and dynamics during the solidification process. This ability offers significant

potential for clarifying complex and rich aspects of solidification both in pure materials and alloys [12, 22]. Hunt and Jackson [23] achieved a big breakthrough on studying transparent model alloys during solidification process and allowed to gain a better knowledge of the behavior of the solid-liquid interface during the solidification and of the associated mechanisms.

Moreover, the *in situ* observation of the solidification of transparent organic materials provides experimental results which reinforce the validation and advances of numerical simulations [24-28]. These simulations are effective in giving precise description of the formation of the morphological instability, either in 2D or 3D work, of the solid-liquid interface and predict its behavior [29-31].

1.2.1 Types of microstructures in an interface with rough morphology

Jackson and Hunt [12] investigated several organic systems which have small entropies of melting and therefore fulfill the condition $\alpha_J < 2$. No evidence of faceting was found at any growth rate, confirming that they solidify in a similar way compared to the metals forming cellular and dendritic microstructures. Timmermans [32] had earlier studied some organic compounds and found that they form cubic and highly plastic phases just below their melting point so they called them “plastic crystals” [33].

(a) Cellular growth morphology

The cellular instability of the initially planar solid-liquid interface occurs above a threshold critical velocity [5, 14] . When the velocities are just above it, the system forms shallow-cellular patterns with high nonlinear process. Anisotropy of the interface is essential for stabilizing the cellular patterns, and to obtain stable axial-cellular patterns, with a specific intercellular spacing range. Figure 1.7 shows the development of an initial perturbation wave evidencing the instability of the flat solid-liquid interface of a succinonitrile-1.61wt% salol alloy [22]. Instability can only develop if the constitutional supercooling criterion allows it, i.e. if the equilibrium temperature profile induced by the partition of the solution is above the actual liquid temperature. If the growth velocity continues to increase, there is a transition from smooth rounded fingers to pointed dendritic shape with side branches.

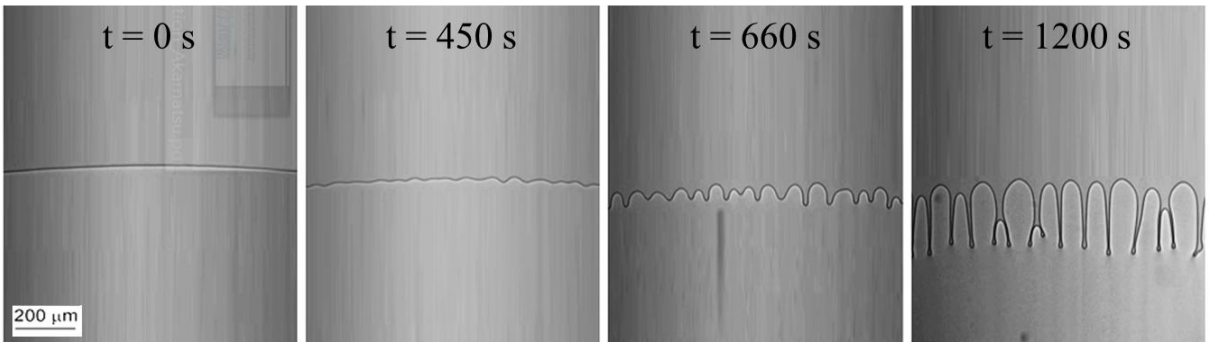


Figure 1.7 – Development of initial perturbation wave for instability of planar interface during directional solidification of succinonitrile-1.61 wt% salol (G = 5 K/mm, V_p = 0.9 µm/s) [22].

(b) Dendritic microstructures

Dendritic growth is the most common morphology among the metallic systems. In the past few years, a lot of studies have been done using transparent materials as analogues to investigate the dendritic growth during solidification. The term dendrite derives from the Greek word "*Dendron*" meaning tree. Indeed, the shape of a metallic dendrite can be seen as tree-like, with a central trunk being the body of the dendrite from which secondary arms extend and the tertiary arms follow. It is worth mentioning that thousands or millions of dendrites can compose a crystallized alloy. The final properties of the cast or welded material depend on the dendrites shape and size [1, 2, 34]. For instance, the hardness or the softness of a material can be influenced by the morphology of dendrites. Hence, the material flexibility or elasticity before it breaks are also influenced by the dendrite morphology [35]. In addition, they can impact the durability of the material and define whether the material has good or poor electrical conductivity [36, 37].

According to Glicksman and Lupulescu [38], the formation of dendrites depends on two key processes that define its characteristic length scales. First, the steady-state growth of the tip region leading to the development of a primary trunk, and second the dynamic behavior of secondary and tertiary side branches. Figure 1.8 illustrates two examples of dendrites in pure organic materials (succinonitrile, that is a body-centered cubic crystal and pivalic acid, that is a face-centered cubic crystal). The perfect shape of a dendrite consists of a smooth paraboloidal shaped tip region followed by a periodic trail of branches spreading from the primary trunk. The dendrites have a complex shape depending on the interfacial anisotropy which makes their studies complex. Experimental demonstration of the dependence of dendritic growth on the

crystallographic anisotropy has been brought by the discovery of the seaweed structures by numerical simulations [39] and directional solidification experiments [40].

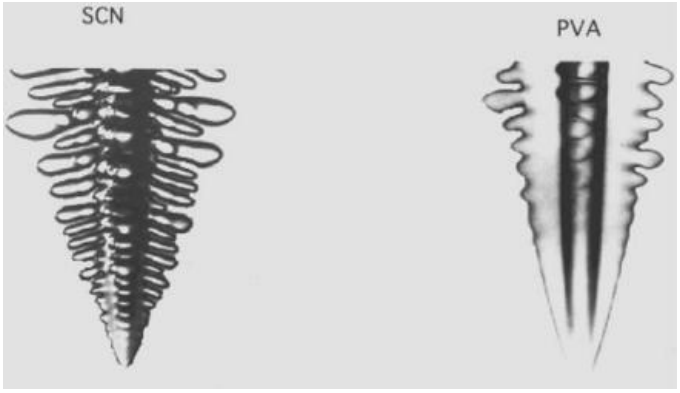
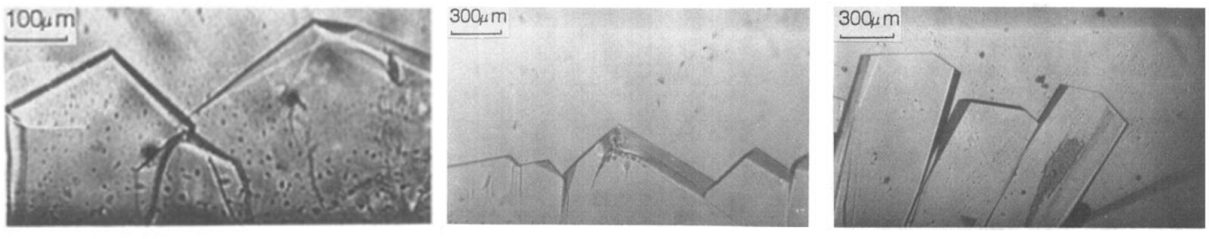


Figure 1.8 – Steady-state dendrites growing in high-purity supercooled organic materials: succinonitrile (SCN) and pivalic acid (PVA)[38].

1.2.2 Faceted morphology

The faceted interface morphology is characterized by a flat surface aligned along specific crystallographic planes. Several research works were done to better understand the facet behavior during solidification of several materials, such as semiconductors like silicon that are semi-faceted and exhibit facets along {111} planes [8, 41-45] .

The solidification of organic systems exhibiting faceted interface has also been studied. In the end of the 80's, Shangguan and Hunt [46-48] were among the pioneers to observe faceted growth *in situ* and to study the physical process and growth mechanisms, using different organic materials (Figure 1.9), such as salol ($\alpha_J \approx 7.4$), thymol ($\alpha_J \approx 8.2$), and o-terphenyl ($\alpha_J \approx 6.3$) [16].



(a) (b) (c)

Figure 1.9 – Images showing growth of a faceted interface of: (a) salol, (b) thymol, and (c) o-Terphenyl [46].

During the 90's, Fabietti and Trivedi [49-51] performed detailed studies on the directional solidification of faceted materials to characterize the growth mechanisms and the relationship between interface morphology and experimental conditions. Dey and Sekhar then gave particular attention to the growth of salol crystals. A combined numerical and experimental work was carried out to determine the conditions for the onset of cracks during directional growth of macroscopically faceted crystals. Still with salol but using a microscopic interferometer, Higashino *et al*. [52] simultaneously measured the growth rate and the temperature and solute concentration profiles in the vicinity of the solid-liquid interface. It was found that the distribution of temperature ahead of the interface is influenced by the released latent heat. Later, these authors studied the influence of gravity on the temperature and concentration distributions in front of the interface [53, 54].

Börzsönyi *et al.* [55] characterized the thin-sample directional solidification of monoclinic biphenyl ($\alpha_J \approx 6.6$) to determine the required conditions to have either a strong growth-induced plastic deformation, or deformation-free weakly faceted growth patterns. The grown facets of biphenyl belong to different type of crystallographic planes and they have different growth behavior. Facets <001> oriented grow slowly due to the lack of dislocations, resulting in flat and stable surfaces. Whereas facets <110> oriented evolve fast due to the presence of dislocations. These authors found that solidification at high growth rates leads to rough growth showing cellular or dendritic patterns on the interface, while when the growth rates are low faceted interface is indeed observed.

Fabietti and Trivedi [51] studied the faceted interface obtained during the solidification of pure naphthalene ($\alpha_J \approx 6.4$) and naphtelene-1wt%camphor alloy. Naphtelene is not only transparent but also exhibits photoelastic properties. Photoelasticity is a property of certain optically homogeneous materials that become birefringent under stress. Transparency to the visible light permits the observation of stress configuration through a set of fringes that characterizes the magnitude of stress. When placed under polarized light, the unstressed polycrystalline birefringent material shows different colors depending on the orientation of each grain. When stress is applied or an internal stress develops during growth, the interaction between the natural optical axis and the stresses results in a set of fringe patterns. The characterization of the growth mechanisms and the relationship between interface morphology and experimental conditions have been established. They found that when highly faceted orientations grow in the direction of the flow, stresses develop when the conditions of growth are ahead of the threshold of the planar interface instability. When the interface is disturbed, stresses are formed and are relieved

by the formation of parallel grain boundaries. Furthermore, experiments were designed and carried out to determine the temperature and composition, at the interface under non-equilibrium conditions. For the first time, the authors showed how defects are produced at the solid-liquid interface during unidirectional solidification experiments in faceted materials. These authors also performed directional solidification in *tert* butyl alcohol-water system ($\alpha_J \approx 2.7$) [49] showing that a morphological transition with both characteristics, faceted and non-faceted can be induced by the solute in a way that is similar to the cellular to dendrite transition in non-faceted materials.

1.3 Defects in crystals and during solidification

During the solidification process, faceted interfaces can present various defects that significantly impact on the materials final properties, performance and quality. These defects arise due to the inherent anisotropy in the crystal growth dynamics and to the complex interplay of the thermal and mechanical factors especially in organic materials [56]. These defects can evolve over time, leading to a non-steady state morphology of the interface which makes the quantitative and the qualitative analyses of facets and their behavior more complex and difficult.

Therefore, defects are broadly categorized into chemical and structural defects. Chemical defects deal with changes in chemical composition and with the presence of precipitates, whereas structural defects are primarily related to physical geometric deviations from the perfect crystal lattice and presence of misorientations (grains and sub-grains). Both types of defects can affect crystal characteristics and properties.

Crystals, whether organic or inorganic, inherently contain defects. These defects can be investigated through in situ techniques, which offer insights into their formation and evolution during growth processes. Primary defects can be classified into several categories: point defects, such as lattice vacancies, (self-)interstitials, molecules in incorrect orientations, deviations from stoichiometry, or impurities; line defects, or dislocations; planar defects, including high- and low-angle grain boundaries, growth striations, growth sector boundaries, twin boundaries, stacking faults, and antiphase boundaries; volume defects, such as inclusions (e.g., bubbles) and precipitates; mechanical defects, including cracks, scratches, and indentations, often resulting from improper handling or storage. Some of these defect types will be described in more detail in the following sub-sections.

1.3.1 Bubbles

Bubbles, which are considered as volume defects [56], refer to gas pockets that nucleate and grow within the liquid phase during the solidification process. Bubbles are usually formed due to the presence of residual gaseous impurities in the melt, which have a lower solubility in the solid compared to the liquid phase. Usually, they are formed if the solidification process is not realized under vacuum. Bubbles can also precipitate when the growth velocity increases beyond a certain threshold. In this case, the ability of the liquid to diffuse gases out of the system is compromised due to the reduced time for diffusion. Sometimes, bubbles adhering to the growth front may absorb additional gas from the melt, forming channels as they move forward with the solidification front. Additionally, bubbles can originate from solid retraction and the difference in density between the liquid and solid phases.

The incorporation of gas bubbles in crystals may be encountered both in nature and industrial applications. In manufacturing processes, bubble incorporation may be an advantage or not. During casting of metals, they generally degrade the mechanical properties of the material [57-60]. But sometimes, ordered cylindrical bubbles may improve some functional properties (impact and acoustic energy absorption, permeability, thermal conductivity…) [61-66].

Many scientists observed bubbles during the solidification process. According to Akamatsu and Faivre [67], whom worked on CBr_4-C_2-Cl_6 system, the formation and growth of gas bubbles during directional solidification are mainly driven by the residual gaseous impurities in the melt. As the solidification front progresses, the gas concentration in the liquid increases, leading to bubble nucleation at critical undercooling temperatures. This nucleation generally occurs in the intercellular grooves during short intervals following upward velocity jumps in the solidification process. After nucleation, the bubbles can either grow into stationary tubular structures or become entrapped by the solid, depending on the growth velocity and microstructural conditions.

Lee and Hunt [68] observed the development of bubbles in real time using X-ray techniques in aluminum alloys, and they found out that when the rate of solidification and the initial hydrogen concentration in the melt increase, the number of bubbles increases, but their size decreases.

Gupta *et al.* [69] made a review on the conditions of pore formation in cast metals and alloys. They mentioned that the solid-liquid interface is the favorable site to the nucleation of a gas bubble. In relation to the advance of the solidification interface, four types of bubble behavior have been distinguished. (i) A bubble can grow as gas diffuses into it from the surrounding

liquid. Once it becomes big enough, it may detach and float away. (ii) The bubble moves with the interface, growing simultaneously until eventually becomes trapped. (iii) The bubble grows at the same velocity as the interface until it becomes incorporated into it and elongates cylindrically. (iv) The bubble can be rapidly overgrown by the interface and be entrapped.

Han [70] observed bubbles moving in the mushy zone with eruption and discontinuous jumping at high growth rates, while they couple with neighboring dendrites at low growth rates. The eruptional and jumping motions of the bubble in the mushy zone are driven by three key forces: the curvature difference at the ends of the bubbles, the internal pressure from gas diffusion, and the dendrite contraction squeezing the bubble out of the liquid pocket. These forces let the bubble move within or out of the mushy zone at high speeds.

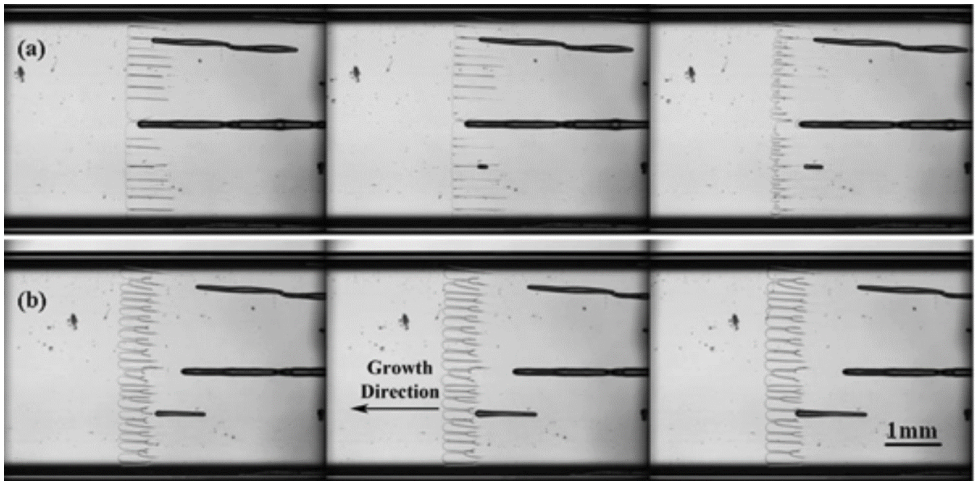


Figure 1.10 – (a) Formation of a bubble in the mushy zone near existing bubbles. (b) Overgrowth of the existing bubbles due to the growth of the new bubble. (V_p = 2.84 μm/s, the time interval of the successive images is 60 s) [71].

Teng *et al*. [71] found that bubbles form in the mushy zone during the directional solidification of succinonitrile (Figure 1.10a). These bubbles nucleate often near the roots of the dendrites, where dissolved gases are concentrated. When new bubbles form and emerge, they can cause existing bubbles to be overgrown and trapped by the solid (Figure 1.10b). The entrapped bubbles are much larger than those formed in the mushy zone, resulting in variations in bubble size in the solid. Moreover, they found that the average spacing between bubbles and the instantaneous bubble spacing varies with the increase of the growth duration. Hence, as more bubbles form in the mushy zone, the spacing decreases. Once a certain number of bubbles form, the average spacing stabilizes while the instantaneous one keeps varying due to the formation

of new bubbles and the entrapped overgrowth ones. In addition, when increasing the pulling velocity, bubbles start to jump towards the liquid zone forming tear dropped bubbles.

1.3.2 Growth striations

Growth striations are visible layers or zones of irregularity that form as crystals grow. These striations, which appear as parallel lines or bands on the surface or within the crystal, are essentially defects that arise during the crystal growth process, whether from solutions or melts. They occur frequently in organic crystals [72]. Early discoveries of striations in semiconductor crystals were made by Goss *et al.* [73] in 1956 who found growth striations parallel to the interface in silicon due to variations in oxygen concentration, and by Bardsley *et al.* [74] in 1962 who determined the true morphology of the germanium cellular structure thanks to the visualization of the growth striations.

Thermal striations are growth-induced inhomogeneities in crystals that align along the faceted or non-facetted growth surface. In the case of faceted growth with step-bunching, these inhomogeneities can be traced back to macrosteps. These often-periodic inhomogeneities emerge because growth rates fluctuate over time due to temperature fluctuations [72], as shown through in cross section of Figure 1.11a.

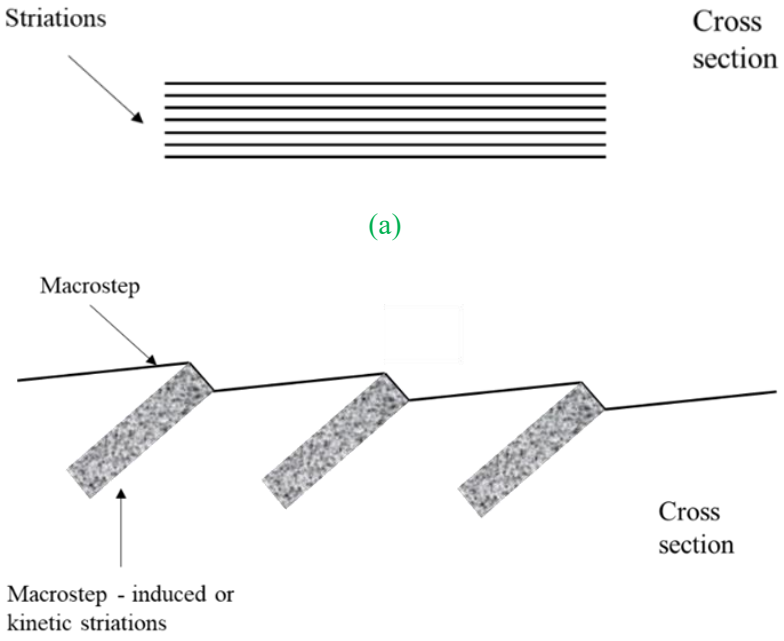
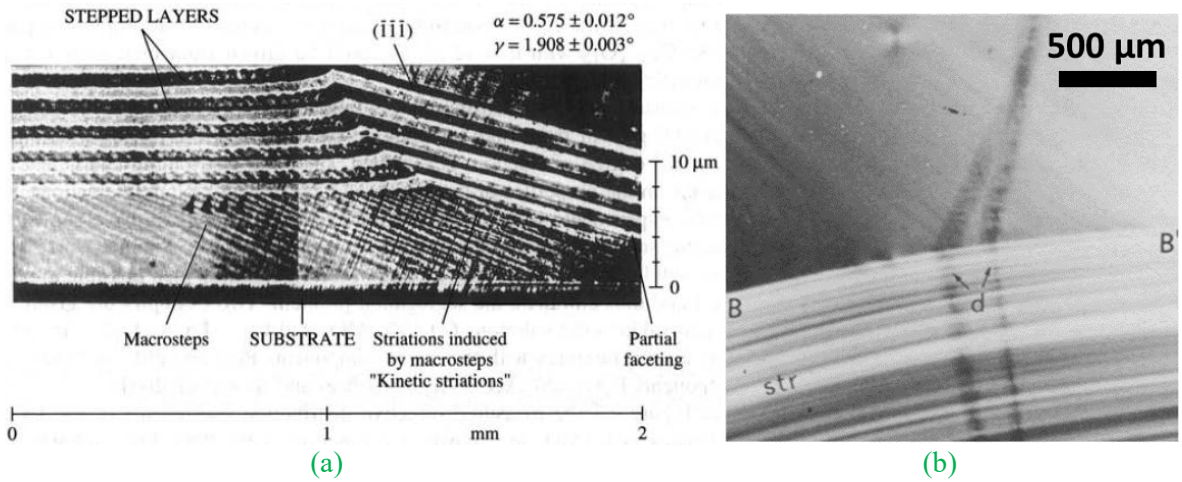


Figure 1.11 – (a) "Thermal striations" caused by temperature fluctuations leading to growth rate variations. (b) "Kinetic striations" caused by macrosteps and lateral growth-rate differences [72].

The second type of growth striations is caused by lateral growth-rate differences and is called macrosteps-induced or kinetic striations (Figure 1.11b). During growth from melt in small temperature gradients such striations are typical to be seen when the interface exhibits faceted morphology. Also, they are very common in growth from solution and from high-temperature solutions [72]. The growth surfaces schematized in Figure 1.11b show macrosteps with a terrace-and-riser structure, having both different growth rates. The terrace grows because of a lateral propagation of a single or double step.

The difference in growth rates can also result in impurity or dopant incorporation leading to growth striations and marking the trace of the macrosteps. In the case of doped crystals such as semiconductors and lasers, the striations are found to be very pronounced. Figure 1.12a illustrates these induced-macrosteps, named kinetic macrosteps, in multilayer liquid phase epitaxy of GaAs [72, 75].

Growth striations can also arise from local variations of impurity content such as contaminants of the solvent (in the case of a solution) or of the melt and deviations from stoichiometry. In addition, they can be created due to variation of concentrations of the system [76-77]. Figure 1.12b presents an example where striations are formed in Czochralski-grown gadolinium gallium garnet due to the deviation from stoichiometry [76]. The crystal rotation causes periodic striations, till *B-B'* where the interface orientation suddenly changes, and no more striations were observed.

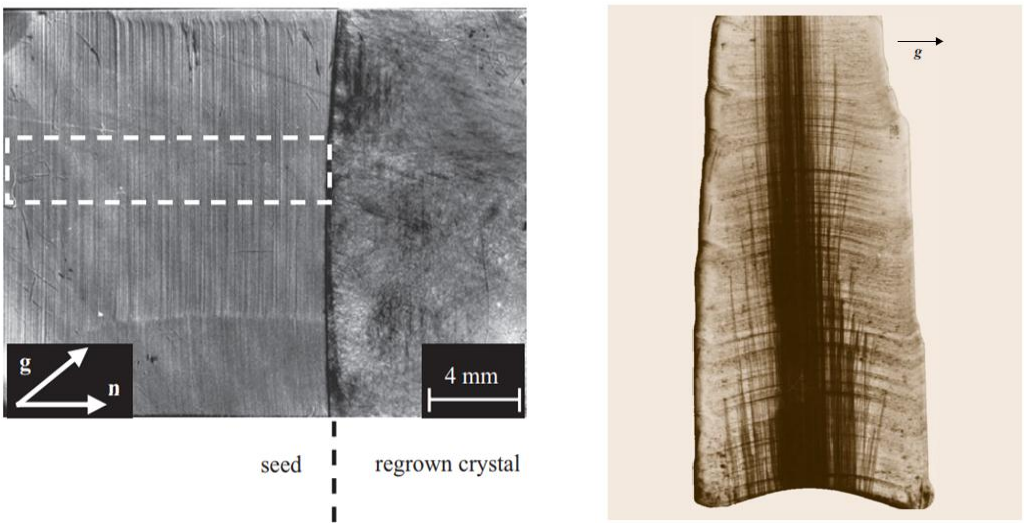


(a) (b)

Figure 1.12 – (a) Composite interference contrast micrograph of a multilayer liquid phase epitaxy of GaAs. On the left side the macrosteps and macrostep-induced striations are clearly visible [72, 75]. (b) Czochralski-grown gadolinium gallium garnet highlighting the presence of dislocations (d) and striations (str) [76].

Growth striations are clearly detected as a contrast in X-ray topographic images as shown in Figure 1.13a [78]. The example highlights a topograph of a (110) plate, 450 µm of thickness, from a GaSb single crystal doped with Si. Figure 1.13b shows an example of a plate cut from the center of a Czochralski boule of the orthorhombic salol [77]. Due to the rounded interface, it exhibits curved striations (horizontal lines), which are accompanied by tiny gas bubbles that can be the source of growth dislocations. These are concentrated in the center of the boule, preserving their growth configuration with straight lines strictly perpendicular to the growth direction.

In general, growth striations lead to local changes of physical properties (e.g., optical birefringence, electric conductivity). This is a major problem in the growth of doped crystals for sophisticated electronic devices, for instance. It exists several solutions in order to reduce growth striations, such as: controlling and stabilizing the thermal gradient which can decrease thermal variations that occur on the solid-liquid interface. Therefore, the development of the formed microstructures is improved, in addition to the reduction of the thermal stresses that can cause cracks in the crystal [77, 79, 80]. Moreover, any vibrations around or rapid changes in the pulling velocity which can lead to the formation of striations should be avoided. The suppression of melt convection by growth under microgravity or in magnetic fields is one of many engineering controls that can improve homogeneity and crystal quality.

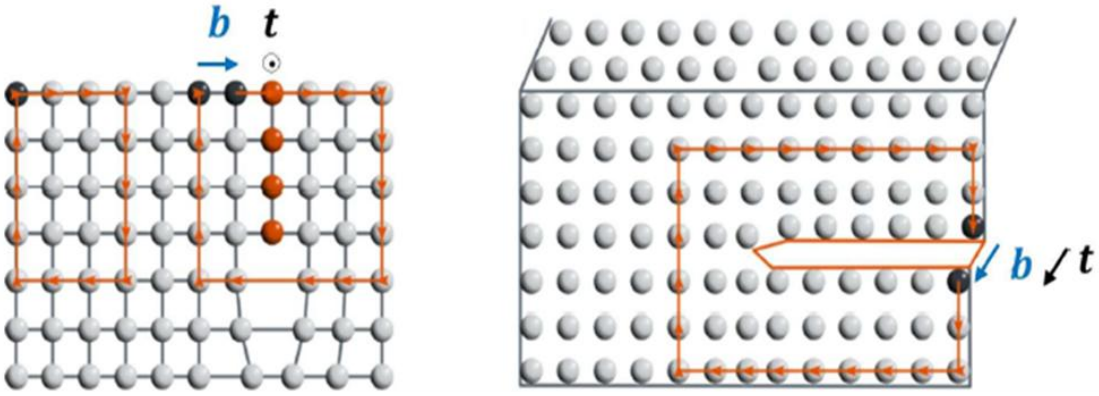


(a) (b)

Figure 1.13 – (a) X-ray topography of an highly doped GaSb crystal grown by the Czochralski method (at the left) and partially regrown by the vertical Bridgman method [78]; (b) Longitudinal cut plate from the center of a Czochralski boule of salol crystal (thickness of 1.3 mm and imaged length is about 40 mm) [77].

1.3.3 Dislocations

Dislocations are line defects within the lattice of a crystal, where the atomic arrangement is disturbed [81]. The idea of a Burgers' circuit helps clarify the definition of a dislocation. A Burgers' circuit is an atom-to-atom path that creates a closed loop in a crystal. But in a crystal that has a dislocation, the circuit cannot be closed. Leaving a gap known as Burgers' vector. The dislocation direction and magnitude are represented by this vector. Moreover, the dislocation type is defined by the angle formed between the line direction of the dislocation which is often referred to as the tangent (***t***) and its Burgers vector (***b***). Dislocations can be categorized into two main types, edge and screw (Figure 1.14). An edge dislocation occurs when ***b*** is perpendicular to ***t***, while a screw dislocation occurs when ***b*** is parallel to ***t***. Mixed dislocations are characterized by an angle between ***b*** and the dislocation line that is neither 0 nor 90°.



(a) (b)

*Figure 1.14 – Schematic drawing of dislocations and their corresponding Burgers' (**b**) and tangential (**t**) vectors: (a) edge dislocation, (b) screw dislocation.*

There are two basic types of dislocation movement. Glide occurs when the dislocation moves in the surface which contains both its line and Burgers vector. Climb occurs when the dislocation moves out of the glide surface, and thus normal to the Burgers vector. Glide of many dislocations results in slip, which is the most common manifestation of plastic deformation in crystalline solids. It can be envisaged as sliding or successive displacement of one plane of atoms over another on so-called slip planes. The slip planes and slip directions in a crystal have specific crystallographic forms. The slip planes are normally the planes with the highest density

of atoms, i.e., those which are most widely spaced, and the direction of slip is the direction in the slip plane corresponding to one of the shortest lattice translation vectors. Often, this direction is one in which the atoms are most closely spaced.

Different factors contribute to the occurrence of dislocations, including differences in temperature that can generate stresses within the materials. Strain and stress can be accumulated also due to the presence of impurities, these features can build up as the interface grows over time leading to the formation of dislocations [82]. The speed at which the solid-liquid interface grows can impact the number and the type of dislocations. It is worth mentioning that the dislocation formation and characteristics during the solidification process are also influenced by the intrinsic characteristics of the material, such as its crystal structure at atomic bonding.

Chen *et al.* [83] used multi-crystalline silicon (mc-Si) samples to investigate crystal defects present in this kind of materials. Figure 1.15 shows an optical micrograph of one of their samples where they found a lot of inhomogeneity of the dislocation distribution. Grain 1 exhibits a low density of dislocations compared to the other grains, while grain 3 exhibits 3 different regions marked as A, B, and C shows a high abundance of slip dislocations that are distributed in inhomogeneous way. The authors found that this inhomogeneity is attributed to the large number of slip dislocations present in mc-Si due to thermal stresses during the solidification process.

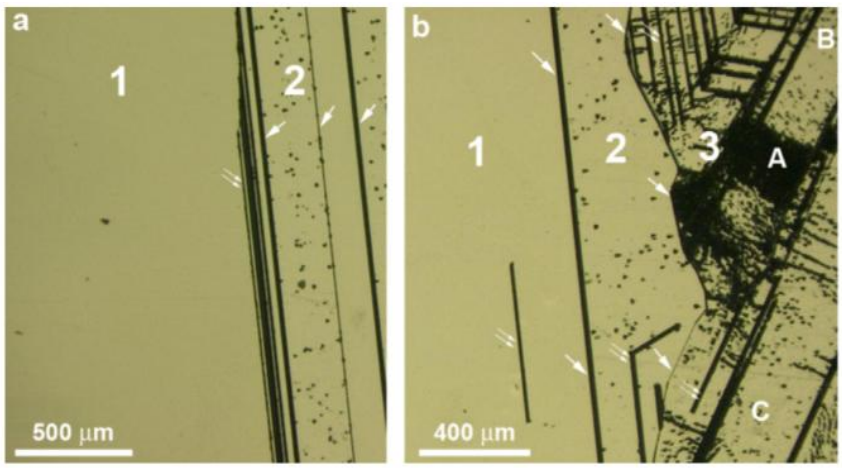


Figure 1.15 – Optical micrographs showing the inhomogeneous dislocation distributions in a multi-crystalline silicon sample grown in industrial directional solidification. Inhomogeneity in dislocation distribution is present both among grains (numbered) and in individual grains. The grain boundaries are highlighted with white single arrows, and some of the stacking faults are marked with double white arrows [83].

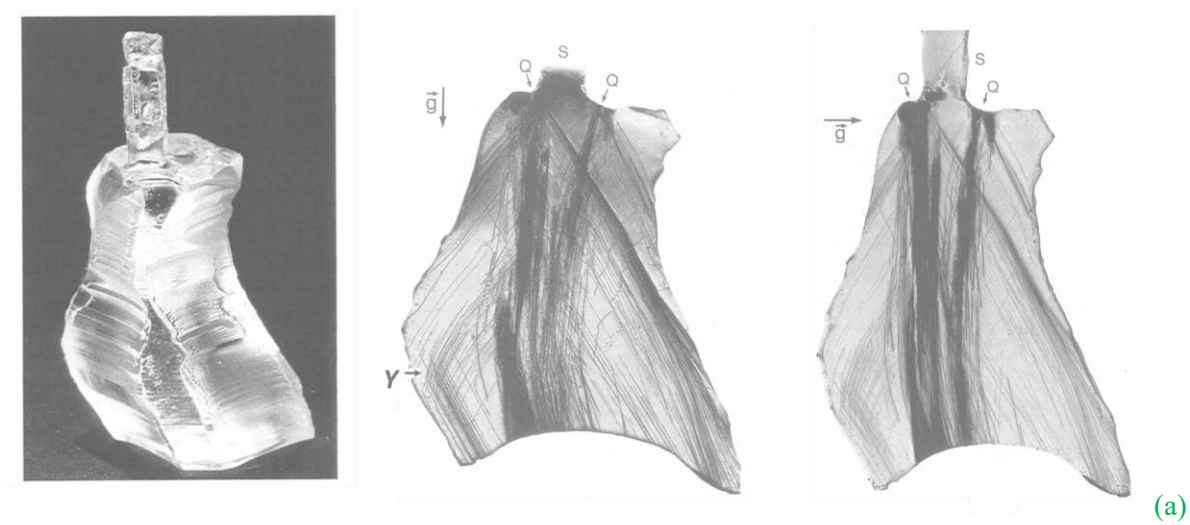
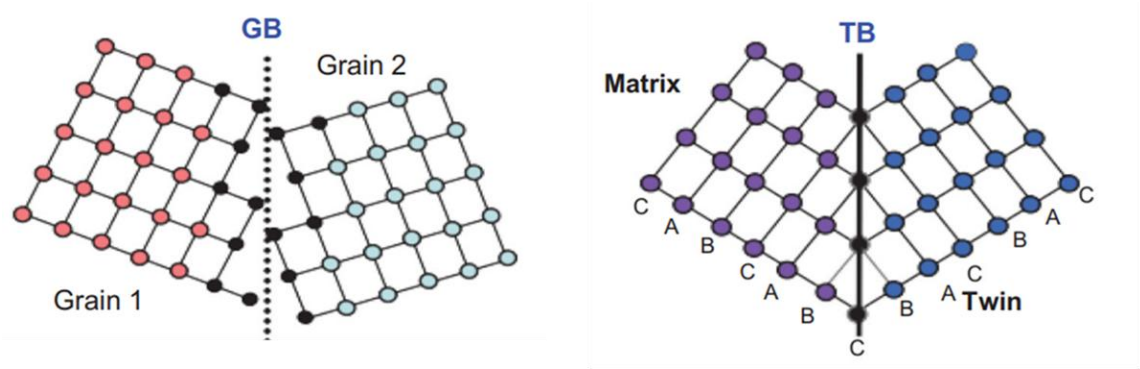


Figure 1.16 – (a) Czochralski-grown salol pulled along [100]. Topographs of longitudinal cut plates oriented close to (010), with a thickness of 1 mm, reflected following the directions: (b) 200 and (c) 002. S is the seed crystal, Q are sources of growth dislocations, $\vec{g}$ are the diffraction vectors, and Y is the change of dislocation line directions due to a change of boule diameter [82].

Figure 1.16 illustrates results obtained during Czochralski growth of salol by Neuroth and Klapper [82]. The images show the defects growing from the seed crystal (S) until the end of its growth. The seed had only one dislocation, and no dislocations were detected at the seed-crystal interface. The authors concluded that the cooling by circulating air generates a concave interface where dislocations are found to be in the center of the boule remaining until the end of the experiment.

1.3.4 Grain boundaries

The interface between two grains with different crystallographic orientations that belong to the same crystal is called grain boundary (Figure 1.17a) [81]. Grain boundaries are considered as planar defect. There is a small zone in this area where the binding energy of atoms is lower than in the bulk material. Grain boundaries break the periodic structure lattice of the crystal which modifies the materials characteristics and properties. If the energy of the grain boundary is large, defects such dislocations, atom misplacement, vacancies, twisted bonds are caused [84]. A favorable location for impurity atoms, which frequently have greater atomic radius than the vacancies in the matrix, is created by the deformation of the crystal lattice at the grain boundary, which spans multiple atomic layers.



(a) (b)

Figure 1.17 – Schematic drawing of: (a) a grain boundary between two grains; (b) a twin boundary between a matrix and a twin crystal [85].

Grain boundaries can be classified as a function of the misorientation between the two adjacent neighbor grains:

- *Low Angle Grain Boundary* (LAGB): the misorientation between the two grains is between 2 and 15°. Sub-grain boundaries are classified as low angle grain boundary, they are formed within a crystal or a grain. According to Read and Shockley [86], LAGB consists of dislocations arrays, with energy and spacing dependent on the misorientation angle. When increasing the misfit on the spacing of dislocations, the sub-grain boundary becomes more distinct. Therefore, the model suggests that the energy of such boundaries is dependent to the dislocation density.
- *High Angle Grain Boundary* (HABG): the misorientation between the two grains is higher to 15°.

Alternatively, grain boundaries can be classified by the specific relationship between their crystallographic orientation:

- *Random Angle Grain Boundary* (RAGB): the grains have no specific geometrical relationship, resulting in a boundary with high energy.
- *Coincidence Site Lattice* (CSL) *boundaries*: the misorientation between the grains is determined by a specific rotation angle relatively to a given axis. They are always HAGB. The grains in this case have lower energy than the RAGB. CSL are called twin boundaries (Figure 1.17b) [87]. Twin boundaries occur when a region of the grown crystal undergoes a uniform

shear, resulting in the creation of new crystal. This process makes the original crystal and the resulting crystal mirror images of each other across a symmetry plane [85, 88].

For instance, {111} facets are observed at the edges of the solid-liquid interface during the growth of silicon ingots, hence a twinning eventually will form and competes with the central grain growing from the seed as shown in Figure 1.18 [8], [42]. Furthermore, Jhang *et al.* [89] developed a 3D model to see where probably the twinning will nucleate at the facets {111}. They found that the twinning is highly probable to nucleate when the {111} facets will be in contact with the sample wall, which can be seen in thin sample configuration and at the edge of the facets where the attachment energy is lower.

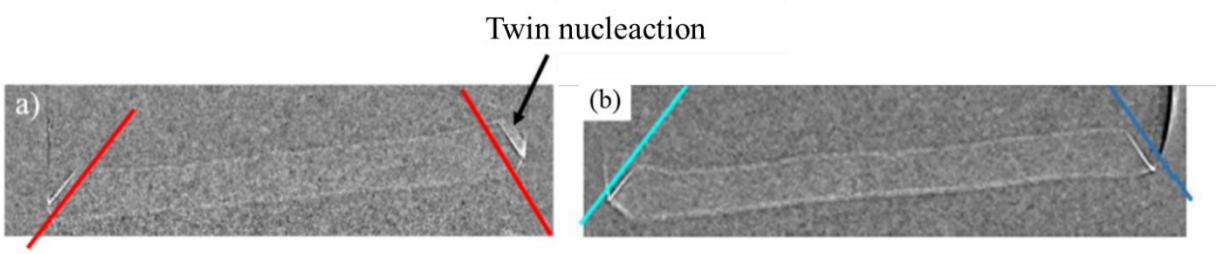


Figure 1.18 – Images of X-ray radiography of the solid–liquid interface of silicon during growth with {111} facets at both edges of the sample; The red and blue lines indicate {111} planes [8, 42].

1.3.5 Stresses

During solidification, the grown crystal is exposed to a variety of stresses that can occur primarily from thermal and chemical origin as well as structural constraints within the material.

(a) Thermal stress

Thermal stress develops during solidification due to the thermal gradient, leading different parts of the crystal to expand or contract with varying pulling velocities. These internal stresses can be either compressive or tensile, and this depends on the temperature distribution within the crystal [90]. Dislocations can occur if the stress exceeds the yield stress of the material, and cracks may happen if the modulus of rupture is attained. In order to control stress, the thermal gradient should be controlled to reduce the defects originating from the thermal stress. Figure 1.19 presents a sequence of images showing the development of a crack due to tensile stress on a single facet of salol [20]. As the growth progresses a crack appears between the root and the

tip of the facet. The crack extends to the body of the facet and then it is left behind as the facet continues to grow. Comparing the experimental observations and the predictions of the combined solidification-thermal and stress model, the authors found that this crack originated from thermally induced stresses.

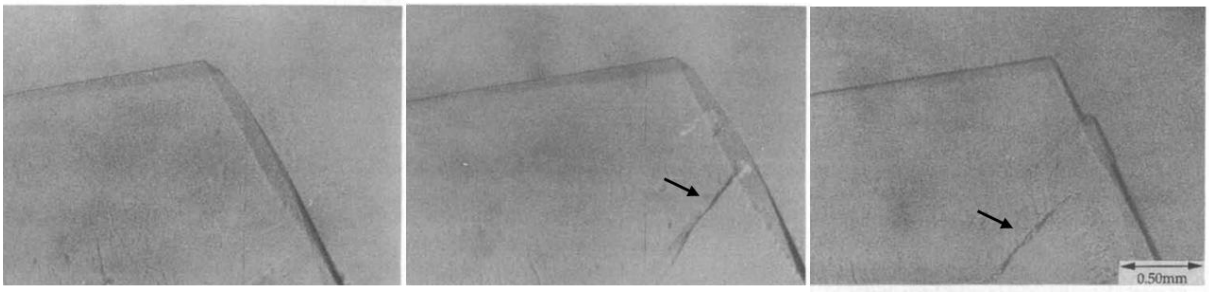


Figure 1.19 – Sequence of images showing the development of a crack appearing on a facet of salol due to thermal stress (V_p = 5 µm/s and G = 3 K/mm) [20].

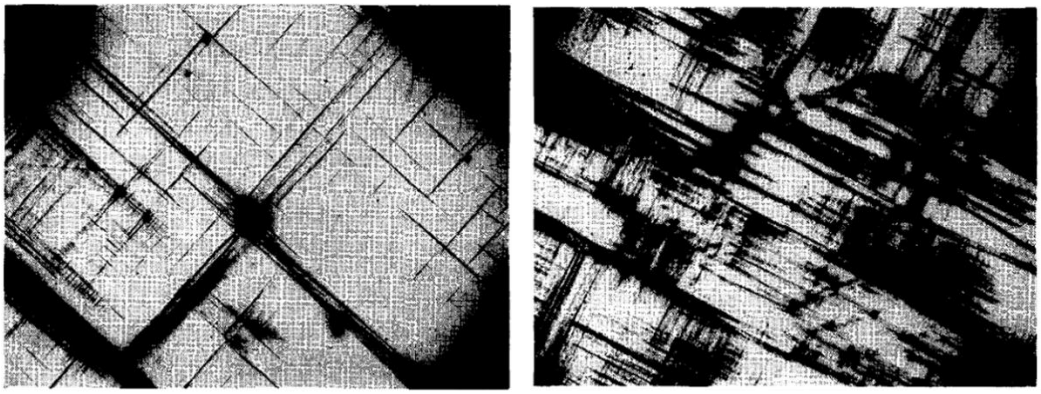
(b) Chemical stress

Segregation of impurities or the deviations from the ideal stoichiometry often lead to a variation in the chemical composition of the material. These chemical variations and inhomogeneities result in stress within the crystal which also lead to the formation of dislocations, growth striations, or twin boundaries [91]. To minimize the occurrence of the chemical stresses, it is requested to control the chemical composition, which is also a hard task to do, of the system and the purity of the materials during the preparation of the samples.

(c) Structural stress

Structural stresses are associated with phase changes that certain materials undergo as they solidify from the melt. When phase transformations occur, it can be at the origin of stress into crystal. Figure 1.20 shows two examples of twinning in an oxide ($Ba_2NaNb_5O_{15}$) single crystal, which at 250°C transforms from tetragonal to orthorhombic structure. This transformation causes mechanical twin formation leading to blocks where *a* and *b* axis interchanged. High twin density is formed due to the growth from non-stoichiometric melts, steep temperature gradients and macroscopic defects (Figure 1.20b). The structural stresses can be reduced with *post*-growth treatments. For example, cooling the crystal while applying pressure can help to prevent

twinning and other defects [91]. Detwinning the material is easier to achieve in low twin density regions (Figure 1.20a).



(a) (b)

Figure 1.20 – Images showing the twin structures in an oxide (Ba2NaNb5O15) single crystal: (a) low density; (b) high density [91].

1.4 The kinetics of the growth of salol

Salol is a transparent organic material that exhibits a highly faceted interface ($\alpha_J \approx 7.4$). Its facets belong to different crystallographic planes. Dey and Sekhar [4, 20] found that during its solidification, the behavior of the facets are impacted by the growth rate, the thermal gradient and the undercooling. When the undercooling is low (from 3 to 7 K), facets are well defined and stable, and the facets apex angle is higher than for higher undercooling (from 7 to 30 K). For high solidification velocities (75 µm/s), the facets destabilize, and the facets apex angles reduces, and for high thermal gradients (5.4 K/mm) the spacing of the facets reduces compromising their stability. When exposed to thermal stress, crack formation is observed in the facets.

Danilov and Malkin [92, 93] reported the growth rate V_f of an isolated polyhedral crystal of salol conforming to the two-dimensional nucleation growth [94]:

$$V_f = K_1 \exp(-K_2/T) \exp(-K_3/T\Delta T) \qquad \textit{Eq. 1.13}$$

K_1, K_2 and K_3 are constants, with $K_1 \exp\left(-\frac{K_2}{T_0}\right) = 520\ \mu m/s$ and $K_3 = 7020\ (°C)^2$, ΔT is the undercooling and T is the temperature. Pollatschek [95] has found that when salol grows in

capillaries of 7.5 mm diameter and 1 mm wall thickness under small undercooling, the growth rate is governed by a screw dislocation mechanism:

$$V_f = 0.4\,\Delta T^{1.7}\ \mu m/s \qquad \textit{Eq. 1.14}$$

In both studies, the crystal planes were not specified. Yet, Danilov and Malkin [92, 93] concentrated on the fastest growing edge facets, whereas Pollatschek on facets along the capillary axes. At an undercooling of 1.5 K, the growth rate obtained in the two studied differs by 3.5 orders of magnitude.

Neumann and Micus [96] worked on salol that grows in capillaries of smaller diameter (0.4 mm) and wall thickness (0.06 mm) giving rise to the growth rate:

$$V_f = 0.156\,\Delta T^{2.3}\ \mu m/s \qquad \textit{Eq. 1.15}$$

These authors mentioned that degassed salol crystallizes as a single crystal in thin layers or narrow capillaries, which indicates a highly ordered crystallographic growth. However, they did not appear to delve into detailed crystallographic analyses, such as specific lattice planes or orientations studied during the growth. Instead, the focus is on the overall crystallization velocity and the morphological effects of thermal and gas-related factors.

Cahn *et al*. [94] compared the experimental findings of Pollatschek [95], on the slowest facet in the direction of the capillary axis, and Neumann and Micus [96] on the fastest growing facets, with the theoretically expected based on the interface diffuseness concept [97]. This concept proposes that the transition from one phase to another is gradual, giving rise to the formation of several atom planes; it is different from the sharp surface where the transition occurs suddenly within a single layer of atoms. They found out that the growth law of type ΔT^2 is observed when the undercooling is higher than 6 K and a linear growth is observed when it is higher than 15 K. The growth kinetic characteristic of two-dimensional nucleation as well as the observation of a parabolic limiting growth law was a strong demonstration of the lateral growth mechanism. When the undercooling ranges between 6 and 15 K, a transitional regime occurs, and the growth changes gradually from lateral to continuous growth [94].

Jackson *et al*. [98] also studied the growth of salol under a variety of undercooling ranges. They concluded that the growth depends on crystal perfection. Below undercooling of 10 K, large facets are observed; when the undercooling is greater than 13 K more facets are created which belong to different crystallographic planes. When the undercooling is between 14 and 40 K, they showed that the growth rates are faster than those found by Neumann and Micus [96]. For

even higher undercooling (50-72 K), the interface kept evolving with faceted patterns indicating high anisotropic growth. However, they did not report on the crystallographic planes.

In order to determine whether salol grows with a lateral or continuous mechanisms, Riveros [99] conducted experiments to study the crystallization rate on the basis of temperature and orientation. After melting a drop of salol and then putting it in a chamber where the temperature is controlled, the author found that the linear crystallization rate perpendicular to the facet (001) follows the law:

$$V_f = (0.50 \pm 0.17)\ \Delta T^{0.65\pm0.25}\ \mu m/s \qquad \textit{Eq. 1.16}$$

And when the crystallization rate is perpendicular to the facet (110) is:

$$V_f = (1.67 \pm 0.50)\ \Delta T^{1.10\pm0.25}\ \mu m/s \qquad \textit{Eq. 1.17}$$

It was also found that when the undercooling is higher than 11 K, the growth of salol on the surface (001) changed from lateral to continuous growth, based on the observation that the end of the crystal near the emergence of the *x* axis took a rounded shape.

Jin *et al*. [100] studied the growth rates of salol reporting on specific crystallographic planes. They studied the relationship between the velocity of the (102), (012) and (112) facets and the interface undercooling (ranges between 0 and 3 K). A threshold undercooling for the growth measured for (102), (012) and (112) was 0.015, 0.55 and 2.04 K, respectively. They showed that if the undercooling is lower than these values, the growth rate is lower than 10^{-3} µm/s. They also found that for the three planes, the growth can be separated into three regimes. At low undercooling, the experimental kinetic data corresponds to two-dimensional nucleation growth, and the growth of the facets is then governed by a lateral regime. At high undercooling, the growth kinetics deviate from the two-dimensional nucleation law, and the growth mode is then continuous. These two regimes are separated by a transitional regime.

Ie *et al*. [101] investigated the free growth of the facet (010) of salol under an undercooling lower than 15 K. The growth rate therefore follows a relation that is close to the ΔT^2 mechanism that relies on screw dislocations:

$$V_f = 0.285\ \Delta T^{2.38}\ \mu m/s \qquad \textit{Eq. 1.18}$$

Dey and Sekhar [4] studied the grow of salol in the presence of a positive temperature gradient, and they found that the non-planar interface is bound by various combinations of (111) planes. The interface undercooling determines the specific planes that are allowed. They found that undercooling is mostly dependent on kinetic, surface energy and stress effects. They also found that at low undercoolings, growth follows a two-dimensional nucleation-controlled mechanism,

and at higher undercoolings, the growth transitions to a continuous growth mode, with a shift in the interface morphology. The kinetic undercooling (ΔT_k) is related to the growth velocity through a relationship incorporating capillary and strain effects. Cracking was observed in thick samples at low velocities, suggesting that strain accumulation plays a role in modifying growth behavior.

The directional solidification of salol was previously studied during the 1990s. Shangguan and Hunt [46-48] were among the first to investigate it, both experimentally and numerically. Their work demonstrated that pattern formation is governed by interactions within the faceted cellular array, such as the creation of new cells and the elimination of existing ones to adjust cell spacing. For a given set of growth conditions, a finite range of stable cell spacing exists, indicating the absence of uniquely selected spacing. Higashino *et al.* [52] advanced earlier studies by measuring temperature profiles ahead of the solid-liquid interface using microscopic interferometry. Dey and Sekhar [4, 20] studied the facet crystallography and morphological transitions, observing a growth interface bounded by a specific family of crystallographic planes. Such a selection is related to the degree of undercooling at the interface. Around the same period, Neuroth and Klapper [82] examined the growth facets of large single crystals of salol grown by the Czochralski technique. Understanding the mechanisms behind defect formation is crucial for optimizing the growth process and enhancing the quality of the resulting crystals. However, detailed observations during directional solidification remained limited. In this work, we aim to enhance the understanding of the mechanisms involved in salol faceted interface growth and defect dynamics.

1.5 Bibliography

[1] W. Kurz, and D. J. Fisher, « Fundamentals of Solidification », Trans. Tech. Publications., 1998.

[2] M. C. Flemings, « Solidification processing », New-York: McGraw-Hill, 1974.

[3] W. Losert, B. Q. Shi, and H. Z. Cummins, « Evolution of Dendritic Patterns during Alloy Solidification: Onset of the Initial Instability », Proceedings of the National Academy of Sciences of the United States of America, vol. 95, p. 431- 438, 1998.

[4] N. Dey, and J. A. Sekhar, « Interface configurations during the directional growth of Salol—I. Morphology », Acta Metallurgica et Materialia, vol. 41, p. 409-424, 1993.

[5] W. W. Mullins, and R. F. Sekerka, « Stability of a planar interface during solidification of a dilute binary alloy », Journal of applied physics, vol. 35, p. 444-451, 1964.

[6] B. Billia, and R. Trivedi, « Pattern Formation in Crystal Growth », In: Handbook of Crystal Growth, edited by D. Hurle, North-Holland, vol.1, 1993.

[7] M. Asta, C. Beckermann, A. Karma, W. Kurz, R. Napolitano, M. Plapp, G. Purdy, M. Rappaz, and R.Trivedi, , « Solidification microstructures and solid-state parallels: Recent developments, future directions », Acta Mater., vol. 57, p. 941-971, 2009.

[8] H. Ouaddah, M. Becker, T. Riberi-Beridot, M. Tsoutsouva, V. Stamelou, G. Regula, G. Reinhart, I. Perichaud, F. Guittonneau, L. Barrallier, J. P. Valade, A. Rack, E. Boller, J. Baruchel, and N. Mangelinck-Noel, « X-ray Based in Situ Investigation of Silicon Growth Mechanism Dynamics-Application to Grain and Defect Formation », Crystals, vol. 10, p. 555, 2020.

[9] D. A. Porter, and K. E. Easterling, « Phase Transformations in Metals and Alloys », Springer, New York, 1992.

[10] S. A. Norris, S. H. Davis, S. J. Watson, and P. W. Voorhees, « Faceted interfaces in directional solidification », J. Cryst. Growth, vol. 310, p. 414-427, 2008.

[11] A. K. Boukellal, A. K. Sidi Elvalli, and J. M. Debierre, « Equilibrium and growth facetted shapes in isothermal solidification of silicon: 3D phase-field simulations », J. Cryst. Growth, vol. 522, p. 37- 44, 2019.

[12] K. A. Jackson, and J. D. Hunt, « Transparent compounds that freeze like metals », Acta Metallurgica, vol. 13, p.1212 -1215, 1965.

[13] K. A. Jackson, « Liquid metals and solidification, Asm, Cleveland, 1958.

[14] W. A. Tiller, K. A. Jackson, J. W. Rutter, and B. Chalmers, « The redistribution of solute atoms during the solidification of metals », Acta metallurgica, vol.1, p. 428–437, 1953.

[15] K. A. Jackson, « Constitutional supercooling surface roughening », J. Cryst. Growth, vol. 264, p. 519-529, 2004.

[16] Y. D. Bensah, « Morphological growth criterion for faceted to non-faceted transition in pure materials », Results Phys., vol. 48, p. 106418, 2023.

[17] D. M. Herlach, « Non-Equilibrium Solidification of Undercooled Metallic Melts », Metals, vol. 4, p. 196-234, 2014.

[18] D. M. Herlach, « Containerless Undercooling and Solidification of Pure Metals », Annu. Rev. Mater. Sci., vol. 21, p. 23-44, 1991.

[19] J. W. Rutter, and B. Chalmers, « A prismatic substructure formed during solidication of metals », Canadian Journal of Physics, vol. 31, p. 15-39, 1995.

[20] N. Dey, and J. A. Sekhar, « Interface configurations during the directional growth of salol—II. Thermal stress cracking », Acta Metall. Mater., vol. 41, p. 425-439, 1993.

[21] D. K. Shangguan, « Cellular Growth of Crystals », 1 ed., Springer Berlin, Heidelberg, 1991.

[22] W. D. Huang, and L. L. Wang, « Solidification researches using transparent model materials — A review », Sci. China Technol. Sci., vol. 55, p. 377-386, 2012.

[23] J. D. Hunt, K. A. Jackson, and H. Brown, « Temperature Gradient Microscope Stage Suitable for Freezing Materials with Melting Points between −100 and +200°C », Rev. Sci. Instrum., vol. 37, p. 805-805, 1966.

[24] F. L. Mota, N. Bergeon, D. Tourret, A. Karma, R. Trivedi, and B. Billia, « Initial transient behavior in directional solidification of a bulk transparent model alloy in a cylinder », Acta Materialia. vol.85, p. 362-377, 2015.

[25] Y. Song, D. Tourret, F. L. Mota, J. Pereda, B. Billia, N. Bergeon, R. Trivedi, and A. Karma, « Thermal-field effects on interface dynamics and microstructure selection during alloy directional solidification », Acta Mater, vol.150, p. 139-152, 2018.

[26] F. L. Mota, K. Ji, L. Strutzenberg Littles, R. Trivedi, A. Karma, and N. Bergeon, « Influence of macroscopic interface curvature on dendritic patterns during directional solidification of bulk samples: Experimental and phase-field studies », Acta Materialia, vol. 250, p. 118849, 2023.

[27] F. L. Mota, J. Pereda, K. Ji, Y. Song, R. Trivedi, A. Karma, and N. Bergeon, « Effect of sub-boundaries on primary spacing dynamics during 3D directional solidification conducted on DECLIC-DSI », Acta Materialia, vol. 204, p. 116500, 2021.

[28] Y. Song, F. L. Mota, D. Tourret, K. Ji, B. Billia, R. Trivedi, N. Bergeon, and A. Karma, « Cell invasion during competitive growth of polycrystalline solidification patterns », Nature Communications, vol. 14, p.2244, 2023.

[29] D. Tourret, Y. Song, A. J. Clarke, and A. Karma, « Grain growth competition during thin-sample directional solidification of dendritic microstructures: A phase-field study », Acta Mater., vol. 122, p. 220-235, 2017.

[30] D. Tourret, J. M. Debierre, Y. Song, F. L. Mota, N. Bergeon, R. Guerin, R. Trivedi, B. Billia, and A. Karma, « Oscillatory cellular patterns in three-dimensional directional solidification », Phys. Rev. E, vol. 92, p. 042401, 2015.

[31] H. Esaka, « Dendrite growth and spacing in succinonitrile-acetone alloys », Thèse Ecole polytechnique fédérale de Lausanne EPFL, 1986.

[32] J. Timmermans, « Plastic crystals: a historical review », Journal of Physics and Chemistry of solids, vol. 18, p. 1-8, 1961.

[33] A. Michils, « Recherches stoechiométriques V.VIII. La plasticité d'un groupe particulier de cristaux organiques », Bull. Sociétés Chim. Belg., vol. 57, p. 575-617, 1948.

[34] J. A. Dantzig, and M. Rappaz, « Solidification », EPFL Press , Switzerland, 2009.

[35] B. L. Silva, N. Cheung, A. Garcia, and J. E. Spinelli, « Thermal Parameters, Microstructure, and Mechanical Properties of Directionally Solidified Sn-0.7 wt.%Cu Solder Alloys Containing 0 ppm to 1000 ppm Ni », J. Electron. Mater., vol. 42, p. 179-191, 2013.

[36] S. W. Kim, W. F. Flanagan, B. D. Lichter, and R. N. Grugel, « Electrical Conductivity in Directionally Solidified Lead-9 and -20 Wt Pct Copper Alloys », Metallurgical Transactions A, vol. 24, p. 975-979, 1993.

[37] J. E. Spinelli, B. L. Silva, and A. Garcia, « Assessment of Tertiary Dendritic Growth and Its Effects on Mechanical Properties of Directionally Solidified Sn-0.7Cu-XAg Solder Alloys », Journal of Electronic Materials, vol. 43, p. 1347-1361, 2014.

[38] M. E. Glicksman, and A. O. Lupulescu, « Dendritic crystal growth in pure materials », J. Cryst. Growth, vol. 264, p. 541-549, 2004.

[39] M. B. Amar, and E. Brener, « Parity-Broken Dendrites », Physical Review Letters, vol. 75, p. 561-564, 1995.

[40] S. Akamatsu, G. Faivre, and T. Ihle, « Symmetry-broken fingers and seaweed patterns in thin-film directional solidification of a non-faceted cubic crystal », Phys. Rev. E, vol. 51, p. 4751-4773, 1995.

[41] V. Stamelou, M. G. Tsoutsouva, T. Riberi-Beridot, G. Reinhart, G. Regula, J. Baruchel, and N. Mangelinck-Noel, « {111} facet growth laws and grain competition during silicon crystallization », J. Cryst. Growth, vol. 479, p. 1-8, 2017.

[42] T. Riberi-Beridot, M.G. Tsoutsouva, G. Regula, G. Reinhart, F. Guittonneau, L. Barrallier, and N. Mangelinck-Noel, « Strain building and correlation with grain nucleation during silicon growth », Acta Materialia, vol. 177, p. 141-150, 2019.

[43] M. G. Tsoutsouva, T. Riberi-Beridot, G. Regula, G. Reinhart, J. Baruchel, F. Guittonneau, L. Barrallier, and N. Mangelinck-Noel, « In situ investigation of the structural defect

generation and evolution during the directional solidification of < 110 > seeded growth Si », Acta Materialia, vol. 115, p.210-223, 2016.

[44] M. Becker, G. Regula, G. Reinhart, E. Boller, J. P. Valade, A. Rack, P. Tafforeau, and N. Mangelinck-Noel, « Simultaneous X-ray radiography and diffraction topography imaging applied to silicon for defect analysis during melting and crystallization », Journal of Applied Crystallography, vol. 52, p. 1312-1320, 2019.

[45] M. G. Tsoutsouva, G. Stokkan, G. Regula, B. Ryningen, T. Riberi-Beridot, G. Reinhart, and N. Mangelinck-Noel, « Random angle grain boundary formation and evolution dynamics during Si directional solidification », Acta Materialia, vol. 171, p. 253-260, 2019.

[46] D. K. Shangguan, and J. D. Hunt, « In situ observation of faceted cellular array growth », Metall. Trans. A, vol. 22, p. 941-945, 1991.

[47] D. K. Shangguan, and J. D. Hunt, « Experimental and numerical study of pattern formation in faceted cellular array growth », Metall. Trans. A, vol. 23, p. 1111-1120, 1992.

[48] D. K. Shangguan, and J. D. Hunt, « Dynamical study of the pattern formation of faceted cellular array growth », J. Cryst. Growth, vol. 96, p. 856-870, 1989.

[49] L. M. Fabietti, and R. Trivedi, « Development of interface morphologies in the tert butyl alcohol-water system », J. Cryst. Growth, vol. 82, p. 185-197, 1997.

[50] L. M. Fabietti, and R. Trivedi, « Nonequilibrium effects during the ledgewise growth of a solid-liquid interface », Metall. Trans. A. vol. 22, p.1249-1258, 1991.

[51] L. M. Fabietti, and R. Trivedi, « In situ observations of stress-induced defect formation at the solid—liquid interface », J. Cryst. Growth, vol. 173, p. 503-512, 1997.

[52] T. Higashino, Y. Inatomi, and K. Kuribayashi, « In-situ observation of unidirectional solidification in transparent organic alloy », J. Cryst. Growth, vol. 128, p. 178-182, 1993.

[53] Y. Inatomi, O. Kitajima, W. Huang, and K. Kuribayashi, « In Situ Observation of Directional Solidification in High Gravity », in: L.L. Regel, W.R. Wilcox (Eds.), Centrifugal Materials Processing, Springer US, Boston, MA, p. 93-108, 1997.

[54] Y. Inatomi, K. Iwamoto, T. Maki, Y. Takagi, and K. Kuribayashi, « Preliminary Experiments of Faceted Cellular Array Growth in Microgravity », Int. J. Microgravity Sci. Appl., vol. 25, p. 579, 2008.

[55] T. Börzsönyi, S. Akamatsu, and G. Faivre « Weakly faceted cellular patterns versus growth induced plastic deformation in thin-sample directional solidification of monoclinic biphenyl », Phys. Rev. E, vol. 80, p. 051601, 2009.

[56] T. Kobayashi, K. Sato, M. Kobayashi, and H. Kappler, « Organic Crystals I: Characterization », 1 ed., Springer Berlin Heidelberg, 1991.

[57] P. S. Wei, Y. K. Kuo, S. H. Chiu, and C. Y. Ho, « Shape of a pore trapped in solid during solidification », International journal of heat and mass transfer, vol. 43, n° 2, p.263-280, 2000.

[58] P. S. Wei, C. C. Huang, Z. P. Wang, K. Y. Chen, and C. H. Lin, « Growths of bubble/pore sizes in solid during solidification—an in situ measurement and analysis », J. Cryst. Growth, vol. 270, p. 662-673, 2004.

[59] M. V. A. Bianchi, and R. Viskanta, « The effect of air bubbles on the diffusion-controlled solidification of water and aqueous solutions of ammonium chloride», Int. J. Heat Mass Tran, vol. 42, p. 1097-1110, 1999.

[60] H. Ouaddah, I. Périchaud, D. Barakel, O. Palais, M. Di Sabatino, G. Reinhart, G. Regula, and N. Mangelinck-Noël, « Role of Impurities in Silicon Solidification and Electrical Properties Studied by Complementary In Situ and Ex Situ Methods », Phys. Status Solidi A, vol. 216, p. 1900298, 2019.

[61] S. Yamamura, H. Shiota, K. Murakami, and H. Nakajima, « Evaluation of porosity in porous copper fabricated by unidirectional solidification under pressurized hydrogen », Mater. Sci. Eng. A, vol. 318, p. 137-143, 2001.

[62] Y. Liu, Y.X. Li, J. Wan, and H.W. Zhang, « Evaluation of porosity in lotus-type porous magnesium fabricated by metal/gas eutectic unidirectional solidification », Mater. Sci. Eng. A, vol. 402, p. 47-54, 2005.

[63] Y. Liu, and Y.X. Li, « A theoretical study of Gasarite eutectic growth », Scr. Mater., vol. 49, p. 379-386, 2003.

[64] Y. Liu, Y. Li, J. Wan, and H. Zhang, « Metal-gas eutectic growth during unidirectional solidification », Metall. Mater. Trans. A, vol. 37, p. 2871-2878, 2006.

[65] S. K. Hyun, and H. Nakajima, « Effect of solidification velocity on pore morphology of lotus-type porous copper fabricated by unidirectional solidification », Mater. Lett., vol. 57, p. 3149-3154, 2003.

[66] S. Deville, « Freeze-casting of porous ceramics: A review of current achievements and issues », Adv. Eng. Mater. vol. 10, p. 155-169, 2008.

[67] S. Akamatsu, and G. Faivre, « Residual-Impurity Effects in Directional Solidification: LongLasting Recoil of the Front and Nucleation-Growth of Gas Bubbles », Journal de Physique I, vol. 6, p.503-527, 1996.

[68] P. D. Lee, and J. D. Hunt, « Hydrogen Porosity in Directional Solidified Aluminum-Copper Alloys: In Situ Observation », Acta Materialia, vol. 45, p. 4155-4169, 1997.

[69] A. K. Gupta, B. K. Saxena, S. N. Tiwari, and S. L. Malhotra, « Pore Formation in Cast Metals and Alloys », Journal of Materials Science, vol. 27, p. 853-862, 1992.

[70] Q. Y. Han, « Motion of Bubbles in the Mushy Zone », Scripta Materialia, vol. 55, p. 871-874, 2006.

[71] Y. Teng, Y. Yang, H. Yu, L. Wang, W. Huang, and Q. Han, « Behavior of Bubbles under Directional Solidification Conditions », AFS Transactions 2012.

[72] H. J. Scheel, « Theoretical and technological solutions of the striation problem », J. Cryst. Growth, vol. 287, p. 214-223, 2006.

[73] A. J. Goss, K. E. Benson, and W. G. Pfann, « Dislocations at compositional fluctuations in germanium-silicon alloys », Acta metallurgica, vol. 4, p.332-333, 1956.

[74] W. Bardsley, J. S. Boulton, and D. T. J. Hurle, « Constitutional supercooling during crystal growth from stirred metls: III. The morphology of the germanium cellular structure », Solid State Electron, vol. 5, p. 395-403, 1962.

[75] H. J. Scheel, « Transition to faceting in multilayer liquid phase epitaxy of GaAs », Appl. Phys. Lett., vol. 37, p. 70-73, 1980.

[76] H. Klapper, « Defects in Non-Metal Crystals », in Characterization of Crystal Growth Defects by X-Ray Methods, B. K. Tanner et D. K. Bowen, Éd., Boston, MA: Springer US, p. 133-160, 1980.

[77] H. Klapper, « Generation and Propagation of Defects During Crystal Growth », in Springer Handbook of Crystal Growth, G. Dhanaraj, K. Byrappa, V. Prasad, et M. Dudley, Éd., Berlin, Heidelberg: Springer Berlin Heidelberg, p. 93-132, 2010.

[78] I. A. Prokhorov, Yu. A. Serebryakov, B. G. Zakharov, I. Zh. Bezbakh, V. V. Ratnikov, and I. L. Shulpina, « Growth striations and dislocations in highly doped semiconductor single crystals », J. Cryst. Growth, vol. 310, p. 5477-5482, 2008.

[79] A. J. Clarke, D. Tourret, S. D. Imhoff, P. J. Gibbs, K. Fezzaa, J. C. Cooley, W. K. Lee, A. Deriy, B. M. Patterson, P. A. Papin, and K. D. Clarke, « X-Ray Imaging and Controlled Solidification of Al-Cu Alloys toward Microstructures by Design », Advanced Engineering Materials, vol. 17, p.454-459, 2015.

[80] L. Xie, G. Wu, P. K. Liaw, W. Wang, D. Li, Q. Peng, J. Zhang, and Y. Zhang, « Temperature gradient enhances the solidification process and properties of a CoCrFeNi

high-entropy alloy: Atomic insights from molecular dynamics simulations », Comput. Mater. Sci., vol. 231, p. 112538, 2024.

[81] D. Hull, and D. J. Bacon, « Introduction to Dislocations », 5th Ed., Oxford: Butterworth-Heinemann, 2011.

[82] G. Neuroth, and H. Klapper, Éd., « Dislocation reactions in Czochralski-grown salol crystals », Z. Für Krist. - Cryst. Mater., vol. 209, p. 216-220, 1994.

[83] N. Chen, S. Qiu, B. Liu, G. Du, G. Liu, and W. Sun, « An optical microscopy study of dislocations in multicrystalline silicon grown by directional solidification method », Mater. Sci. Semicond. Process., vol. 13, p. 276-280, 2010.

[84] K. Fujiwara, R. Maeda, K. Maeda, and H. Morito, « In situ observation of twin boundary formation at grain-boundary groove during directional solidification of Si », Scr. Mater., vol. 133, p. 65-69, 2017.

[85] P. Uttam, V. Kumar, K.-H. Kim, and A. Deep, « Nanotwinning: Generation, properties, and application », Mater. Des., vol. 192, p. 108752, 2020.

[86] W. T. Read, and W. J. P. R. Shockley, « Dislocation models of crystal grain boundaries », Physical review, vol. 78, p.275, 1950.

[87] W. Z. Zhang, « Reproducible Orientation Relationships Developed from Phase Transformations—Role of Interfaces », Crystals, vol. 10, n° 11, p.1042, 2020.

[88] K. Shiga, A. Takahashi, L. Chuang, K. Maeda, H. Morito, and K. Fujiwara, « Twin boundary formation at a grain-boundary groove during the directional solidification of InSb », J. Cryst. Growth, vol. 577, p. 126403, 2022.

[89] J. W. Jhang, G. Regula, G. Reinhart, N. Mangelinck-Noël, and C. W. Lan, « Heterogeneous twinning during directional solidification of multi-crystalline silicon », J. Cryst. Growth, vol. 508, p. 42-49, 2019.

[90] H. S. Fang, S. Wang, L. Zhou, N. G. Zhou, and M. H. Lin, « Influence of furnace design on the thermal stress during directional solidification of multicrystalline silicon », J. Cryst. Growth, vol. 346, p. 5-11, 2012.

[91] B. Cockayne, « Developments in melt-grown oxide crystals », J. Cryst. Growth, vol. 3-4, p. 60-70, 1968.

[92] V. I. Danilov, V. I. Malkin, and Z. Fiz. Khim, « Experimental Verification of the Theory of Crystal Growth and the Relation between the Equilibrium Forms and the Growth Forms », vol. 27, p. 1837, 1954.

[93] V. I. Malkin, « On the Rate of Crystal Growth of Salol in the Glassy State », Z. Fiz. Khim, vol. 28, 1966.

[94] J. W. Cahn, W. B. Hillig, and G. W. Sears, « The molecular mechanism of solidification ». Acta Metallurgica, vol. 12, p.1421 -1439, 1964.

[95] H. Pollatschek, « The Determination of the Temperature at the Solid-Liquid Boundary During the Crystallization of Undercooled Melts », Z. Phys. Chem. A , vol. 142, p. 289-300, 1929.

[96] K. Neumann, and G. Micus, « The Linear Crystallization Rate of Salol in Thin Layers », Z. Phys. Chem. vol. 2, p. 25-39, 1954.

[97] J. W. Cahn, « Theory of crystal growth and interface motion in crystalline materials », Acta Metall, vol.8, p. 554-562, 1960.

[98] K. A. Jackson, D. R. Uhlmann, and J. D. Hunt, « On the nature of crystal growth from the melt », J. Cryst. Growth, vol. 1, p. 1 - 36, 1967.

[99] H. G. Riveros, « Growth of salol crystals », J. Cryst. Growth, vol. 2, p. 173-177, 1968.

[100] W. Q. Jin, J. Lin, and H. Komatsu, « Experimental studies on growth kinetics of salol crystals from the melt », J. Cryst. growth, vol. 99, p. 128- 133, 1990.

[101] T. H. Ie, and R. F. Strickland-Constable, « Mechanism of growth from the melt based on experiments with salol », J. Cryst. Growth, vol. 21, p.243-253, 1974.

CHAPTER 2: EXPERIMENTAL APPARATUS AND PROCEDURES

The study of directional solidification aims to understand the process of solidification of many materials, such as metallic alloys, semiconductors, ceramics, etc., in the presence of a temperature gradient, focusing on its fundamental aspect. However, this research faces significant challenges. Such materials have in general high melting points and most of them are opaque to the visible light, making it difficult to monitor the interface dynamics *in situ,* requiring intense X-ray sources and bulky and expensive devices. Therefore, transparent analogues of these materials that allow the real-time observation of similar behaviors with more practical and easy to use experimental setup were introduced [1]. In this thesis, solidification experiments of organic transparent materials that behave like the materials of interest concerning solidification will be discussed with a particular focus on materials with a facetted solid-liquid interface.

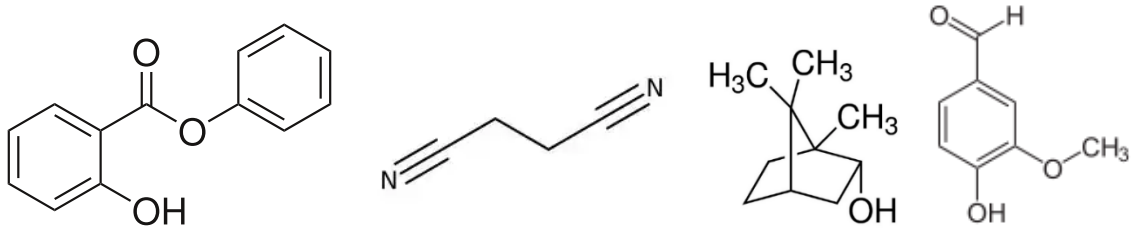
This chapter is divided into six sections, with the first one providing detailed information on the materials used in our experiments, highlighting salol, succinonitrile-borneol and succinonitrile-vanillin. The second one outlines the method of purification of these materials and is followed by section explaining the fabrication of thin samples used to achieve two-dimensional growth. The following sections introduce the experimental setup, the thermal gradient measurement and the method of preparing the initial seed. And the last section focuses on the detailed protocol and steps used during experiments.

2.1 The materials

In this study, directional solidification experiments will be performed using materials presenting a faceted interface during growth. The chosen organic materials are transparent to visible light, and their melting temperatures are lower than 100°C.

2.1.1 Salol

Salol, also known as phenyl salicylate, is a benzoate ester that is the phenyl ester of salicylic acid, with the chemical formula $C_{13}H_{10}O_3$ (Figure 2.1a) and melting temperature T_M = 41.5°C [2, 3]. Salol has a primitive orthorhombic crystallographic structure with cell dimensions: a = 23.40 Å, b = 11.26 Å and c = 7.96 Å [4]. It is a birefringent material that allows visualization of grains and stress fields with the use of polarized light [5]. In addition, according to Jackson's criterium [6] (cf. Chapter 1), the high entropy of melting leads to a highly faceted solid-liquid interface during growth ($\alpha_J = \frac{\Delta H_m}{RT_m} \approx 7$).



(a) (b) (c) (d)

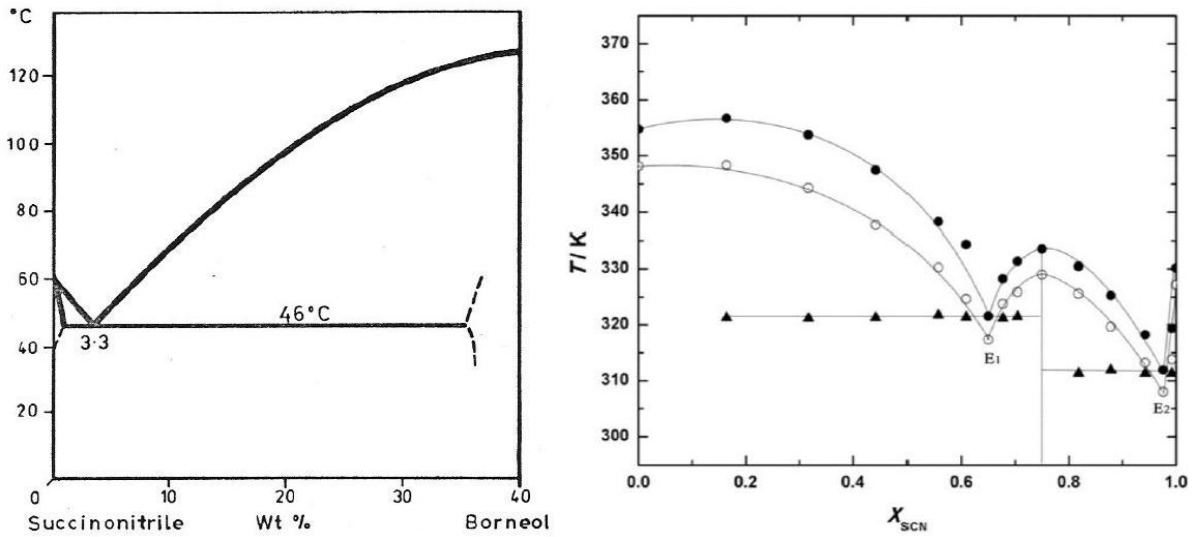
Figure 2.1 – Chemical structures of: (a) salol, (b) succinonitrile, (c) borneol and (d) vanillin.

2.1.2 Succinonitrile-borneol

Succinonitrile (SCN) is an organic chemical compound with the formula $C_4H_4N_2$ (Figure 2.1b) and a melting temperature of 58.05°C [3]. It solidifies like metals, presenting a rough interface during solidification [1] and, at room temperature, it has a cubic centered crystal structure with the cell dimension a = 6.37 Å, with two molecules per cubic unit cell [7]. Borneol (BN), a bicyclic monoterpenoid, can be found in the essential oils of various plants, such as *Salvia Rosmarinus* and *Salvia officinalis*. Renowned for its antimicrobial properties, this compound is utilized in traditional Chinese medicine. Borneol can be effectively presented through its chemical formula $C_{10}H_{18}O$ (Figure 2.1c) and its melting point of 206°C giving a face cubic centered crystal with the cell dimension a = 10.25 Å [8, 9].

According to Fisher and Kurz [8], the structures formed by the system SCN-borneol (Figure 2.2a) in the eutectic domain are similar to those of the aluminum-silicon system. Succinonitrile is the non-faceted phase (similarly to aluminum in Al-Si); borneol is also non-faceted above the polymorphic transition (72°C), but forms facets below. So, between the eutectic composition (3.3wt%) and the composition corresponding to the polymorphic transition

(≈11wt%), this eutectic system has a parameter $\alpha_J \approx 2.4$ and working temperatures below 100°C (eutectic temperature of 46°C). The fact that the α_J of this system exceeds 2 in this composition range indicates that the system exhibits a faceted solid-liquid interface what makes it an interesting system under the framework of this thesis.



(a) (b)

Figure 2.2 – (a) Succinonitrile-borneol partial phase diagram [8], (b) Temperature-composition diagram for succinonitrile-vanillin system: ▲, solidus temperature; ●, liquidus temperature; ○, nucleation undercooling [10].

2.1.3 Succinonitrile-vanillin

Vanillin (VAN), with the chemical formula $C_8H_8O_3$ (Figure 2.1 d), is available both in its natural state and through synthetic production. It finds applications in flavorings, culinary products, perfumes, and pharmaceuticals. Additionally, vanillin serves as a crucial chemical intermediate in the production of various essential drugs and other significant products. Vanillin melts at 81.95°C [3] and, according to Kavuru *et al.* [11], it has polymorphous crystallography. Form I, the stable one, presents a monoclinic crystalline structure with cell dimensions a =14.02 Å, b = 7.85 Å and c = 14.98 Å. Form II, a rare metastable form, presents an orthorhombic structure with cell dimensions a =16.43 Å, b = 3.88 Å and c = 45.84 Å [12]. Despite some controversy existing concerning the value of the melting enthalpy of pure vanillin (one leads to a Jackson's parameter $\alpha_J \approx 2.6$ and the other to a value between 6 and 7), the eutectic system

succinonitrile-vanillin is interesting since it also exhibits faceted behavior during solidification (Figure 2.2b) and reasonable working temperatures [10, 13].

2.2 Purification of materials

The purification of chemical compounds is a crucial step to ensure superior purity standards by physically separating the substance of interest from foreign or contaminating substances. The materials available for this work are the commercial ones with purity of at least 99% (Sigma Aldrich). Purification procedures are performed in order to avoid impurities which can affect the properties and performance of the material. While the range of chemical purification methods is extensive, this work primarily employs three specific techniques: distillation, sublimation, and recrystallization. The most suitable technique was chosen to each material.

2.2.1 Distillation

Distillation is the process of separating the components of a liquid mixture through selective boiling and condensation. The difference in volatility between the various components of the combination allows them to be separated. The most volatile component has the lowest boiling point and hence is the first to evaporate.

2.2.1.1 The distillation unit

Rather than using a conventional distillation setup, a rotary evaporator (Figure 2.3) is used which offers enhanced efficiency. This apparatus facilitates substance evaporation through distillation, followed by condensation and individual component separation based on their distinct boiling points. Notably, it can be integrated with a vacuum system to reduce the pressure. By rotating the sample, the evaporative surface area increases, accelerating the evaporation process. Furthermore, the equipment features a regulated heating mechanism, in order to optimize the distillation procedure.

As shown in Figure 2.3, the rotary evaporator comprises a rotary motion and lifting unit (A), distillation apparatus typically made of glass, and a heating unit which is a normally thermoregulated bath (B). Its components incorporate vacuum equipment for decreasing the internal pressure utilizing a Woulfe flask, an adjustable-height column, and a spiral

condensation column (C) that is connected to a circulating bath. In this work, rather than using a round flask for gathering the distillate, a Pauli separator (D) is introduced following the condensation column, with multiple recovery flasks attached to it. This provides a more automated and precise method for fraction collection, improving both the quality and efficiency of the distillation process.

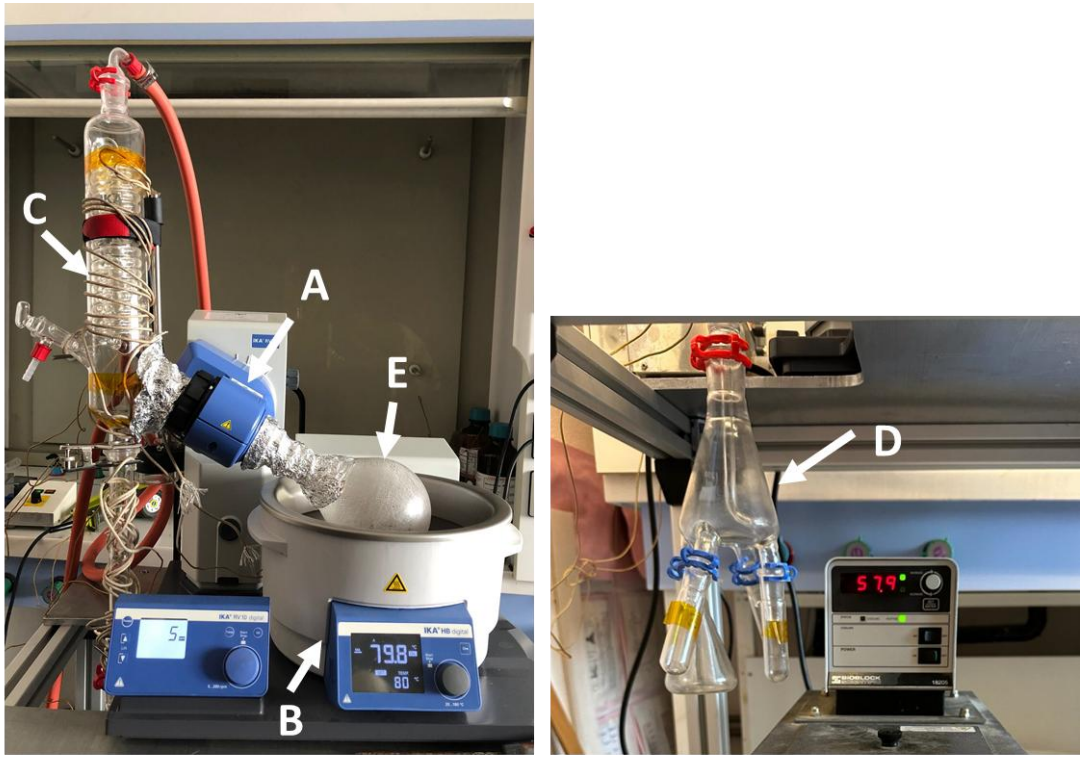


Figure 2.3 – Rotary evaporator used for distillation (IKA RV 10 basic).

The glassware is cleaned with acetone, ethanol and distilled water, and then dried in an oven at 100°C. Afterward, the cleaned parts are assembled with vacuum grease applied and ensuring a secure and contamination free seal. The final step involves filling the evaporator flask (E) with the material to be distilled, effectively sealing the system. The flask is submerged in either water or oil, and then the temperature-controlled bath and rotation system are activated. Subsequently, using the vacuum pump, the atmospheric pressure is lowered, facilitating the separation of solvents from the solute. Throughout the experiment, the vacuum level, which indicates the airtightness of the setup, is monitored using the provided pressure gauge.

To operate the rotary evaporator safely, it is crucial to be aware of the boiling and melting points of the substances being processed to avoid equipment overheating. All used components of the system, including the column, distillation head, cooler, Pauli separator, and recovery vessels, are maintained at a temperature close to the melting point of the compound to be purified. In addition, heating wires are used to stop any solid blockage that can affect the vacuum work, and the balloon and the steam pipes are wrapped with foil to help keep the temperature stable.

2.2.1.2 The distillation process

When dealing with substances that have high boiling points (e.g., > 300°C), it is common to use distillation under reduced pressure. By reducing the operating pressure, the boiling temperature is lowered, making distillation a simpler process. To determine the boiling temperature of a substance under reduced pressure based on its boiling temperature at atmospheric pressure, Vapor Pressure Temperature (VPT) nomographs like the one shown in Figure 2.4 are used [14] to control the distillation process. The tilted lines in the middle represent different groups of chemical compounds. The compounds are grouped as a function of structural and physical properties to provide comprehensive and practical tools for the calculation of the vapor pressure-temperature relationships for a wide variety of substances (diverse chemical classes, wide range of physical properties, …). For instance, anthracene or anthraquinone belong to the same group (1) because they share several structural and chemical similarities, such as: both are polycyclic aromatic compounds with a flat, planar structure, which contributes to their aromatic stability; they can both undergo electrophilic substitution reactions, such as halogenation or nitration; both are crystalline solids at room temperature, are nonpolar and hydrophobic, showing low solubility in water but good solubility in organic solvents. By drawing a straight line between the material boiling temperature at atmospheric pressure and the apparatus pressure, one may calculate the respective boiling temperature.

Among the materials used in this work, succinonitrile and salol are purified by distillation. The SCN boiling temperature is 266°C at atmospheric pressure (760 mmHg), and is 173°C at 12 mmHg for salol [3]. None of them are included in the list of chemical compounds. However, there are compounds from the same chemical families. For succinonitrile: hydrogen cyanide, which is used to produce SCN, belongs to group 3; and cyanogen, which has two -CN groups similarly to SCN, belongs to group 4. One may deduce from these considerations that SCN belongs to one of those groups. So, if the pressure is reduced to 6 mmHg (for example with the

use of the vacuum pump IKA MVP 10 basic), SCN should boil at around 115°C. For salol: methyl salicylate, which differs from the salol only by the methyl group, belongs to group 2, so it is inferred that salol belongs to group 2 as well. So, the pressure needs to be lower than 1 mmHg, in order to have a boiling temperature around 115°C.

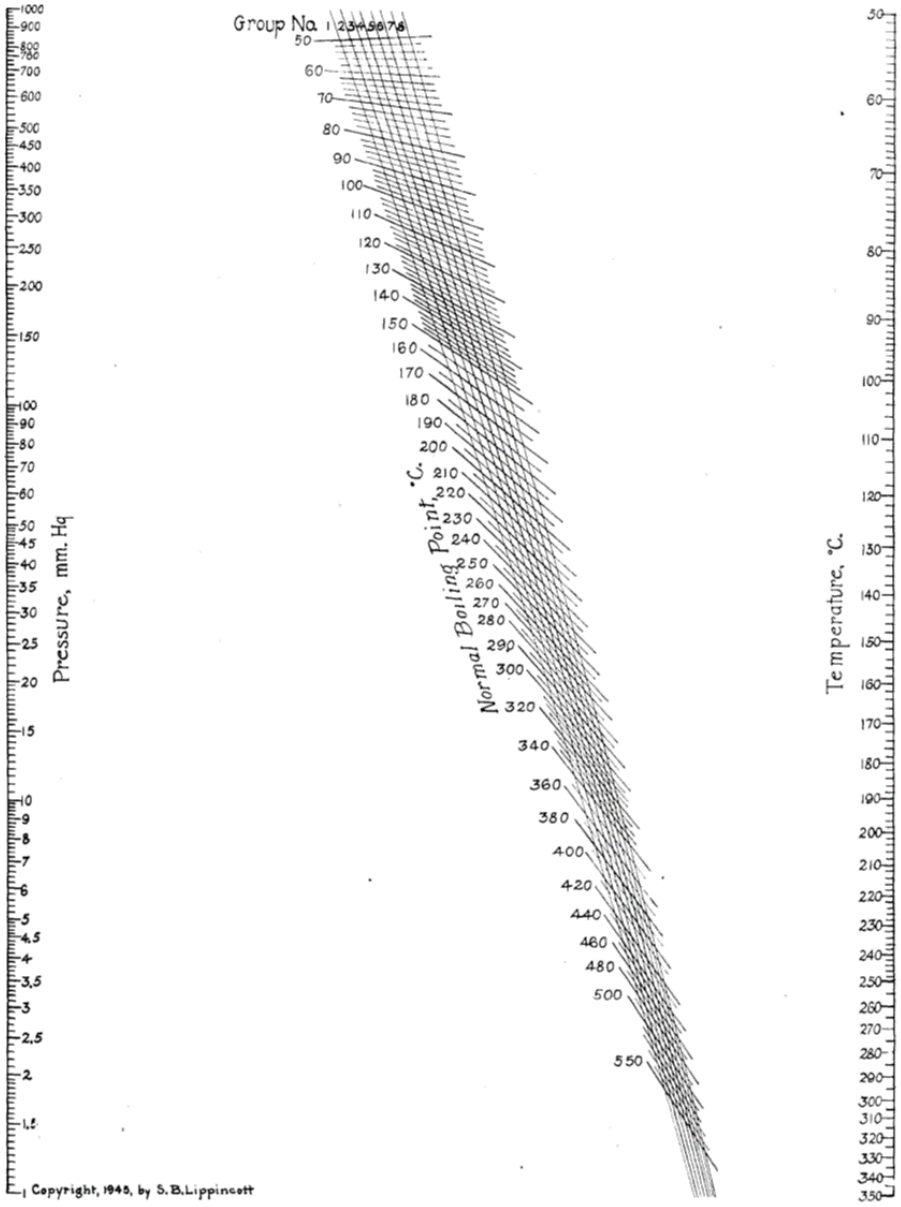


Figure 2.4 – Vapor Pressure-Temperature Nomograph for the determination of the boiling temperature at a given pressure [14].

Initially, the temperature of the heating bath is set close to the material melting temperature to facilitate melting. The temperature is then gradually increased until boiling begins. The vapors

ascend and upon reaching the top of the column, they are directed towards the cooler where they condense. Using a circulation bath, the cooler temperature is set between a value slightly higher than the melting temperature and lower than the boiling point (at apparatus pressure). The circulating bath is set to 70°C and 50°C for succinonitrile and salol, respectively.

The first drops of distillate are gathered in a small intermediate recovery beaker, disregarded due to their low-boiling impurities. Once the temperature stabilizes at the column apex, the Pauli separator is turned, and the distillate is directed into the appropriate container. Throughout distillation, it is imperative to sustain the temperature at the column apex equal to the material boiling temperature under the applied vacuum. When flask heating ceases, the remaining drops are collected in another small container, also set aside.

2.2.1.3 Troubleshooting and Key Observations in Distillation

Various trials were conducted to optimize the distillation process. Despite the manometer reading showing around 6-7 mbar (4.5 - 5.25 mmHg) at the device outlet, the pressure inside the balloon could be significantly higher due to multiple pressure drops. In the case of SCN distillation using the VACUUBRAND RE 2.5 pump, which reduces pressure to about 0.075 mmHg, allows SCN to start boiling at 65°C, and the process last approximately 3 hours. The distillation of salol was realized using the same vacuum pump. The heating bath temperature needs to be as high as 110°C to start seeing vapor in the column, and at 130°C to accelerate the process.

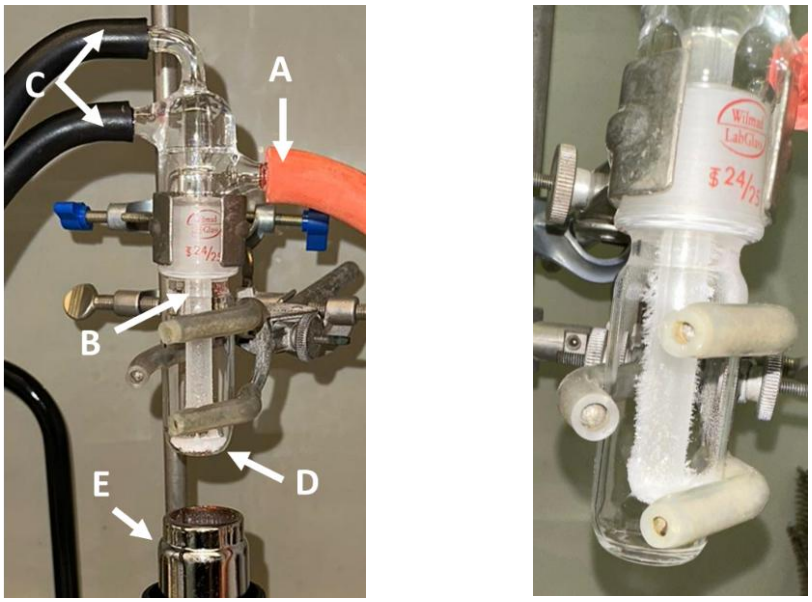
Furthermore, SCN samples underwent Nuclear Magnetic Resonance (NMR) spectroscopy for molecular characterization (BRUKER Avance III 600MHz). NMR analysis facilitated the identification of organic molecules, including impurities. Weak signals possibly indicating impurities were observed, with slightly fewer residual signals in the doubly distilled sample compared to the singly distilled one. Notably, the signal corresponding to water decreased from 0.002 to 0.001%. NMR analyses were also conducted on salol, but only in the commercial material. Impurity signals were clearly detected along with the predominant signals of salol. The water signal was measurable, accounting for 0.001% of the total. The purity of the distilled solid was judged to be higher than 99.5% by melting point measurements using a single cell calorimetry system (DSC600, Linkam).

2.2.2 Sublimation

The process of sublimation is the direct transition of a solid into a gas phase without first going through a liquid phase. Sublimation is an analogous process to boiling, as it occurs when a compound vapor pressure equals its applied pressure. The difference is that sublimation involves a solid vapor pressure instead of a liquid. Most solids do not have an appreciable vapor pressure at easily accessible temperatures, and for this reason the ability to sublime is uncommon. Compounds that are capable of sublimation tend to be those with weak intermolecular forces in the solid state. As relatively few solids are capable of sublimation, the process can be an excellent purification method when a volatile solid is contaminated with non-volatile impurities. Of the solids with appreciable vapor pressures at room temperature, many still require rather high temperatures to actively sublime (when their vapor pressure equals the atmospheric pressure of nearly 760mmHg). As a consequence, some char and decompose during the process. For this reason, it is very common to perform sublimation under a reduced pressure (vacuum sublimation).

2.2.2.1 The sublimation unit

A sublimation apparatus, like the one shown in Figure 2.5a, can be created from a filter flask, where the side neck is connected to an aspirator or vacuum trap (A). The neck is equipped with a cold finger (B), which is a tube filled with ice water or another chilling substance (C). The cold finger is inserted into the filter flask after impure materials have been added to the bottom (D). Carefully heated using a hot plate or with a heat gun (E), the material is kept from melting or boiling thanks to the reduced pressure inside the filter flask. As the organic component starts to sublimate, the gas instantly crystallizes as it reaches the cold finger (Figure 2.5b), making collection possible.



(a) (b)

Figure 2.5 – (a) Sublimation apparatus. (b) Detail of the formation of crystals during the sublimation process.

2.2.2.2 The sublimation process

Among the materials used in this work, it has been demonstrated in the literature that borneol can sublime [15, 16]. It looks like a white crystal-colored lump-solid with melting and boiling points of 202 and 212°C, respectively [3], and it has a vapor pressure of 0.05 mmHg (at 25°C) [17]. Its sublimation was performed at a pressure equal to 1.73 mmHg, and with cold water circulating inside the finger. The solid material at the bottom of the filter flask was heated using an air-gun set to 50°C. After having all of the borneol sublimed on the finger, we turn off the vacuum pump and the cold-water circulation. The sublimed borneol is scratched off the finger with a scalpel and recovered in a clean recipient that is kept inside a glovebox to avoid contamination.

2.2.2.3 Troubleshooting and key observations in sublimation

NMR analyses (BRUKER Avance III 600MHz) were performed on borneol samples. In the commercial sample, impurity signals were discernible in addition to the borneol signals. The integration of signals relating to contaminants did not significantly alter between the commercial borneol sample and after sublimation. The reason is the superposition of the borneol and water signals, making it impossible to separate them and therefore impossible to

quantify. Elemental analysis (Thermo Finnigan EA 1112) were additionally performed in the sublimated sample confirming its purity higher than 99.5%.

2.2.3 Recrystallization

The process of recrystallization is commonly employed to purify solid compounds. During recrystallization, an impure solid compound is dissolved in a hot liquid until the solution is saturated. Subsequently, the solution is allowed to cool down leading to the formation of crystals. Ideally, impurities present should remain dissolved in the solution, and not get incorporated into the growing crystals. The crystals can then be separated from the solution using filtration. It is important to note that complete recovery of the compound may not be possible as a portion may dissolve in the solution and become lost. Recrystallization is not generally thought of as a separation technique; rather, it is a purification technique in which a small amount of an impurity is removed from a compound.

2.2.3.1 The recrystallization unit

The equipment typically used for recrystallization includes a heat source, such as a hot plate, a filtration setup (such as a Büchner funnel and filter paper), a solvent for dissolving the impure compound, and a suitable container for recrystallization, such as an Erlenmeyer flask. Additionally, a thermometer and a stirring device may be used to control the temperature and aid in the recrystallization process. The required equipment and steps are described in Figure 2.6.

The compound to be recrystallized and the solvent are placed in separated Erlenmeyer flasks. The one with the solvent is heated to boiling in a hotplate. The hot solvent is added to the flask containing the compound (at room temperature) in small portions, swirling after each addition, until the compound being completely dissolved (Figure 2.6, step 1). One should not add more hot solvent than necessary, just enough to dissolve the sample. Then a hot filtration is done though fluted filter paper into a heated flask (Figure 2.6, step 2) in order to eliminate any impurities that will not dissolve even with hot solvent. The flask containing the solution is then left undisturbed, covered with a watch glass to prevent evaporation and contamination, until it cools to room temperature (Figure 2.6, step 3). Once the crystals have formed (Figure 2.6, ex. 3a), the flask is placed in an ice bath to ensure that the maximum amount of crystals is obtained

(Figure 2.6, step 4). It should be left undisturbed at least 1 h or till the compound appears to have completely crystallized out of solution (Figure 2.6, ex. 4a). The crystals are then isolated by vacuum filtration, using a Büchner funnel (Figure 2.6, step 5). The crystals on the Büchner funnel are rinsed with a small amount of fresh, cold solvent to remove any impurities that may be sticking to the crystals. The crystals are transferred to a Petri box (Figure 2.6, ex. 5a) that is placed in a desiccator with silica gel (Figure 2.6, step 6) for several hours or days.

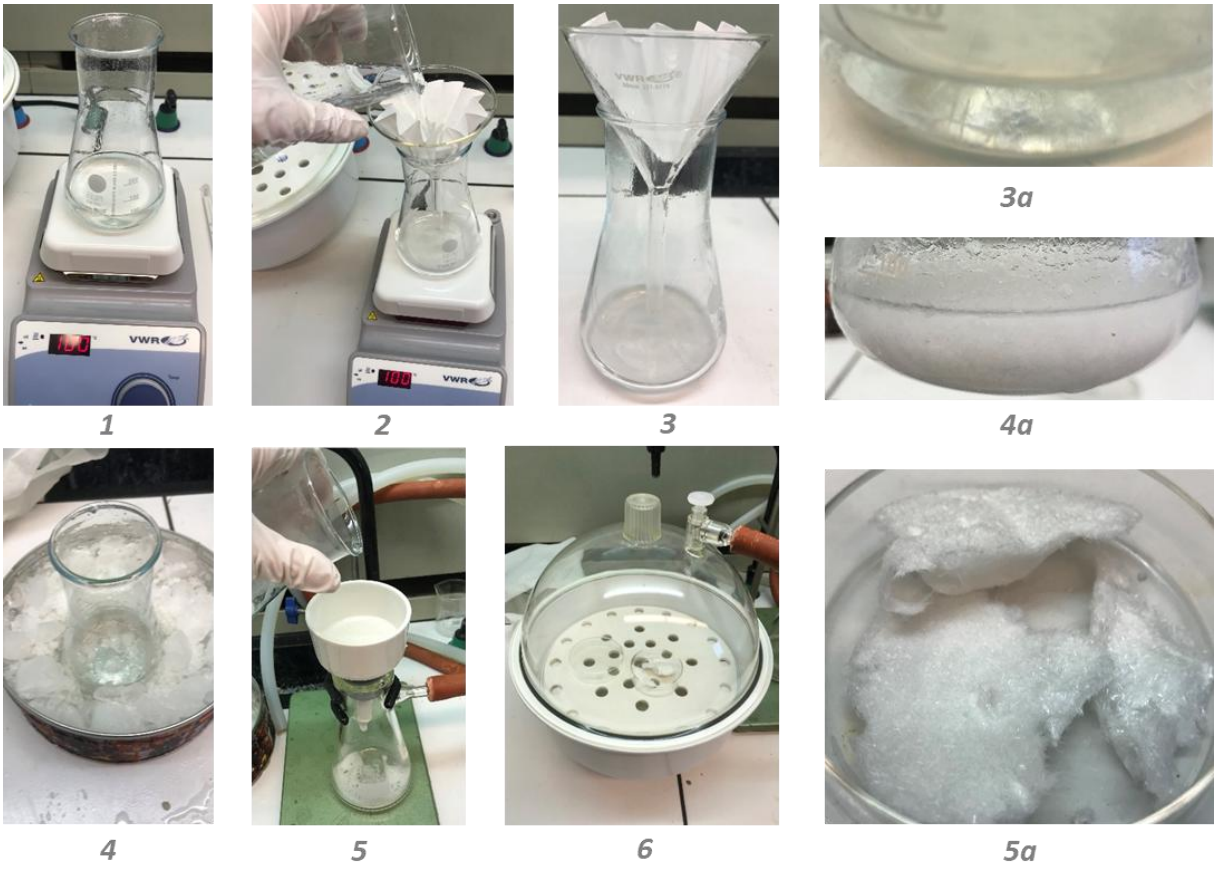


Figure 2.6 – General working process of a purification by recrystallization.

2.2.3.2 The recrystallization process

Finding a solvent with correct characteristics to perform the recrystallization is critical. The solid compound should be insoluble in the cold solvent but substantially soluble in the hot solvent because typically, solids have higher solubility in hot liquids than cold ones. The solvent chosen should have a boiling point of at least 40°C so that there is a significant temperature difference between boiling and room temperature. Its boiling point must also be below the

melting point of the solute to enable crystallization; this will induce the formation of fewer nucleation sites, and favor larger and purer crystals. Additionally, the solvent must be un-reactive with the solid compound.

Between the materials used in this work, vanillin is purified by recrystallization. In order to select the recrystallization solvent, a literature review was done on the solubility of vanillin in pure and mixed solvents [18-21].Vanillin was found to be freely soluble in most of the solvents, and it has relatively low solubility in cold water. Even if it is best to use a single solvent for crystallization, a first trial using an ethanol-water mixed solvent was performed since this mixture fills the criteria required for a recrystallization solvent. However, the recrystallization did not work out since it oiled-out (the dissolved compound came out of solution above its melting point and formed a liquid instead of a solid). Initially, we had ruled out water because its boiling point (100°C) is higher than the vanillin melting point (81-83°C). However, vanillin is too soluble in the majority of solvents commonly used for recrystallization. Consequently, water is used as the recrystallization solvent. This means that the cooling of the solution is rapid inducing the formation of many nucleation sites and so the growth of many small crystals.

The purity of solid is judged by melting point measurements using a single cell calorimetry system (DSC600, Linkam).

2.3 Thin samples preparation

In this section, we present the different steps of preparation of the thin samples and how the various materials are confined inside. First, we describe how the crucibles are prepared and then filled.

2.3.1 Preparation of alloys

Different transparent organic systems are considered in this thesis to study the solidification. Salol is used directly after its purification by distillation, whereas the other two materials, succinonitrile-borneol and succinonitrile-vanillin are alloyed before filling.

Pre-weighed glass bottles are filled with melted SCN inside a glovebox, sealed, and weighed to measure the SCN amount. The mass of solute (borneol or vanillin) is weighed separately and added gradually to the melted SCN until a complete dissolution. We have to ensure that the

temperature of dissolution remains below 70°C for borneol and 80°C for vanillin to avoid polymorphic transitions.

Based on the phase diagrams (Figure 2.2) and the expected faceted solid-liquid interface during solidification, we prepare the following samples: 4.8, 6.6 and 9.6 wt% of SCN-BN, and 24.7, 29.1 and 34.9 wt% of SCN-VAN. The prepared alloys are kept inside the glovebox under an inert atmosphere. Those of SCN-VAN are covered with aluminum foil because they may be sensitive to light [22-24].

2.3.2 Preparation of the crucible

The crucibles must be resistant, transparent and leakproof. The latter is necessary for safety reasons, due to the very frequent toxic nature of the materials. They must also be very good thermal conductors and compact. The use of thin-samples avoids the effects of convection in the liquid phase, which would lead to variations of concentration in front of the interface and consequently perturb the solidification [25, 26] .

In order to prepare the crucible, we use two borosilicate glass slides of lateral dimensions 200× 26 mm² and 150×130 mm², and nominal thickness 0.3 mm. The slides are separated by a Mylar spacer (Polyethylene terephthalate, PET) with a given thickness (usually 50 µm in this work).

In order to avoid contaminations, we did a deep cleansing of the glass slides using an ultrasonic bath. The cleansing process is composed of many stages. Firstly, we put all of the glass slides in a bath filled with water for 20 minutes. This cleansing is repeated with acetone, then with a laboratory cleaning detergent (RBS) and finally distilled water. The slides are placed in an oven at 80°C to dry. The Mylar spacers are cleaned with acetone.

The Mylar spacer is placed over the bigger slide, and we glue the extremities of the Mylar spacer with UV-curable glue (NOA81, Norland) that dries within 5 minutes using a UV light (Figure 2.7a). The smaller slide is placed over the Mylar spacer (Figure 2.7b), and the "sandwich" is transferred under a home-made mechanical press (Figure 2.7c). A pressure is applied while monitoring carefully the fragility of the slides. We apply epoxy glue to the edges of the slides, while the crucible is always under the press, and we let it dry at least 24h (Figure 2.7d). After removing the crucible from the press, we apply epoxy to one of the extremities and we let it dry (in general 24h).

Epoxy resin is a polymer with excellent electrical, thermal, and chemical resistance, it is commonly used for glass slide assemblies and it resists a large number of substances as detailed in the chemical resistance table given in [27]. Epoxy should have a good resistance to salol since it has an excellent or good chemical resistance to esters and compounds presenting saturated cyclic chains. Borneol, a terpene derivative and chiral molecule, should be compatible with epoxy, similarly to turpentine, a terpene derivative, or other chiral compounds. Vanillin, a phenolic aldehyde, is also compatible as epoxy resists to vanillic acid and related compounds. Consequently, we expect that epoxy present an excellent chemical resistance to the materials used in this work.

Several tests were done in order to find the best shape of the Mylar spacer. In the first one, thin slices of Mylar spacers are placed in between the glass slides in the middle; they can be removed from the open extremity without being glued to the crucible but after removal, heterogeneities in the thickness of the sample are present. In the second one, the spacers are cut to form a selector channel opening into a specific "V"-shaped space (funnel) as exemplified in Figure 2.7. The aim of this is to select a small number of crystals at the beginning of the solidification, to obtain large grains that grow and spread out in the funnel. In the third one, we cut thin slices of Mylar spacers, similarly to the first option, but we place them very close to the edges of the smaller glass slide. In that way, the half of the Mylar is inside the crucible and the other half outside. We apply epoxy glue over the Mylar and the glass slides.

2.3.3 Sample filling

The filling takes place under a glovebox with inert nitrogen atmosphere. The liquid material is introduced with the help of Pasteur pipettes (sterilized) at the opened extremity, with the sample in a vertical position. Filling is driven by gravity. The sample is then let to solidify naturally. The samples are then sealed with the epoxy glue (Figure 2.8).

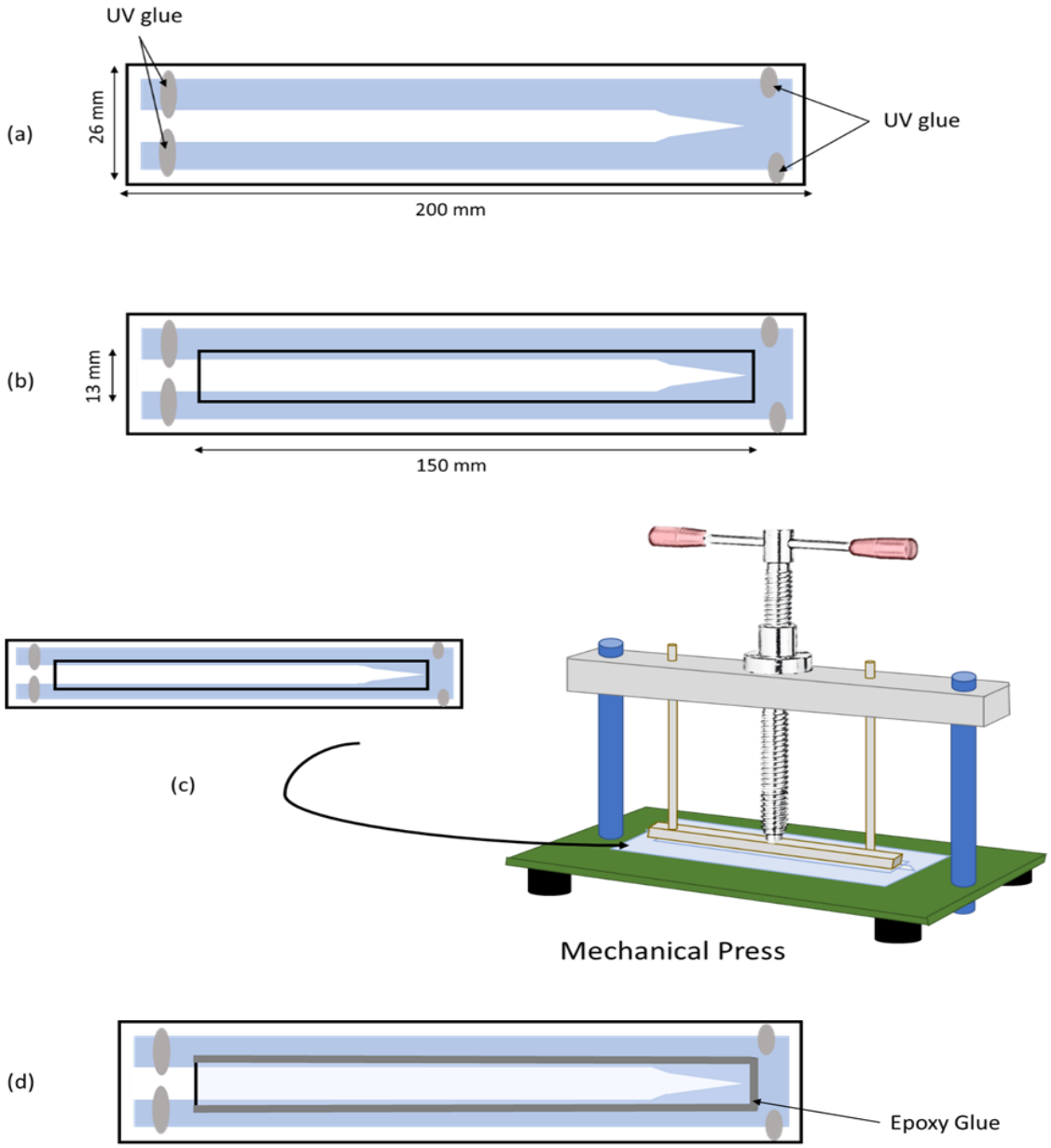


Figure 2.7 – Schematic steps of thin-sample crucible preparation.

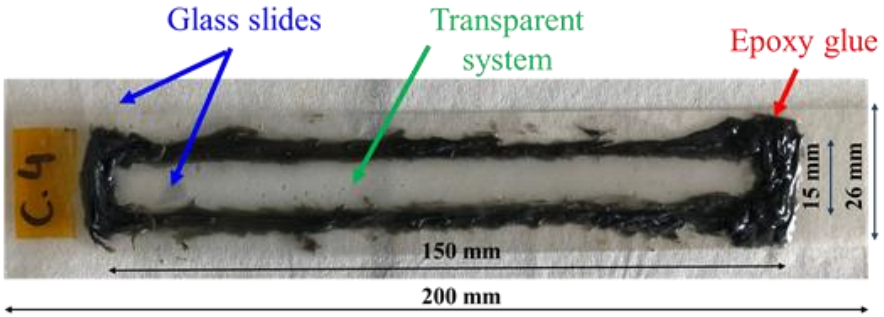


Figure 2.8 – Picture of a thin-sample filled with salol and completely sealed.

Some difficulties were encountered during the filling of the samples with salol: samples that were full in the liquid state present empty volumes when solid. Solid shrinkage is a well-known phenomenon in metallurgy, and the volumic thermal expansion coefficient of salol (2.1 x 10^{-4} $°C^{-1}$ for solid and 7.95 x 10^{-4} $°C^{-1}$ for liquid [28]), at least one order of magnitude higher than those for metals, justifies this contraction. During thermal contraction as the temperature decreases, the volume reduces, causing the density to increase. Since both the literature data on salol expansion coefficient and density [29] are quite old, this motivated us to revisit the density as function of temperature which will allow us to estimate the thermal expansion coefficient. Densities at the appropriate temperature were determined with a Gay-Lussac type calibrated pycnometer (5 mL, m_0). The pycnometer is a glass flask equipped with a closely glass stopper having a fine capillary hole. To determine the density of the solid, the pycnometer is partially filled with the solid, then it is weighed and lastly filled with water before weighing it again. The difference in mass before and after adding the water permits to calculate the volume of the solid, and consequently the density. In order to measure the liquid density, the pycnometer is filled with liquid salol under controlled temperature environment. The results for the salol densities are shown in Figure 2.9. These data can be used to estimate the thermal expansion coefficient β using the relation $\beta = -\frac{1}{\rho_0}\frac{\rho_1-\rho_0}{T_1-T_0}$. If we consider T_0 = 37°C and T_1 = 60°C, we have β = 7.42 x 10^{-4} $°C^{-1}$ which is very close to the literature value. So, when one of our samples is completely full with liquid salol at 60°C (0.0975 mL), the corresponding volume in solid state is 0.0886 mL, leading to a considerable volume difference (8.9 x 10^{-3} mL i.e. ≅ 10 % of the initial volume). Since the sample filling was done under nitrogen environment, this empty space was filled with nitrogen. Upon melting, the nitrogen is dissolved in the liquid and originates bubbles when solidifying again. In our work, filling the samples under nitrogen atmosphere is probably a better choice than vacuum, since filling the sample under vacuum would lead to the same solid contraction but even quickly due to the absence of internal pressure. This would increase the risk of structural stresses and fractures during filling. These measurements did not have a direct impact on the sample preparation used in this work. However, they may be useful for future device improvements, such as the development of a system of volume compensation like what is done in bulk samples [30-32].

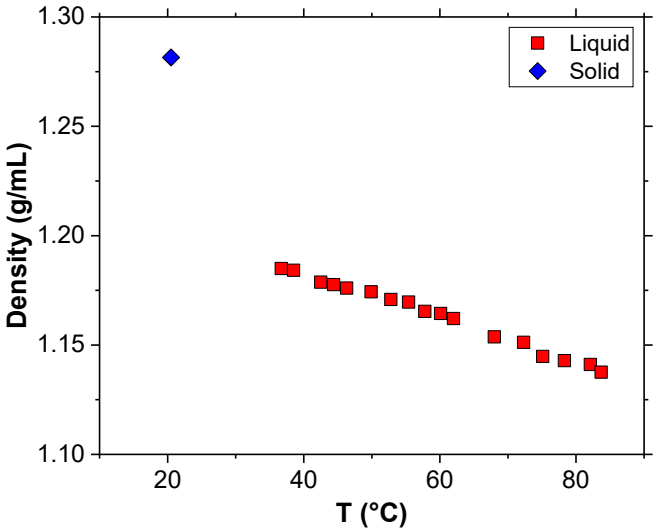


Figure 2.9 – Densities of salol as a function of temperature.

2.4 Experimental solidification device

In situ observation of the solid-liquid interface requires an experimental device capable of imposing a temperature gradient and moving the sample while allowing visualization. The first device of directional solidification with *in situ* observation of transparent samples was initially conceived in the 1960's by Hunt *et al.* [33], and then frequently used and improved by numerous teams till nowadays. In this work, to carry out *in situ* observations of the solidification of organic transparent materials, the Experimental setup for COnfined DIrectional Solidification (ECODIS) is used (Figure 2.10). It enables to study thin rectangular samples from 25 µm to 1 cm. During an experiment in this device, a sample is moved at a controlled speed V_p through a controlled thermal gradient G while observing the solid – liquid interface from the side.

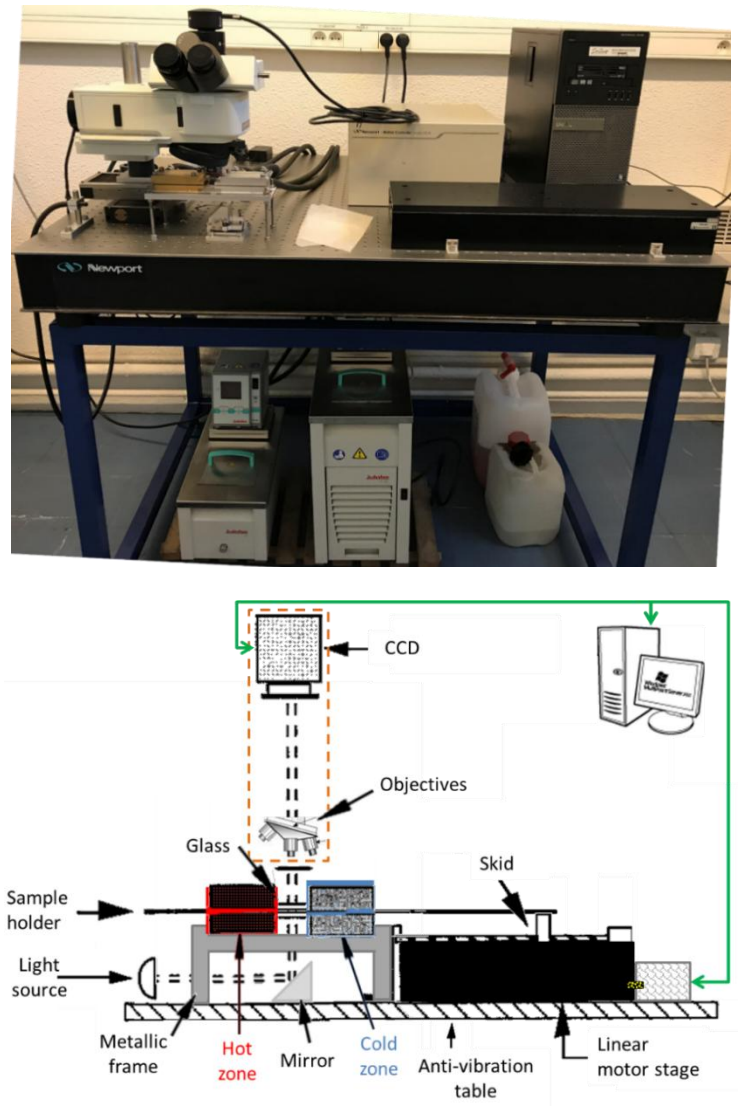


Figure 2.10 – Picture and schematic of the ECODIS device used for in situ observation of directional solidification.

2.4.1 Thermal control

The system must generate a constant thermal gradient across the sample with the solid-liquid interface located within this thermal gradient zone. The sample moves through two thermal zones, the cold zone on one side and the hot zone on the other side. The hot zone is set at a temperature well above the melting point of the material (60 to 75°C), and the cold well below (5 and 10°C). Both zones are separated by a gap "d" (Figure 2.11) which can be adjusted between 5 and 35 to the need of the experiments.

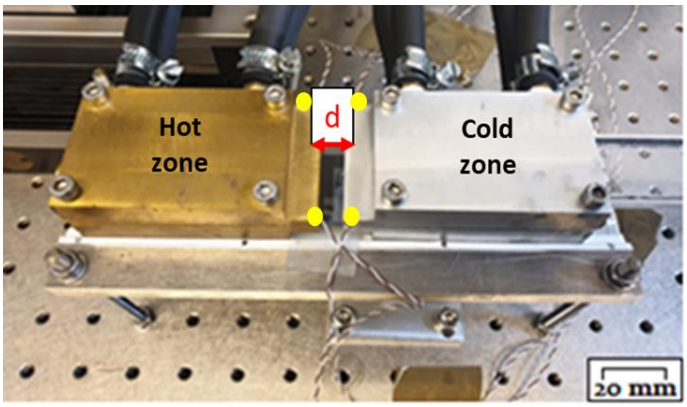


Figure 2.11 – Image of the hot and the cold zones separated by a gap d.

The hot zone is composed of two brass blocks ($8 \times 5 \times 1.5$ cm^3) that are stacked on top of each other, and the cold zone is composed of two aluminum blocks ($8 \times 5 \times 1.5$ cm^3) that are stacked in the same way. The two blocks in each zone take the sample in "sandwich" allowing its displacement. Both zones are regulated by fluid circulation from thermostatic baths. T-type thermocouple (diameter 0.2 mm) are positioned in the thermal zones in order to master their temperature, as shown by the yellow dots in Figure 2.11. A USB 2.0 full-speed thermocouple input module (USB-TC series, Measurement Computing) with ±0.080 V precision was used to read the thermocouples output (using the DAQami^{TM} software, acquisition frequency 1 Hz). The typical thermocouple accuracy specification is ±0.34°C.

Due to the dimensions of the microscope objectives (the optical system will be described in the next sub-section), the thermal system shown in Figure 2.11 could not be used with the lower magnification objective (PLAPON1.25X, Evident Olympus). This objective has a working distance of 5 mm. The L-shape of the brass/aluminum blocks prevents us from reaching this working distance. New blocks had to be manufactured, without this L-shape, so that we could use such an objective. The gap between the two blocks need to be higher in this case (31 mm) and the working thermal gradient will be lower.

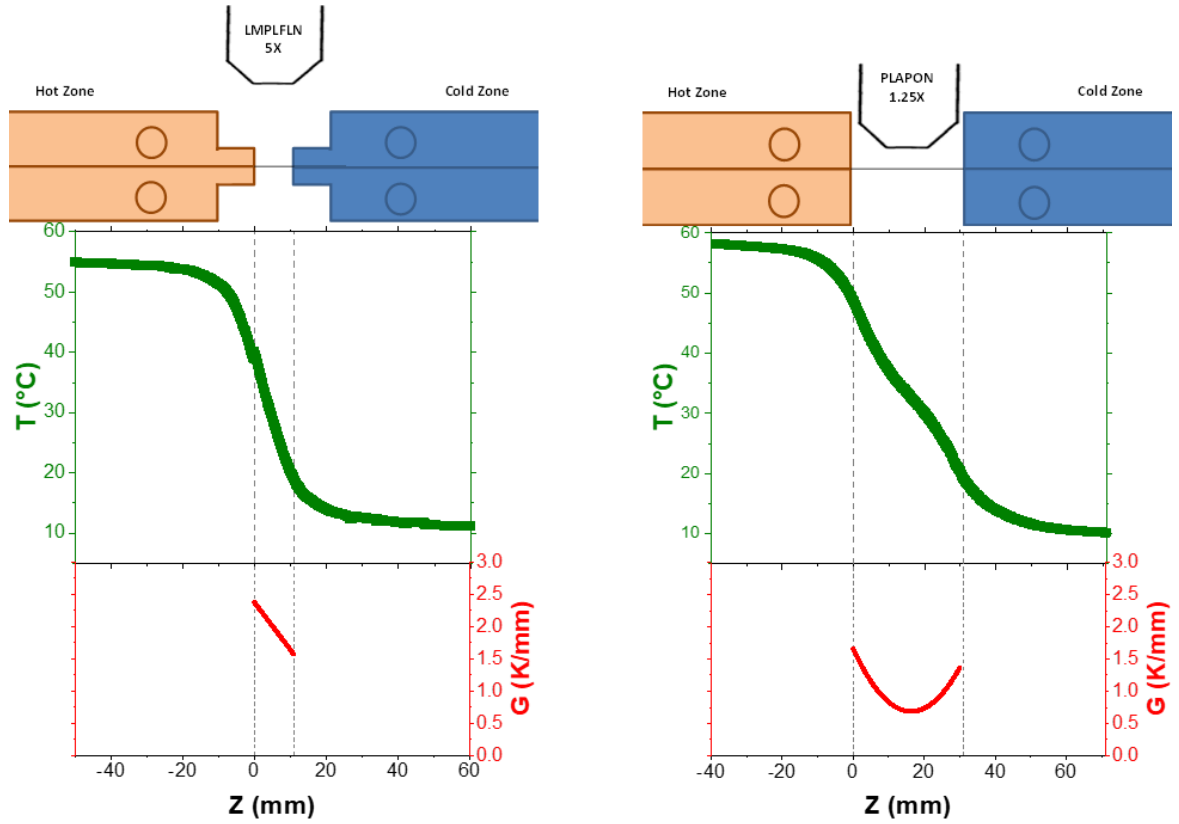
2.4.1.1 Thermal gradient measurement

The thermal arrangement is adapted to each specific material, not only the temperatures imposed in the thermal zones but also the gap between them (Figure 2.11). Specific experiments were achieved to measure the axial temperature gradient *G* in the non-regulated zone.

A thermocouple (TC) is moved through the furnace, from the hot zone to the cold zone, in order to record the local temperature along the non-regulated zone. To do so, an ultra-fine wire PFA thermocouple Type K (0.08 mm in diameter) is used. The TC is trapped in a crucible filled with ethylene glycol. First, this material was chosen due to its thermal conductivity (0.251 W/m.K at room temperature [34]) comparable to the one of the succinonitrile (0.223 W/m.K for liquid and 0.225 W/m.K for solid [35]). It turns out that it is also very similar to salol as well (0.238 W/m.K for liquid and 0.34 W/m.K for solid [36]). It is assumed that ethylene glycol is a good choice due to its conductivities close to the materials used in this work, as well as by the simple manipulation. The assembly is then placed in the solidification furnace in a way that the tip of the thermocouple is placed far away from the non-regulated zone inside of the hot zone. A given pulling velocity is applied and the motion data as well as the temperatures are recorded as a function of time (frequency of 2 points/s). Pulling is stopped once the thermocouple tip is far away from the non-regulated zone inside the cold zone.

We perform some preliminary tests using different velocities and directions of pulling. No hysteresis appears when pulling from the hot towards the cold zone, or from the cold towards the hot zone; both lead to the same temperature profile.

Figure 2.12 shows two examples of the evolution of the temperature for a velocity of 10 μm/s. The limits of the non-regulated zone are indicated by the two dashed vertical lines. As can be seen comparing the temperature curves and the furnace schemes at the top, the temperature begins to shift before reaching the non-regulated zone and continues to decrease well after it. We can see a inflection point on the temperature profile of Figure 2.12b, associated with a locally much weaker gradient. Consequently, the temperature data as function of the distance within the non-regulated zone are fitted by a 3rd oder polynome. The derivate of the fitting curve allows to obtain the local gradient. Its variation is shown at the bottom of Figure 2.12 as function of the distance in the non-regulated zone. As can be noticed, the local thermal gradient is not constant, it is higher near the hot zone and lower near the cold one. If the interface at rest is located at around 1 mm from the border of the hot zone (as currently observed), the local G is equal to 2.3 K/mm in Figure 2.12a (T_H = 60°C, T_C = 10°C, d = 11 mm) and 0.93 K/mm in Figure 2.12b (T_H = 65°C, T_C = 5°C, d = 31 mm). This procedure was repeated for different imposed temperatures and gaps between thermal zones.



(a) (b)

Figure 2.12 – Temperature profiles and thermal gradients G obtained with the thermocouple sample: (a) T_H = 60°C, T_C = 10°C, d = 11 mm; (b) T_H = 65°C, T_C = 5°C, d = 31 mm.

2.4.1.2 Thermal field characterization

It is commonly assumed that during solidification in thin-samples, assumption of a frozen thermal field is acceptable [37, 38]. This assumption implies that the thermal gradient remains stationary throughout the entire process, without any changes due to solidification dynamics. It is clearly not the case for bulk samples [39, 40] as isotherms shift due to the evolution of thermal exchanges induced by pulling ("instrumental recoil") and to the latent heat release which perturbs the thermal field. Akamatsu and Faivre [41] also reported this kind of thermal inertia in a thin-film directional solidification stage. Therefore, we decided to characterize our thermal system in order to verify if the frozen temperature assumption can be applied within the non-regulated zone.

Eight ultra-fine wire PFA thermocouples Type K (0.08 mm in diameter) were placed over the bigger glass slide (200×26 mm²), evenly spaced as far as possible. The smaller glass slide (150×130 mm²) is placed over to create a specific sample filled with ethylene glycol. The exact

positions of the thermocouples are measured with the help of the optical microscope (Figure 2.13). The assembly is placed in the solidification furnace in a way that the tip of the last thermocouple is placed at the beginning of the non-regulated zone. At least 1 hour of stabilization is waited. A given pulling velocity is applied and the motion data as well as the temperatures of the different thermocouples are recorded as a function of time. Pulling is stopped once the first thermocouple tip arrives at the end of the non-regulated zone. This procedure is repeated for different imposed temperatures and pulling velocities.



Figure 2.13 – Photo of the sample with the eight thermocouples.

The result is a series of curves (Figure 2.14a) where the time can be converted in distance since one knows the positions of the thermocouples. It should be mentioned that even if eight thermocouples were placed at the beginning, two of them run out of service, and once the samples are sealed, they cannot be opened. This is why only six profiles are represented. One may notice in the example shown in Figure 2.14b that the curves are almost superimposed. If one considers a fixed position z and represent the temperature measured by the different thermocouples (Figure 2.14c), one can see that there is no significant difference in time. The slight difference may be attributed to the noise in the temperature profiles or to the fact that the thermocouples are not positioned exactly along the same x line (as can be seen in Figure 2.13). So, we consider that there is no isotherm shift due to instrumental recoil. Combining the measurements at different pulling velocities, we estimated the uncertainty in the thermal gradient within the non-regulated zone (Figure 2.14d). Even if these results cannot be extrapolated to the directional solidification experiments due to the different thickness of the samples, they allowed us to have an order of magnitude for the uncertainty.

In order to evaluate the effect of the latent heat, a similar sample needs to be filled with the material whose solidification will be studied. The results will not be presented in this thesis.

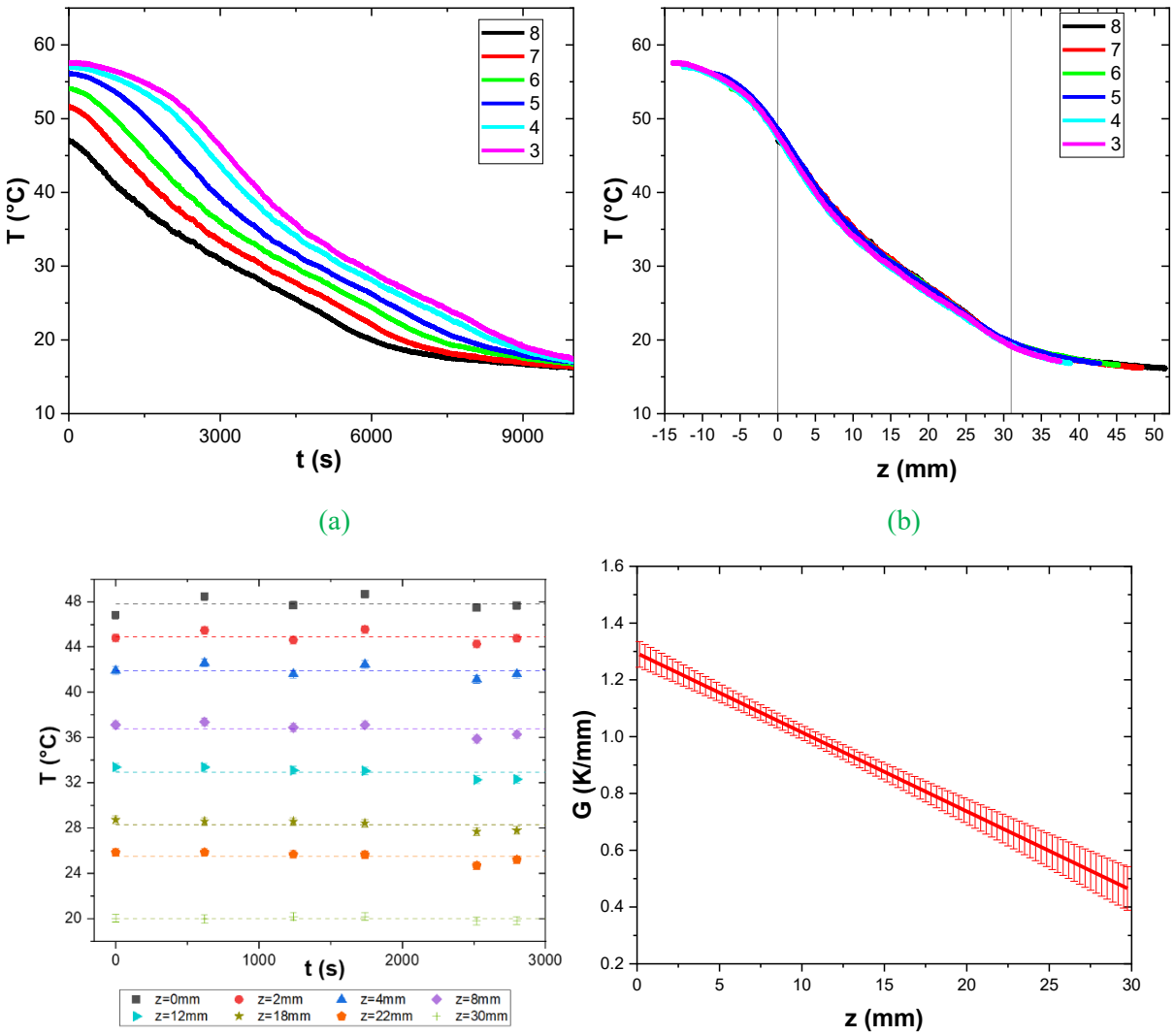


Figure 2.14 – Temperature profiles measured by the six thermocouples as function of (a) time t and (b) distance z. The vertical dashed lines are the limits of the non-regulated zone. (c) Temperature as function of time at given positions within the non-regulated zone. The dashed lines correspond to the average values. (d) Mean local thermal gradient G within the non-regulated zone. (T_H=75°C, T_C=5°C, d=31mm, V=5µm/s)

2.4.2 Optical system

Obtaining high-quality images of the interface during solidification with non-disruptive equipment is a significant experimental challenge. Thanks to the organic systems transparency, solidification is observed *in situ* and in real time using a standard optical microscope (BXFM), Evident Olympus by transmitted light. The used fiber optic cold light source (KL1600LED-2, Evident Olympus) is an attractive alternative to conventional halogen light sources. The

microscope is also equipped with a compact brightfield reflected light illuminator (BX3M-KMA-S, Evident Olympus) with two filter slots, one slot for polarizer and one slot for analyzer. Objectives with magnification from 1.25x to 20x are available (spatial resolution: 3.6 – 0.2 µm/px; field-of-view (FoV): 9.1 x 6.8 mm² - 0.6 x 0.4 mm²). The light source is initially directed parallel to the heated area, but light is transmitted perpendicular to the interface through the positioning of a mirror above the observation area (Figure 2.10). To position the mirror at the desired angle, it is mounted on a homemade goniometer. A digital camera (SC50, Evident Olympus) with resolution equal to 15 frames per second is attached to the microscope to capture images and videos.

2.4.3 Movement system

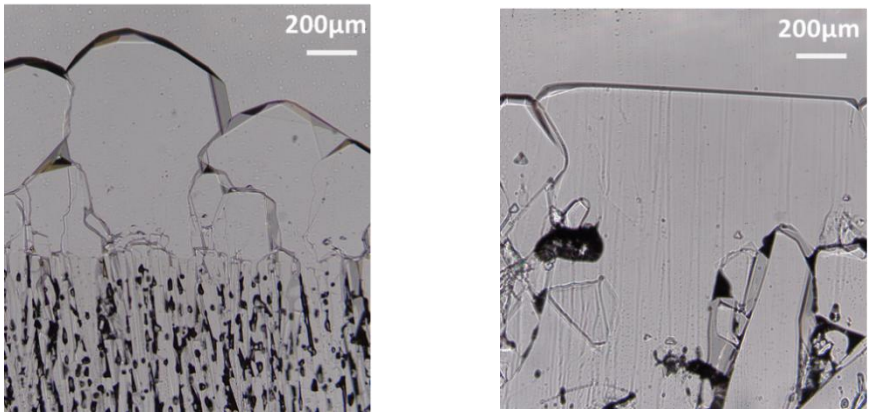
The sample is positioned on a sample holder and must be moved at a precise speed. To accomplish this, we use an ultra-precision linear motor stage (XML350-S, Newport) combined with a universal high-performance axis motion controller and driver (XPS-D, Newport), as shown in Figure 2.10. This configuration guarantees progressive and carefully regulated movement (from 0 to 300 mm), with speeds of the order of micrometers per second. The XPS controller calibration is an essential step to ensure precise and reliable movement. A micrometer specimen and well-synchronized chronometer are used to perform its calibration: for a given period of time, the displacement of the specimen is measured, and that for several speeds in native units. The following relationship is found: $V(\mu m/s) = 1006.8V(n.u.) - 0.0148$.

2.5 Initial solid seed preparation

In faceted growth, the crystallography of the system determines the morphology of the structures, and the control and study of the orientation of the crystals is essential. When a material solidifies without specific precaution, numerous grains nucleate with varying crystal orientations. So, a monocrystalline sample should be favored over a polycrystalline to avoid the multitude of orientation changes that would occur.

However, the preparation of a monocrystal is not a trivial task considering the geometry of our samples and our V-shaped selector which is large, the furnace design and the crystallographic properties of the materials. We applied a specific procedure in order to try to reduce the number of grains at the beginning of the solidification experiments. The sample is placed in the gradient

furnace, and then it is melted at controlled velocity. In general, we melt the first ¾ of the sample at 40 µm/s, and then we reduce the velocity until having a small quantity of solid. In the ideal case, we should have only one seed of the material, but it is very hard to achieve (if not impossible with our device). Once grains have nucleated, they grow and the size of some of them extends, while it decreases for others which ultimately disappear. Preliminary tests showed that if the sample is melted in a controlled way, i.e. placed at the level of the cold zone and melted with a precise pulling rate, rather than placed directly at the level of the hot zone, a flatter interface was obtained at rest. Figure 2.15 shows a comparison between the solid-liquid interface of salol of a sample that was placed in the furnace in the solid state, so it was directly melted under the effect of the thermal gradient, and a sample that was melted with a controlled rate. We can see that in the second case, the interface is flatter and the number of defects is reduced. The reason is that using a quite high melting rate, the crystallographic planes along which the facets grows are eroded uniformly and quickly, leaving less time for the interface to develop irregularities or steps between different crystallographic planes, resulting in a smoother, flatter interface. Also, the sharper thermal gradient around the interface tends to suppress localized instabilities, promoting a more uniform, planar retreat of the interface.



(a) (b)

Figure 2.15 – Photos of the interface of salol after being stabilized for 5 hours: (a) sample is directly placed in the furnace; (b) sample is melted before being placed in the furnace.

Depending on the grain parameters, the selection mechanism is linked either to the velocity of the solid-liquid interface, likely to be orientation dependent and then different for each grain, or to the surface energy of the interface, which is also orientation dependent [42, 43]. Fujiwara

et al. [44, 45] found that there is a critical velocity for which the selection mechanism changes from surface energy to kinetic. They found that when the growth rate is very low, a grain with planes having the lower surface energy tends to expand to the lateral direction during the crystal growth. While when the growth rate is high enough to create differences in the speed between grains, the faster growing grain takes over and expands laterally.

Given the novel and experimental nature of this thesis and based in procedures previously applied by other authors, two techniques were used in this work to produce an initial solid seed. Both techniques started with a small solidified region acting as nucleation point. Then, they are solidified, in the first one using a controlled cooling (imposed pulling rate) and in the second making a quenching trial (rapid solidification without controlling the pulling rate). The first technique seems to be more appropriated to highly faceted materials, like salol, in order to try to favor the growth of grains with specific orientations. The second one seems adapted to systems whose type of growth depend on the orientation, such as the succinonitrile-borneol alloy where we have a mixed growth between rough and faceted. Each trial will help refine the process until a reliable method for creating the desired seed is found.

In the first technique, after the controlled melting, the sample is solidified at a controlled velocity for at least 15 mm. Figure 2.16 shows an example of a solid-liquid interface of salol just before this step where we can clearly see a small amount of crystals showing an orthorhombic structure.

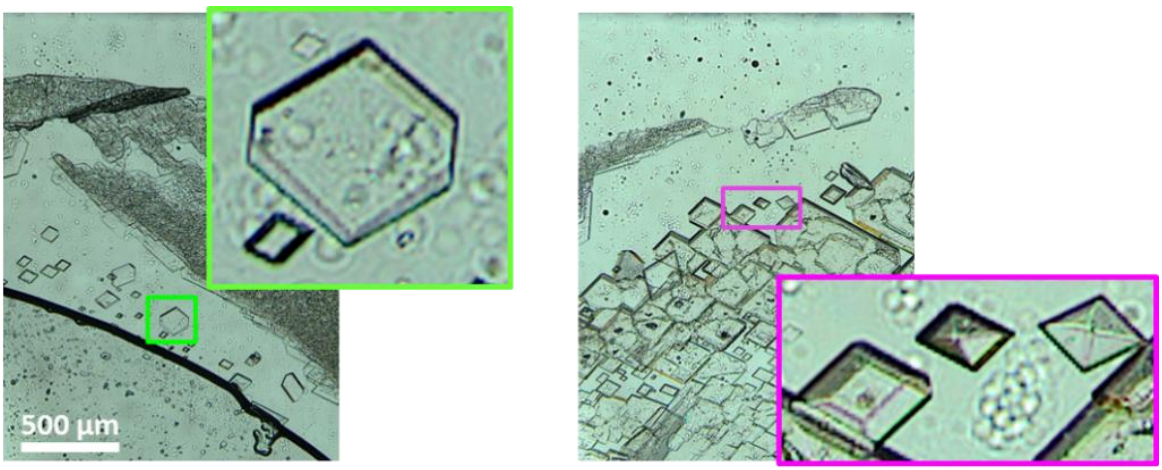


Figure 2.16 – Example of the solid-liquid interface during melting before the solid seed preparation (salol, G = 2.4 K/mm).

In the second technique, the sample is rapidly solidified several times until needles or faceted dendrites had grown parallel to the heat flux. Once such a crystal is found, it is grown under controlled rate until being the only grain present across the width of the sample (Figure 2.17). Several millimeters of this crystal should be kept unmelted afterwards in order to keep the orientation before performing a solidification experiment.

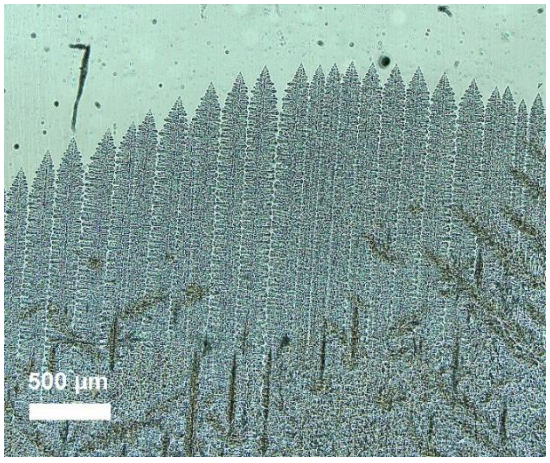


Figure 2.17 – Example of the solid-liquid interface during rapid solidification for the solid seed preparation (succinonitrile-9.6wt% borneol).

In both techniques, the sample is held stationary in a positive thermal gradient, at least 12 hours, in order to obtain a quasi-flat solid-liquid interface at rest and to reduce the grain number by coarsening. Figure 2.18 illustrates the macroscopic shape obtained after an overnight stabilization for a salol sample, where we observe a quasi-flat solid-liquid interface. The black zone on the top of the image is in fact the shadow of the hot zone since for these thermal conditions the melting isotherm is very close to the entrance of the hot zone.

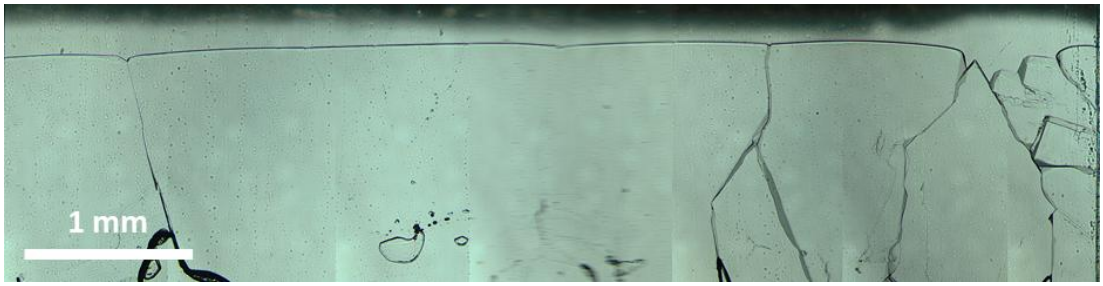


Figure 2.18 – Macroscopic shape of the solid-liquid interface at rest (salol, G = 2.4 K/mm).

2.6 Experiments

Our experiments are dedicated to conducting directional solidification of materials presenting a faceted solid-liquid interface during growth. The liquid material is solidified by moving the sample into the cold zone, controlling process parameters namely, the thermal gradient G and the pulling velocity V_p. Usually, the thermal gradient is fixed, and cycles of melting-stabilization-solidification sequences are performed, varying only the pulling rates.

After preparing the initial solid seed as previously described, we can proceed with the directional solidification, at a given pulling rate, for at least 6 cm. For each experiment, the temperature and the motor stage position are recorded throughout the solidification process. The image acquisition is run during the whole solidification, and the image acquisition frequencies are chosen as a function of the pulling velocity (0.5 Hz for $V_p \geq 5$ µm/s, and 0.25 Hz for $V_p < 5$ µm/s). In this way, a typical experiment produces around 6000 RGB images (1920 x 2560 pixels or 960 x 1280 pixels). The amount of raw data affords an extremely rich analysis of the phenomena at the interface, and characteristics like the interface undercooling, facet interplanar angle, facet angle, size and velocity.

Two microscope objectives are used, magnification 1.25x and 5x (PLAPON1.25X and LMPLFLN5X, Evident Olympus). Because of its external diameter (27.1 mm) and working distance (5 mm), the 1.25x objective can only be used when the gap separating the hot and cold zones is higher than 30 mm. This means that only experiments with low thermal gradients are achievable with this objective. Additionally, it is not possible to follow the whole solidification experiment only using this objective. To overcome this difficulty, the solidification experiments where one wants to follow the interface using the 1.25x objective are initiated with the 5x objective (FoV of 1.7 x 2.3 mm²). The interface position is followed in real time, and once it reaches a quasi-stationary position, we change to the 1.25x one (FoV of 6.8 x 9.1 mm²).

The different solidification experiments performed which will be analyzed in the following chapters, are summarized in Table 2.1, where the acronyms used throughout this thesis are listed.

Table 2.1 – Experimental matrix summarizing the experiments conducted in this work, where G is the thermal gradient, V_p the pulling velocity and δ the sample thickness.

	Material	Salol			
	δ (µm)	50			
	***G* (K/mm)**	2.4	2.1	1.2	1.1
***V_p* (µm/s)**	2.5			SAL_G3_3	
	5		SAL_E3_1	SAL_G1_4	
	10	SAL_E4_2			SAL_G1_5
	20				SAL_G8_6

2.7 Vesta software

VESTA (Visualization for Electronic and STructural Analysis) is a comprehensive software tool designed for three-dimensional visualization of crystal structures and volumetric data, including electron densities, nuclear densities from neutron diffraction, wavefunctions, and electrostatic potentials derived from electronic structure calculations [46]. Its functionality significantly aids in the analysis and understanding of structural and physical properties in three dimensions. It was used in this work because it allows the construction of crystal structures, provided that one has the information regarding the space group and the fractional coordinates of the crystal. On the basis of the crystallographic information (lattice parameters, atomic structure and atomic bonds) given by Bilgram et al. [4], it was possible to create the salol crystal structure. Then, based on its typical morphology [47, 48], the main crystal faces were specified considering their Miller indices, i.e., {100}, {010}, {111}, {210} and {211}. The remaining faces were automatically generated by the corresponding symmetry. In order to create a macroscopic crystal and not only a unit cell in size, it is possible to specify in VESTA how far the corresponding lattice plane should be from the origin. Once the crystal is built in VESTA, it can be rotated in any direction. This tool was used to interpret the experimental observations by rotating the crystal shape obtained using VESTA until a correspondence with the experimental one is obtained. This approach allows to determine the orientation of the symmetry axes (a, b and c) with respect to the crucible wall for the different crystals. In order

to index the facets observed experimentally, the theoretical angles between faces are compared to the experimentally measured angles. Volumetric data such as electron and nuclear densities are also available through VESTA and can be displayed as isosurfaces, two-dimensional sections with contours or bird's eye views. This tool was especially useful to determine the densest planes in salol.

2.8 Bibliography

[1] K. A. Jackson, and J. D. Hunt, « Transparent compounds that freeze like metals », Acta Metallurgica, vol. 13, p.1212 -1215, 1965.

[2] G. Kuriakose, and N. Nagaraju, « Selective synthesis of phenyl salicylate (salol) by esterification reaction over solid acid catalysts », J. Mol. Catal. Chem., vol. 223, p. 155-159, 2004.

[3] NIST Chemistry WebBook, [Online]. Available: https://webbook.nist.gov/chemistry/,

[4] J. H. Bilgram, U. Dürig, M. Wächter, and P. Seiler, « Zone refining and structure determination of salol crystals », J. Cryst. Growth, vol. 57, p. 1-5, 1982.

[5] H. G. Riveros, « Growth of salol crystals », J. Cryst. Growth, vol. 2, p. 173-177, 1968.

[6] K.A. Jackson, « Liquid metals and solidification », American Society for Metals , Cleveland, 1958.

[7] H. Fontaine, and M. Bée, « Sur la structure du succinonitrile dans sa phase plastique », Bull. Minéralogie, vol. 95, p. 441-450, 1972.

[8] D. J. Fisher, W. Kurz, « The growth mechanism of faceted/non-faceted eutectics ». Proc. Int. Conf. on the Solidification and Casting of Metals, 1977.

[9] G. Chandra, and S. S. N. Murthy, « Dielectric and thermodynamic study of camphor and borneol enantiomers and their binary systems », Thermochim. Acta, vol. 666, p. 241-252, 2018.

[10] J. Singh, P. Gupta, S. S. Das, and N. B. Singh, « Phase Diagram Study of Succinonitrile-Vanillin Organic Alloy System », Mol. Cryst. Liq. Cryst., vol. 605, p. 240-258, 2014.

[11] P. Kavuru, S. J. Grebinoski, M. A. Patel, L. Wojtas, and K. Chadwick, « Polymorphism of vanillin revisited: the discovery and selective crystallization of a rare crystal structure », CrystEngComm, vol. 18, p. 1118-1122, 2016.

[12] S. Sundareswaran, and S. Karuppannan, « Nucleation control and separation of vanillin polymorphs I and II through the swift cooling crystallization process », CrystEngComm, vol. 23, p. 1634-1642, 2021.

[13] M. Svärd, S. Gracin, and Å. C. Rasmuson, « Oiling out or molten hydrate—liquid–liquid phase separation in the system vanillin–water », J. Pharm. Sci., vol. 96, p. 2390-2398, 2007.

[14] S. B. Lippincott, and M. M. Lyman, « Vapor Pressure–Temperature Nomographs », Ind. Eng. Chem., vol. 38, p. 320-323, 1946.

[15] Y. H. Wang, H. Y. Tian, A. M. Wang, H. X. Wang, and C. L. Zou, « A Green and Solvent-Free Process for Preparation of High- Purity (–)-Borneol from Leaves of Blumea balsamifera (L) DC », Trop. J. Pharm. Res., vol. 13, p. 41, 2014.

[16] N. Lertsuphotvanit, S. Senarat, S. Tuntarawongsa, and T. Phaechamud, « Sublimation/evaporation behaviors of borneol in-situ forming matrix », Mater. Today Proc., 2023.

[17] I. Fichan, C. Larroche, and J. B. Gros, « Water Solubility, Vapor Pressure, and Activity Coefficients of Terpenes and Terpenoids », J. Chem. Eng. Data, vol. 44, p. 56-62, 1999.

[18] F. Shakeel, N. Haq, and N. A. Siddiqui, « Solubility and thermodynamic function of vanillin in ten different environmentally benign solvents », Food Chem., vol. 180, p. 244-248, 2015.

[19] H. F. Mao, H. Chen, M. M. Jin, C. Y. Wang, Z. B. Xiao, and Y. W. Niu, « Measurement and correlation of solubility of o-vanillin in different pure and binary solvents at temperatures from 273.15 K to 303.15 K », J. Chem. Thermodyn., vol. 150, p. 106199, 2020.

[20] H. M. Zhang, K. L. Zhang, M. Yu, J. Guo, S. J. Xu, and Y. F. Wang, « Insight into solid-liquid and liquid-liquid phase equilibrium behavior of vanillin and ethyl vanillin », J. Mol. Liq., vol. 365, p. 120059, 2022.

[21] K. Hussain, G. Thorsen, and D. Malthe-Sørenssen, « Nucleation and metastability in crystallization of vanillin and ethyl vanillin », Chem. Eng. Sci., vol. 56, p. 2295-2304, Apr. 2001.

[22] The Merck Index. 9th ed. Rahway, New Jersey: Merck & Co., Inc., 1976.

[23] S. A. Jethwa, J. B. Stanford, and J. K. Sugden, « Light Stability of Vanillin Solutions in Ethanol », Drug Dev. Ind. Pharm., vol. 5, p. 79-85, 1979.

[24] N. C. Jana, S. Sethi, R. Saha, and B. Bagh, « Aerobic oxidation of vanillyl alcohol to vanillin catalyzed by air-stable and recyclable copper complex and TEMPO under base-free conditions », Green Chem., vol. 24, p. 2542-2556, 2022.

[25] F. L. Mota, L. M. Fabietti, N. Bergeon, and R. Trivedi, « The effect of confinement on thermal convection and longitudinal macrosegregation in directionally solidified dilute succinonitrile–camphor alloy », Comptes Rendus Mécanique, vol. 351, p. 249-262, 2023.

[26] R. Trivedi, and K. Somboonsuk, « Pattern formation during the directional solidification of binary systems », Acta Metall., vol. 33, p. 1061-1068, 1985.

[27] « Epoxy - Chemical Resistance », Disponible sur: https://www.engineeringtoolbox.com/chemical-resistance-epoxy-d_786.html

[28] M. Cukierman, J. W. Lane, and D. R. Uhlmann, « High-temperature flow behavior of glass-forming liquids: A free-volume interpretation », J. Chem. Phys., vol. 59, p. 3639-3644, 1973.

[29] R. B. Badachhape, M. K. Gharpurey, and A. B. Biswas, « Density and Surface Tension of Phenol, (Mono-, Di-, and Tri-)-chlorophenols, Salol, and (o- and m-) Chloronitrobenzenes. », J. Chem. Eng. Data, vol. 10, p. 143-145, 1965.

[30] F. L. Mota, M. Medjkoune, L. S. Littles, A. Karma, and N. Bergeon, « Solidification furnace for in situ observation of bulk transparent systems and image analysis methods », Rev. Sci. Instrum., vol. 94, p. 065111, 2023.

[31] R. P. Mooney, L. Sturz, G. Zimmermann, and S. McFadden, « Thermal characterisation with modelling for a microgravity experiment into polycrystalline equiaxed dendritic solidification with in-situ observation », Int. J. Therm. Sci., vol. 125, p. 283-292, 2018.

[32] S. Akamatsu, S. Bottin-Rousseau, V. T. Witusiewicz, U. Hecht, M. Plapp, A. Ludwig, J. Mogeritsch, M. Şerefoğlu, N. Bergeon, F. L. Mota, and L. Sturz, « Microgravity studies of solidification patterns in model transparent alloys onboard the International Space Station », Npj Microgravity, vol. 9, p. 83, 2023.

[33] J. D. Hunt, K. A. Jackson, and H. Brown, « Temperature Gradient Microscope Stage Suitable for Freezing Materials with Melting Points between -100 and +200°C », Rev. Sci. Instrum., vol. 37, p. 805-805, 1966.

[34] C. Selvam, D. M. Lal, and S. Harish, « Thermal conductivity enhancement of ethylene glycol and water with graphene nanoplatelets », Thermochim. Acta, vol. 642, p. 32-38, 2016.

[35] B. W. Mangum, « The succinonitrile triple-point standard: a fixed point to improve the accuracy of temperature measurements in the clinical laboratory. », Clin. Chem., vol. 29, no 7, p. 1380-1384, Jul. 1983, doi: 10.1093/clinchem/29.7.1380.

[36] Ü. Bayram, K. Keşlioğlu, S. Aksöz, and N. Maraşlı, « Thermal Conductivity of Solid Phases for Naphtol, Camphene, Salol, and Bezil », J. Thermophys. Heat Transf., vol. 30, p. 730-736, 2016.

[37] W. Losert, B. Q. Shi, and H. Z. Cummins, « Evolution of Dendritic Patterns during Alloy Solidification: Onset of the Initial Instability », Proc. Natl. Acad. Sci. U. S. A., vol. 95, p. 431-438, 1998.

[38] J. A. Warren, and J. S. Langer, « Prediction of dendritic spacings in a directional-solidification experiment », Phys. Rev. E, vol. 47, p. 2702-2712, 1993.

[39] F. L. Mota, N. Bergeon, D. Tourret, A. Karma, R. Trivedi, and B. Billia, « Initial transient behavior in directional solidification of a bulk transparent model alloy in a cylinder », Acta Mater., vol. 85, p. 362-377, 2015.

[40] Y. Song, D. Tourret, F. L. Mota, J. Pereda, B. Billia, N. Bergeon, R. Trivedi, and A. Karma, « Thermal-field effects on interface dynamics and microstructure selection during alloy directional solidification », Acta Mater., vol. 150, p. 139-152, 2018.

[41] S. Akamatsu, and G. Faivre, « Residual-Impurity Effects in Directional Solidification: Long-Lasting Recoil of the Front and Nucleation-Growth of Gas Bubbles », J. Phys. I, vol. 6, p. 503, 1996.

[42] T. Duffar, « Comprehensive review on grain and twin structures in bulk photovoltaic silicon », Recent Res. Dev. Cryst. Growth, vol. 5, p. 61–111, 2009

[43] H. A. Atwater, C. V. Thompson, and H. I. Smith, « Mechanisms for crystallographic orientation in the crystallization of thin silicon films from the melt », J. Mater. Res., vol. 3, p. 1232-1237, 1988.

[44] K. Fujiwara, Y. Obinata, T. Ujihara, N. Usami, G. Sazaki, and K. Nakajima, « In-situ observations of melt growth behavior of polycrystalline silicon », J. Cryst. Growth, vol. 262, p. 124-129, 2004.

[45] K. Fujiwara, Y. Obinata, T. Ujihara, N. Usami, G. Sazaki, et K. Nakajima, « Grain growth behaviors of polycrystalline silicon during melt growth processes », J. Cryst. Growth, vol. 266, p. 441-448, 2004.

[46] K. Momma, and F. Izumi, « For three-dimensional visualization of crystal, volumetric and morphology data », Journal of Applied Crystallography, vol. 44, p. 1272-1276, 2011.

[47] G. Neuroth, H. Klapper, Dislocation Reactions in Czochralski-Grown Salol Crystals, ZKri, vol. 209, p. 216-220, 1994.

[48] G.N. Wyrouboff, Sur la forme cristalline du salol, Bulletin de Minéralogie, p. 443-445, 1889.

CHAPTER 3: PHENOMENOLOGICAL ANALYSIS OF FACET AND DEFECT BEHAVIOR DURING DIRECTIONAL SOLIDIFICATION OF SALOL

This chapter includes a detailed description of the directional solidification experiments of salol. Additionally, we give a benchmark study of the defects observed during the experiments performed, such as bubbles, facet splitting, growth striations, twin crystals and other features that affect the growth and the facet dynamics.

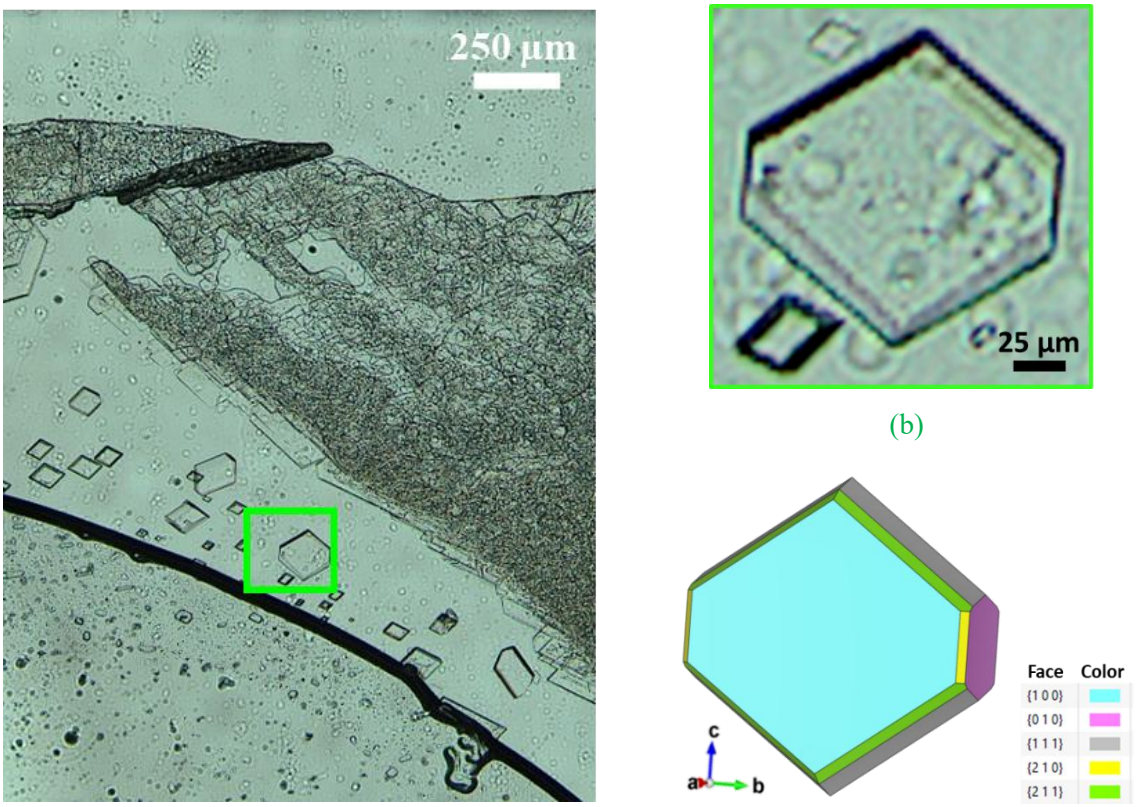
3.1. Pattern formation

The growth of salol using the directional solidification is conducted by adjusting the experimental parameters pulling velocity V_p and thermal gradient G. During experiments, these parameters are systematically varied to observe their effects on the morphological evolution of salol. Data are collected to monitor the growth dynamics and analyze the resulting morphology. In this section, I describe the detailed experimental protocol for a given experiment (*SAL_E4_2*) but, as mentioned in Chapter 2, it is similar for the other experiments. This thorough description provides a clear understanding of how the experiments are conducted and the results are obtained.

As mentioned in Section 2.5, it is preferable to start a solidification experiment with an interface or seed, as much as possible, flat and free from defects at rest. Therefore, before the solidification experiment, the thermal gradient that will be used in the experiment is imposed in the furnace and the sample is melted at V_p = 40 µm/s until a small and thin quantity of solid is obtained consisting of numerous small crystals (Figure 3. 1a). The seed surrounded in green is zoomed in b: its shape looks very similar to the typical morphology of salol crystals grown from solution or from supercooled melt (Figure 3. 1c) [1-4]. The external shape of the solid corresponds to that of the orthorhombic crystals displaying a large dominating pinacoid, smaller facets of orthorhombic pyramids, and small faces of pinacoid as shown in the shape obtained using the VESTA software (Figure 3. 1c).

Then, around 25 mm of the sample are solidified at 20 µm/s, and the sample is kept steady in a positive thermal gradient overnight (for approximately 15 hours), still the same thermal gradient

that will be used in the solidification experiment. This step is essential to ensure uniform temperature distribution and to mitigate thermal stresses; stabilize the growth front; minimize defects within the crystal and promote, as much as possible, monocrystalline growth [5, 6]. Since the whole solid-liquid interface cannot be observed at once, several images are captured along the sample width, and then they are combined to obtain a complete view of the solid-liquid interface at rest (Figure 3. 2). As can be seen, despite the long thermalization time some defects remain (such as grain boundaries), but the macroscopic shape of the interface is quasi-flat and we can proceed with the solidification.



(a) (b) (c)

Figure 3. 1 – (a) Solid-liquid interface of salol during melting (SAL_E4_2, Vp = 40 µm/s, G = 2.4 K/mm). (b) Zoom on a small seed presenting a shape characteristic of orthorhombic crystals. (c) Schema of the typical morphology of a salol crystal obtained using VESTA software [7, 8].

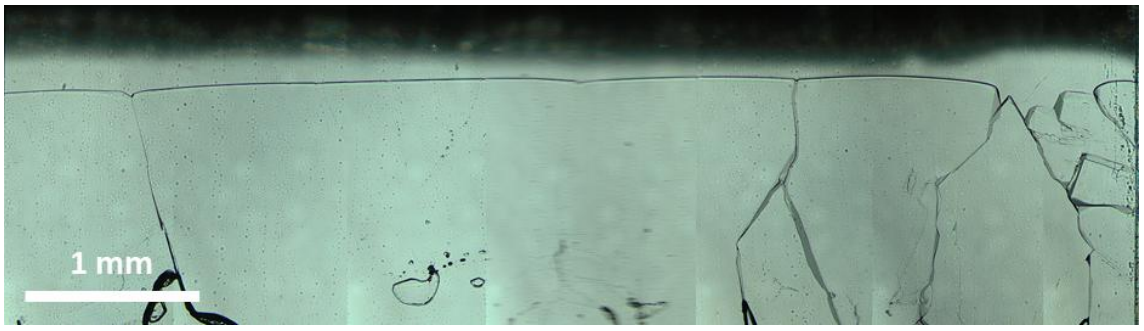


Figure 3. 2 – Macroscopic shape of the salol solid-liquid interface at rest after a stabilization of 15 hours (SAL_E4_2, G = 2.4 K/mm).

From this initial stage, the directional solidification is carried out, at a pulling velocity (V_p) of 10 µm/s and a thermal gradient (G) of 2.4 K/mm (*SAL_E4_2*). Figure 3. 3 shows the evolution of the interface over time. The process of crystal growth begins with an initial almost smooth interface between the liquid and solid phases. At $t = 0$ min, the black zone at the top is a shadow of the hot zone of the furnace since, within the applied thermal gradient, the solid-liquid interface is very close to it. As the sample is pulled, solid-liquid interface evolves towards a highly faceted solid-liquid interface until the end of the solidification experiment (after almost 3h). The observed facets correspond to specific crystallographic planes within the orthorhombic structure of salol [1-4]. Despite de low sample thickness (d = 50 µm), the interface may appear either as three-dimensional (3D) or more two-dimensional (2D). In the first case, the inclination of facets within the sample thickness is clearly visible (e.g., the facet indicated by the green arrow), while in the second case, the facets are roughly normal to the crucible (e.g., the facet indicated by the yellow arrow). These observations are linked to the orientation of the crystal symmetry axes (*a, b, c*) relative to the wall of the crucible: when the *a*-axis is perpendicular to the crucible wall, the thickness of the facet becomes indistinguishable.

Throughout the experiment, a very rich and complex growth dynamics of the interface is observed. *In situ* observations reveal, for example, numerous bubbles (indicated by the white arrows). The colored markers in Figure 3. 3 are added in order to track a facet between two images. They testify to the strong growth dynamics and its unsteady character: we notice a lot of competition between different grains, leading to the elimination/overgrowth of certain facets.

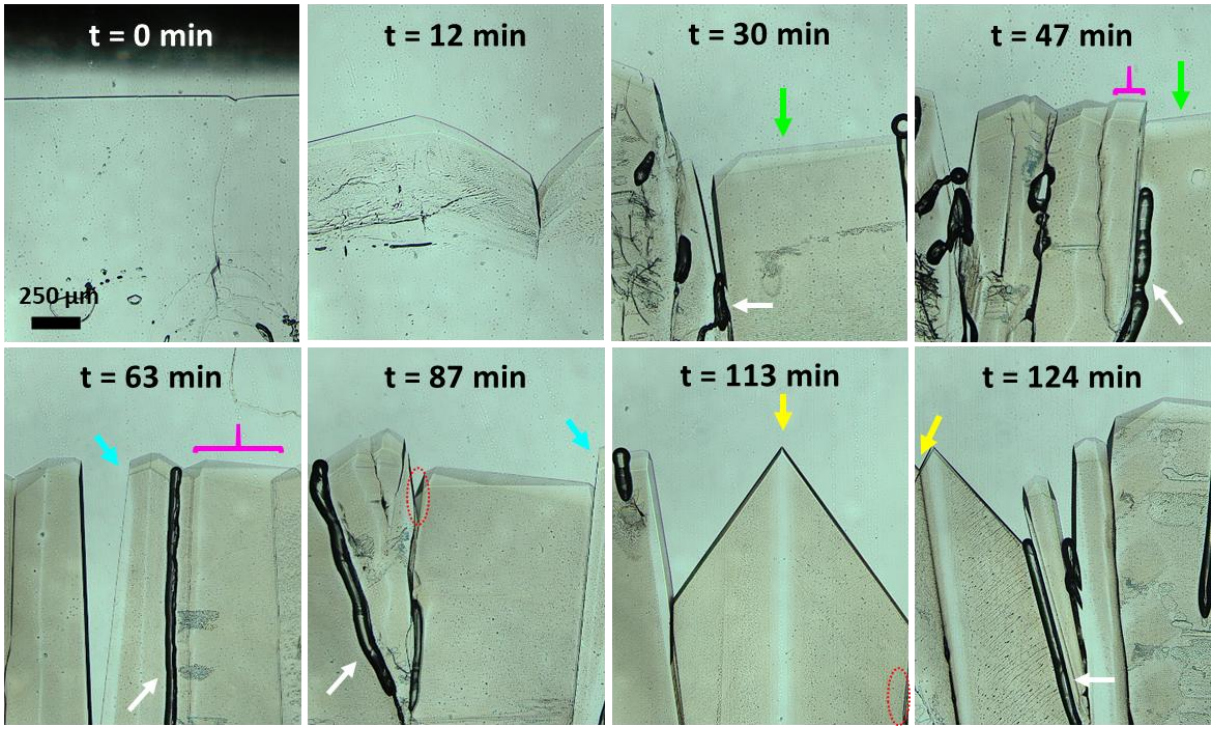


Figure 3. 3 – Time evolution of the faceted solid-liquid interface during a typical experiment of directional solidification of salol (SAL_E4_2, Vp = 10µm/s, G = 2.4 K/mm).

The images of Figure 3. 3 show the instantaneous structure of the interface. However, by superimposing images taken at different times, it is possible to reconstruct the final grain structure of the sample after solidification (Figure 3. 4). The colors are related to the colored markers in Figure 3. 3. We can see for example that: bubbles appear not only in the grain boundaries but are also trapped between the solid and the crucible wall inside the grains (e.g. white arrows in the green filled grain). Facet nucleation takes place when two neighbor grains are going in opposite directions creating an empty space between them (e.g., black dashed lines and arrows). Some grain boundaries have zigzagged shapes (e.g., zone circled in red). The faceted cell seen at 113 min in Figure 3. 3 (yellow arrow), whose left and right facets corresponds to (111) and $(11\bar{1})$ planes respectively, shows up at 95 min and grow until 127 min (yellow filled grain in Figure 3. 4).

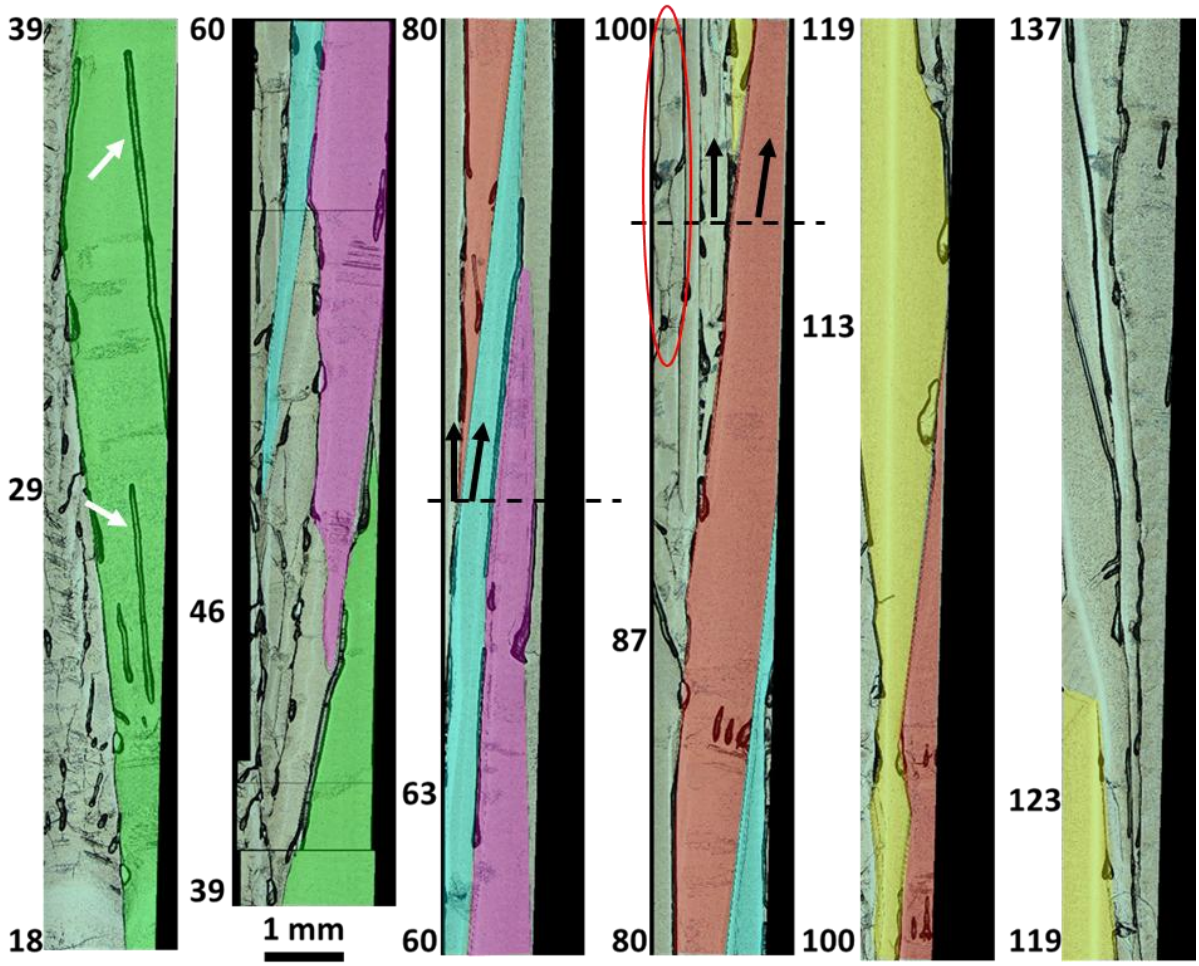
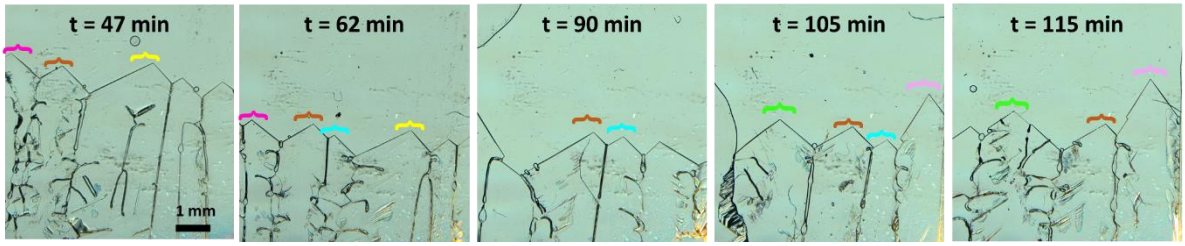
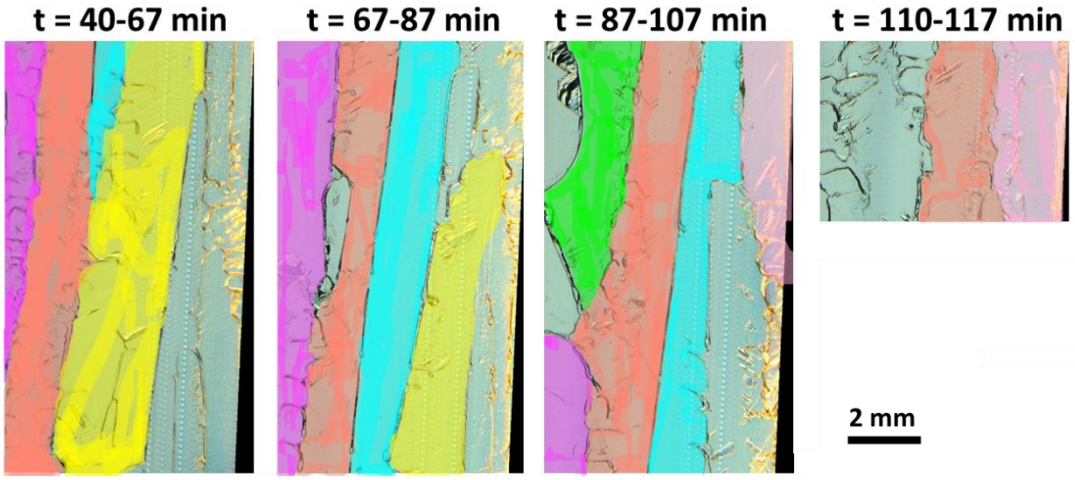


Figure 3. 4 – Reconstruction of the solidified sample where the numbers represent the solidification time (in min) and colored grains are linked to Figure 3. 3. (SAL_E4_2, V_p = 10µm/s, G = 2.4 K/mm)

Experiment *SAL_G1_5*, performed with the same pulling rate (10 µm/s) and lower thermal gradient (1.1 K/mm), shows a slightly different behavior (Figure 3. 5). It is worth mentioning that the two experiments do not start with the same solid seed so that the crystallographic orientation of the solid seed is maybe different, influencing the interface morphology and behavior. It is notably seen that the majority of the facets persist in the field of view for the whole solidification length, despite the presence of bubbles that developed and the splitting that occurred resulting in the formation of new facets. In *SAL_G1_5*, performed at the lower gradient, all the grains seem to have similar orientation, and the faceted tips are growing in a direction almost aligned with the thermal gradient. On the contrary to *SAL_E4_2*, facets oriented perpendicularly to the thermal gradient are not observed in this experiment.



(a)



(b)

Figure 3. 5 – (a) Images of the solid-liquid interface of salol as function of time where some colored markers are added. (b) Reconstruction of the solidified sample with corresponding colors. (SAL_G1_5, V_p = 10 µm/s, G = 1.1 K/mm)

3.2. Comparison of the solid-liquid interface morphologies in different experiments

In all experiments, the interface exhibits a rich and complex nature, with bubbles always seen and being trapped in the solid and at the grooves of the facets with similar defects. However, the interface morphology varies with velocity (V_p), gradient (G) and solid seed orientation. Figure 3. 6 shows a comparison between interface morphologies at different experimental conditions (V_p and G), at different solidified lengths ($L = t.V_p$).

At the lower G, the effect of pulling velocity on the interface morphology can be seen. At 2.5 µm/s, the facets are growing in multiple directions leading to the formation of new facets exhibiting well-defined shape but also displaying irregularities at the level of the facets. These features are repeated all through the experiment. When the velocity is increased to 5 µm/s, the creation of new facets is still observed, but the facets appear to develop to well-defined shaped

and of longer length compared to those formed at 2.5 µm/s. At 10 µm/s, the facets are well-defined and sharper facetted cells are observed together with a notable reduction in the irregularities at the level of the facets. A striking observation is that the same facets are growing throughout the whole experiment, highlighting their stability.

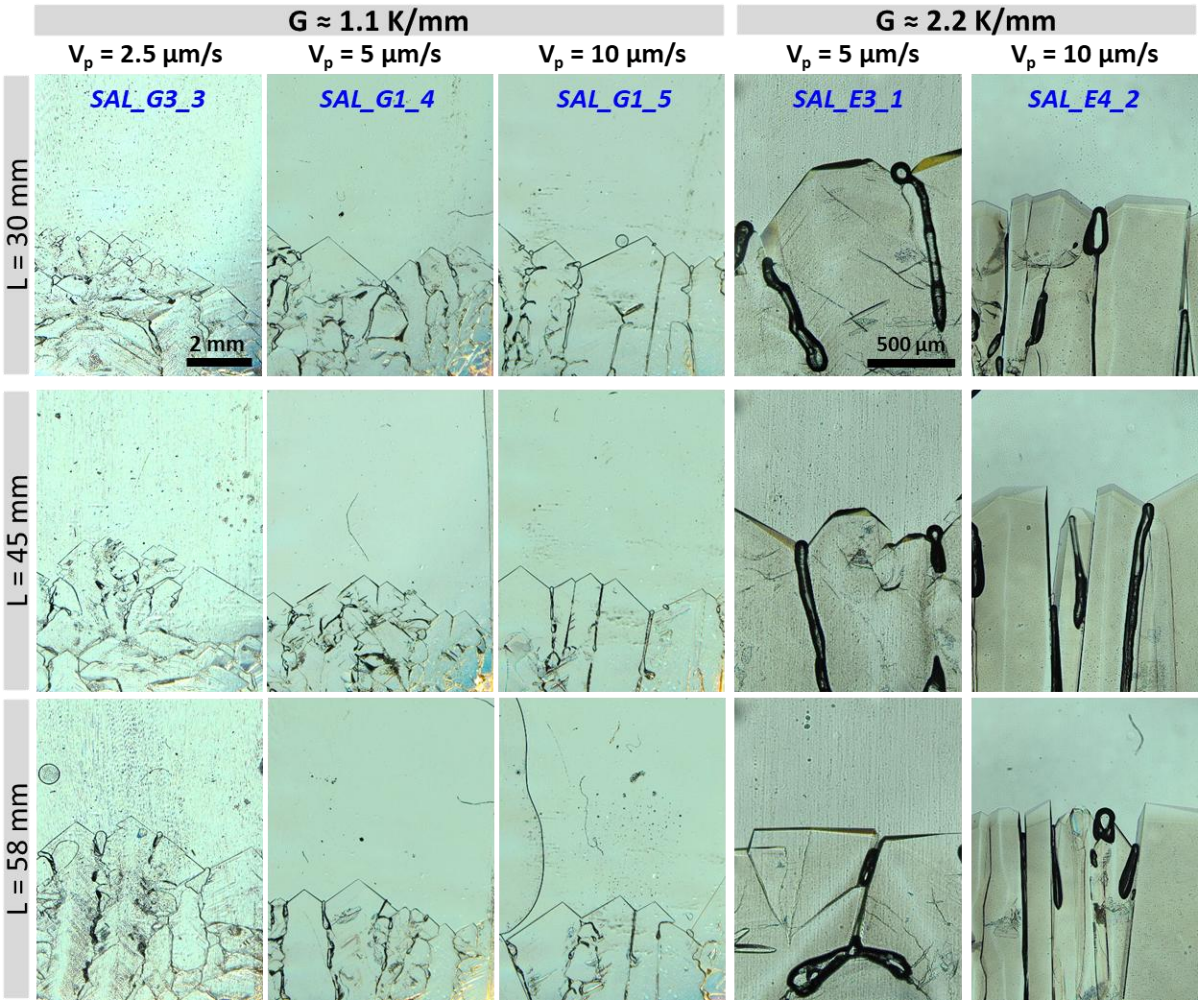


Figure 3. 6 – Salol solid-liquid interface morphology during solidification for different experimental conditions (pulling rate V_p, thermal gradient G, and solidified lengths L). The experiment name is given in blue in the first row.

At higher thermal gradient, the facets in both experiments also exhibit a well-defined shape across all the length. Here, we are using a microscope objective of higher magnification giving a more focused view of the facets what allowed the observation of defects of smaller scales. As for the lower gradient, the effect of the pulling velocity can be seen in the interface morphology with well-defined facets at the highest velocity.

3.3 Investigation of defects observed during growth

Crystals are never perfect, and the organic crystals contain the same types of defects as inorganic materials [9] allowing to study them by *in situ* investigations. The type of defects appearing in crystals during solidification depends on factors such as inheritance of defects from the seed crystal, growth variables including thermal conditions, purity of the material, or stresses. The formation and distribution of defects impact the quality and properties of the final crystal structure [10].

Stresses can be caused by temperature gradients, chemical composition variations, and crystal distortions due to structural defects [9-14]. Whatever the value of the thermal gradient, variations and inhomogeneities in the thermal field during the solidification arise at several scales, causing the expansion or the contraction of the crystal. The intensity of the stress can cause the development of defects if it exceeds the materials yield stress [14,15], and direct contact between the crystal and the crucible material can be an additional cause of stresses [11]. The thermal expansion coefficient of salol (8.0×10^{-4} K^{-1}) [16] is around three orders of magnitude higher than that of the glass ($<5.0 \times 10^{-7}$ K^{-1}) [17], and this difference can be at the origin of additional stresses in the growing crystal. Moreover, since there is a relatively large contraction during the solidification of salol, where its volumic thermal expansion coefficient is equal to 2.1×10^{-4} $°C^{-1}$ for the solid phase and 7.95×10^{-4} $°C^{-1}$ for liquid phase [16], this may result in additional defects at the solid-liquid interface [16, 18, 19].

The aim of this section is to describe and analyze the defects observed during the different experiments performed during my thesis. Please note that in the following, *t* stands for the solidification time and *t'* corresponds to the difference between the solidification time and the moment at which the corresponding events starts to be followed.

3.3.1 Bubbles

Bubble origin

One of the most common defects observed during growth in our experiments is bubbles that can be classified as volume defect. Bubbles may arise from solid retraction and the density disparity between the liquid and solid phases [20]. Several works [21-25] have found that the formation and growth of gas bubbles during directional solidification are mainly driven by the residual gaseous impurities in the melt. Their nucleation generally occurs in the grooves during

the solidification process, because of the highest concentrations of the dissolved gas in the liquid at the grooves, due to the segregation of the dissolved gas and the small foreign particles that are trapped in the solid phase. And when the concentrations of gas decrease the growth of the bubbles stop [26]. After nucleation, the bubbles can either grow into stationary tubular structures [9] or become entrapped by the solid [27], depending on the growth velocity and morphological conditions.

Frequently gas bubbles are formed if growth is not performed under vacuum, due to a frequently rather high gas solubility in the melt [9, 28]. In our experiments, samples are filled under nitrogen atmosphere, before being completely sealed. There are several studies on the solubility of gas nitrogen in various organic liquids [29], though we could not find specific data on its solubility in salol. However, general solubility trends of nitrogen in similar organic compounds suggest low solubility so that nitrogen bubble formation is the most likely cause of bubbles in our experiments.

Another reason of the presence of bubbles in our experiments is the existence of defects, such as splitting facets, stress accumulation, distortions, traces of morphological defects that precede the formation of the bubbles. In Figure 3. 7, we present the evolution of a bubble that nucleated in the middle of a facet. The bubble appears after a trace emerges in the solid phase, highlighted by yellow dotted circle. Initially, the bubble nucleates with a rounded shape (≈29 µm of radius). It is then incorporated between the two neighbor faceted tips following the groove between them. This type of nucleation is common in our experiments.

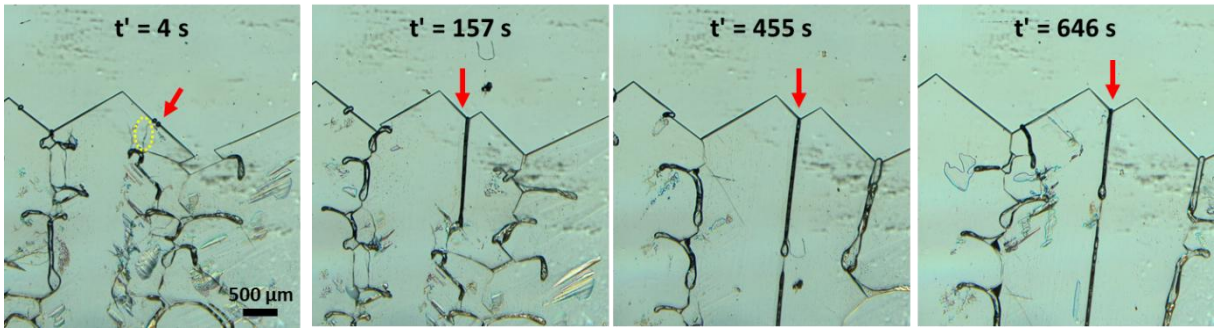


Figure 3. 7 – Temporal evolution of a bubble that nucleated in the middle of two facets becoming elongated. (SAL_G1_5, V_p = 10 µm/s, G = 1.1 K/mm)

Apart from the bubbles that nucleate at the solid-liquid interface, two cases of bubbles generated in the liquid phase and interacting with the solid-liquid interface are shown in Figure 3. 8. The

first bubble can be seen in the field of view after 47 min of solidification, and it has a rounded shape (radius of 162 µm). The bubble retains its rounded shape until contact with one of the interface facets leading to its deformation and got incorporated in the solid phase resulting in facet splitting, probably due to the strains caused by the bubble at this position relieved by a split. A second bubble appears in the field of view, after 60 min of solidification, with a perfect rounded shape (≈105 µm of radius). It is rapidly incorporated into the solid, momentarily disturbing the facet upon incorporation, then the facet continues its growth without any long-term impact on its morphology. In both cases, the bubble does not grow at all, it just moves with the applied pulling velocity till attaining the solid-liquid interface. This is a sign that the quantity of gas dissolved in the melt is very low. The fact that it moves with the applied velocity excludes any buoyancy effect.

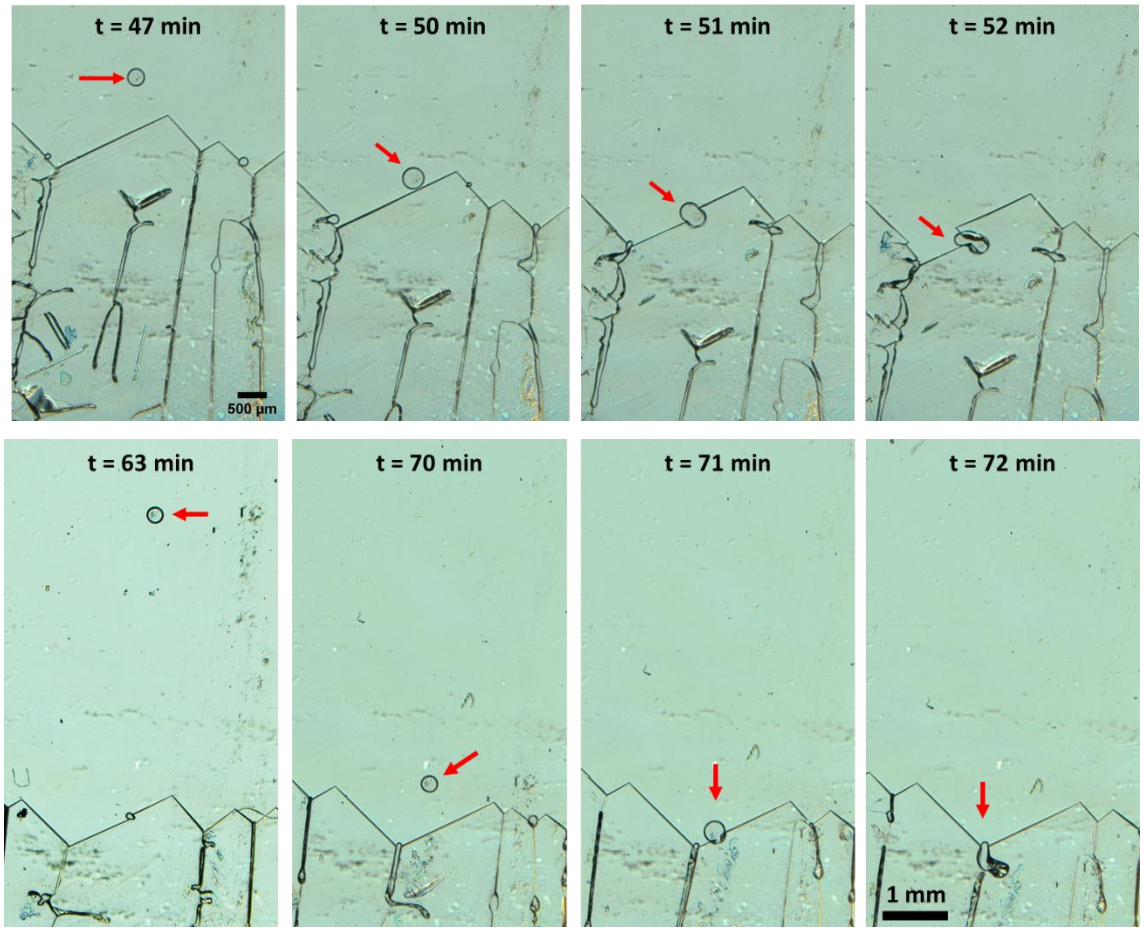


Figure 3. 8 – Evolution of two bubbles generated in the liquid. (SAL_G1_5, Vp = 10 µm/s, G = 1.1 K/mm)

Bubble shape

The bubbles shape depends on its nucleation point and surroundings during the solid-liquid interface progress. All of them nucleated in the solid-liquid interface with different configurations. We notice that bubbles nucleate mainly with a round shape. Independently of the puling velocity, the minimum radius observed is 14.8 ± 5.0 µm and the average 43.2 ± 4.4 µm, after counting around 985 events (Figure 3.9).

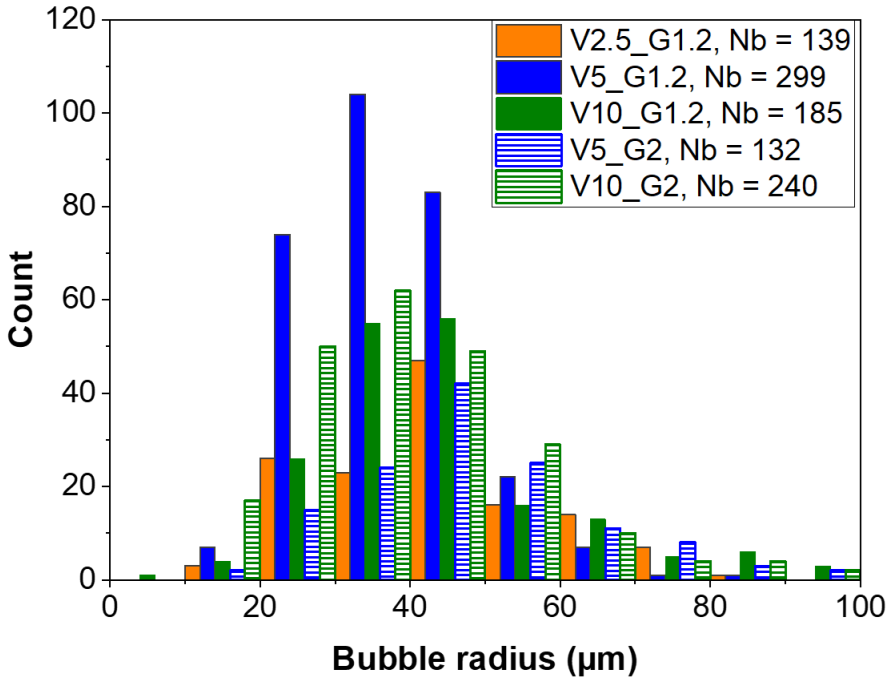


Figure 3.9 – Bubble radius distribution under varying pulling velocities V_p and thermal gradients G.

Figure 3.10 shows an example of a typical evolution of a bubble, from its nucleation with rounded shape till being trapped in the solid, where it is deformed according to the surrounding growing grains. This bubble nucleates in the middle of two facets growing in opposite directions.

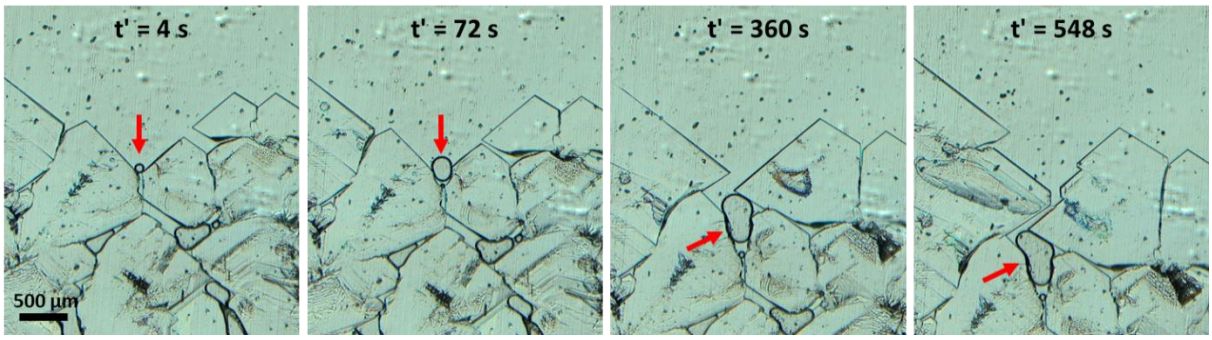


Figure 3.10 – Temporal evolution of a bubble from its nucleation and its deformation due to the solid-liquid interface. (SAL_G3_3, V_p = 2.5 µm/s, G = 1.2 K/mm)

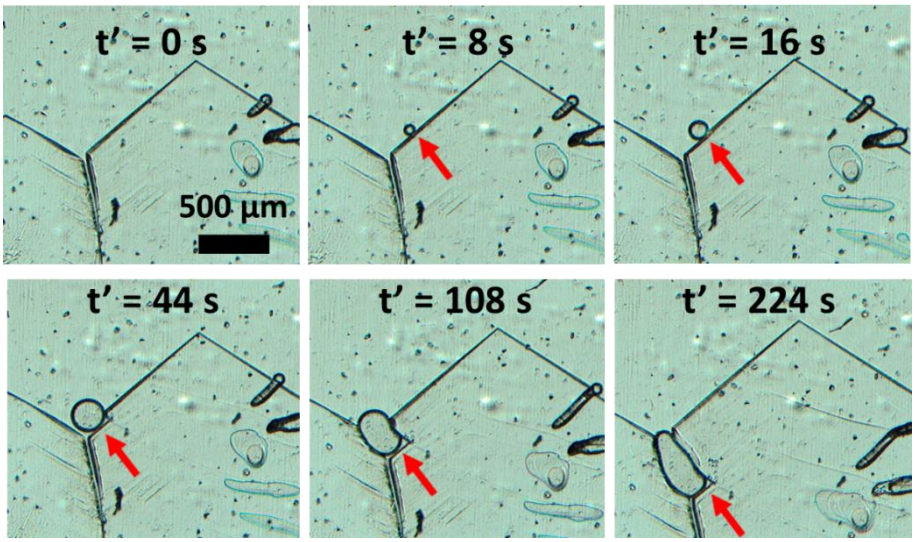


Figure 3.11– Evolution of a bubble generated at the solid-liquid interface (SAL_G3_3, V_p = 2.5 µm/s, G = 1.2 K/mm)

In Figure 3.11, the origin of the bubble is challenging, as no preceding defects are detected and it does not nucleate at the grooves. The bubble highlighted by the red arrow nucleates at the interface in a small and rounded shape (radius of 47 µm). As the interface continues to evolve, the bubble continues to grow in a rounded shape until attaining a maximum radius of 120 µm within 36 s. The bubble maintains contact with the facet where it generated first, and as the facet splits, the bubble starts to be in contact with another facet. The bubble then deforms in an elongated shape and gets stuck between the facets and trapped in the solid phase.

Another bubble shape observed is the bifurcated one, as exemplified in Figure 3.12. Both bubbles (indicated by the green and red arrows) nucleate with a rounded shape, with a radius lower than 30 µm, but they only keep it for few seconds. They are very quickly squeezed, and then they become elongated. A zoom is made at the nucleation of the first bubble (green arrow).

It looks like the sample thickness is not completely filled with solid: the neighbor facets seem to be in different layers and the bubble nucleates between them. It is probably the reason for the subsequent complicated grain boundary. The bubbles take this bifurcated shape because of part of the growing facet is blocked (indicated by the black arrow).

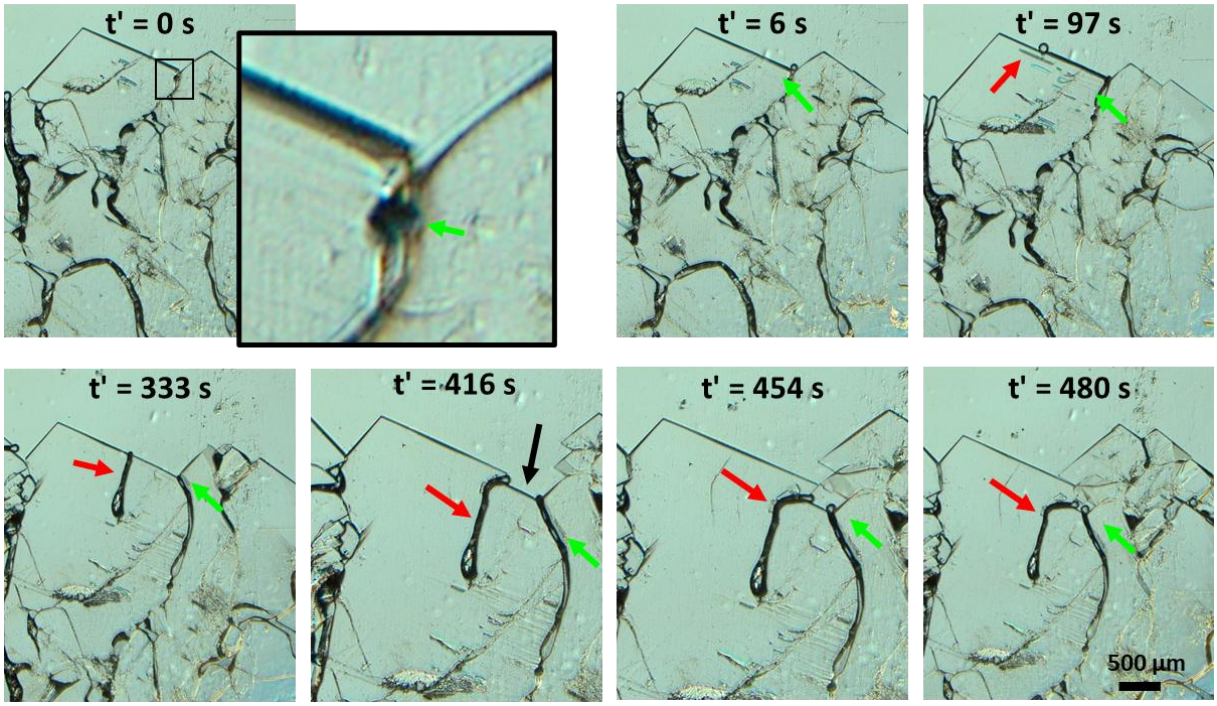
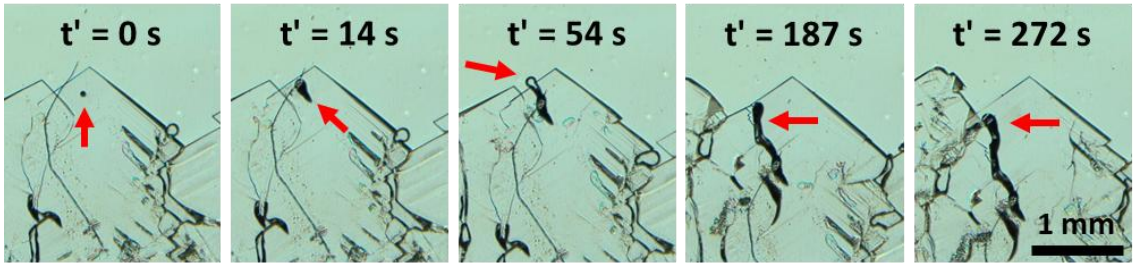
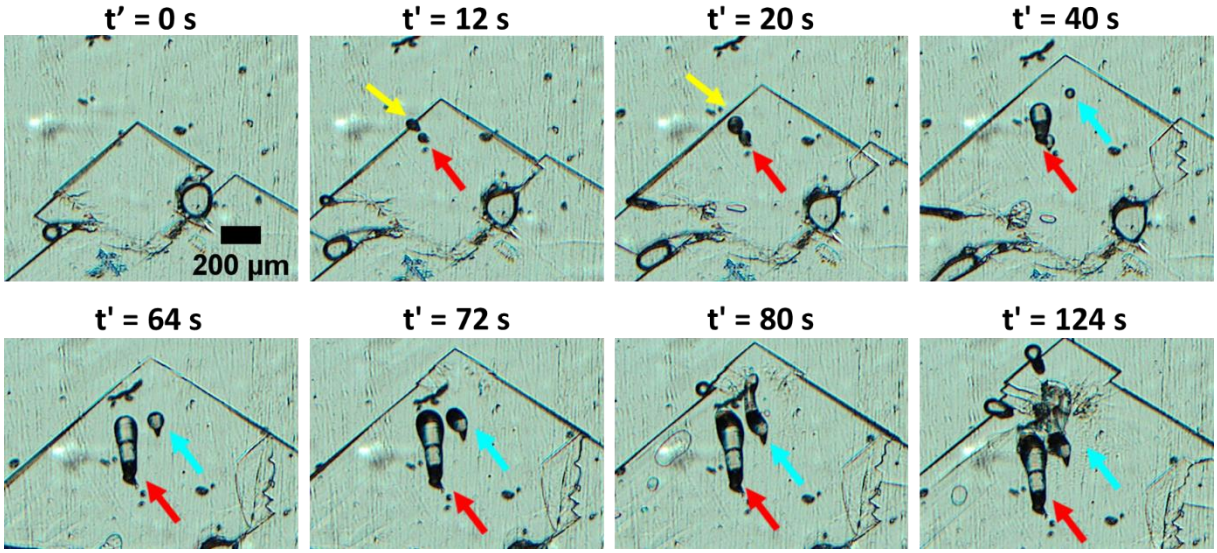


Figure 3.12 – Temporal evolution of bifurcated bubbles. (SAL_G1_4, V_p = 5 µm/s, G = 1.2 K/mm)

Figure 3.13 shows the evolution of a bubble nucleated in the gap between the solid phase and the sample wall near the tip (red arrows). In Figure 3.13a, the bubble quickly migrates upwards and is subsequently squeezed in the solid due to the pressure from the solid and the sample wall. When these two bubbles merge, they continue the growth between the gap of the solid phase and the sample wall as one elongated bubble. Another bubble generated also in the gap of the sample (cyan arrow) grew in an elongated shape (Figure 3.13b). However, at some point it disturbed the facet leaving behind defects and traces possibly when the crystal is filling the remaining liquid gap and approaches the glass plate.



(a)

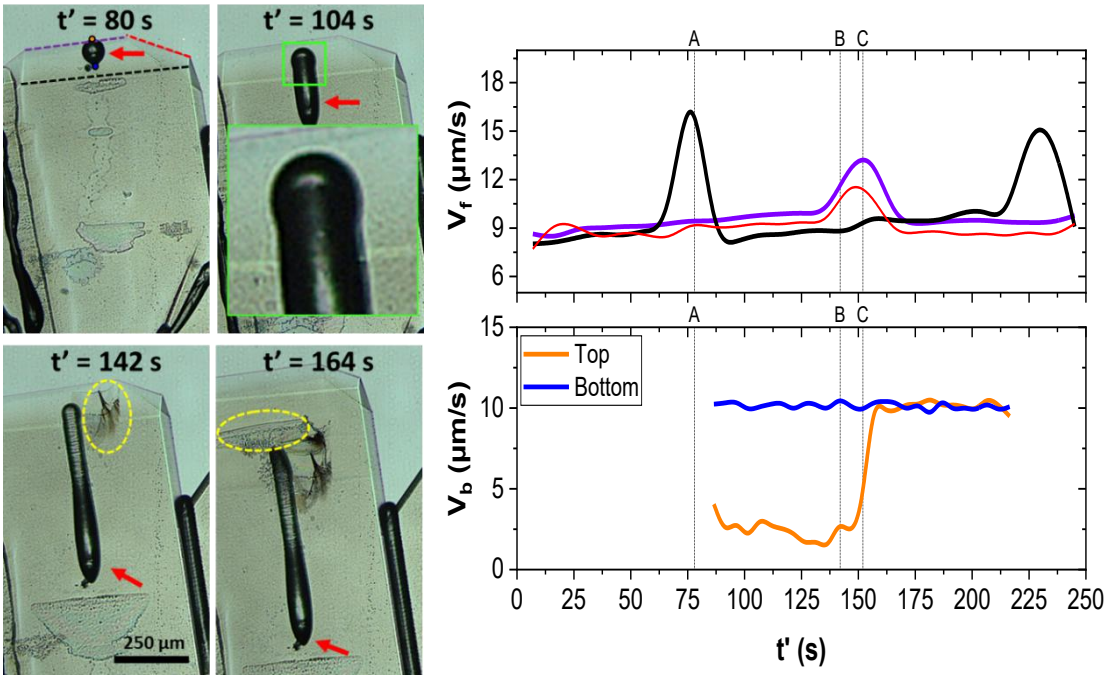


(b)

Figure 3.13 – Evolution of bubbles generated in the gap between the crystal and the glass plate at V_p: (a) 5 and (b) 2.5 µm/s (SAL_G1_4 and SAL_G3_3, G = 1.2 K/mm).

Figure 3.14 presents an interesting example of a bubble behavior (red arrow). The bubble initially nucleates in small, rounded shape (diameter of 45 µm) at the facet delimited by the purple, black and red dashed lines at 80 s. It can be clearly seen that this facet is not perpendicular to the crucible wall, giving the corresponding 3D appearance. The bubble size increases very fast and within few seconds it attains a size limited by the sample thickness (50 µm). It is then distorted to be accommodated close to the solid-liquid interface. The growth velocity of the facet is characterized by measuring the black, purple and red lines evolution as a function of time (Figure 3.14b-top). Initially all are evolving at the same velocity (8.6 ± 0.2 µm/s), the purple and black towards the left, and the red towards the right. Around 55 s, the red velocity slightly decreases, and the black one starts to increase considerably attaining a maximum around 76 s. Just after the peak, the bubble nucleates (vertically dashed line A). One hypothesis is that during the growth of this facet, it attains or is close to the sample walls,

leading to a perturbation in local composition or temperature evidenced by the change in velocity, and highlighted by the bubble nucleation.



(a) (b)

Figure 3.14– (a) Evolution of a bubble generated at the solid-liquid interface. (b) Velocity of the lines and dots highlighted at 80 s. (SAL_E4_2, V_p = 10 µm/s, G = 2.4 K/mm)

The position of the tip and the bottom of the bubble (orange and blue dot at 80 s of Figure 3.14a, respectively) are also followed in order to better understand its behavior. The respective velocities are given in Figure 3.14b-bottom. It can be seen that while the bottom of the bubble is moving with a uniform velocity equal to the pulling velocity, the top of the bubble changes during the solidification. First, the fact that the bottom is moving with the pulling velocity means that the bottom of bubble is stuck to the crucible wall. It can be seen for example in the green zoomed zone at 104 s that the edge of the facet (white) is behind, and it is not distorted by the presence of the bubble. As the sample continues to be pulled, the bubble starts to elongate vertically in the pulling direction. However, the movement of the top of the bubble is influenced both by the pulling and by the facet growth in opposite directions, this is why its velocity is much lower. Around 135 s, the velocities of the purple and red lines start to increase, and sometime later, a noticeable perturbation at the top (yellow dashed circle at 142 s, and vertical dashed line B) appears. A few seconds later another perturbation is observed (yellow dashed

circle at 164 s, and vertical dashed line C). The response to these perturbations is the bubble detachment from the solid-liquid interface. From this instant, it follows the solid, moving with the pulling velocity.

Figure 3.15 shows images from different experiments changing the experimental conditions (pulling velocity V_p and thermal gradient G) in order to compare the behavior of the bubbles. The top row shows instantaneous snapshots of the solid-liquid interface while the bottom row presents a larger scale-view of the grains growth through the solidification process. The red arrows refer to the same evolving facets between the top and the bottom images, and the white dashed line in the bottom images refer to the instant at which the top image is taken. For the higher pulling velocity, it is noticeable that facets persist almost throughout the entire reconstruction, with the bubbles essentially drawing the boundaries between different grains. As the pulling velocity decreases, the bubbles seem to migrate and travel more freely.

Facet velocity and bubble effect

The presence of bubbles can influence the facet velocity V_f, which is the growth velocity in the direction normal to the facet, by either reducing or increasing it. Some regions of the interface may grow slower due to the presence of bubbles, while others may grow faster where bubbles are absent, causing heterogeneity of the interface [30]. Their presence can change the thermal conductivity at the interface, and since gas has lower thermal conductivity compared to solids or liquids, bubbles can slow down heat dissipation [5]. Bubbles can also alter the diffusion of molecules from the liquid towards the solid-liquid interface what can slow down or even block the growth of the facets [6, 31]. Finally, bubbles can introduce surface tension gradients at the interface, leading to convective flows in the surrounding liquid, and consequently affecting the growth of the entire facet or specific regions [32]. For all these reasons, we consider it important to make a deep analysis of the facet velocity in the presence of bubbles.

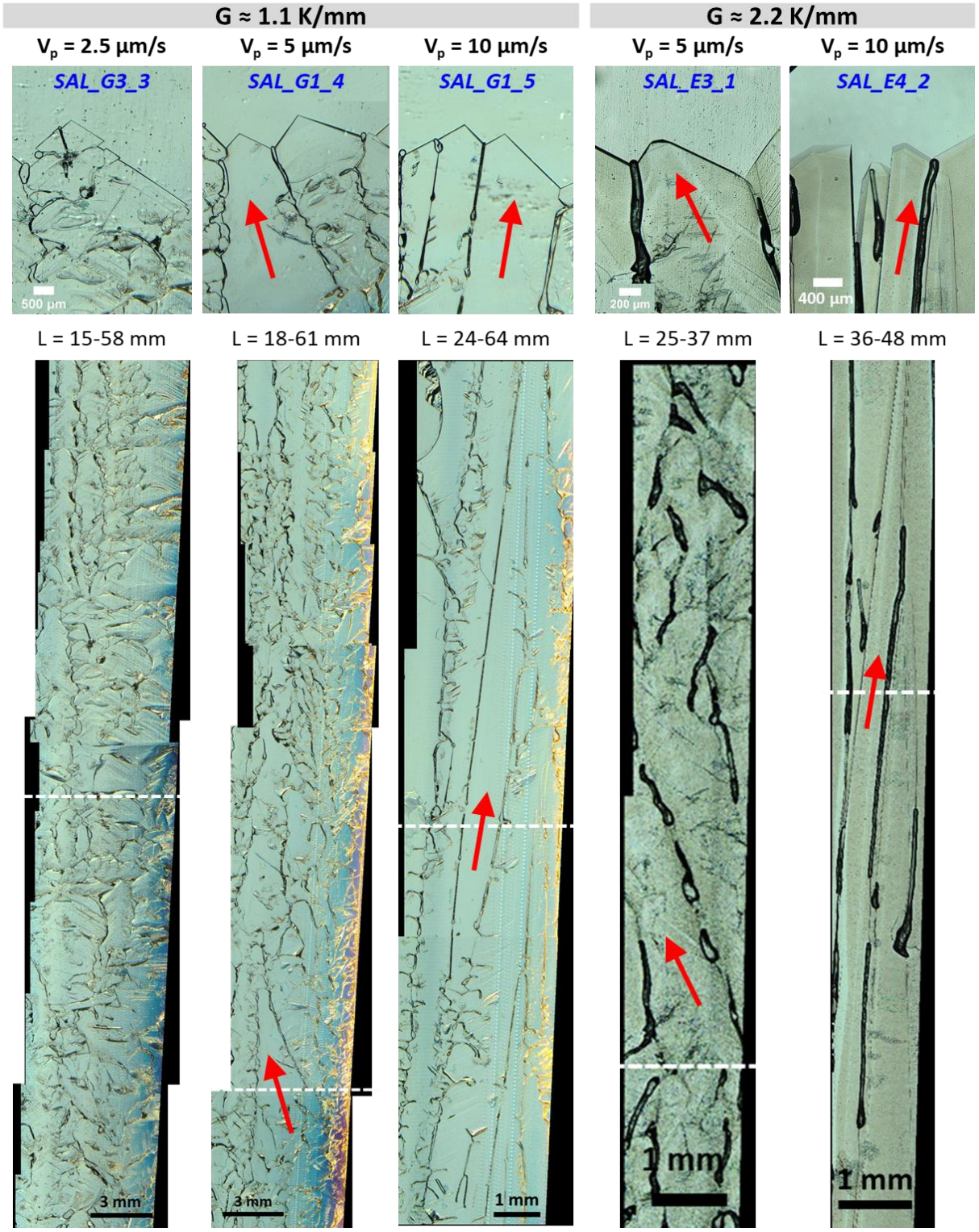
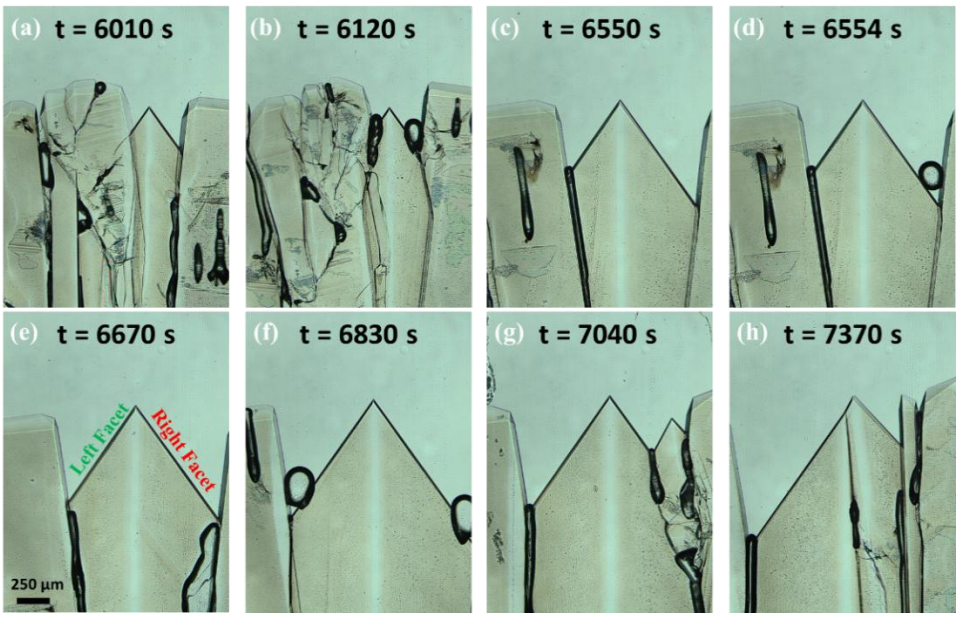


Figure 3.15 – Instantaneous solid-liquid interface images (at the top) and respective reconstruction for the given solidified length (L) range (at the bottom) for different experimental conditions. The experiment name is given in blue in the first row.

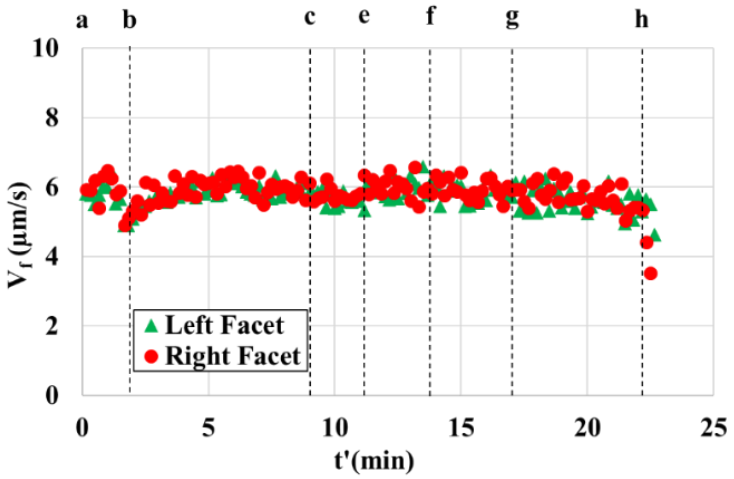
Let us consider the example of the facets identified in Figure 3.16a at 6670 s as left and right whose movement is followed during around 23 min of solidification. As can be seen in Figure 3.16b, they grow with the same average velocity V_f of 5.8 ± 0.4 µm/s. Between 6100 and 6120 s (b-dashed line in Figure 3.16b), we detect an instantaneous decrease in the velocities of the left (from 5.6 to 4.8 µm/s) and right (from 5.9 to 4.9 µm/s) facets, which is a noticeable decrease compared to the average value of the facet velocity (5.8 ± 0.4 µm/s). It can be related to the bubbles on each side of the corresponding crystal and to growth competition among neighboring crystals that obstructed their trajectory before they eventually continue to grow. Between 6550 and 6554 s, a bubble appears next to the red facet and at 6830 s, another bubble nucleates close to the left facet. The measurements show that the bubbles have no significant effect on the growth velocity (variations within the experimental error). At the end (h-dashed line in Figure 3.16b), these two facets are eliminated and a major reduction in velocities is observed.

In Figure 3.17a, the bubble close to the right facet at 1.2 min nucleates in the grain boundary during a period where the facet velocity is increasing. The increase of the velocity of the right facet is spotted in the graphic presenting the evolution of the facet velocity overtime, and it is highlighted by the dotted red line. The bubble then got entrapped in the grain boundary and the facet velocity decreased to the average value (2.3 ± 0.5 µm/s). The bubble near the left facet at 3.1 min nucleates during a period when the facet velocity is considerably decreasing and keeps decreasing after the bubble nucleation. This bubble is quite mobile and moves along the boundary reemerging at the interface around 1 min later. The facet velocity progressively increases till a moment when the bubble split and a rounded one nucleates at the interface. The velocities then stabilize at 2.9 ± 0.6 µm/s and 2.7 ± 0.3 µm/s at the left and right, respectively. In Figure 3.17b, the first bubble nucleates at 4.0 min, just at the end of the facet velocity peak that can be seen between 3 and 5 min. Nevertheless, when the bubble first appears, the velocity starts to decrease, and another bubble nucleated at 4.5 min. The velocity then come back to its average value (3.3 ± 0.8 µm/s). Later on (around 6 min), this facet split at the level of both bubbles.

The correlation between the presence of bubbles and the facet velocity changes is not systematic. However, it is found that the bubbles are most frequently the symptom of a variation of the facet growth velocity rather than the reverse.

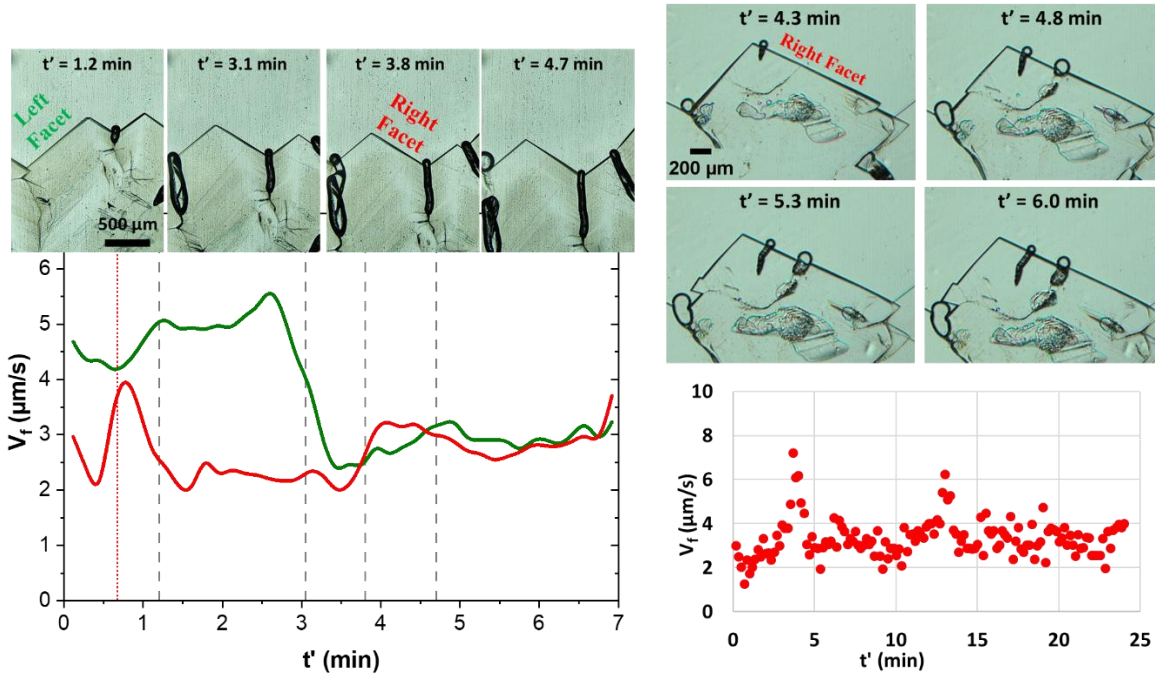


(a)



(b)

Figure 3.16 – (a) Solid-liquid interface of salol during growth in the presence of bubbles. (b) Growth velocities V_f of the facets identified as Left (green) and Right (red) over time. The vertical dashed lines correspond to the times of the images in (a). (SAL_E4_2, V_p = 10 µm/s, G = 2.4 K/mm)



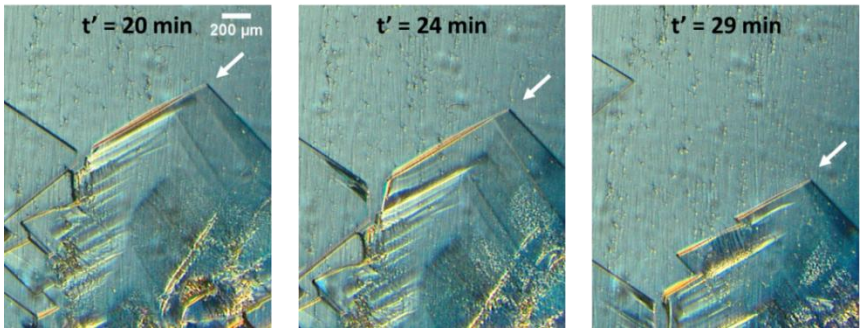
(a) (b)

Figure 3.17 – Images illustrating the interface morphology at given times (top) and facet velocities as a function of time (bottom), at V_p = 5 µm/s and G: (a) 2.1 and (b) 1.2K/mm. (SAL_E3_1 and SAL_G1_4 experiments, respectively)

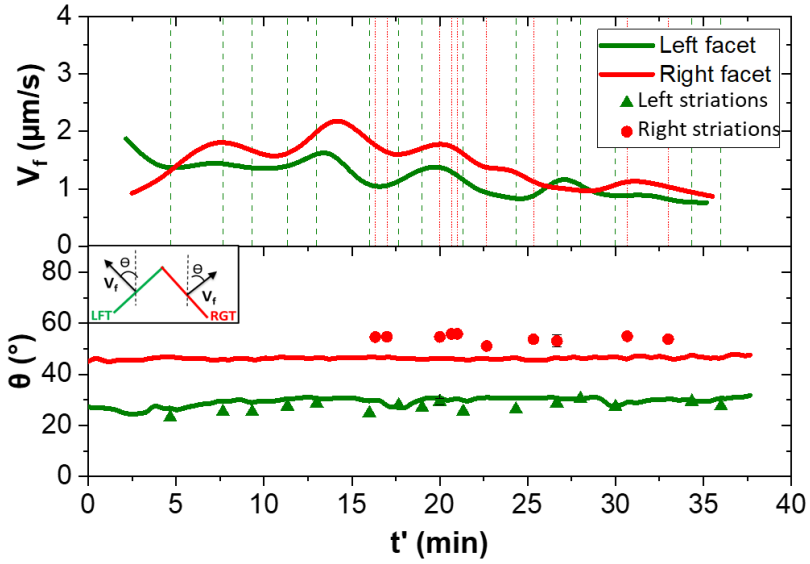
3.3.2 Growth striations

In our experiments, we observe different striations on the crystals, for example, those shown in Figure 3.18a where the same area of the crystal is shown at subsequent times. The dynamics of the crystal indicated by the white arrow is followed in order to further understand the formation of these growth striations and its relation to the facet growth. For that, facet velocities and orientations are measured (Figure 3.18b). The vertical green dashed and red dotted lines indicate the times at which we notice striations. There are more striation occurrences on the left facet side than on the right one, and their apparition does not have a fixed periodicity (even if in the left facet it seems more evenly spaced, every 2.2 ± 0.8 min). Given the oscillating behavior of the velocities (without a characteristic period or amplitude), no obvious link appears between velocity and striations. Striations do not have exactly the same orientation as the facet itself. The difference is more visible in the right (≈8° more than the facet) than in the left (≈2° less than the facet).

This oscillating behavior of the facet velocities is systematically found in the experiments performed, and is associated to the rich and complex dynamics of the salol growth. Hence, the formation of growth striations is not directly linked to the facet velocity.



(a)

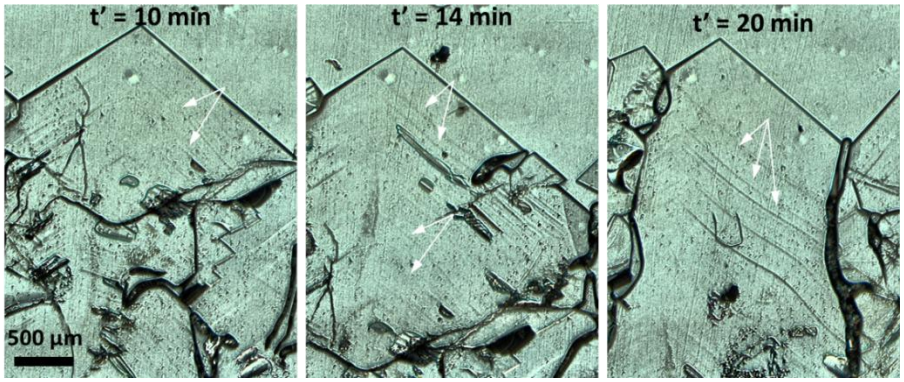


(b)

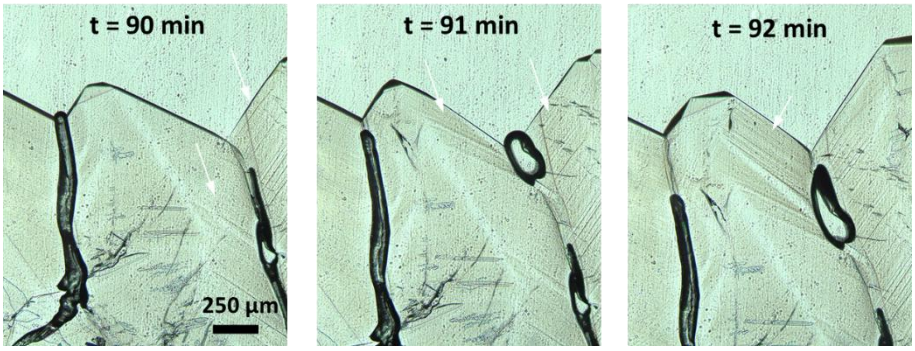
Figure 3.18 – (a) Interface images showing growth striations on two facets. (b) Respective velocity and orientation relatively to the vertical direction as function of time. The green dashed and red dotted lines indicate times at which growth striations were noticed. (SAL_G3_3, V_p = 2.5 µm/s, G = 1.2 K/mm)

It is well known that the growth of a faceted interfaces occurs by the motion of steps and different mechanisms can be at their origin [10, 33] , such as nuclei on the growing interface, dislocations.. However, those observed in Figure 3.18a have several microns in height which represents a substantial change in the growth front compared to regular growth striations. One hypothesis is that the initial crystal does not fill the complete thickness of the sample. During

growth, it touches the crucible wall creating a perturbation and disrupting the natural growth. The crystal surface is then displaced creating a terrace (Figure 1.14). Since this happens several times, stepped terraces, observed as parallel lines, come out on the crystal surface. The formation of macroscopic trains of steps was previously seen at the junction of the interface and the crucible wall during the growth of naphthalene-camphor alloys [34]. The steps, once formed, propagates along the interface. The changes in the interface shape primarily occurs through the collapse of steps or through the changes in inter-step distances.



(a)

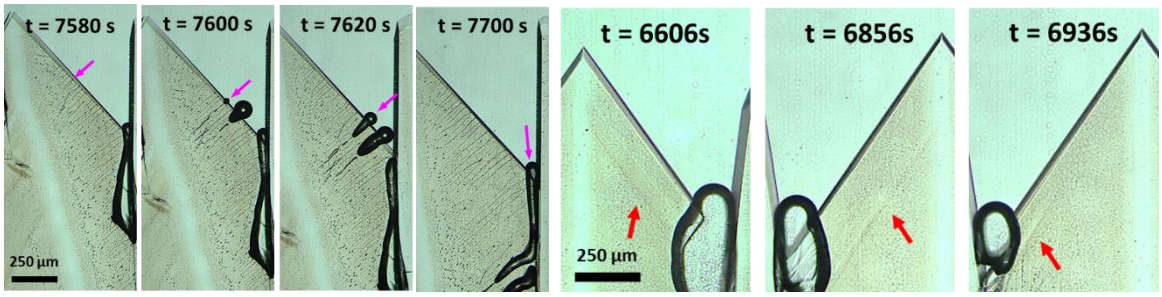


(b)

Figure 3.19 – Sequence of images showing growth striations on facets: (a) Vp = 5 µm/s and G = 1.2 K/mm (SAL_G1_4); (b) Vp = 10 µm/s and G = 2.4 K/mm (SAL_E4_2).

In Figure 3.19 other examples are shown of the same phenomena. In the three instants shown in Figure 3.19a, the line orientation is very similar to the one of the facets. In Figure 3.19b, it depends on the facet: for the one at the right, the lines are parallel to the facet; for the one at the left, one can clearly distinguish two regions where at the top the lines have similar inclination as the facet, and at the bottom they are more inclined. Two hypotheses can be postulated.

These lines may correspond to growth striations that are visible layers or zones of irregularity that form as crystals grow. This kind of defect appears as parallel lines or bands on the surface or within the crystal, and it occurs frequently in low purity organic crystals [9, 10, 22, 35]. If impurity is present, it is rejected by the growing crystal and its concentration is the highest at the centers of the facets. Such a distribution leads to a distortion of the facet planes for both thermodynamic and kinetic reasons (affecting the undercooling or growth rate, respectively) [11, 33]. Growth striations were previously observed during Czochralski growth of salol [36]. It was shown that the growth striations marking the interface at different stages of growth are also associated to tiny gas bubbles. An example of tiny bubbles along the growth striations are observed in our experiments (Figure 3.20a), which are at last responsible for a huge bubble that kept stuck close to the interface. The orientation of the lines is higher than the facet itself, and it progressively increases till the moment at which the huge bubble touches the neighbor grain.

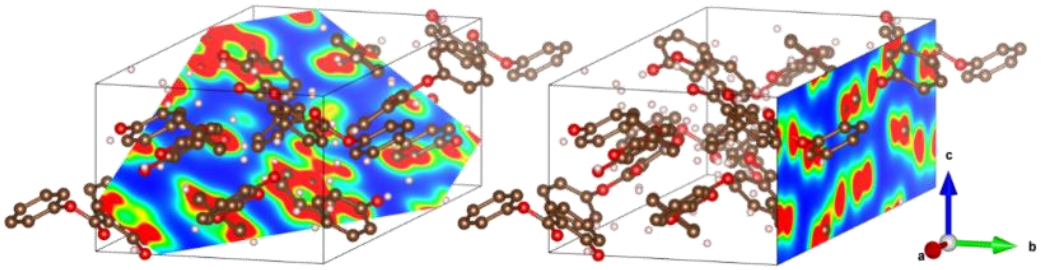


(a) (b)

Figure 3.20 – Images showing (a) growth striations containing tiny bubbles, and (b) the formation of growth striations after the incorporation of bubbles. (SAL_E4_2, V_p = 10 µm/s, G = 2.4 K/mm)

The other hypothesis is that these lines are traces of dislocation or gliding planes. Dislocations are the most prevalent and significant extended defects in organic crystals [9, 13, 22, 35]. The gliding plane is typically a plane of highest atomic density. In molecular crystals like salol, the densest planes refer to planes where the molecules pack most efficiently. Detecting one or other in organic crystals using optical microscopy is challenging due to their nanoscale nature well below our resolution, but when plastic deformation occurs in an organic crystal, it may result in visible macroscopic effects such as macroscopic steps or ridges on the crystal. Similarly, dislocations might cause surface defects, such as steps or distortions which can sometimes be visible under polarized light.

In an orthorhombic crystal structure, the gliding planes and directions are more complex compared to cubic systems, and they depend heavily on the specific atomic arrangement and bonding within the crystal. Identifying them requires knowing the material-specific slip systems, which is not always straightforward and need detailed crystallographic analysis. Literature data on the salol crystal structure (unit cell dimensions, atoms positions and bond lengths) [37] are used in order to identify those planes using a software dedicated to the 3D visualization of structural models, volumetric data and crystal morphologies (VESTA [7, 8]). It is used to explore the planes of the typical morphology of salol crystals shown in Figure 3. 1c [4]. It is found that the densest planes belong to the {111} family (Figure 3.21a) followed closely by those of {010} family (Figure 3.21b).



(a) (b)

Figure 3.21 – Molecular and crystalline structure of salol. The dimensions of the unit cell are a = 23.402 Å, b = 11.258 Å, and c = 7.961 Å. The colored maps represent electron densities from highest in red to lowest in blue, for: (a) {1 1 1}) and (b) {0 1 0} planes.

There are different sources of growth dislocations: they can start from external or internal surfaces (e.g. grain boundaries), from stress or from other defects of different dimensions. Defects may arise from all kinds of inclusions (e.g., foreign particles, liquid inclusions, bubbles, solute precipitates). Our *in situ* observation of the solid-liquid interface during its growth shows that the appearance of these striations is systematically accompanied by defects. In Figure 3.20b, an example of the apparition of the striations (red arrows) following the incorporation of bubbles is shown. Once the large bubble has been blocked in the solid phase (6606 s), two growth striations parallel to the facet appear. Similarly, rounded bubbles in contact with the facet lead to the appearance of two striations: one tall striation at 6856 s and another shorter line at 6936 s. In the three cases presented above, the growth striations appear during a period where the bubbles make the facet velocity to slightly decrease.

In order to evidence the relation between the growth striations and the crystallographic nature of facets, the example of Figure 3.22 is given, where the growth striations are highlighted by the red arrows and several facet crystallographic orientations are determined. Within the time interval during which the facets 2 and 3 are followed, their velocities remain constant. The facets are indexed as shown at 9495 s, using VESTA [7, 8] combined with the comparison of the experimental interplanar angles (noted in the image) with the theoretical ones. The facets that get in contact with each other on the side can disturb their growth and lead to their deformation, creating a stress accumulation eventually relieved by the appearance of the growth striations. The growth striations may originate when {111} planes growing in opposite directions have a coincidence plane of type {010}. Similarly, at 10643 s, different {111} planes are at the origin of the interface shape highlighted by dashed yellow circles, and consequently the formation of growth striations. These observations are in good agreement with the fact that growing striations may be an indirect indicator of dislocation that would glide along the densest planes.

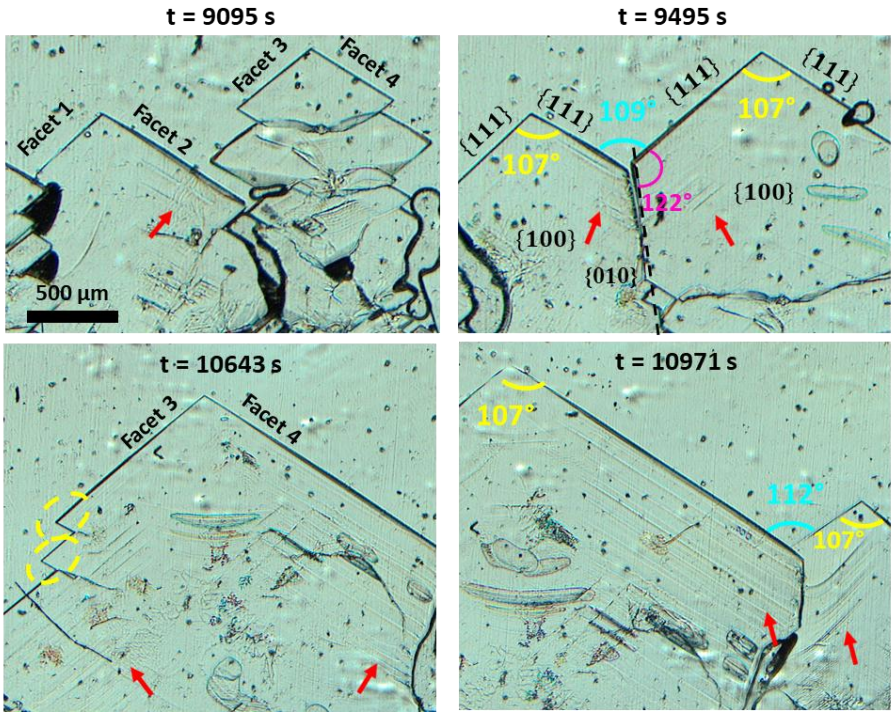


Figure 3.22 – Appearance of growth striations after the interaction between competing crystals (SAL_G3_3, V_p = 2.5 µm/s, G = 1.2 K/mm).

At higher pulling velocity, facet 1 in Figure 3.23 shows multiple growth striations along with its growth. Several ones appear as a consequence of the deformation at the facet that happened between 4143 and 4203 s. The facet velocity attains a peak of 14.1 µm/s much higher than the average rate of 7.7 ± 0.5 µm/s. This facet evolves for a long time with several splitting events or bubbles nucleation, and the growth striations appear frequently. At 5323 s, the facet reaches a quite high size (2618 µm) with several growth steps parallel to it. However, no variation in the facet velocity is detected. Around 5543 s, the facet undergoes a splitting accompanied by bubbles and defects. As a consequence, the facet velocity decreases from 9.1 to 5.6 µm/s. To confirm the crystallographic orientation of the facet having these growth striations, the interplanar angle between facet 1 and 2 is measured, 105.6 ± 0.6°, which corresponds to an interplanar angle between {111} planes. Additional measurements give values of 128 and 123° aligning with {010} and {111} planes. This is in favor with the hypothesis of dislocation movement leading to the creation of growth striations on the crystal surface.

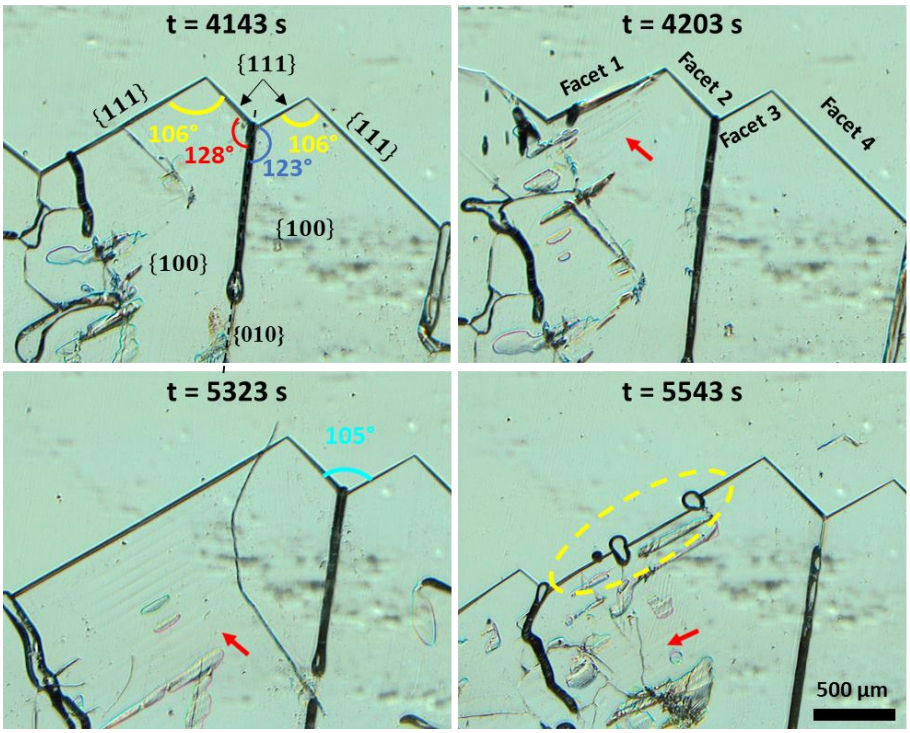


Figure 3.23 – Formation of the growth striations on facet 1 after being exposed to several defects during the solidification. (SAL_G1_5, V_p = 10 µm/s, G = 1.1 K/mm)

Figure 3.24 shows an example of the growth striations (red arrows) formed after the disappearance of facets (green braces). Besides causing the adjacent facets to be eliminated and

subsequently incorporated in their structure, Facet 1 has also a large bubble at the groove. These factors can contribute to a stress accumulation that is relieved through the appearance of growth striations. Another factor that can contribute to the formation of the growth striations is its splitting, evidenced by the yellow dashed circles at 7540 s. These factors result in an increase in its velocity from a 5.5 to 8.5 µm/s. The measured interplanar angle between facet 1 and 2 is equal to 72.2 ± 1.5°. It is interesting to note that the growth lines are parallel to facet 1, but it is less evident concerning facet 2. The neighborhood of facet 2 is slightly different. The closest facet noted by the purple dashed line at 7540 s seems to belong to a {211} plane, given the measured angle 44° very close to the theoretical one between {111} and {211} planes (44.6°). This means that growth competition with facets belonging to another crystallographic nature may prevent the formation of growth striations.

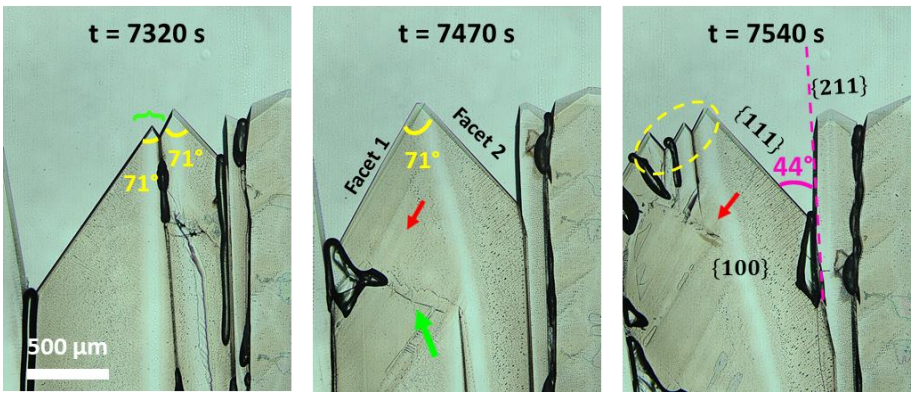
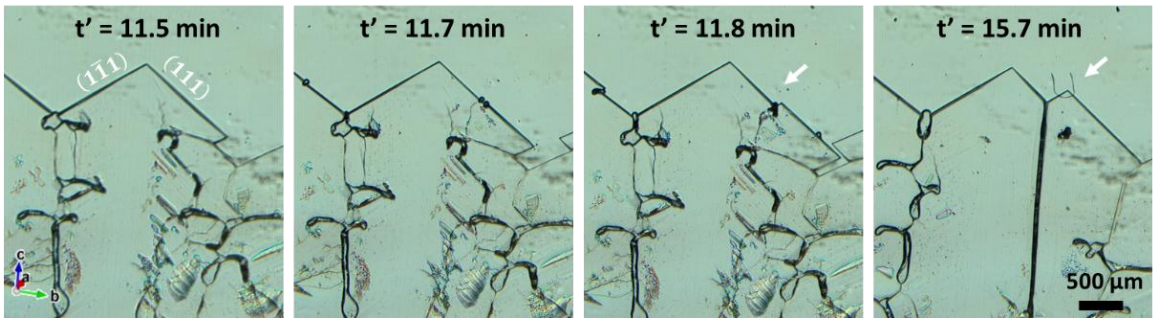


Figure 3.24 – Formation of growth striations after the elimination and split of neighboring facets. (SAL_E4_2, V_p = 10 µm/s, G = 2.4 K/mm)

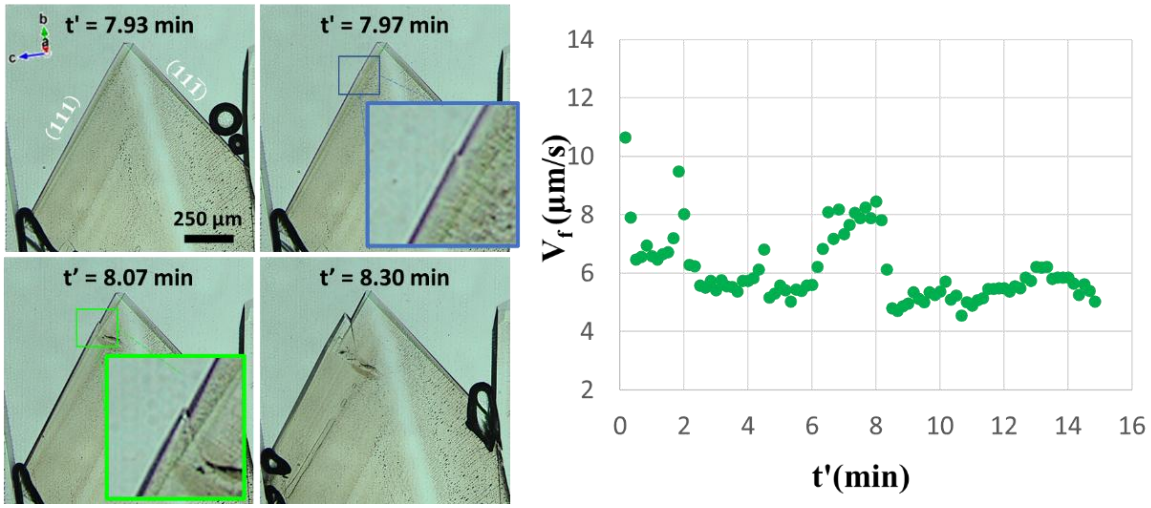
The analyses show that the appearance of the growth striations during the solidification process is promoted by several factors, including stress accumulation from facets interacting with each other, the deformation occurred by facet splitting, the disturbance caused by the trapped bubbles at the grooves, and the dislocation movement causing structural constraints. The growth striations form in the solid phase as the facets grow during the solidification process and as such, no direct relationship is found between the growth striations and the facet velocity. In addition, crystallographic analyses demonstrate that the facets exhibited growth striations correspond predominantly to {111} planes.

3.3.3 Facet splitting

Another frequent observation during our experiments is the facet splitting during growth, giving rise to new facets. Figure 3.25 presents a sequence of images showing two of these examples. In Figure 3.25a, we can clearly see that the split leads to the formation of a new tip (white arrow), where both interplanar angles are equal (104 ± 0.5°). The initial and new facets are separated by a bubble that makes a long channel decorating the groove of the facet during growth. Both tips evolve then in a stable way. In Figure 3.25b, while the facets are initially flawless, a small split start to develop at the top left edge. A defect can be seen at some point (7.97 min), and a new tip, with the same orientation, can be clearly distinguished at 8.30 min. Figure 3.25b shows the evolution of the facet velocity with time. The splitting event happens at a moment at which the facet is growing with a velocity higher than the average, because it is overgrowing a neighbor grain.



(a)



(b)

Figure 3.25 – Images showing a splitting event on a facet at V_p = 10 µm/s and G: (a) 1.1 and (b) 2.4 K/mm, with the respective facet velocity evolution with time. (SAL_G1_5 and SAL_E4_2 experiments)

It seems interesting to show the example of Figure 3.26a because the split occurs in a facet with well-defined 3D appearance. As can be seen in the first image (at 42.6 min), the facet at the top-right has a brownish color evidencing a slight inclination with respect to the container wall. The left image in Figure 3.26b is a schematic 3D representation using VESTA [7, 8]. The apparent area of the brownish region increases linearly till 43.0 min where its color become a little lighter and we see a small dark spot (zoomed in the green square). The area then progressively decreases and, at some point, the new tip is clearly distinguished (as zoomed in the cyan square). The right image in Figure 3.26b is the respective schematic 3D representation. Both tips keep stable and evolve with slightly higher growth velocities for the facets of the initial structure than those of the new one. The facets outlined with the same color (red, green, orange, and blue at 45.7 min) are growing parallel to each other. The experimentally measured interplanar angles are the same ($110 \pm 0.38°$) and in good agreement with the theoretical angles between planes $(1\bar{1}1)$ and (111). In this example, it seems that during the growth of the facet indexed as (111), a perturbation happened. One hypothesis is that it touches the container wall, what lead to a stress accumulation and, consequently, to the facet splitting. It was previously observed during the growth of organic transparent systems that a significant amount of stress can be relieved by the formation of a boundary [34, 38]. The other hypothesis is that its lateral surface attained a critical value [33]. This results in splitting into two parallel plates of smaller thickness, with a macrostep transforming into an overhanging layer.

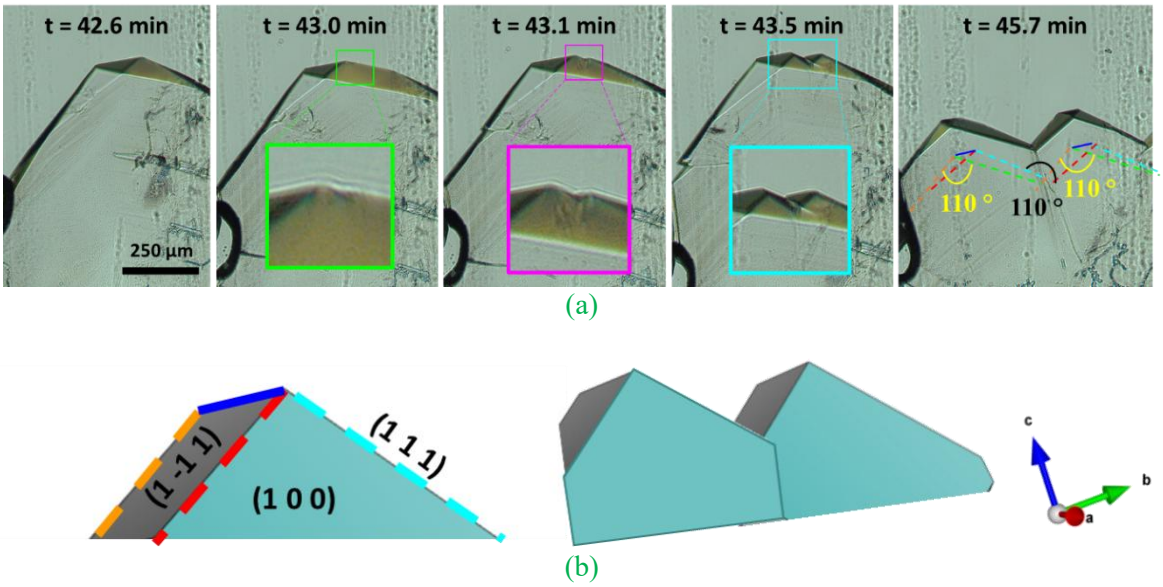
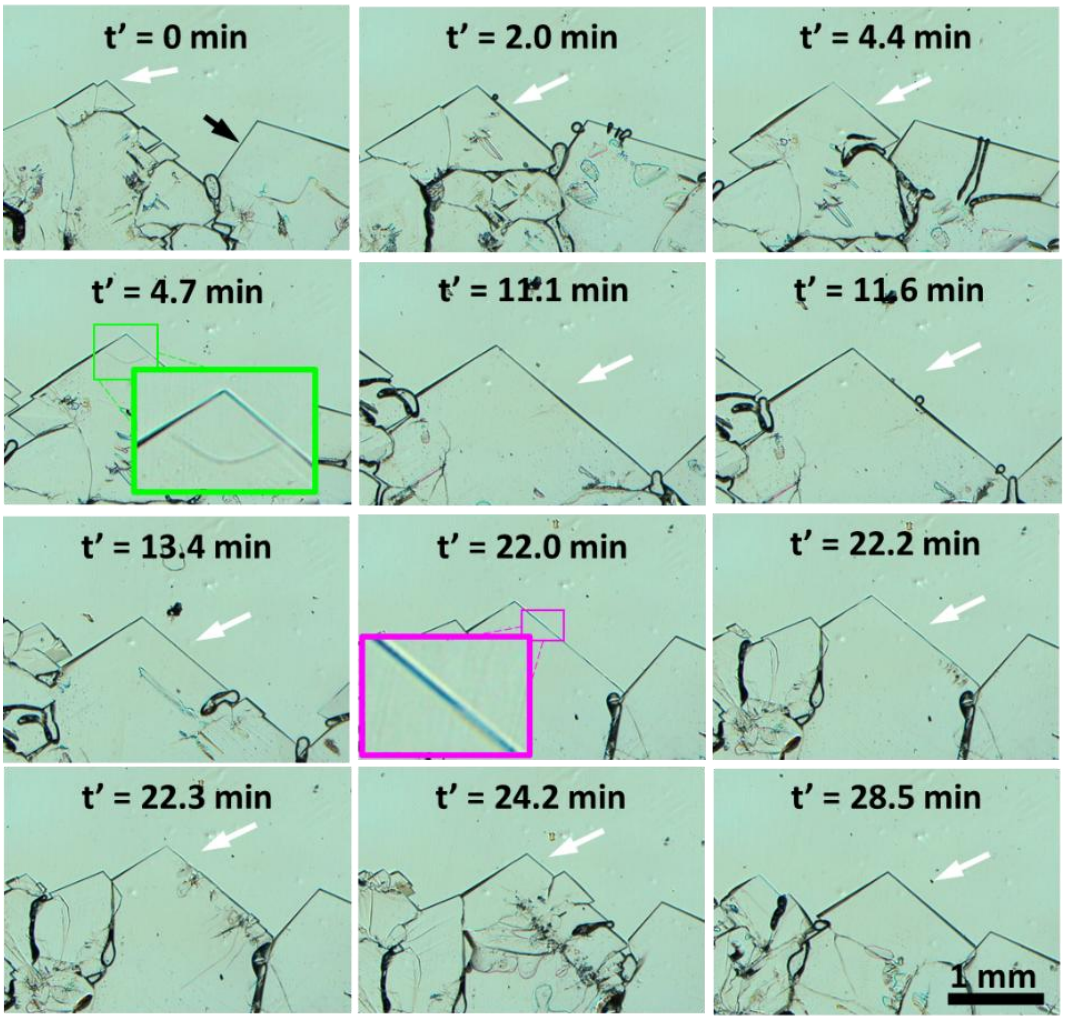
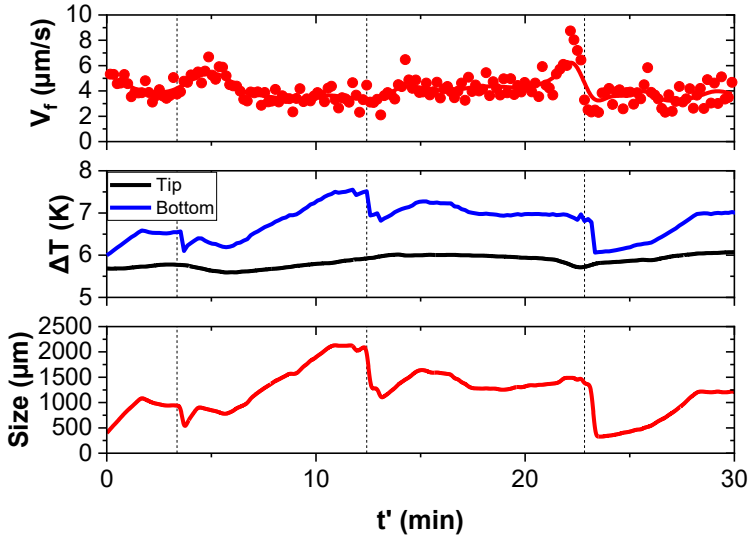


Figure 3.26 – (a) Sequence of images showing a facet split event occurring in a well-defined 3D facet. (b) 3D schematic representation of the facets using VESTA. (SAL_E3_1, V_p = 5 µm/s, G = 2.1 K/mm)



(a)



(b)

Figure 3.27 – (a) Evolution of a facet (white arrow) that kept stable despite several splitting events. (b) Respective evolution of growth velocity (V_f), undercooling (ΔT) and size. The dashed vertical lines indicate instants at which splitting happened. (SAL_G1_4, V_p = 5 µm/s, G = 1.2 K/mm)

Figure 3.27a shows the evolution of a facet (white arrow) that has undergone splitting events several times but has always managed to grow normally afterwards and even overgrowth other neighbor facets. The plots of the respective evolution of size, undercooling, which is the difference between melting temperature T_M and the actual temperature of the liquid T, and growth velocity are presented in Figure 3.27b. Moreover, in this example, we show the evolution of the undercooling of the tip and of the bottom of the facet (marked with the white arrow) during its growth. At the beginning, the facet size is increasing laterally considerably fast till ≈1.7 min where it collides with the facet indicated by the black arrow that is growing in opposite direction. Just after that, a dark spot and a bubble are observed emerging close to the tip (2.0 min). The splitting happens sometime later (3.3 min) and the bubble draws its place. The facet is able to restart its growth and again, when it collides with a neighbor, a defect appears at the tip (zoomed in the green square at 4.7 min). In this case, the defect does not lead to a splitting. The facet keeps growing and overgrows its neighbors. Its size then increases linearly until it reaches a large size (≈2100 μm) compared to what is regularly observed in our experiments. It is well known that facets become unstable if they become too large, and the splitting is the most common mechanism to adjust the spacing [18, 38, 39]. Since in our case it collides with a neighbor grain, one cannot say how big the facet would be able to grow without adjusting its size by splitting.

After the collision, defects appear along the facet and a new splitting happens sometime after. Due to its environment after this splitting, the facet size is not able to increase as much as previously. And, it is interesting to notice that the facet velocity stabilizes at a value slightly higher than before this split (4.2 ± 0.5 and 3.6 ± 0.4 μm/s, respectively). At ≈20.0 min, the facet starts to compete with a neighbor that has the same undercooling, and both evolve stably. From ≈21.3 min, we observe a color change in the facet (magenta square at 22.0 min), and a sudden increase of the facet velocity. The observed color change can be attributed to a relief mechanism resulting from a stress accumulation. Eventually, the facet becomes completely unstable, a lot of defects appear, and it splits.

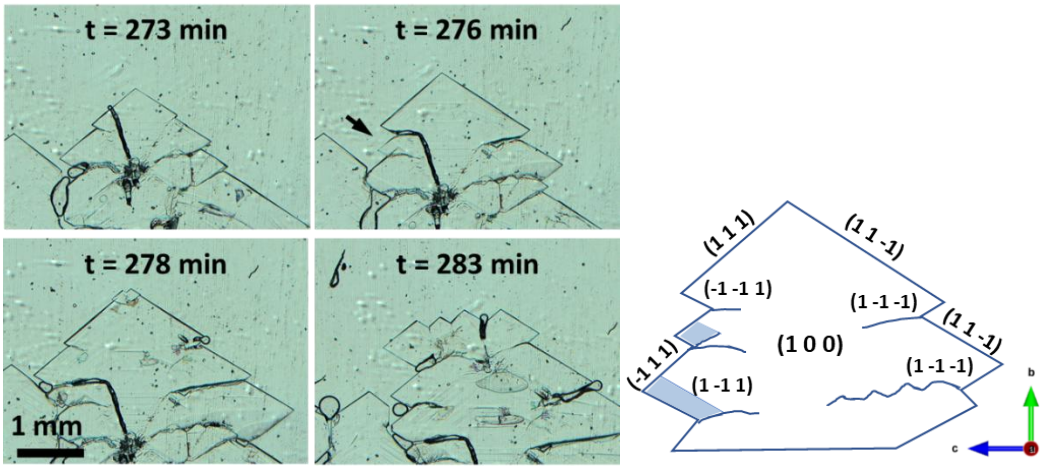
What is different in the example described compared to the previous ones is that none of the splitting events lead to stable tips. Small faceted tips are always overgrown by lager facets. However even large facets cannot extend beyond the melting isotherm leading to a decrease in the size of the facet resulting a split. [40-44]. This was previously observed in other organic compounds: once the tip approaches the melting isotherm, it flattens; the flattened tip is then further dumped becoming unstable, and creating new tips [45]. Even if we do not see tips

flattening, we look at the facet undercooling (taken at its tip and bottom). As can be seen in Figure 3.27b, the tip undercooling does not approach zero (melting isotherm) and consequently this is not the reason for the splitting events. However, the undercooling difference between the tip and the bottom can change locally the thermal gradient inducing localized stresses, leading to splitting as the system responds to these stresses.

Figure 3.28a shows an example where the splitting happened really in the tip, which is less frequently observed in our experiments compared to facet splitting. In this case, the tip undercooling is lower than the rest of the growth front, and the tip is marginally ahead of its closet neighboring faceted tips. It is then growing with a velocity (3.1 ± 0.6 μm/s) slightly higher than its closes neighbors (2.5 ± 0.6 μm/s). This tip is highly unstable and we observe explosive, successive splits at the tip that lead to new tips. The new tips grow with the same morphology and direction as the mother tip (interplanar angles of 107 ± 0.24°). Successive splitting events are observed during the growth of a faceted-faceted organic eutectic system leading to the formation of spherulites [46, 47]. In their case, splittings occur along one direction where there is a very large growth and the spherulites become finer at a much larger undercooling. In our case, we can also notice a particular interface morphology at some places (black arrow). Defects appear along the facet leading to a split at those places. This allows other crystallographic planes to grow, and gas bubbles are captured during the growth making the crystal to have this periodic morphology. A tentative indexation of the planes is given in Figure 3.28b based on the 3D reconstruction using VESTA. The hypothesis of this “tooth” shape being other crystallographic planes is supported by the measurement of the interplanar angles in the experiments which are in good agreement with the theoretical ones.

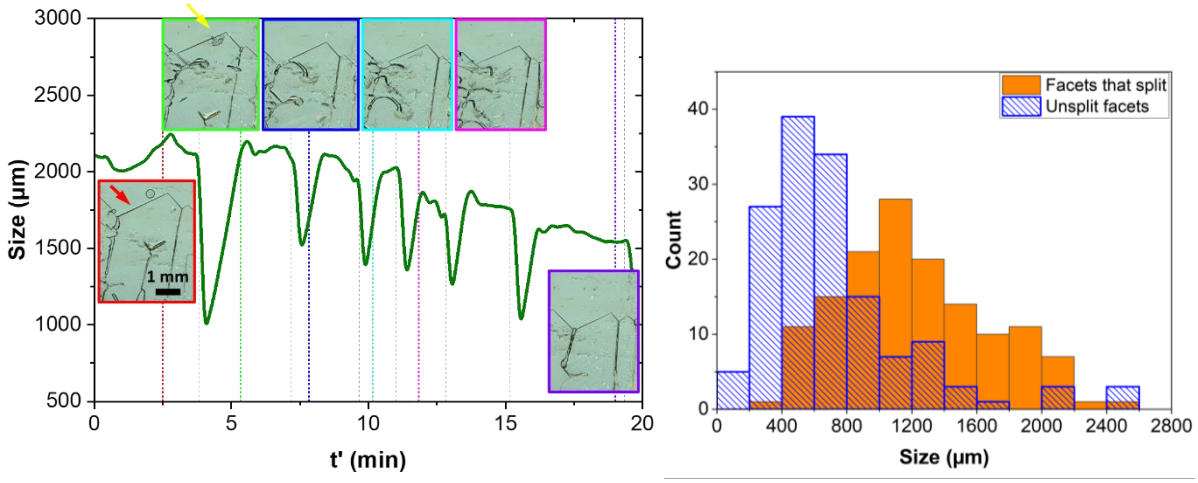
The example of Figure 3.29a deserves further attention because of the evolution of the facet size. The facet highlighted by the red arrow has a quite big size (≈2000 μm) and the first splitting (highlighted by the yellow arrow) happens due to the bubble coming from the liquid (3.83 min). After that, the facet grows again till the same size, and the cycle happens several times. Even if in this example the facet size is conditioned by the competition with neighbors, this motivated us to look into all the splitting events that we detected in our experiments, and check if there is a size threshold. Figure 3.29b shows the respective histogram and, in our experiments, splitting is not necessarily associated to the bigger facets, it can even happen in the smaller ones. The majority of the events happens however for sizes higher than 1000 μm. The inclination of the facet seems to favor the splitting, as approximately 70% of the splitting events occur for facets

whose orientation with respect to the pulling direction is in the range of 30 to 45°, both for the left- and right-oriented facets.



(a) (b)

Figure 3.28 – (a) Images of a tip overgoing successive splitting events. (b) Schematic representation of the grain morphology using VESTA. (SAL_G3_3, V_p = 2.5 µm/s, G = 1.2 K/mm)



(a) (b)

Figure 3.29 – (a) Evolution of a facet size as function of time. The grey dashed lines represent moments at which splitting events happened. The color dotted lines are linked to the images of the solid-liquid interface. (SAL_G1_5, V_p = 10 µm/s, G = 1.1 K/mm) (b) Histogram of the size at which splitting events happened in all the performed experiments.

3.3.4 Crystal distortion

In this section, we will present examples of the formation of crystal distortions which are considered as microscopic defects where the regular arrangement of the crystal is locally strained. These distortions, associated with mechanical stress, can, in some cases, lead to dislocations and further to macroscopic defects such as cracks, fractures, or fissures in the solidified material. Cracks on a macroscopic facet along the solid-liquid interface during solidification of salol was previously observed by Dey and Sekhar [14, 27]. These authors associated it to a large size facet obtained at low interface velocities and undercooling.

Figure 3.30 illustrates one of those examples, where the facets are indexed as shown at t' =0 using VESTA [7, 8] combined with experimental measurements of angles. We identify that the green facet corresponds to $(2\bar{1}\bar{1})$ plane, while the red facet to $(2\bar{1}1)$ plane. The red one is growing stably with a velocity of 9.6 ± 0.6 µm/s, when around 24 s, probably due to the competition with a grain on the right, its growth velocity almost double. During the period when the red facet velocity is returning to its average value, a distortion (white arrow) appears that is even clearer at 36 s. This distorted region remains stable without growing further. This observation is not in agreement with the literature reporting that the growth rate of a facet is frequently seen to increase when a crack appears in the crystal [27]. Despite this, both crack and distortion tend to occur following or during an acceleration phase, inducing high thermomechanical stresses leading to cracks or distortions.

During this rapid growth of the red facet, we see the emergence of a facet with different orientation (blue square at 34 s). The angle measured between this facet and the green one, 136.1 ± 0.7°, is in good agreement with the theoretical angle (134.5°). This new facet is not stable and is overgrown by the green and red ones. Just before its disappearance we can see a black spot (white arrow at 42 s), and just after (44s) a new distorted zone. It then behaves like the first one, with a fixed length, till 60 s when its size suddenly got more than 3 times bigger (as indicated by the red arrow). This explosive increase of the size happens during a period when the green facet and the left grain are getting closer and few seconds after the undercooling in the grain boundary attained its maximum value. The undercooling in the grain boundary then decreases very quickly leading most likely to local accumulation of thermal stress [10, 11, 48]. The relaxation of stress can then be at the origin of the defect (distorted area) observed.

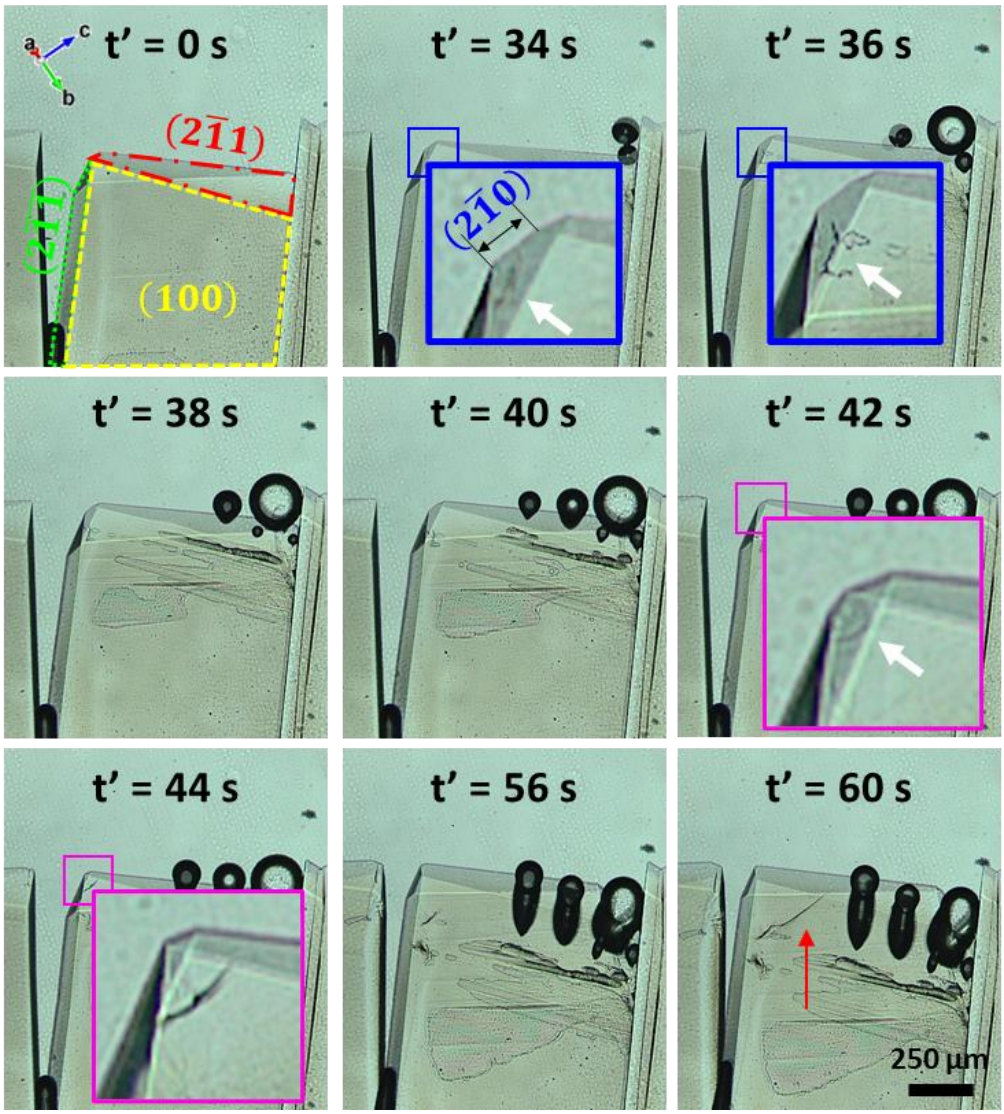


Figure 3.30 – Image sequence of the solid liquid-interface showing the appearance of distorted areas. (SAL_E4_2, V_p = 10 µm/s, G = 2.4 K/mm)

Another interesting example is shown in Figure 3.31 for which we can take advantage of the birefringence of salol and of the use of polarized light in our experiments. As previously done, we index the bigger facet aligned with the container wall as a (100) plane. The three other facets that one can see at the beginning are {111} planes. At some point, we observe the emergence of facets with different orientation (at 6320 s we can see a horizontal one that was not there before). The yellow color begins to fade, and a faint perturbation appears at the top of the facet (withe the arrow at 6326 s) indicating distortions on the crystal. The perturbation further expands, and the stress generation further increases ultimately resulting in the formation of a distorted

zone (pointed out by yellow arrow at 6344 s). Two other distorted areas are formed sometime later (6354 and 6398 s). At the end, the facets morphology is very similar to the beginning.

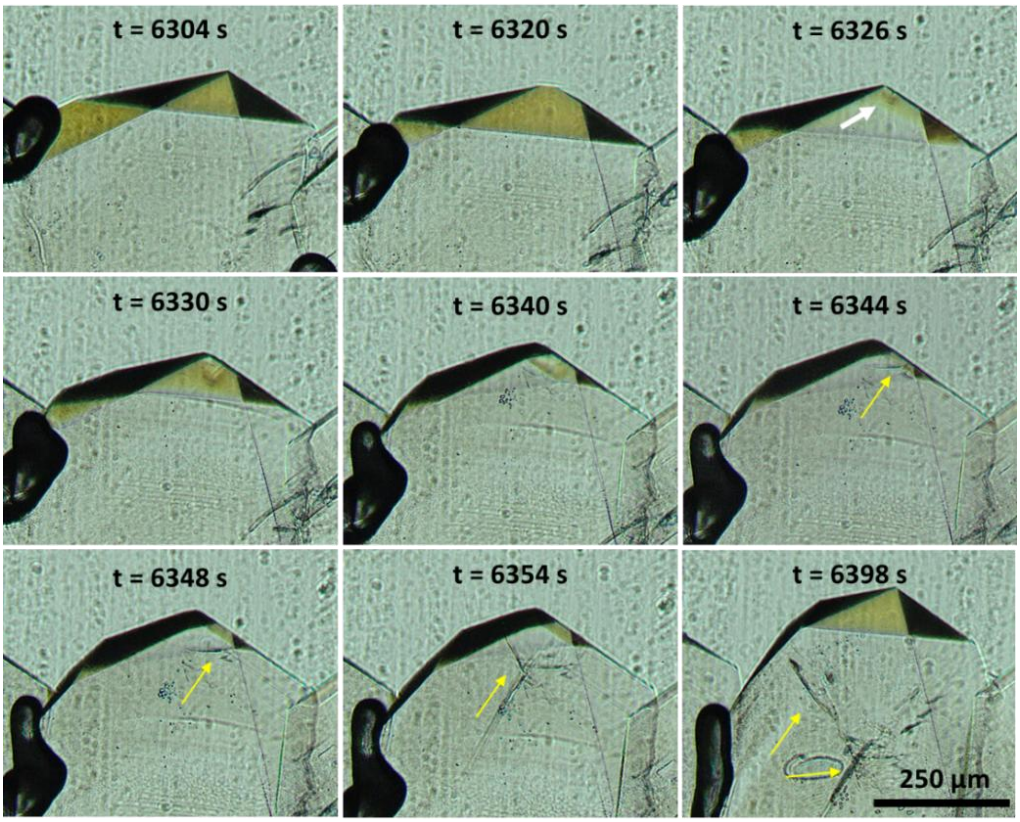
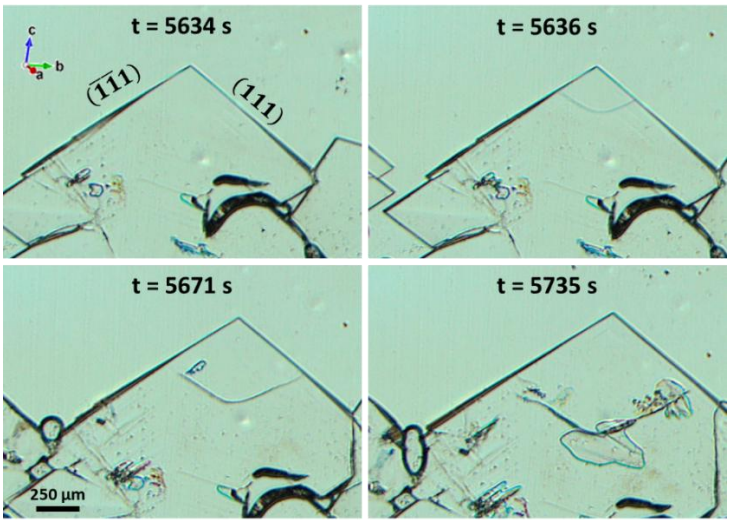


Figure 3.31 – Images showing a distorted zone appearance along the solid liquid-interface after a perturbation. (SAL_E3_1, V_p = 5 µm/s, G = 2.1 K/mm)

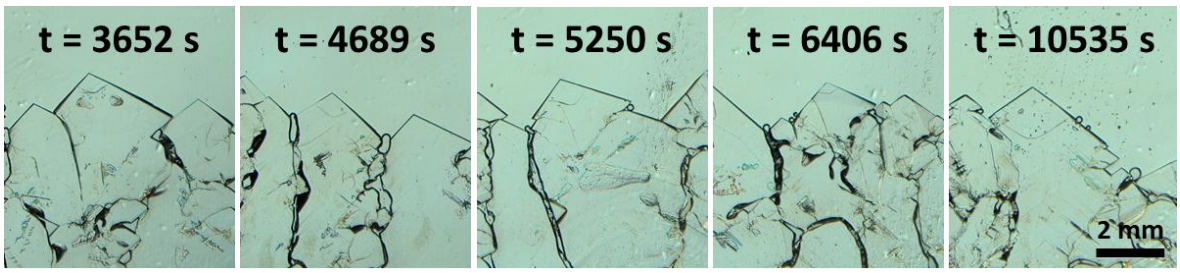
One hypothesis for the observed in the previous examples is that the crack appeared along growth-sector boundaries, regions formed by the trajectory, during growth, of the edge between the two faces involved [9, 35, 36]. Growth-sector boundaries can act as planes of weakness due to differences in crystal orientation and stress distribution. Fabietti and Trivedi [38] also observed stress fringes appearing around a perturbation during the solidification of purified naphthalene. In their case, once a grain or sub-grain boundary is created, the stresses are released and the fringes disappear. In both cases, growth-sector boundaries or grain boundaries, structural or mechanical defects may propagate along them because they often have lower cohesion compared to the internal structure of the crystal.

Figure 3.32a shows an example where the distorted area has a particular shape. As growth progress and the facets marked by the white arrows collide, a distortion suddenly appears (5636

s), extending from the left- to the right-oriented facets with an arc shape. During around 83 s, this distortion moves with the solid while its size increases. After that, it remains stable without changing. The same type of distortion is observed several times during this experiment (Figure 3.32b). One may notice that it happens when the lateral facets of {111} type are quite big (> 600 µm). It is also interesting to point out that it happens when the respective tip undercooling is lower than its closest neighbors and, its growth velocity slightly higher what can originate thermomechanical stresses.



(a)



(b)

Figure 3.32 – (a) Sequence of images showing an arc shaped defect extending over the faceted tip. (b) Same type of event observed during solidification. (SAL_G1_4, V_p = 5 µm/s, G = 1.2 K/mm)

Other examples exhibiting the same shape for these features are found in another experiment (Figure 3.33). The first one happened in the tip of a facet highlighted by the red arrow at 4385 s. This tip has a complex neighborhood, which can promote stress accumulation. Stress can be relieved resulting in the appearance of a distorted area evidenced by the yellow arrow at 4412

s. Furthermore, another smaller arc shaped feature appears parallel to the previous one (4416 s). It is worth mentioning that between 4385 and 4412 s, the velocity of the sided facet increases from 5.8 to 7.2 µm/s. This facet exhibits an unstable growth, having a lot of defects. Another arc shaped feature appears later just after a splitting (dashed yellow circle at 7325 s). A decrease of the facet velocity is detected 5.5 to 2.7 µm/s from the moment the split happened.

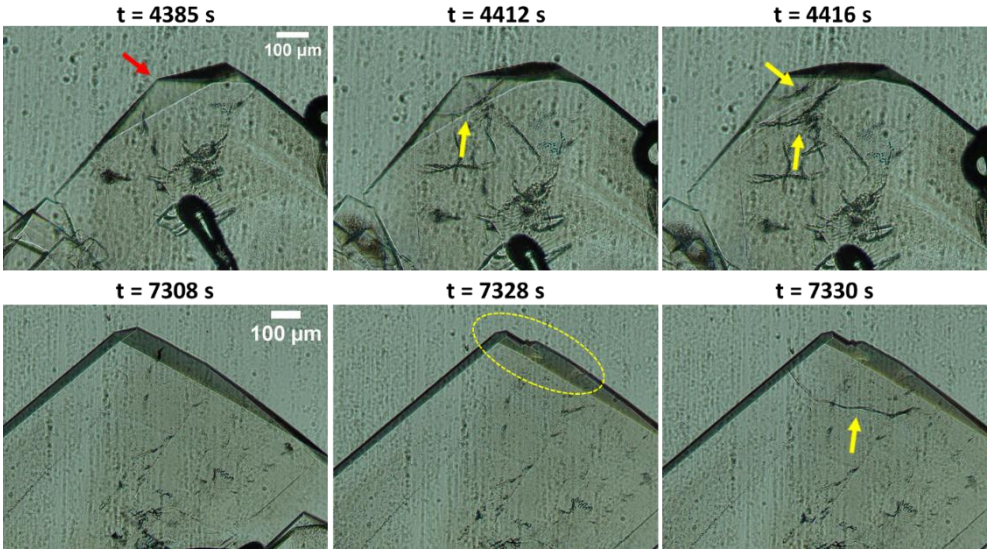
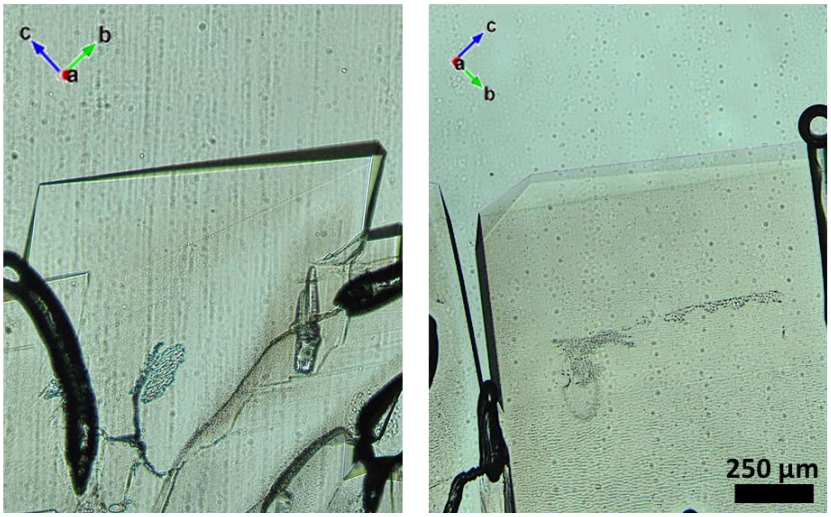


Figure 3.33 – Snapshots of the formation of arc shaped defects near the faceted tip (SAL_E3_1, Vp = 5 µm/s, G = 2.1 K/mm).



(a) (b)

Figure 3.34 – Examples of facets where no distorted area is observed during a long-solidified length: (a) V_p = 5 µm/s, G = 2.4 K/mm (SAL_E3_1); and (b) V_p = 10 µm/s, G = 2.1 K/mm (SAL_E4_2).

Crystal distortions are observed in all the performed experiments during the whole solidification. We can, however, show two examples where facets have grown for a long time without suffering any distortion (Figure 3.34). It is interesting to notice that, the crystals without distortions have one facet growing in the pulling rate. Moreover, in the few examples, the a-axis is systematically perfectly perpendicular to the crucible wall. In this configuration, the crystal might experience more uniform cooling and less thermal expansion mismatch between the crystal and the crucible, reducing internal stresses that would lead to defects. The crystal misorientation from the alignment perpendicular to the wall can lead to stress distribution within the crystal as it solidifies and an increased likelihood of stress and structural defects up to cracks.

3.3.5 Twin crystals

Among the planar defects frequently observed in organic crystals, there are the twin boundaries, a specific type of grain boundary where two crystals of the same phase have a specific orientation relationship. In some cases, the two crystals are oriented as mirror images of each other across the boundary [9, 10, 13, 36, 49-55]. Growth twinning is one of the most serious macroscopic defects in industry, the presence of which makes a crystal of no commercial use because of the twin-induced growth disorientation over the whole crystal body. Former studies on silicon growth have given particular attention to the twining occurrence [50, 55], with some supporting the hypothesis of its origin in enhanced temperature and stress accumulation and some relating it to the orientation due to different kinetic undercooling. Growth conditions enhancing twin appearance are: temperature instabilities, presence of impurities, foreign particles on the melt surface, or the presence of dislocations.

Figure 3.35 shows an example of a twin crystal formation observed during our experiments, where the facets are indexed as shown at t = 11474 s. Over time, the $(1\bar{1}1)$ facet changes in color and gradually fades, with a fine line becoming visible at 11480 s. This corresponds to the emergence of a $(2\bar{1}1)$ plane. Slightly before, we observe a dark spot appearing (white arrow in the magenta square). The emergence of the $(2\bar{1}1)$ facet induces a stress field and the subsequent nucleation of the twin boundary is observed. The new grain is divided in two sides one of them with the same morphology as the initial grain. Both sides expand creating a more distinct separation between them: at 11584 s the grey shaded zone indicates the twin crystal, and the white dashed line identifies the twin boundary. The twining plane is identified as the

$(1\bar{1}\bar{1})$ plane, and there is 178°of rotation between the parent and the twin crystal. This indicates that twin boundary is a Σ3 twin. It was previously observed during the silicon growth that the occurrence of disoriented grains in the grain boundary grooves may be dominated by a twinning mechanism [50, 55-58]. The twin-boundary formation described in this example is also very similar to what was found by Lenart *et al.* [59] in low-temperature quartz. However, these authors found that the formation of a straight twin boundary in quartz is related to the earliest stage of crystal growth, while in this work it was found during the quasi-stationary stage.

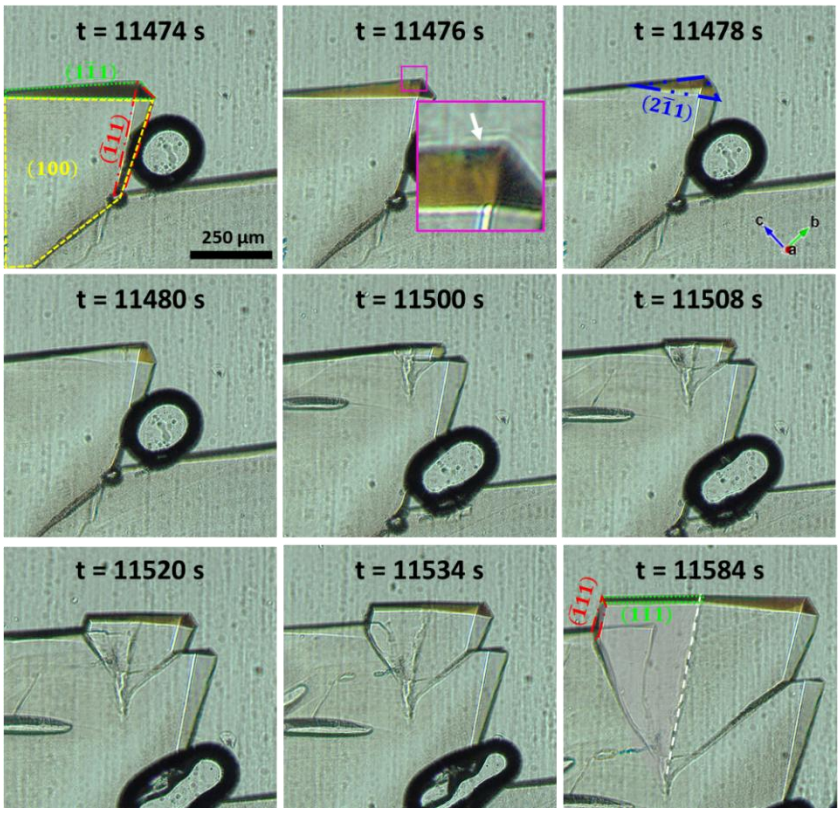


Figure 3.35 – Sequence of images showing the appearance of a twin crystal and its subsequent growth. (SAL_E3_1, V_p = 5 µm/s, G = 2.1 K/mm)

In Figure 3.36 initially, the horizontal facet indexed as (111) exhibits a well-defined edge. Then a visible distortion develops creating a site where a new crystal started to grow (yellow arrow at 5974 s). At 5982 s, the crystal starts to form boundaries with the neighboring crystals. These boundaries are straight at first (white arrow) but, by 5986 s, it starts to have a wavy pattern due to the presence of multiple growth striations along the facet aligned with the crucible wall. Over time, the growth becomes more complex, hence we observe how the new formed

crystal is expanding and is distinctly separated from the original facet (black arrows). The facets are indexed as shown at 6002 s, and the twinning plane is identified as $(1\bar{1}\bar{1})$. The twinning crystal is rotated by 157° comparing to the parental crystal. Since the rotation is different from 180°, this suggests a different type of grain boundary or a more complex twinning mechanism that does not fit within the Σ3 classification.

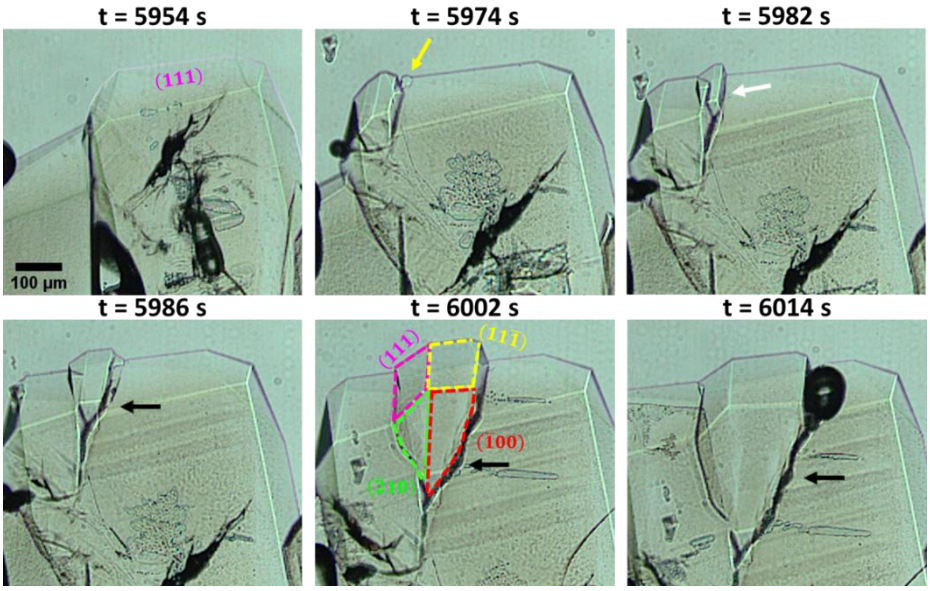


Figure 3.36 –Images of the formation of a twin crystal. (SAL_E4_2, V_p = 10 µm/s, G = 2.4 K/mm)

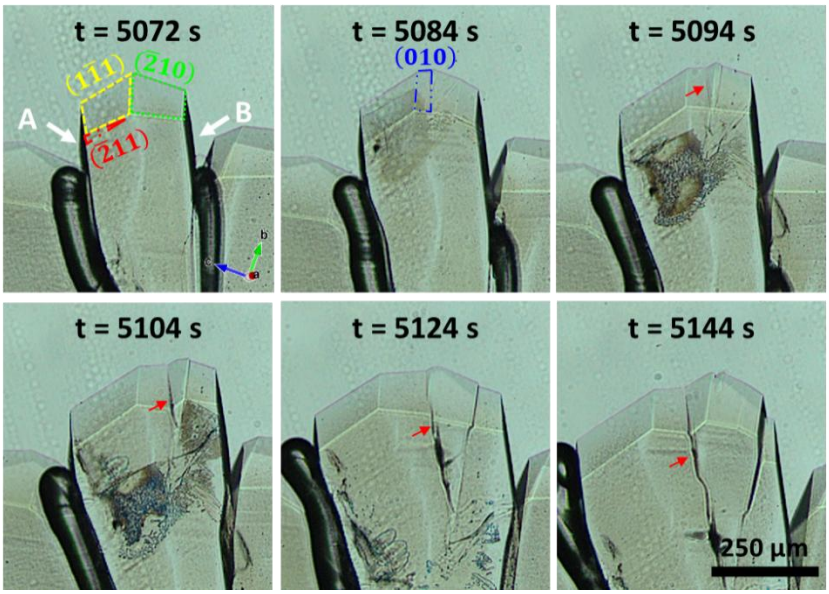


Figure 3.37 – Sequence of images showing the development of a twin boundary from a facet after a defect occurrence (SAL_E4_2, V_p = 10 µm/s, G = 2.4 K/mm).

Figure 3.37 shows another example of twining observed during our experiments, where the facers are indexed as shown at 5072 s. The lateral black facets may correspond to: $(\bar{1}\bar{1}1)$ or $(\bar{2}\bar{1}1)$ for A, and $(\bar{1}\bar{1}1)$ or $(\bar{2}\bar{1}1)$ for B. At some point, a perturbation happens, probably due to contact with the container wall, that locally changed the facet velocities. The crystal slightly turns and this allow us to observe another crystallographic plane (010) that is behind and now appears as a horizontal facet. A few moments later, we observe the twin boundary emerging that grew and can be clearly distinguished at 5144 s. The twining plane is identified as the $(11\bar{1})$, and the twin crystal is rotated by 176° when compared to the parent crystal.

In all the given examples, the twin boundary is originated in a small perturbation, whose nature could not be precisely determined. But a dislocation arriving perpendicularly or almost to the facet would be enough to the twin nucleation. In all the cases, the twining plane is of type {111}, which are also the densest planes in salol. In two of them, the relative rotation between the parent and the twin crystals is 180° which indicates that the twin boundary is a Σ3 twin. These twins are easily formed during growth as they correspond to a low energy cost [54, 60]. In salol the twining occurs less frequently comparing to silicon. Molecular crystals have weaker intermolecular forces than the semiconductors where there are stronger covalent bonds. Consequently, molecular crystals are more stable in non-twinned growth directions.

3.4 Conclusions

This chapter focuses on the phenomenological analysis of the faceted solid-liquid interface obtained by the directional solidification of salol and the diverse types of defects that occur during the growth. Through the experiments that revealed a rich and a complex dynamical behavior of the faceted interface, we look at how changing the experimental conditions can affect this behavior.

One of the most commonly observed defects are bubbles, a volume defect resulting from impurities inclusion. There are specific examples illustrating how the bubble shape evolves based on their initial configurations, their sites of nucleation and the orientation of facets. Moreover, we find out that the quantity of bubbles has no direct relation with the velocity, their presence is systematic.

Systematically, we observed growth striations within the crystalline structures. They can be either growth striations, or they can be an indicator of dislocations that can glide along gliding

planes. In salol, the gliding planes, which correspond to the densest planes in molecular crystals, belong to the {111} family of crystallographic planes. The analyses show that the growth striations appeared parallel (or almost) to facets indexed as {111} planes. Whereas growth striations can occur due to kinetic changes at the interface, in our experiments, we do not find any relationship between their appearance and the velocity of the facets. Hence, the observed growth striations are more likely to be traces of gliding planes due to the observed deformations instead of being growth striations.

We also witness facet splitting which is a frequent defect arising during the growth of the interface. It is associated with stress accumulation, from different sources such as interaction with the crucible walls, dislocations or bubbles surrounding the facets, leading to split and the formation of new tips.

Stress can also induce the appearance of distorted areas in the solidified material. Their occurrence is related to the crystallographic nature of the facets, but in some cases also to localized thermal stresses and perturbations of the solid-liquid interface.

Finally, twin crystals are also seen in few examples. It occurs when a perturbation hits the solid-liquid interface causing two crystals mirroring each other across a boundary. The twinning is influenced by the crystallographic nature of the facets, and it was found that the twinning plane is of {111} nature and the twin crystals are mostly Σ3 twins in our experiments.

3.5 Bibliography

[1] G. N. Wyrouboff, « Sur la forme cristalline du salol », bulmi, vol. 12, p. 443-445, 1889.

[2] H. G. Riveros, « Growth of salol crystals », J. Cryst. Growth, vol. 2, p. 173-177, 1968.

[3] G. Neuroth, and H. Klapper, « Dislocation reactions in Czochralski-grown salol crystals », Z. Für Krist, vol. 209, p. 216-220, 1994.

[4] G. Neuroth, and H. Klapper, « The Generation of Growth Dislocations by Inclusions and Growth-Face Damages: An Experimental Study », Crystal Research and Technology, vol. 55, p. 1900159, 2020.

[5] M. E. Glicksman, « Principles of Solidification », New York, Springer New York, 2011.

[6] W. Kurz, and D. J. Fisher, « Fundamentals of Solidification », Trans. Tech. Publications., 1998.

[7] K. Momma, and F. Izumi, « For three-dimensional visualization of crystal, volumetric and morphology data », Journal of Applied Crystallography, vol. 44, p. 1272-1276, 2011.

[8] VESTA, Visualization for Electronic and STructural Analysis. https://jp-minerals.org/vesta/en/).

[9] T. Kobayashi, K. Sato, M. Kobayashi, and H. Kappler, « Organic Crystals I: Characterization », Springer Berlin Heidelberg, 1991.

[10] M. Li, C. Zhang, M. Li, , F. Liu, , L. Zhou, , Z. Gao, , J. Sun, , D. Han, and J. Gong, , « Growth defects of organic crystals: A review », Chemical Engineering Journal, vol. 429, p. 132450, 2022.

[11] H. J. Scheel, and T. Fukuda, « Crystal Growth Technology », Wiley, 2003.

[12] N. Ming, and C. Ge, « Direct observation of defects in transparent crystals by optical microscopy », J. Cryst. Growth, vol. 99, p. 1309-1314, 1990.

[13] I. A. Olson, A. G. Shtukenberg, B. Kahr, and M. D. Ward, « Dislocations in molecular crystals », Rep Prog Phys, vol. 81, p. 096501, 2018.

[14] N. Dey, and J. A. Sekhar, « Interface configurations during the directional growth of salol—II. Thermal stress cracking », Acta Metallurgica et Materialia, vol. 41, p. 425-439, 1993.

[15] T. Li, L. Zhao, Z. Huang, L. Zhao, Y. Shi, S. Li, Y. Ren, G. Lv, and W. Ma, « Investigation of the Influence of Solid–Liquid Interface Shape Based on the Jordan Model on Cz-Silicon Dislocation Defects », Silicon, vol. 16, p. 1343–1356, 2024.

[16] M. Cukierman, J. W. Lane, and D. R. Uhlmann, « High-temperature flow behavior of glass-forming liquids: A free-volume interpretation », J. Chem. Phys., vol. 59, p. 3639-3644, 1973.

[17] T. Khan, « Glass: An Overview », from https://www.azom.com/article.aspx?ArticleID=1021, 2024).

[18] D. K. Shangguan, « Cellular Growth of Crystals », 1 ed., Berlin/Heidelberg: Springer-Verlag, 1991.

[19] J. Koppensteiner, W. Schranz, and M. R. Puica, « Confinement effects on glass forming liquids probed by dynamic mechanical analysis », Physical Review B, vol. 78, 2008.

[20] T. S. Piwonka, and M. C. Flemings, « Part VIII - Pore Formation in Solidification », The American Institute of Mining, Metallurgical, and Petroleum Engineers, 1967.

[21] S. Akamatsu, and G. Faivre, « Residual-Impurity Effects in Directional Solidification: Long-Lasting Recoil of the Front and Nucleation-Growth of Gas Bubbles », J. Phys. I France, vol. 6, p. 503-527, 1996.

[22] Th. Scheffen-Lauenroth, H. Klapper, and R. A. Becker, « Growth and perfection of organic crystals from undercooled melt », J. Cryst. Growth, vol. 55, p. 557-570, 1981.

[23] T. Werner, M. Becker, J. Baumann, C. Pickmann, L. Sturz, and F. Kargl, « In situ observation of the impact of hydrogen bubbles in Al–Cu melt on directional dendritic solidification », J Mater Sci, vol. 56, p. 8225-8242, 2021.

[24] K. Yoshimura, T. Inada, and S. Koyama, « Growth of Spherical and Cylindrical Oxygen Bubbles at an Ice−Water Interface », Crystal Growth & Design, vol. 8, p. 2108-2115, 2008.

[25] H. Jamgotchian, R. Trivedi, and B. Billia, « Interface Dynamics and Coupled Growth in Directional Solidification in Presence of Bubbles », J. Cryst. Growth, vol. 134, p. 181-195, 1993.

[26] Y. Teng, Y. Yang, H. Yu, L. Wang, W. Huang, and Q. Han, « Behavior of Bubbles under Directional Solidification Conditions », AFS Transactions 2012.

[27] N. Dey and J. A. Sekhar, « Interface configurations during the directional growth of Salol—I. Morphology », Acta Metallurgica et Materialia, vol. 41, p. 409-424, 1993.

[28] W. A. Tiller, K. A. Jackson, J. W. Rutter, and B. Chalmers, « The redistribution of solute atoms during the solidification of metals », Acta Metallurgica, vol. 1, p. 428-437, 1953.

[29] R. Battino, T. R. Rettich, and T. Tominaga, « The Solubility of Nitrogen and Air in Liquids », Journal of Physical and Chemical Reference Data, vol. 13, p. 563-600 , 1984.

[30] R. Trivedi, and W. Kurz, « Solidification microstructures: A conceptual approach », Acta Metallurgica et Materialia, vol. 42, p. 15-23, 1994.

[31] M. Rappaz, and Ch. A. Gandin, « Probabilistic modelling of microstructure formation in solidification processes », Acta Metallurgica et Materialia, vol. 41, p. 345-360, 1993.

[32] D. M. Anderson, G. B. McFadden, and A. A. Wheeler, « Diffuse-interface methods in fluid mechanics », Annual review of fluid mechanics, vol. 30, p.139-165, 1998.

[33] A. A. Chernov, « Stability of faceted shapes », J. Cryst. Growth, vol. 24-25, p. 11-31, 1974.

[34] L. M. Fabietti, and R. Trivedi, « Nonequilibrium effects during the ledgewise growth of a solid-liquid interface », Metall Trans A, vol. 22, p. 1249-1258, 1991.

[35] H. Klapper, « Defects in Non-Metal Crystals », in Characterization of Crystal Growth Defects by X-Ray Methods, B. K. Tanner et D. K. Bowen, Éd., Boston, MA: Springer US, p. 133-160, 1980.

[36] G. Dhanaraj, K. Byrappa, V. Prasad, and M. Dudley, « Crystal Growth Techniques and Characterization: An Overview », Springer Handbooks. Springer, Berlin, Heidelberg, p. 3-16, 2010.

[37] J. H. Bilgram, U. Dürig, M. Wächter, and P. Seiler, « Zone refining and structure determination of salol crystals », J. Cryst. Growth, vol. 57, p. 1-5, 1982.

[38] L. M. Fabietti, and R. Trivedi, « In situ observations of stress-induced defect formation at the solid—liquid interface », J. Cryst. Growth, vol. 173, p. 503-512, 1997.

[39] T. Borzsonyi, S. Akamatsu, and G. Faivre, « Weakly faceted cellular patterns versus growth-induced plastic deformation in thin-sample directional solidification of monoclinic biphenyl », Physical Review E, vol. 80, p. 1601, 2009.

[40] D. K. Shangguan, and J. D. Hunt, « Experimental and numerical study of pattern formation in faceted cellular array growth », Metall. Trans. A, vol. 23, p. 1111-1120, 1992.

[41] H. Fredriksson, and U. Akerlind, « Solidification and crystallization processing in metals and alloys », Chichester, West Sussex, 2012.

[42] K. A. Jackson, « The Surface-Roughening Transition», Kinetic Processes, p. 283-310, 2004.

[43] F. Minari, and B. Billia, « Mixed cells in directional solidification of In-doped GaAs; cellular profile and shape-induced stresses », J. Cryst. Growth, vol. 140, p. 264-276, 1994.

[44] T. Borzsonyi, and S. Akamatsu, « Surface effects in nucleation and growth of smectic B crystals in thin samples », Physical Review E, vol. 66, p.051709, 2002.

[45] D. K. Shangguan, and J. D. Hunt, « In situ observation of faceted cellular array growth », Metall. Trans. A, vol. 22, p. 941-945, 1991.

[46] B. L. Sharma, « Structural models of faceted-faceted eutectic system vanillin-acenaphthene », Materials Chemistry and Physics, vol. 78, p. 691-701, 2003.

[47] B. L. Sharma, S. Tandon, and S. Gupta, « Characteristics of the binary faceted eutectic: benzoic acid – salicylic acid system », Crystal Research and Technology, vol. 44, p. 258-268, 2009.

[48] B. Cockayne, « Developments in melt-grown oxide crystals », J. Cryst. Growth, vol. 3-4, p. 60-70, 1968.

[49] K. Fujiwara, L. C. Chuang, and K. Maeda, « Dynamics at crystal/melt interface during solidification of multicrystalline silicon », High Temperature Materials and Processes, vol. 41, p. 31-47, 2022.

[50] K. Fujiwara, R. Maeda, K. Maeda, and H. Morito, « In situ observation of twin boundary formation at grain-boundary groove during directional solidification of Si », Scripta Materialia, vol. 133, p. 65-69, 2017.

[51] D. Hull, and D. J. Bacon, « Introduction to Dislocations », 5th Edition, Oxford: Butterworth-Heinemann, 2011.

[52] L. Priester, « Les joints de grains, De la théorie à l'ingénierie », 1ère édition, 2006.

[53] F. Yang, L. C. Chuang, K. Maeda, J. Nozawa, H. Morito, K. Fujiwara, and T. Duffar, « Dislocation interaction with vicinally faceted groove at grain boundary in multi-crystalline silicon », J. Cryst. Growth, vol. 639, p. 127722, 2024.

[54] T. Riberi-Beridot, M. G. Tsoutsouva, G. Regula, G. Reinhart, F. Guittonneau, L. Barrallier, and N. Mangelinck-Noel, « Strain building and correlation with grain nucleation during silicon growth », Acta Materialia, vol. 177, p. 141-150, 2019.

[55] M. G. Tsoutsouva, T. Riberi-Beridot, G. Regula, G. Reinhart, J. Baruchel, F. Guittonneau, L. Barrallier, and N. Mangelinck-Noel, « In situ investigation of the structural defect generation and evolution during the directional solidification of < 110 > seeded growth Si », Acta Materialia, vol. 115, p.210-223, 2016.

[56] M. Trempa, C. Reimann, J. Friedrich, G. Müller, and D. Oriwol, « Mono-crystalline growth in directional solidification of silicon with different orientation and splitting of seed crystals », J. Cryst. Growth, vol. 351, p. 131-140, 2012.

[57] A. Tandjaoui, N. Mangelinck-Noel, G. Reinhart, B. Billia, T. Lafford, and J. Baruchel, « Investigation of grain boundary grooves at the solid–liquid interface during directional solidification of multi-crystalline silicon: in situ characterization by X-ray imaging », J. Cryst. Growth, vol. 377, p. 203-211, 2013.

[58] A. Tandjaoui, N. Mangelinck-Noel, G. Reinhart, B. Billia, and X. Guichard, « Twinning occurrence and grain competition in multi-crystalline silicon during solidification », Comptes Rendus Physique, vol. 14, p. 141-148, 2013.

[59] A. Lenart, Z. Samardžija, M. Godec, B. Mirtič, and S. Šturm, « Twin-boundary formation in Japan-law twinned quartz crystals », European Journal of Mineralogy, vol. 24, p. 509-517, 2012.

[60] T. Duffar, « Comprehensive review on grain and twin structures in bulk photovoltaic silicon », Recent Research Developments in crystal growth, vol. 5, p. 61-111, 2010.

CHAPTER 4: QUANTITATIVE ANALYSIS OF THE FACET GROWTH DURING THE DIRECTIONAL SOLIDIFICATION OF SALOL

This chapter presents the quantitative studies and measurements conducted to characterize the salol facets, including their interplanar angles, size, growth velocity, and undercooling.

4.1 Solid-liquid interface movement

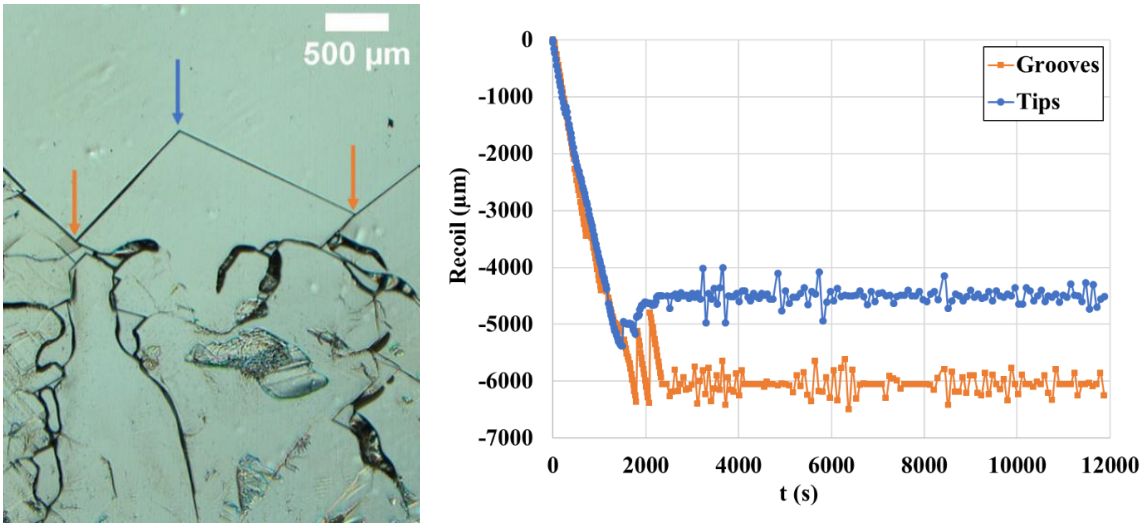
In situ and real-time observation during directional solidification enables monitoring the solid-liquid interface position over time. When a sample is pulled at a constant velocity during directional solidification, the solid-liquid interface initially undergoes recoil within the temperature frame. This motion occurs as the interface transits from rest to a steady-state position [1]. The interface position relatively to the melting temperature isotherm is linked to the undercooling at the interface. In the case of a faceted interface, kinetic undercooling is dominant and plays an important role in the morphological stability of the interface. Furthermore, the relationship between the interface growth rate and kinetic undercooling corresponds to different types of interface growth [2].

To determine the undercooling in our experiments, the interface movement is analyzed. The interface position is identified at each instant of time *t*. Given the faceted nature of the salol solid-liquid interface, we consider both the positions of the tips and the grooves between facets (identified by blue and orange arrows in Figure 4.1a, respectively). The front recoil is defined as the difference between the instantaneous position and the position at rest. However, measuring at the grooves is significantly more complex and less accurate, because, in the majority of cases, the end of the groove is not visible. For that reason, only the tip positions are considered in the following analysis.

An example of front recoil measurement is given in Figure 4.1b, with both the tips and grooves considered. The recoil curves are characterized by two stages: a transient stage, roughly occurring within the first 2200 s (11 mm), and a steady-state stage, where the interface stabilizes in the non-regulated thermal zone. Even during the transient stage, two distinct behaviors can be observed: initially, the interface moves rapidly to its lowest position, reaching around 1500 s (7.5 mm) for the tips or 1800 s (9.0 mm) for the grooves; then, over the next 840 s (11.8 mm),

the interface moves upward at a slower velocity before stabilizing. This behavior is probably due to the different contributions to the interface movement. The rapid movement is associated with the interface's transition from rest (where its velocity is zero) to a stationary state imposed by the pulling velocity, causing the interface to recoil within the thermal field.

As the recoil occurs, the growth rate increases, the facets begin to grow, and the kinetic undercooling of the interface increases concomitantly, as it depends on the interface velocity. As expected, the grooves stabilize at a lower position than the tips. Even after reaching a quasi-stable position, the interface exhibits slight fluctuations, which are mostly attributed to experimental noise. The main purpose of measuring the front recoil is to determine the total interface undercooling. Knowing the applied thermal gradient, the front recoil can be converted in undercooling with un uncertainty of ±1 K.



(a) (b)

Figure 4.1 – (a) Solid-liquid interface of salol during solidification where the arrows indicate the tips (blue) and the grooves (orange) at 3956 s. (b) Evolution of the grooves and tips recoil as function of time. (SAL_G1_4, V_p = 5 µm/s, G = 1.2 K/mm)

This recoil behavior over time is consistently observed across all our experiments. Regardless of the experimental conditions, a difference is observed between the recoil and undercooling at the tips and grooves, with the grooves exhibiting larger values. The results at steady-state are compared between experiments in Table 4.1. The increase of pulling velocity leads to a higher interface recoil and, consequently, higher undercooling, except in the experiment at 2.5 µm/s, where the recoil is higher than at higher velocities. However, this experiment must be

considered separately due to the continuous evolution of the interface during solidification, with regular grain nucleation and competition. Overall, our results confirm the trend that highlights the effect of the kinetic component on undercooling, showing an increase in undercooling with an increase in pulling velocity.

Table 4.1 – Interface recoil ($Recoil_{ss}$) and respective undercooling (ΔT_{ss}) at steady state (ss) at the tips in different experiments. sd is the standard deviation.

G (K/mm)	V_p (µm/s)	$Recoil_{ss}$ (mm)	sd	ΔT_{ss} (K)	sd
2.4	5	2.3	0.2	4.8	0.4
	10	3.5	0.1	6.9	0.2
1.1	2.5	5.3	0.1	6.2	0.1
	5	4.5	0.1	5.4	0.1
	10	5.8	0.1	6.3	0.1

Besides to determining the undercooling, the front recoil curves are also used to define the period during which quantitative measurements are made. In the following analysis, facet growth velocity, size, and interplanar angles are exclusively measured during periods in which the interface exhibits quasi-stationary behavior.

4.2 Facet size

Facet size refers to the dimensions of the flat, planar surfaces formed by the facets that define the boundaries of a crystal during its growth. These facets typically correspond to the slower-growing planes of the crystal, resulting in distinct, well-defined flat surfaces. Several factors influence the size of the facets, including the pulling velocity V_p, the thermal gradient G, the crystallographic orientation, and defect occurrence during the solidification process [3, 4].

The *in situ* experiments performed allow us to measure the facet size, which is defined as the facet length measured in the images. Some examples are shown in Figure 4.2, the facet length is highlighted by the white arrows. It can be clearly seen that the facet sizes are very heterogeneous. Very frequently, it is not possible to measure the facet size because rather its bottom is not in the field-of-view (for ex. in the right side of Figure 4.2a) or it is behind another

neighboring facet. As shown in Figure 4.2b and c, the facet extremities can also be hidden by bubbles, making the exact measurement of the facet size more difficult. When well-defined facets with clear extremities are present, such as in Figure 4.2d-e, the facet size can be accurately followed.

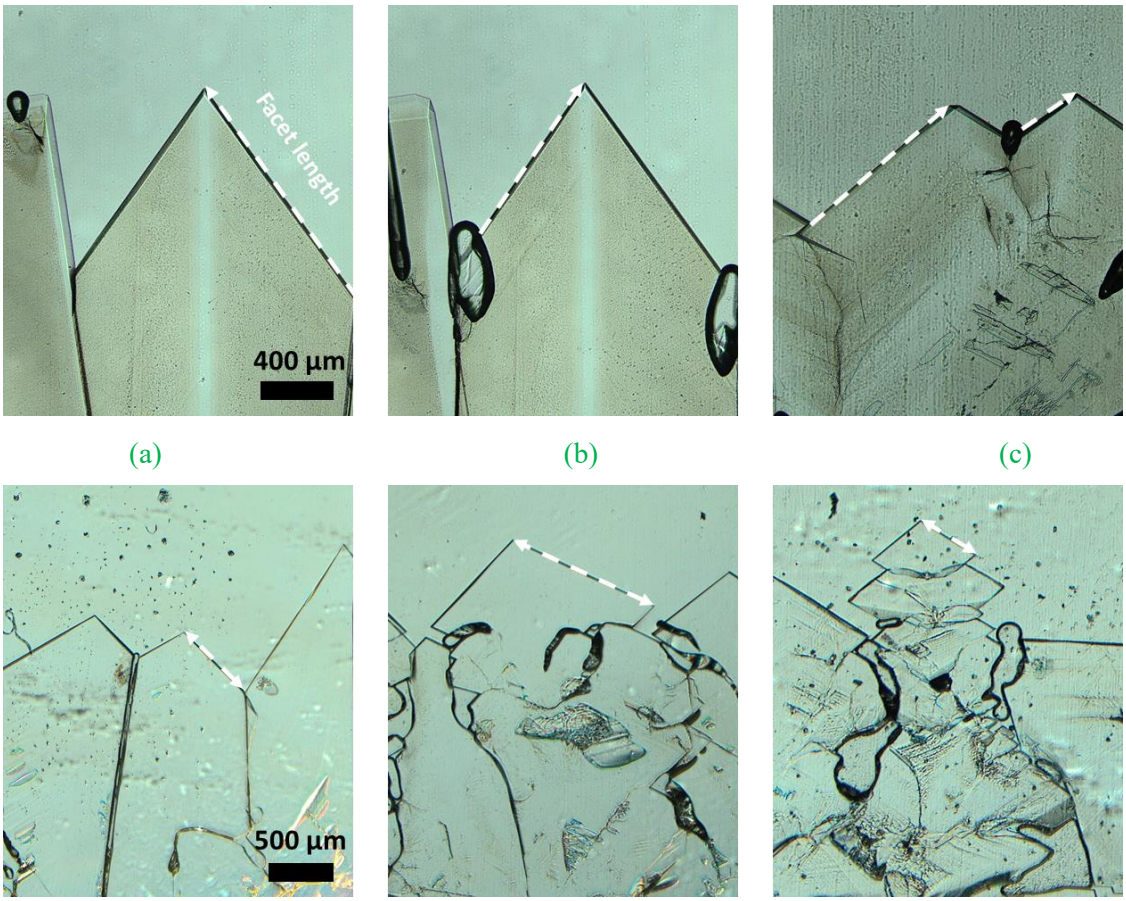
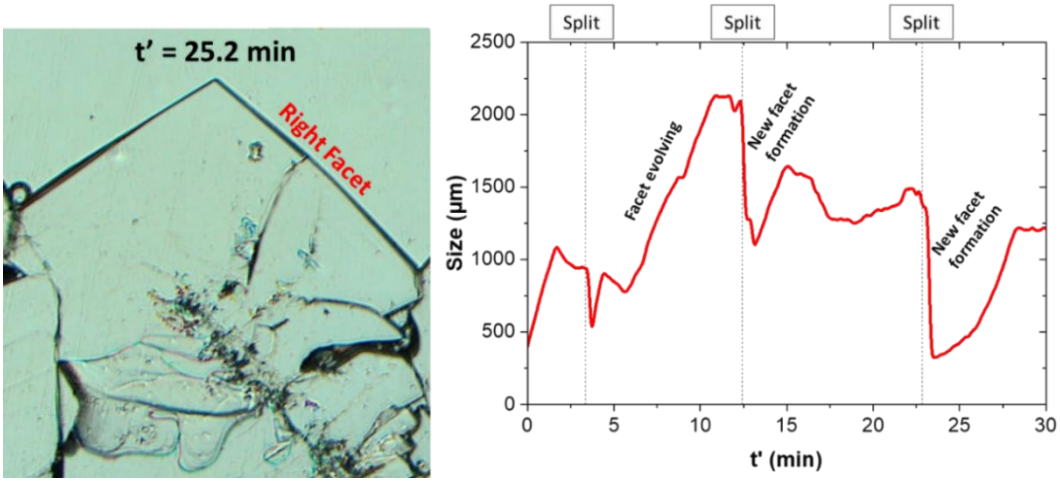


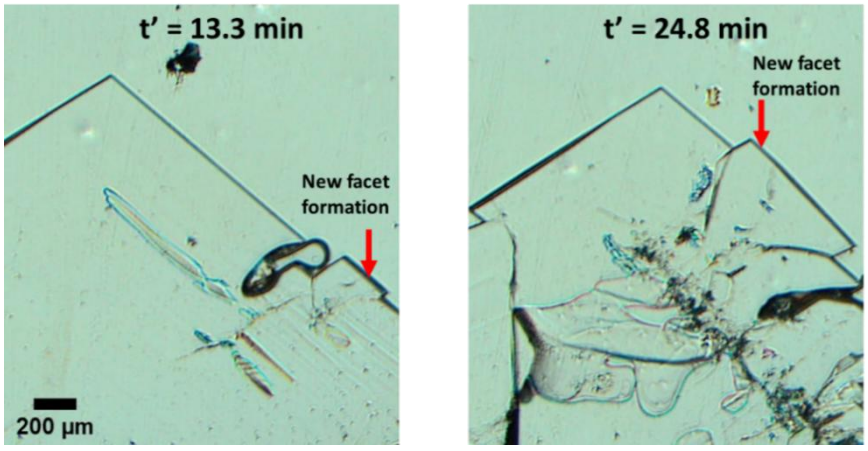
Figure 4.2 – Images evidencing the heterogeneity of facet sizes: for G = 2.4 K/mm at (a)-(b) 10 (SAL_E4_2) and (c) 5 µm/s (SAL_E3_1); for G = 1.2 K/mm at (d) 10 (SAL_G1_5), (e) 5 (SAL_G1_4), and 2.5 µm/s (SAL_G3_3).

We have measured the size of several facets during their evolution overtime. The size evolution is closely related to the presence of defects and to the dynamics of the facets. Especially when we observe a facet split, the size of the facet drastically decreases. One example is given in Figure 4.3. This facet undergoes split events at different moments (vertical dashed lines), leading to the subsequent decrease of its size. The size then increases again. Around 11 min, this facet reaches its largest size (2138 µm). At this point, it comes into contact with another

facet growing towards the left, making it unstable. In some cases, this instability can lead to the facet splitting later on, resulting in the formation of a new facet, as shown in Figure 4.3b. Another significant decrease in size is detected around 22 min, occurring due to the split at the right facet, leading also to the formation of a new facet (Figure 4.3c). As the solidification progresses, the right facet continues to grow and eventually becomes bigger. In the following examples of this chapter, *t* represents the solidification time, while *t'* denotes the time difference between the solidification time and the moment when a corresponding event begins to be followed.



(a)



(b) (c)

Figure 4.3 – (a) Temporal size evolution of the facet labeled as "Right Facet". The vertical dashed lines represent moments when split events were observed, (b) and (c) Images showing the formation of new facets after the split of the "Right Facet". (SAL_G1_4, V_p = 5 µm/s; G = 1.2 K/mm).

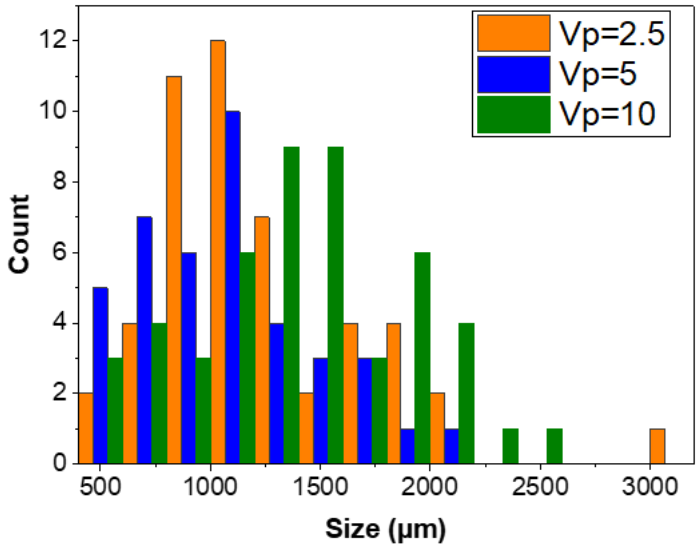


Figure 4.4 – Distribution of facets size for three different pulling velocities under the two thermal gradients (1.1 and 2.4 K/mm).

We compare the results for different pulling velocities to highlight how the facet sizes evolve. Figure 4.4 shows the average facet size as function of pulling velocities at both thermal gradients. Several significant insights can be drawn from these data. The reduction of the thermal gradient lead to an increase in facet size, as also observed in the literature [5]. These authors found that the facet size is inversely proportional to the square root of the thermal gradient. However, contrarily to what is previously observed in other works [6-8], the effect of pulling rate is not clear in our experiments. During directional solidification of salol, Dey and Sekhar [7] and Shangguan and Hunt [6] have found that when increasing the pulling velocity, the size of the facets reduces. At 5 µm/s, if we compare our results to those of Dey and Sekhar [7] (G = 5.4 K/mm), the facet sizes are in the same order of magnitude. Comparing to Shangguan and Hunt [6], with similar gradient (1.1 K/mm), the facet size decreases with the velocity consistent with their observations of distance between tips.

The quantitative differences observed can be related to the polycrystalline nature of our samples. In Figure 4.5, a great heterogeneity of facet sizes can be distinguished along the interface. This suggests that growth competition during the solidification process can promote the development of irregular facets in terms of size that do not follow the rule where typically the facet size decreases with the pulling velocity.

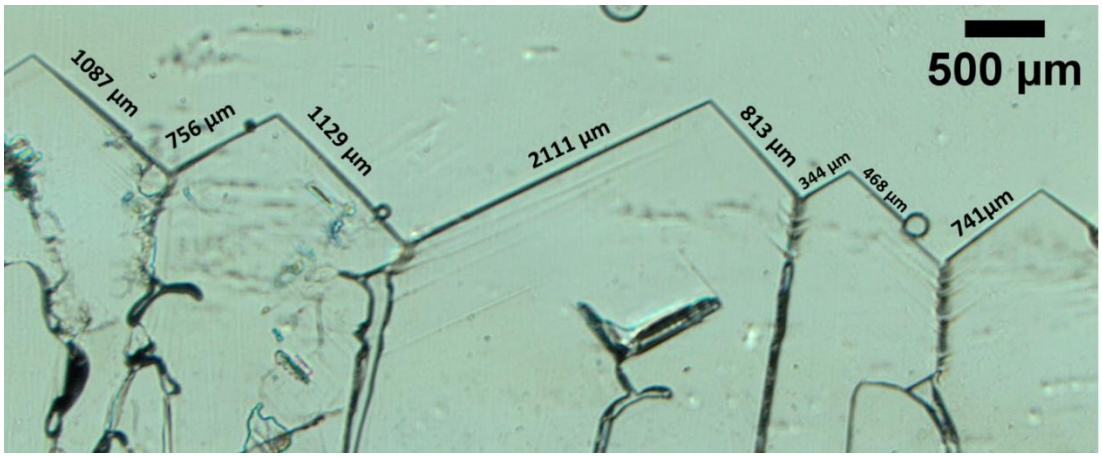


Figure 4.5 – Image of several facets with their size in µm. (SAL_G1_5, V_p = 10 µm/s; G = 1.1 K/mm)

4.3 Interplanar angle

The interplanar angle γ is the angle formed between two neighboring facets. It provides information about the orientation and relationship between facets. It is a key parameter in crystallography, enabling the crystallographic indexation of facets [9, 10]. Salol exhibits a highly faceted solid-liquid interface [7], with each facet corresponding to a crystallographic plane. To identify the crystallographic plane family to which a facet belongs, the interplanar angles between facets are measured.

First, it is useful to remember that salol has an orthorhombic structure, illustrated in Figure 4.6, with lattice parameters a = 23.40 Å, b = 11.26 Å and c = 7.96 Å [11, 12]. This orthorhombic unit cell belongs to the space group *Pcab*. The angle formed by the normal vectors to the planes is equal to the angle formed between the planes themselves. The interplanar angle γ between two planes of indices (h_1 k_1 l_1) and (h_2 k_2 l_2) in an orthorhombic system, whose unit cell dimensions are a, b and c, can be calculated using the relation:

$$\cos\gamma = \frac{\frac{h_1h_2}{a^2}+\frac{k_1k_2}{b^2}+\frac{l_1l_2}{c^2}}{\sqrt{\left(\frac{h_1^2}{a^2}+\frac{k_1^2}{b^2}+\frac{l_1^2}{c^2}\right)\left(\frac{h_2^2}{a^2}+\frac{k_2^2}{b^2}+\frac{l_2^2}{c^2}\right)}} \qquad \textit{Eq. 4. 1}$$

Considering the morphology shown in Figure 4.6 and Equation 4.1, the interplanar angles observed in salol growth are presented in Table 4.2. Our analysis is limited to planes with indices less than or equal to 2, as these are the most common and most frequently reported in the literature.

These angles are represented in the quarter-unit circle of Figure 4.7a. In some cases, the interplanar angles between different crystallographic plane families are very close to each other.

This makes it difficult to identify the crystallographic nature of the facets experimentally by measuring angles alone, as will be explained after. Since, in all the performed experiments, a large facet aligns with the container wall, and given the crystal morphology with a big pinacoid growing along {100} (Figure 4.6), we assume that the facets growing along the crucible walls in our experiments correspond to {100} planes.

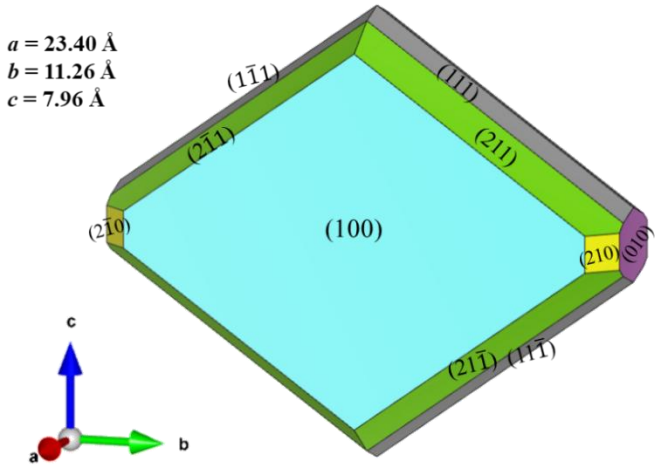
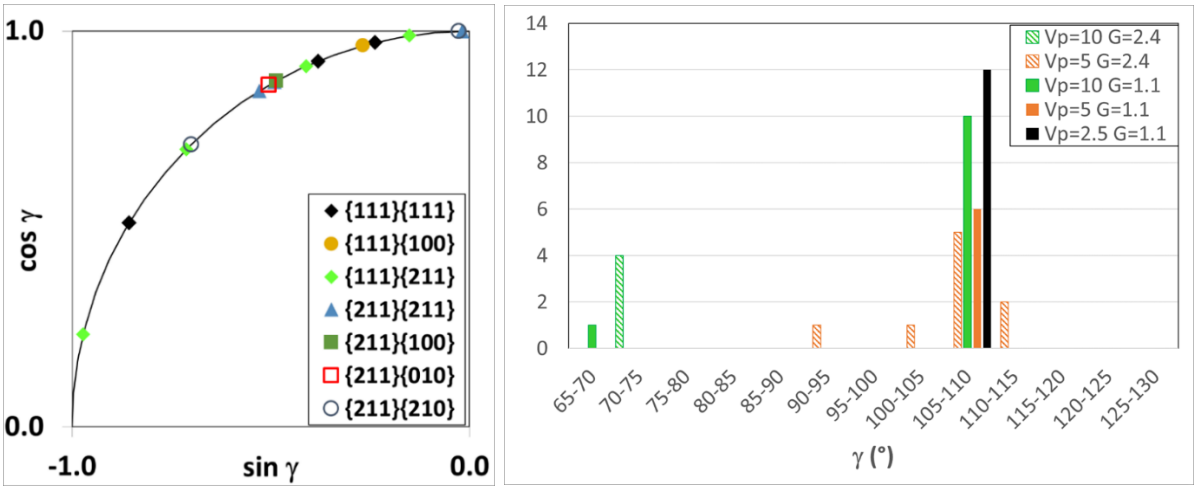


*Figure 4.6 – Illustration of the orthorhombic crystalline structure of salol with its lattice parameters realized using **V**isualization for **E**lectronic and **ST**ructural **A**nalysis (VESTA) software [13, 14].*

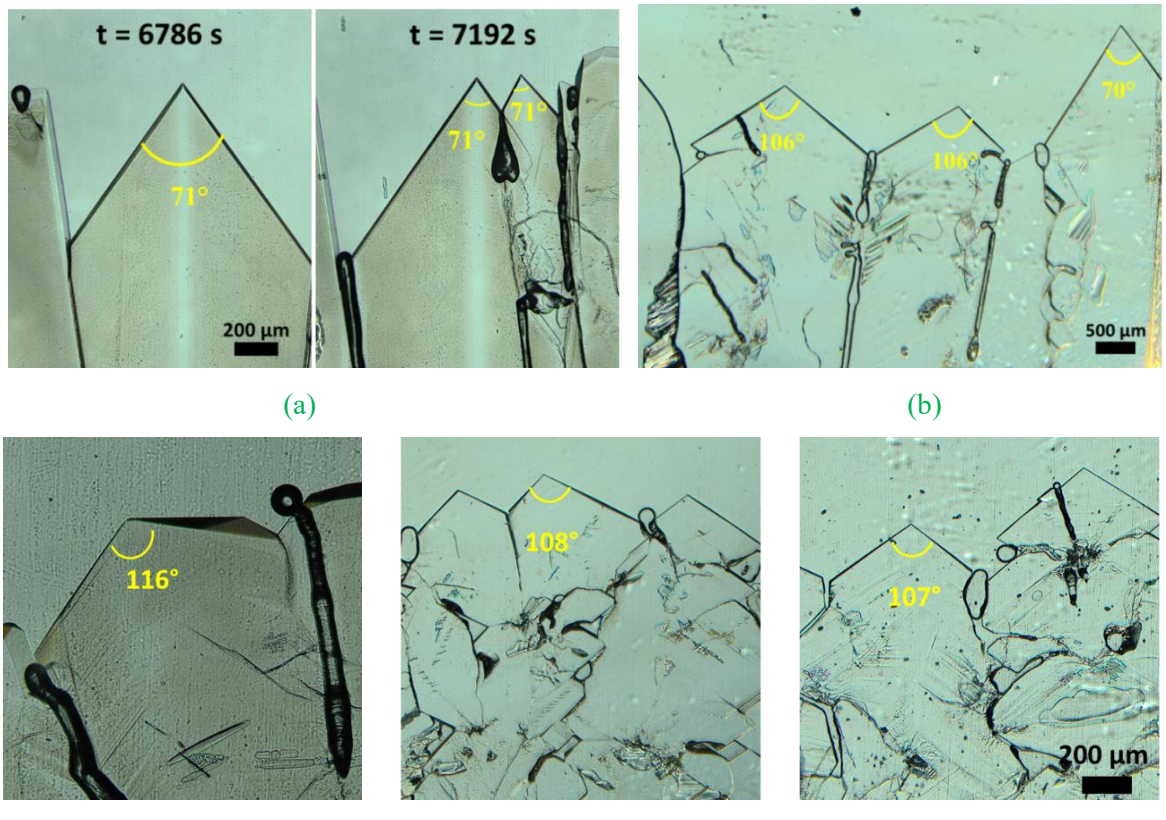
Table 4.2 – Possible theoretical interplanar angles between different family of planes in salol.

Plane 1	Plane 2	Possible angles (°)
{111}	{111}	31.0, 67.6, 76.2, 103.8, 112.4, 148.9
	{100}	74.5, 105.5
	{211}	13.5, 44.6, 65.8, 81.3, 98.7, 114.2, 135.4, 166.5
	{210}	54.1, 77.6, 102.4, 125.9
	{010}	56.2, 123.8
{211}	{100}	60.9, 119.1
	{211}	58.1, 60.6, 88.9, 91.1, 119.4, 121.9
	{210}	45.5, 88.5, 91.5, 134.5
	{010}	59.7, 120.3
{100}	{100}	0, 180
	{210}	46.1, 133.9
	{010}	90
{010}	{010}	0, 180
	{210}	43.9, 136.1
{210}	{210}	0, 87.8, 92.2, 180



(a) (b)

Figure 4.7 – (a) Theoretical interplanar angles γ between different families of crystallographic planes of salol represented in the unit circle. (b) Histogram of interplanar angles between facets measured in all the experiments performed.



(a) (b)

(c) (d) (e)

Figure 4.8 – Salol interface with some interplanar angles noted, at V_p = 10 µm/s and G (a) 2.4 (SAL_E4_2) and (b) 1.1 K/mm (SAL_G1_5); V_p = 5 µm/s and G (c) 2.0 (SAL_E3_1) and (d) 1.1 K/mm (SAL_G1_4); and (e) V_p = 2.5 µm/s and G = 1.2 K/mm (SAL_G3_3).

We systematically measured interplanar angles for different facets during solidification, with some examples shown in Figure 4.8. In Figure 4.8a, for instance, the measured angles are equal to 70.9 ± 0.8°. This experimental value is close to the theoretical angles between two {111} planes (67.6°) or between {111} and {100} planes (74.4°). However, assuming that a {100} plane is growing along the crucible wall, the remaining facets must belong to the {111}. In Figure 4.8b, different angles are observed: one measuring 69.8 ± 0.3° and another 105.7 ± 0.6°. Likewise, these values are close to the theoretical angles between {111} planes (67.6 and 103.8°).

Similar analyses are performed for all realized experiments and for different faceted tips. The results are resumed in Table 4.3, where, based on the theoretical angles of the orthorhombic structure of salol, we suggest various possible plane combinations to which the facets belong. It is interesting to notice that, similarly to previous works [7, 15], our findings confirm that the growth interface of salol is bounded by various combinations of {111} planes.

Figure 4.7b shows the results in the form of a histogram. Despite finding no effect of pulling rate on the apex angles, it is interesting to notice that facets with the lowest angles (65-75°) are only observed at the higher pulling velocity (10 μm/s), whereas at the lower pulling velocity (2.5 μm/s), the facets exhibit only angles between 105-110°. Based on the work of Dey and Sekhar [7], the interface is always bounded by {111} planes for undercooling higher than 3K. As the velocity increases, the undercooling also increases, influencing the selection of specific {111} planes. When growth conditions change, they observe a transition in the angles, minimizing them by shifting from high to smaller angles. In addition, they report an average angle of 99.5° at 5 μm/s and G = 5.4 K/mm, with a minimum angle of 70° and maximum 113°. Our results are in good agreement with their findings. Similarly, Shangguan and Hunt [6] found angles around 108° at V_p = 8.6 μm/s and G = 1.8 K/mm. These authors also have performed experiments on salol in capillary tubes, and they found that this configuration led to considerably higher angle (120°).

Table 4.3 – Interplanar angles (γ) measured between facets in different experiments, and respective hypothesis on the crystallographic nature of facets.

G **(K/mm)**	***V_p*** **(µm/s)**	**Fig.**	**γ (°)**	**sd**	**Hypotheses on crystallographic nature**
2.4	10	4.8	71.4	0.9	{111}/{111}
			71.2	0.8	
			71.0	0.5	
			71.8	0.9	
	5		114.9	0.9	{111}/{111}
			110.2	1.1	
			112.8	1.0	
			108.9	0.5	
			108.1	0.5	
		4.9a	86.7	0.9	**{211}/{211}**; {210}/{210}; {210}/{211}
			96.4	0.9	{211}/{111}
			98.7	0.7	
			103.7	0.7	{111}/{111}
			105.9	0.5	
			109.5	0.9	{111}/{111}
		4.13a	109.3	0.4	{111}/{111}
		4.8c/ 4.10b	116.2	0.4	**{111}/{111}**; {211}/{111}; {211}/{211}
			121.4	0.8	{010}/{111}; **{211}/{211}**; {211}/{010}
1.1	10		106.5	0.6	{111}/{111}
		4.9b	107.6	0.3	
			107.5	0.3	
		4.8b	105.9	1.2	
			106.2	0.5	
			105.8	0.7	
			107.3	0.3	
			105.6	0.6	
			106.4	0.5	
			105.8	0.5	
		4.8b	69.8	0.4	{111}/{111}
	5		108.1	0.9	{111}/{111}
			107.4	0.9	
			110.0	0.6	
		4.8d	107.7	1.2	
			108.7	1.2	
			109.7	1.4	
			107.2	0.6	
	2.5		105.9	0.6	{111}/{111}
			106.6	0.8	
			108.2	0.4	
		4.13b	108.7	0.6	
		4.13b	108.4	0.5	
			107.3	1.1	
			107.5	0.8	
		4.8e	106.9	0.4	
			106.9	0.7	
			108.9	1.0	
			107.3	0.9	
			105.8	0.7	

As observed in Table 4.3, some facets can correspond to various plane families, leaving us with only hypotheses and several possibilities to consider. However, we can still narrow down these options to determine the crystallographic orientation of the facets by comparing the crystallographic structure with the experimentally obtained crystal and/or by relying on the neighboring facets. Figure 4.9a illustrates this scenario with a quasi-horizontal facet. Measuring the angle between this facet and the one at its left gives 135.5 ± 0.5°, while the angle to the right is 131.8 ± 0.5°. Several possibilities exist regarding their crystallographic nature: {111}/{211}, {211}/{210} or {210}/{010}. Additionally, measuring the angle between the lateral facets (highlighted by the yellow line) gives 86.7 ± 0.9°, allowing us to eliminate one hypothesis—the lateral facets are not of type {111}. Finally, by comparing our experimental observations with the morphology of a salol crystal (Figure 4.6), we determine that the quasi-horizontal facet corresponds to a {210} plane, while the side facets correspond to {211} planes.

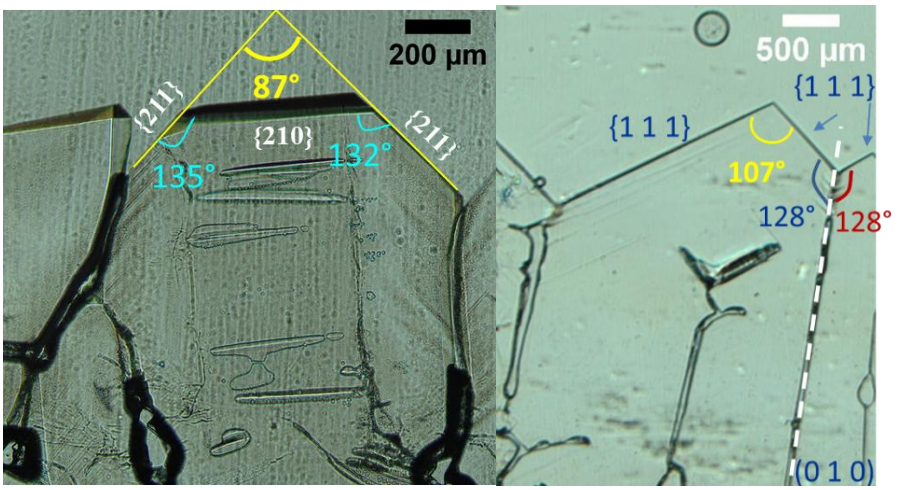


Figure 4.9 –Experimental examples of salol interface with the corresponding interplanar angles: (a) V_p = 5 µm/s, G = 2.1 K/mm (SAL_E3_1); and (b) V_p = 10 µm/s, G = 1.1 K/mm (SAL_G1_5).

The above procedure also helps confirm the hypothesis when there is no ambiguity, as in the example shown in Figure 4.9b. As evidenced in Table 4.3, the facets are already indexed as {111} planes. To check their nature, we measure the angles between these facets and the groove (highlighted by the white dashed line), obtaining 128.5 ± 0.5° (blue) and 128.1 ± 0.5° (red). These values are very close to the theoretical interplanar angle between {111} and {010}, confirming that the side facets correspond to {111} planes

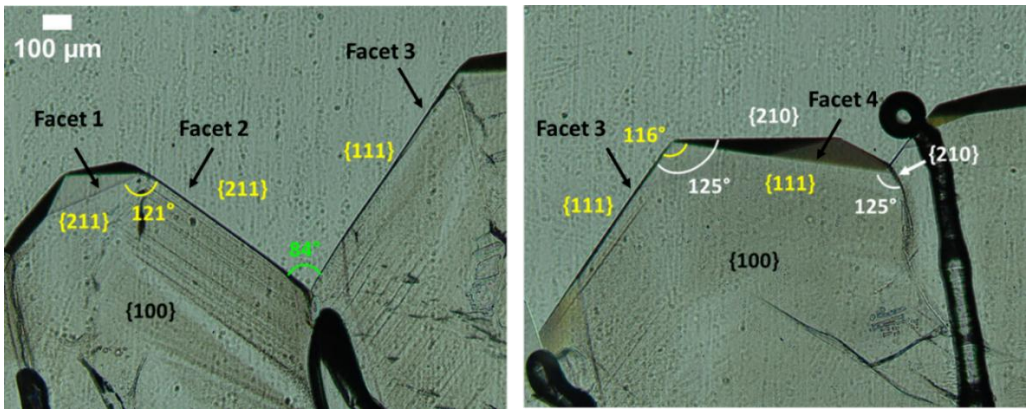


Figure 4.10 – Experimental examples of salol interface with the corresponding interplanar angles. (SAL_E3_1, V_p = 5 µm/s, G = 2.1 K/mm)

Figure 4.10 shows another two examples where multiple hypotheses regarding the combination of crystallographic planes are possible. Using the same measurement and comparison strategy, we determine that facets 1 and 2 belong to {211}, while facets 3 and 4 correspond to the {111}.

Thus, by analyzing interplanar angles between neighboring facets and comparing our crystal to the simulated orthorhombic salol crystal, we are able to identify the crystallographic families of the facets and narrow the possibilities down to a single hypothesis.

4.4 Faceted tip velocity

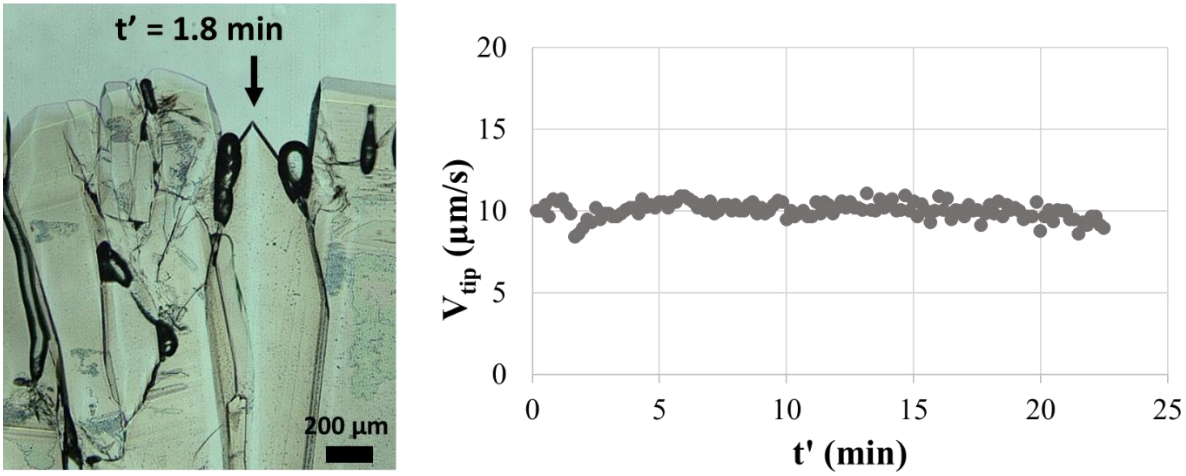
During the directional solidification, the average speed at which the solid-liquid interface advances correspond to the applied pulling velocity after a transient stage. However, the velocity of the tips and of the facets are measured locally and instantaneously, and they can be influenced by several factors. Notably, the presence of defects can significantly impact tip velocity [16].

Experimentally, tip velocity is measured by tracking the movement of the solid-liquid interface over time. By capturing images at regular intervals and analyzing the interface displacement, the velocity can be accurately determined. Understanding the velocity of a faceted tip is essential, because it reveals the dynamic behaviour of the interface and helps identify the conditions that optimize the material growth.

Morphologically, when the tips face upwards and grow in a direction close to the overall growth direction, this can be attributed to the facets competition or selection, which favors their alignment with the thermal gradient. On the other hand, defects can influence the growth

velocity, thereby affecting the tips as well. As a result, the growth velocity may no longer correspond to the pulling velocity.

An example is shown in Figure 4.11, where the facet indicated by the black arrow in (a) is tracked for several minutes. Initially, the tip velocity oscillates, decreasing by 20% due to bubbles surrounding the facets. After 2 min, the bubbles become trapped in the solid, and the tip velocity stabilizes at an average value of 10.1 ± 0.5 µm/s. In this case, the tip velocity matches the pulling velocity, and the bisector direction of the two facets aligns parallel to the thermal gradient in the upward direction.



(a) (b)

Figure 4.11 – (a) Faceted interface and (b) evolution of the black arrow tip velocity as function of time. (SAL_E4_2, V_p = 10 µm/s; G = 2.4 K/mm)

Another example is presented in Figure 4.12, where several fluctuations are observed due to defects occurring during solidification, as shown in the corresponding images. Fluctuation 1 corresponds to the appearance of a distortion at the tip, causing an increase in tip velocity to a maximum of 7.2 µm/s, which persists as the facets continue to grow. After 10 min, fluctuation 2 occurs, leading to a significant velocity increase to 9.4 µm/s —almost the double of the pulling velocity. This variation is again attributed to defects appearing on the side facet, causing several facet splits, which in turn affect tip growth. Fluctuations 3 and 4 arise due to similar factors.

In both examples, despite the defects causing variations in tip velocity, the overall mean velocities remain close to the corresponding pulling velocity, as expected during stationary growth.

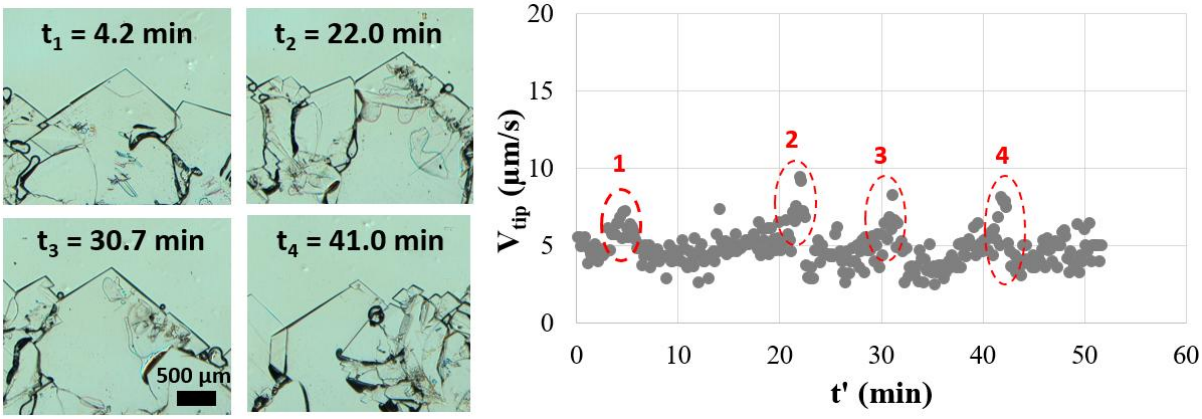


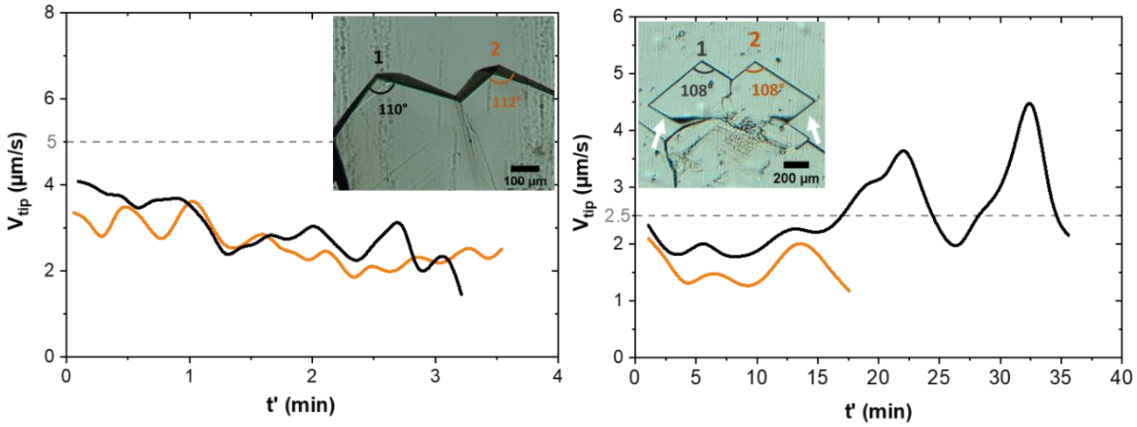
Figure 4.12 – Series of images showing several defects that appeared on the tip and evolution of the tip velocity as function of time. (SAL_G1_4, V_p = 5 µm/s; G = 1.2 K/mm)

On the other hand, numerous cases are observed where the tip velocity does not match the pulling velocity, highlighting the complexity of facet growth. Figure 4.13 shows examples of this behavior, with corresponding interface images shown in the insets of the plots. Notably, the tip velocities are lower than the pulling velocity (represented by dashed lines in the plots). In Figure 4.13a, the tips are affected by a neighboring crystal to the left of Tip 1, which has a lower undercooling and grows towards the right at a higher velocity. This competition causes the withdrawal of the affected tips, leading to a progressive decrease in their velocity over time. In Figure 4.13b, both tips originate from a tip splitting event, with the sequence shown in Figure 4.14. Tip 2 is eventually overgrown by Tip 1 after around 15 min of growth. From that point, its velocity quickly increases to align with the interface. Additionally, the formation of new facets belonging to {111} planes, oriented downward (as shown by the white arrow in the inset), coupled with the ongoing growth of Tip 1 and 2 are growing, results in intermittent slowdowns of the tip velocity.

In both Figure 4.12 and Figure 4.13, the tips are defined by the contact of {111} planes. So, the mismatch between the tip velocity and pulling velocity is not related to crystallographic effects but instead clearly associated to growth competition processes.

These findings highlight the complexity of interface growth dynamics. Even when the facets defining the tips belong to the same crystallographic family, their growth behavior can vary due to several factors occurring during the solidification process. These include competitive growth between neighboring facets, interaction with growth defects, thermal and kinetic constraints, or interfacial instabilities. An example is shown in Figure 4.15, where the facet highlighted by the

white arrow undergoes two splitting events within a span of 2 minutes. A noticeable color change indicates facet instability during its growth, most probably due to defects, as evidenced by the contrast at the splitting location.



(a) (b)

Figure 4.13 – Evolution of the tip velocities over time, at: (a) V_p = 5 µm/s, G = 2.1 K/mm (SAL_E3_1); (b) V_p = 2.5 µm/s, G = 1.2 K/mm (SAL_G3_3).

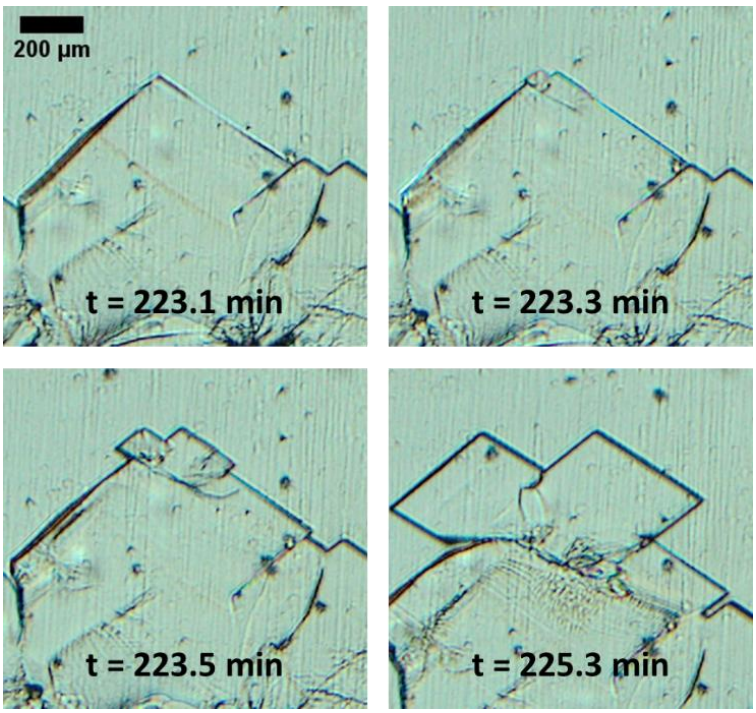


Figure 4.14 – Sequence of images showing the morphological evolution of two faceted tips originated from a splitting event. (SAL_G3_3, V_p = 2.5 µm/s; G = 1.2 K/mm)

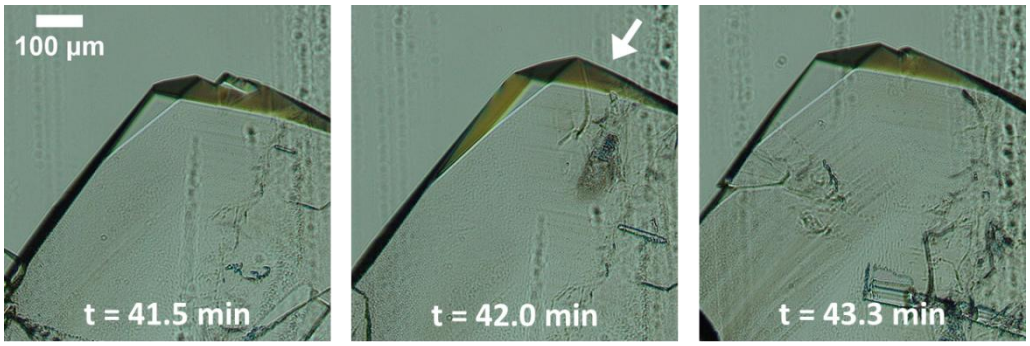


Figure 4.15 – Sequence of images showing the morphological changes of the facet highlighted with the white arrow overtime. (SAL_E3_1, V_p = 5 µm/s; G = 2.1 K/mm)

4.5 Facet velocity

Even more important than the tip velocity is the growth velocity in the direction normal to the facets, referred to as the facet velocity V_f in the following [17]. The facet velocity, along with its slope θ_f (orientation with respect to the pulling direction), provides valuable quantitative data for understanding facet behavior. Under stationary conditions, the facet velocity can be interpreted as the projection of the pulling velocity, depending on the angle between the facet's growth direction and the imposed solidification direction, which is governed by the thermal gradient and pulling velocity V_p, as illustrated in Figure 4.16.

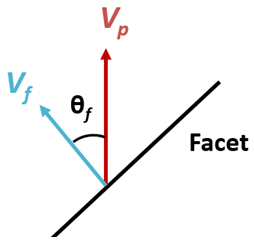
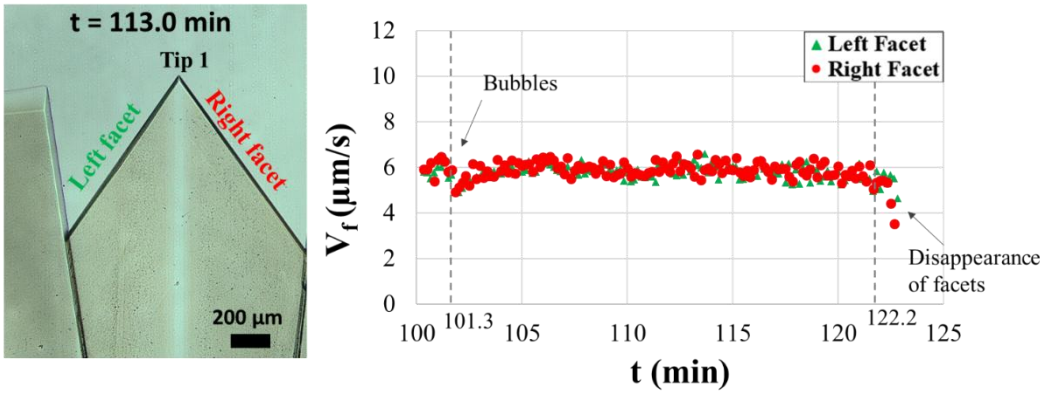


Figure 4.16 – Illustration of the facet velocity V_f along with its slope θ_f , and the pulling velocity V_p.

To illustrate, we consider the facets shown in Figure 4.17a that exhibit well-defined, flat surfaces that intersect at specific angles. Their velocity variations over time are analyzed and depicted in Figure 4.17b. Both facet velocities are nearly equal, averaging of 5.8 ± 0.3 for the left (green triangles) and 5.9 ± 0.4 µm/s for the right (red circles) facets, with minor fluctuations indicating a stable growth rate under the given experimental conditions. The theoretical velocity of the left facet, calculated as the projection of the pulling velocity at an angle θ_f = 55.2 ± 0.5°, is 5.7 ± 0.1 µm/s. Similarly, for the right facet, with θ_f = 54.1 ± 0.8°, the theoretical velocity is 5.8 ± 0.2 µm/s for. At around 101.3 min into the experiment, a decrease in velocity is observed

for both facets, suggesting an external influence. This can be attributed to the presence of bubbles at the grooves between these facets and their closest neighbors (Figure 4.11a), which hinder their movement and prevent them from maintaining the nominal velocities imposed by the growth parameters. More generally, changes in facet velocity are regularly observed when a bubble comes into contact with a facet. These changes can be either significant or minor, with the velocity typically returning to its normal rate once the bubble becomes trapped in the solid phase. In this example, a velocity change is observed on both the left and right facets from the moment the bubbles appear until they are fully trapped in the solid. On the left facet, the velocity decreases from 6.4 to 4.9 µm/s, while on the right facet, it drops from 6.3 to 5.1 µm/s. Another decrease in the velocity occurs at around 122.2 min, coinciding with an event depicted in Figure 4.18. This figure illustrates the gradual disappearance of the facets as they become overgrown by another tip, indicated by the yellow arrow in Figure 4.18.

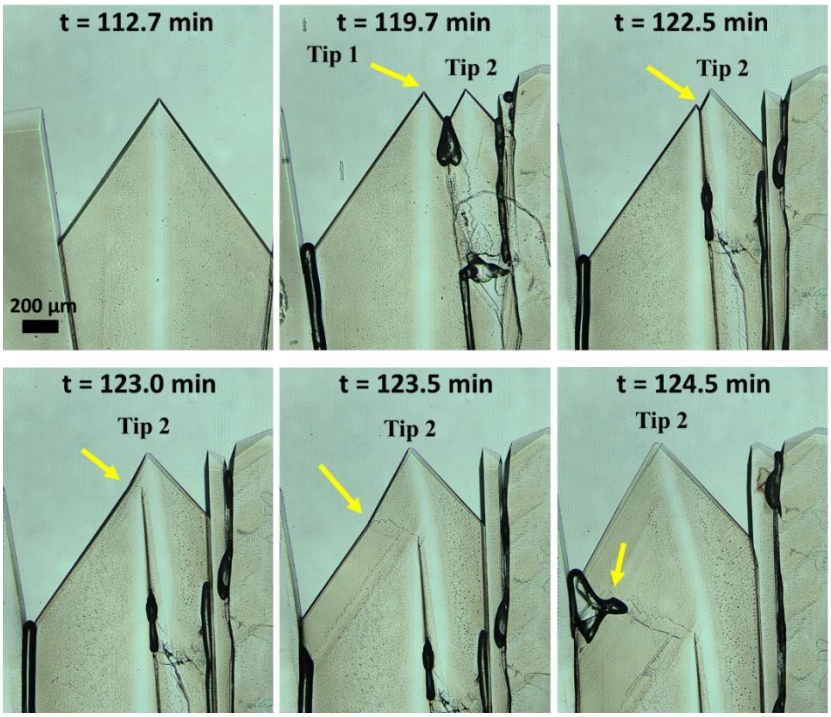


(a) (b)

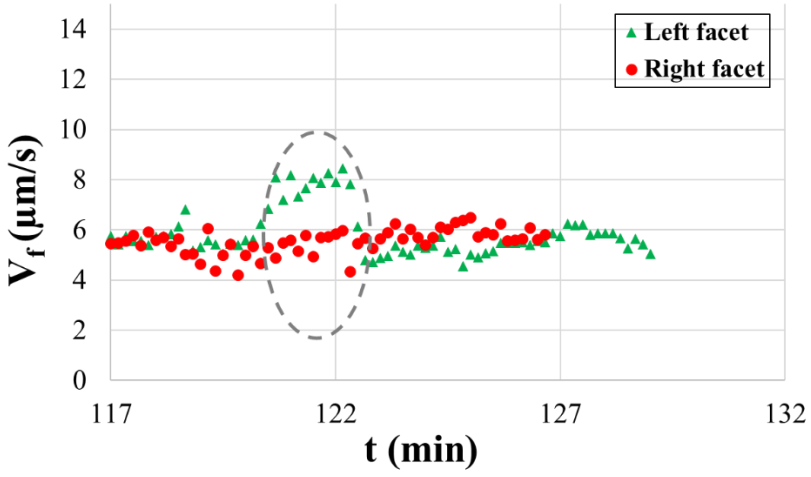
Figure 4.17 – (a) Image of the faceted interface of salol; (b) Time-resolved evolution of the facet velocities identified by Left and Right in (a). (SAL_E4_2, V_p = 10 µm/s; G = 2.4K/mm)

To further investigate the disappearance of both facets of Tip 1, as shown in Figure 4.17, we measure the velocities of another facet associated with Tip 2 (Figure 4.18), which ultimately outcompeted Tip 1, resulting in its disappearance within 2 min. At the beginning, both facets of Tip 2 exhibit velocities of 5.7 ± 0.7 and 5.9 ± 0.8 µm/s, respectively for the left and the right facets. However, as the left facet of Tip 2 begins to outcompete the right facet of Tip 1, a significant increase in velocity is observed, reaching a mean velocity of 7.6 ± 0.7 µm/s. Following this competitive interaction, the left facet velocity returns to its normal value as both

Tip 2 facets continue their growth over time. This observation highlights how the dominance of a grain can influence the overall growth dynamics of neighboring facets.



(a)



(b)

Figure 4.18 – (a) Images showing the gradual disappearance of a facet from Tip 1. (b) Evolution of the facet velocities as a function of time for Tip 2. (SAL_E4_2, V_p = 10 µm/s; G = 2.4 K/mm)

Figure 4.19 presents another typical example, where the “Left facet” evolves with a mean velocity of 7.7 ± 0.5 µm/s. The images correspond to the period between the events marked "First incident” and “Second incident” in Figure 4.19b. The “first incident” is an unusual and rarely observed phenomenon. A third solid phase emerges between the two facets, initially appearing rough. This phase likely originates either from the interface being in contact with the sample wall or from crystal nucleation within the groove, either in front of or behind it. This newly formed solid remains for a period, growing rapidly before eventually disappearing, allowing the original two facets to resume their growth as the solidification progresses. This leads to a subsequent rapid growth of both facets. The rough aspect of this transient solid may be attributed to rapid nucleation followed by faceted growth. The second incident is more frequently observed and is associated with the appearance of bubbles and facet splitting.

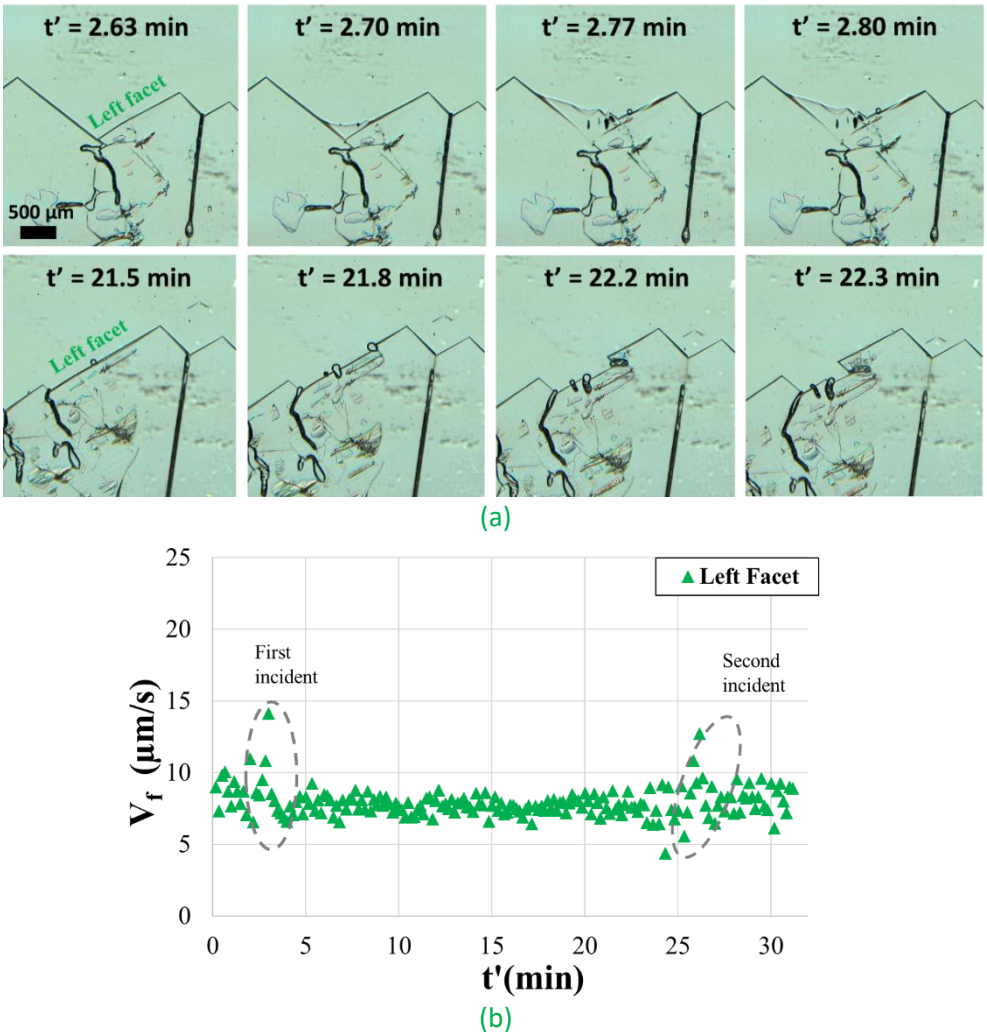
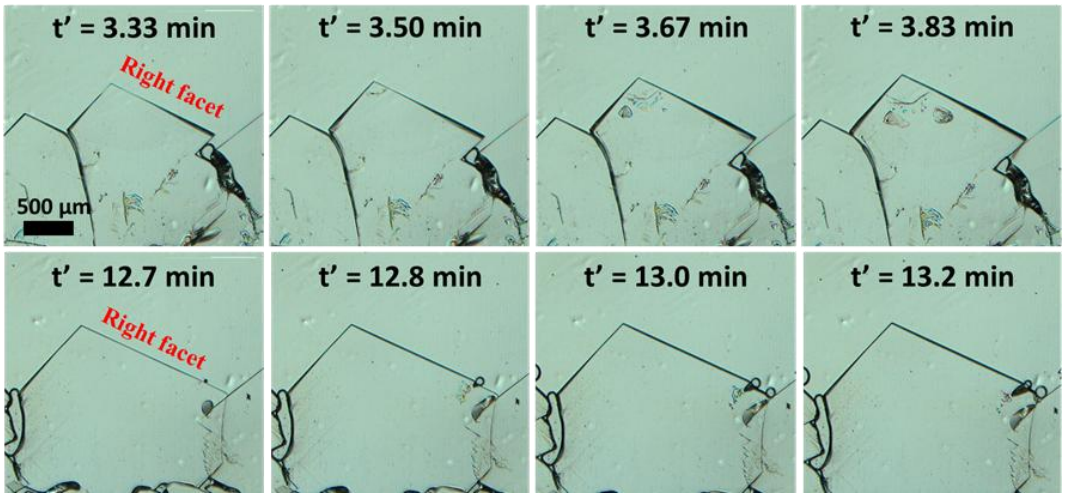
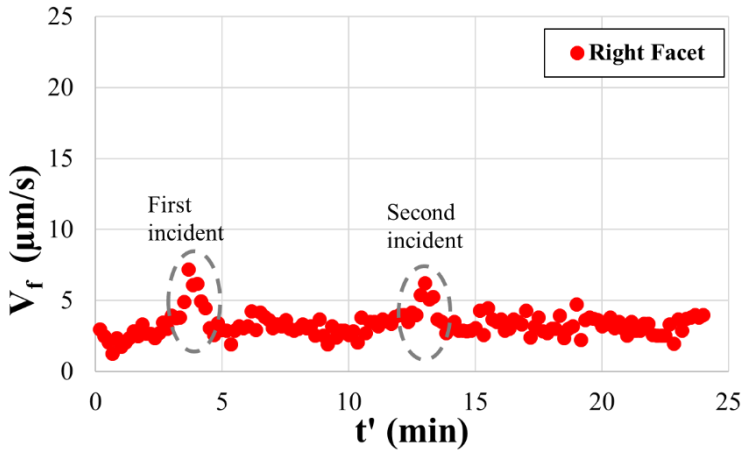


Figure 4.19 – (a) Sequence of images showing the morphological evolution of the facet labeled as “Left facet”; (b) Velocity evolution as a function of time. (SAL_G1_5, V_p = 10 µm/s; G = 1.1K/mm)

The growth velocity of the "Right facet" in Figure 4.20 is measured over time, with a mean value of 3.2 ± 0.5 µm/s. A first incident causes an increase in the facet velocity, reaching a maximum of 7.2 µm/s. This acceleration occurs after the development of a crystal distortion within the facet. The presence of this distortion alters the growth dynamics, temporarily increasing the velocity. However, once the distortion is left behind, the velocity returns to its normal value, and the facet resumes stable growth. A second acceleration in velocity further highlights the effect of a bubble on facet growth, reinforcing the influence of defects and external factors on solidification dynamics.



(a)



(b)

Figure 4.20 – (a) Sequence of images showing the growth of the "Right facet"; (b) Evolution of the facet velocity as a function of time. (SAL_G1_4, V_p = 5 µm/s, G = 1.2 K/mm)

When two grains face each other with two facets, the grain boundary (GB) orientation corresponds to the bisector of the two facets, provided they grow at the same velocity [18]. Based on this principle, we measure the GB orientation φ, which represents the angle between the actual boundary of the facets and their bisector, across multiple experiments. Figure 4.21a presents a typical example, with the corresponding schematic shown in Figure 4.21b. Duffar and Nadri [18] proposed an relation (Eq. 4.2) to estimate the facet velocity $V_{f,\ theo}$, incorporating the pulling velocity V_p, the grain boundary orientation (φ), and the angle between the facets (θ_r). To confirm its validity to our measurements, we determine φ and θ_r across a series of examples. Table 4.4 resumes all of the experimental and theoretical findings for the selected facets, corresponding to {111} planes of that we have studied. The estimated steady-state facet velocity, calculated as the projection of the pulling rate, $V_{f,ss}=Vp.\cos(\boldsymbol{\theta_f})$, is also give for comparison. These data will be used in the following analysis to demonstrate the boundary aligning with the facets' bisector.

$$Vf, \text{theo} = \frac{V_p \sin(\theta_r/2)}{\cos\varphi} \qquad \textit{Eq. 4.2}$$

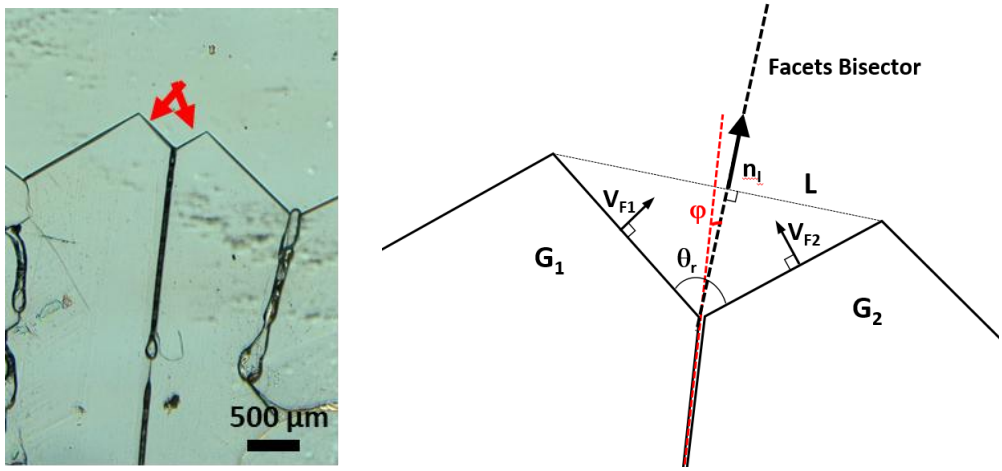


Figure 4.21 – (a) Snapshot of the solid-liquid interface (SAL_G1_5, V_p = 10 µm/s, G = 1.1 K/mm). (b) Growth configuration of the faceted-triple phase line, where n_l follows the bisector.

Table 4.4 – Facet growth velocity (experimentally measured $V_{f\,exp}$, theoretical $V_{f\,ss}$, and defined by Eq. 4.2 $V_{f,theo}$), groove undercooling (ΔT_{groove}), the angle between the facets (θ_r) and the grain boundary orientation (φ), and angle with respect to the pulling direction (θ_f).

Experimental conditions	**#**	**$V_{f\,exp}$ (µm/s)**	**θ_f (°)**	**$V_{f\,ss}$ (µm/s)**	**θ_r (°)**	**ΔT_{groove} (K)**	**φ (°)**	**$V_{f\,theo}$ (µm/s)**
G =1.1 K/mm V_p =10 µm/s **Groove**	1	7.9 ± 1.6	44.9 ± 0.7	7.1 ± 0.1	106.4 ± 0.4	6.4 ± 0.0	0.9 ± 1	8.0
	2	8.0 ± 2.0	29.5 ± 0.7	8.7 ± 0.1				
G =1.1 K/mm V_p =10 µm/s **Groove**	3	8.3 ± 1.4	38.4 ± 0.7	7.8 ± 0.1	102.6 ± 0.2	6.9 ± 0.6	0.5 ± 0.5	7.8
	4	8.5 ± 1.4	37.6 ± 0.8	7.9 ± 0.1				
G =2.4 K/mm V_p =10 µm/s **Groove**	5	5.1 ± 0.8	50.8 ± 0.4	6.3 ± 0.0	67.7 ± 0.9	7.8 ± 0.5	0.5 ± 0.6	5.6
	6	5.1 ± 0.8	63.2 ± 0.7	4.5 ± 0.1				
G =1.1 K/mm V_p =10 µm/s **Groove**	7	6.1 ± 1.9	47.9 ± 0.6	6.7 ± 0.1	102.4 ± 0.3	6.7 ± 0.1	0.4 ± 0.7	7.8
	8	6.0 ± 1.7	32.2 ± 2	8.5 ± 0.2				
G =1.1 K/mm V_p =5 µm/s **Groove**	9	1.4 ± 1.9	25.9 ± 0.9	4.5 ± 0.0	108.8 ± 0.6	4.6 ± 0.1	0.5 ± 0.7	4.1
	10	1.4 ± 2.0	45.7 ± 1.2	3.5 ± 0.1				
G =1.1 K/mm V_p =5 µm/s **Grain boundary**	11	3.4 ± 1.8	25.4± 0.5	4.5 ± 0.0	101.4 ± 0.6	6.7 ± 0.1	11.5 ± 1.5	4.0
	12	4.1 ± 1.8	54.0 ± 0.3	2.9 ± 0.0				
G =1.1 K/mm V_p =10 µm/s **Grain boundary**	13	7.6 ± 0.8	49.0 ± 0.4	6.6 ± 0.1	93.7 ± 0.2	6.9 ± 0.0	1.8 ± 0.1	7.3
	14	8.2 ± 0.6	37.6 ± 1.1	7.9 ± 0.1				

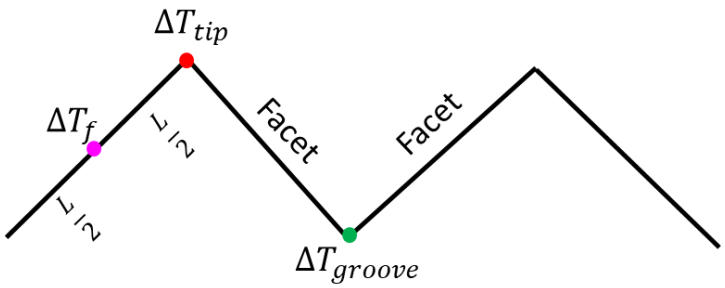


Figure 4.22 – Schematic illustrating different undercoolings regions in a crystal.

Figure 4.22 represents a schematic focusing on undercooling at different locations of a facet. The red dot indicates the undercooling at the tip, the pink dot marks the undercooling at the center of the facet, and the green dot represents the undercooling at the groove between two facets.

Facet 1 and 2 (Figure 4.21a) exhibit growth velocities measured with uncertainty, equal to 7.9 ± 1.6 µm/s and 8.0 ± 2 µm/s, respectively. These values match their theoretical facet velocity ($V_{f\ theo}$) calculated using $V_f = V_p \cos(\theta_f)$. Their boundary forms an angle φ of 0.9° with the bisector. Given the uncertainty of the experimental measurements (± 1°), this indicates that the boundary aligns with their bisector. Similar cases are observed for Facet 3 and 4, as well as Facet 5 and 6 (Figure 4.23a and b). This represents an ideal case where the boundary between two facets follows their bisector. These facets correspond to the {111} planes, where φ is expected to tend toward zero, indicating that both facets grow at the same rate. Figure 4.23c presents Facets 7 and 8, which grow at the same velocity (Table 4.4). However, facet 8 has a velocity of 6.5 ± 1.7 µm/s, deviating from the theoretical velocity of 8.5 ± 0.2 µm/s. This discrepancy arises due to growth competition. Facet 8 is constrained and is progressively eliminated by facet 7, even though φ remains close to zero. A similar case is shown in Figure 4.23d, where facets 9 and 10 grow at equal velocities. Yet, both facets show a significant difference between their measured and theoretical velocities, while φ remains small. This deviation is attributed to the fact that the interface has not yet reached its stationary phase.

The example in Figure 4.23e shows facets 11 and 12, which grow at different velocities, and exhibit different θ_f values. Additionally, φ is 11.5°, indicating a clear deviation from bisector alignment. Finally, the example in Figure 4.23f shows facets 13 and 14, growing at same velocities exhibiting different θ_f values. Yet, their φ is 1.8°, indicating a that the boundary between these two facets align with their bisector.

The facet boundaries primarily align with their bisectors, as demonstrated by multiple examples. In ideal cases, the facet velocity matches its theoretical value, supporting the validity of bisector alignment. However, in some cases, we observe variations from the theoretical facet velocity. Despite these variations, the boundary remains following the bisector.

Finally, as shown in Table 4.4, the values obtained from Duffar and Nadri's equation (Eq. 4.2) align remarkably well with our experimental measurements. Even when φ does not tend to zero, the calculated facet velocity V_f closely matches the experimental values. This agreement validates the applicability of this theoretical model and its reliability in predicting facet

velocities under various conditions. Table 4.5 gathers the measurements of facet velocities and orientation, with their respective undercooling, where all the facets correspond to {111} crystallographic planes.

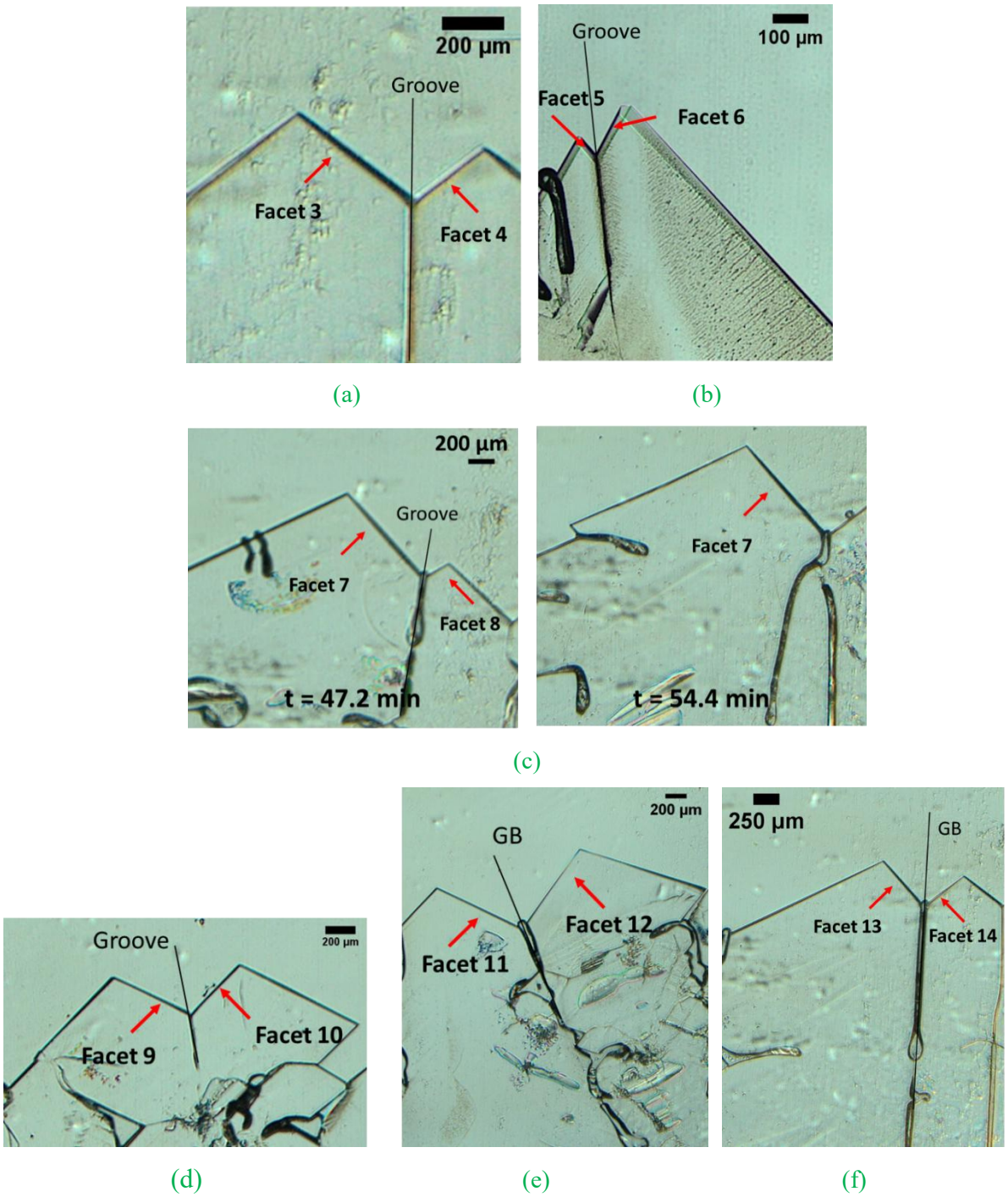


Figure 4.23 – Images showing the gain boundary (GB) and grooves between two facets at: (a), (c), (f) V_p = 10 µm/s, G =1.1 K/mm (SAL_G1_5); (b) V_p = 10µm/s, G =2.4 K/mm (SAL_E4_2); and (d), (e) V_p = 5 µm/s, G =1.2 K/mm (SAL_G1_4).

Table 4.5 – Tip and facet undercooling (ΔT_{tip}, ΔT_f), facet growth velocity (V_f) and orientation with respect to the pulling direction (θ_f). All the values are given with the respective standard deviation.

G (K/mm)	V_p (μm/s)	ΔT_{tip} (K)	Left			Right		
			V_f (μm/s)	θ_f (°)	ΔT_f (K)	V_f (μm/s)	θ_f (°)	ΔT_f (K)
2.4	10	7.1 ± 0.1	5.8 ± 0.3	55.2 ± 0.5	7.8 ± 0.2	5.9 ± 0.4	54.1 ± 0.8	7.7 ± 0.3
		7.1 ± 0.1	5.7 ± 0.7	62.6 ± 1.1	7.3 ± 0.2	5.9 ± 0.8	47.4 ± 0.6	7.5 ± 0.6
		7.1 ± 0.0	5.7 ± 0.7	60.5 ± 0.8	7.4 ± 0.2	5.2 ± 0.2	50.5 ± 0.9	7.2 ± 0.1
		7.0 ± 0.2	6.3 ± 0.7	59.8 ± 0.9	7.1 ± 0.2	5.9 ± 0.9	48.7 ± 0.9	7.2 ± 0.2
	5	4.2 ± 0.1	5.5 ± 0.9	54.0 ± 2.0	4.3 ± 0.1	3.9 ± 0.9	13.5 ± 0.9	4.3 ± 0.1
		4.4 ± 0.3	1.3 ± 0.6	52.9 ± 0.9	4.5 ± 0.2	2.5 ± 0.7	24.1 ± 0.7	4.5 ± 0.3
		4.3 ± 0.3	1.8 ± 0.8	42.7 ± 0.9	4.8 ± 0.3	2.0 ± 1.0	25.2 ± 1.5	4.4 ± 0.3
		4.7 ± 0.3	2.9 ± 0.7	40.4 ± 0.3	5.1 ± 0.2	2.6 ± 0.8	31.7 ± 0.8	5.0 ± 0.4
		4.6 ± 0.2	2.3 ± 0.5	36.6 ± 0.2	4.8 ± 0.2	2.4 ± 1.0	35.3 ± 0.8	4.7 ± 0.2
		5.1 ± 0.1	2.4 ± 0.3	40.4 ± 0.9	5.3 ± 0.1	3.6 ± 0.9	31.2 ± 0.5	5.2 ± 0.1
		4.5 ± 0.0	4.1 ± 0.9	49.7 ± 3.5	4.9 ± 0.1	3.5 ± 0.8	35.4 ± 3.7	4.8 ± 0.1
		4.6 ± 0.9	4.2 ± 0.9	46.2 ± 1.9	5.2 ± 0.1	3.1 ± 0.9	40.6 ± 0.7	4.9 ± 0.1
		4.3 ± 0.1	5.8 ± 0.6	48.1 ± 1.0	4.6 ± 0.1	-	-	-
		4.0 ± 0.2	2.6 ± 0.9	40.2 ± 0.5	4.4 ± 0.3	6.3 ± 0.9	34.5 ± 0.8	4.2 ± 0.1
1.1	10	5.9 ± 0.4	8.1 ± 0.8	29.5 ± 0.7	6.4 ± 0.1	8.0 ± 0.9	44.7 ± 1.1	6.4 ± 0.1
		6.0 ± 0.6	7.4 ± 0.7	25.2 ± 0.9	6.7 ± 0.5	7.5 ± 0.8	48.2 ± 0.8	6.3 ± 0.5
		6.2 ± 0.6	6.8 ± 0.9	31.8 ± 1.6	6.3 ± 0.5	6.5 ± 0.8	43.6 ± 0.9	6.8 ± 0.2
		6.4 ± 0.1	8.3 ± 0.7	30.6 ± 1.2	6.5 ± 0.1	8.5 ± 0.9	44.5 ± 0.4	6.8 ± 0.1
		6.6 ± 0.1	8.0 ± 0.9	37.2 ± 0.9	6.8 ± 0.1	7.9 ± 0.7	38.1 ± 1.5	6.7 ± 0.1
		6.7 ± 0.1	8.1 ± 0.6	38.3 ± 1.4	6.8 ± 0.1	7.9 ± 0.4	37.6 ± 1.4	6.8 ± 0.1
		5.9 ± 0.2	7.4 ± 0.8	35.6 ± 1.1	6.0 ± 0.2	7.5 ± 0.8	37.9 ± 1.5	6.4 ± 0.3
		6.4 ± 0.2	7.9 ± 0.9	29.9 ± 0.9	6.6 ± 0.3	7.8 ± 0.6	44.9 ± 0.6	6.4 ± 0.2
		6.4 ± 0.4	7.8 ± 0.7	29.6 ± 0.8	6.5 ± 0.2	7.9 ± 0.7	44.7 ± 0.6	6.8 ± 0.1
		6.4 ± 0.4	7.9 ± 0.8	34.5 ± 1.1	6.8± 0.4	8.2 ± 0.6	40.3 ± 0.7	6.7 ± 0.3
		5.5 ± 0.7	6.2 ± 0.7	57.3 ± 0.5	6.1 ± 0.7	6.0 ± 0.5	53.1 ± 0.7	5.5 ± 0.1
	5	5.6 ± 0.5	3.3 ± 0.8	46.8 ± 0.6	5.9 ± 0.5	3.3 ± 0.9	25.6 ± 0.6	5.9 ± 0.4
		5.7 ± 0.5	2.0 ± 0.8	47.1 ± 1.2	5.9 ± 0.4	2.2 ± 0.5	26.5 ± 1.6	5.8 ± 0.4
		5.6 ± 0.3	3.0 ± 0.8	37.6 ± 0.8	5.7 ± 0.3	3.1 ± 0.7	35.2 ± 1.4	5.8 ± 0.2
		5.3 ± 0.5	2.9 ± 0.5	31.7 ± 0.8	5.5 ± 0.5	3.3 ± 0.7	42.1 ± 1.6	5.7 ± 0.4
		5.1 ± 0.5	3.2 ± 1.0	30.1 ± 1.9	5.2 ± 0.4	2.7 ± 0.8	44.1 ± 1.2	5.3 ± 0.5
		5.9 ± 0.1	4.0 ± 0.5	54.1 ± 0.8	6.1 ± 0.2	3.8 ± 0.5	18.7 ± 0.9	5.9 ± 0.1
		6.1 ± 0.4	3.7 ± 0.8	32.1 ± 0.7	6.4 ± 0.3	3.9 ± 0.6	40.6 ± 0.9	6.5 ± 0.3
	2.5	4.0 ±0.2	1.9 ± 0.8	43.4 ± 1.6	4.4 ± 0.1	1.4 ± 0.7	29.6 ± 1.2	4.4 ± 0.3
		6.3 ± 0.2	1.8 ± 0.5	42.7 ± 0.7	6.5 ± 0.2	1.6 ± 0.5	30.3 ± 1.6	6.4 ± 0.1
		5.5 ± 0.2	2.1 ± 0.6	40.3 ± 0.8	5.9 ± 0.2	2.2 ± 0.6	32.9 ± 1.2	6.0 ± 0.2
		6.8 ± 0.2	1.9 ± 0.6	40.6 ± 0.9	7.1 ± 0.2	1.9 ± 0.7	32.4 ± 0.9	7.1 ± 0.3
		7.0 ± 0.4	1.0 ± 0.2	38.8 ± 1.2	7.1 ± 0.4	1.4 ± 0.5	33.1 ± 0.5	7.5 ± 0.6
		6.8 ± 0.4	0.5 ± 0.2	39.7 ± 2.5	6.9 ± 0.4	1.2 ± 0.5	35.6 ± 1.9	6.9 ± 0.3
		7.0 ± 0.2	0.7 ± 0.3	38.9 ± 1.6	7.2 ± 0.2	0.6 ± 0.3	35.1 ± 1.6	7.1 ± 0.2
		6.2 ± 0.3	1.4 ± 0.6	35.2 ± 1.1	6.4 ± 0.2	1.3 ± 0.5	37.9 ± 1.0	6.4 ± 0.2
		4.8 ± 0.1	2.5 ± 0.7	40.2 ± 0.5	5.3 ± 0.1	2.4 ± 0.5	33.1 ± 0.6	5.5 ± 0.1
		5.3 ± 0.2	1.8 ± 0.6	42.0 ± 1.4	5.6 ± 0.2	1.9 ± 0.7	32.3 ± 1.0	5.4 ± 0.1
		4.7 ± 0.3	1.8 ± 0.7	38.5 ± 1.7	5.0 ± 0.3	2.1 ± 0.6	35.6 ± 0.7	4.9 ± 0.2
		4.4 ± 0.3	1.7 ± 0.5	37.4 ± 1.4	4.7 ± 0.3	1.9 ± 0.7	37.6 ± 0.9	4.6 ± 0.3

When the facet and undercooling are only related to the pulling rate, the facet velocity can be expressed as $V_f = V_p \cos(\theta_f)$, where θ_f represents the facet orientation relatively to the pulling direction. This relationship indicates that the facet velocity increases proportionally with the pulling velocity, regardless of the thermal gradient. Figure 4.24 presents the evolution of each facet velocity measured in our experiments (Table 4.5) as a function of θ_f for each facet. The full lines represent the theoretical curves for the different pulling velocities.

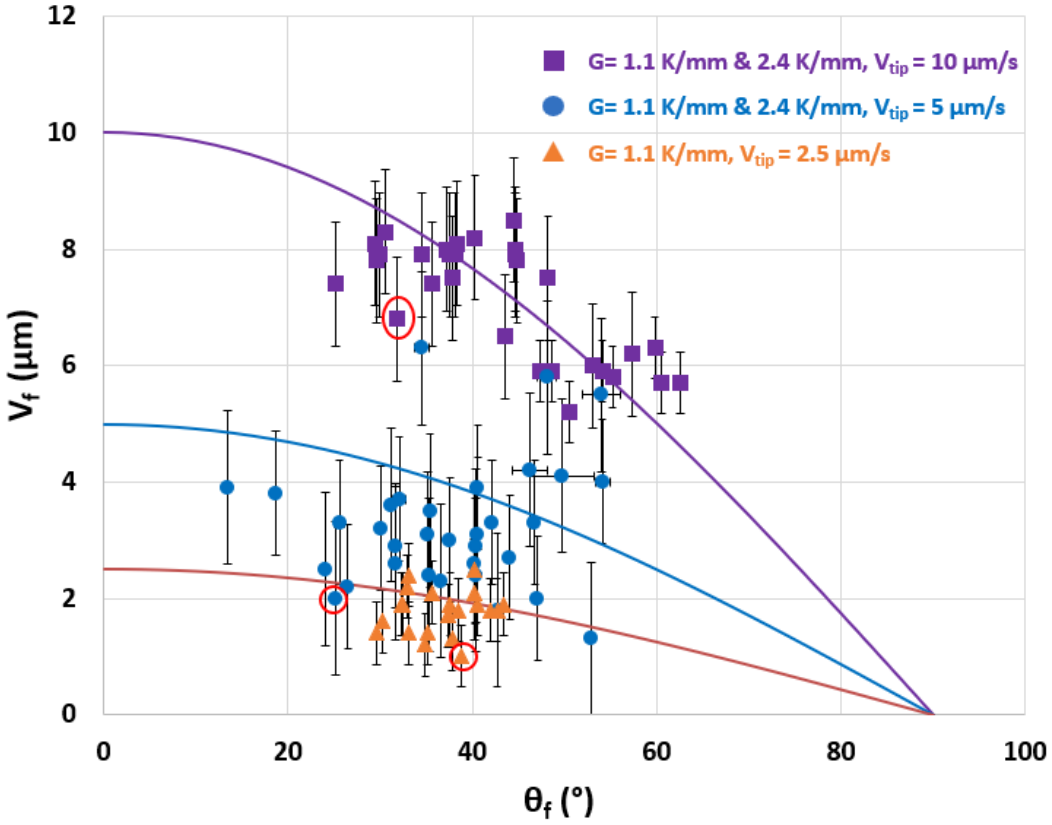
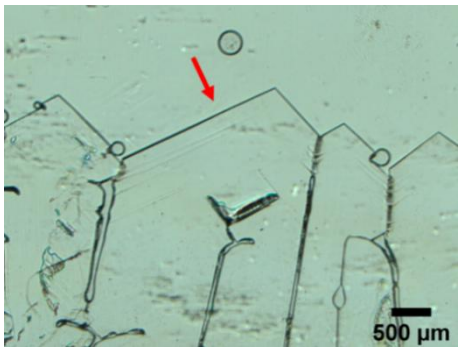


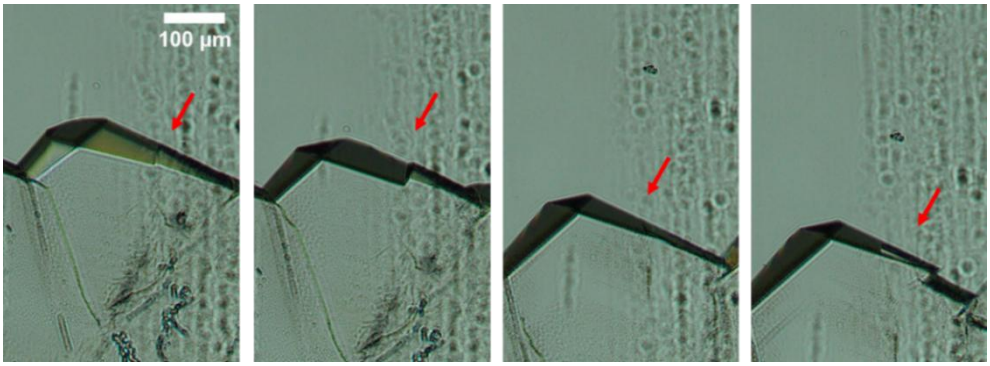
Figure 4.24 – Facet velocities as function of the orientation with respect to the pulling direction (θ_f), alongside the theoretical predictions, for different pulling velocities: 10 µm/s (purple), 5 µm/s (blue), and 2.5 µm/s (orange).

At V_p = 10 µm/s, the experimental data points generally align with the theoretical curve. However, despite following a downward trend similar to the theoretical curve, some points deviate considerably from the predicted values. Experimental fluctuations or instabilities can explain this discrepancy, which may arise from variations in facet growth orientation, changes in crystallographic orientation, or perturbations in the thermal field. For instance, in Figure

4.25a, we present an example of a facet, marked by the red arrow, which exhibits an orientation different from the neighboring facets. The data point corresponding to this facet is highlighted by a red circle in Figure 4.24. Theoretically, this facet should have a velocity around 9 µm/s, whereas the experimental velocity is equal to 7.4 µm/s. This difference can be attributed to the multiple splitting that occurred along the facet during its growth, contributing to a reduction in velocity compared to the theoretical prediction.



(a)



(b)

Figure 4.25 – Facets exhibiting significant difference between experimental and theoretical velocities: (a) V_p = 10 µm/s, G = 1.1 K/mm (SAL_G1_5); (b) V_p = 5 µm/s, G = 2.1 K/mm (SAL_E3_1).

At 5 µm/s, the experimental data points exhibit a pronounced scatter and do not align perfectly with the theoretical curve. However, when considering the uncertainty in velocity measurements, most data points correspond to the predicted values. As for the other pulling velocities, fluctuations and instabilities can influence the experimental findings. Figure 4.25b presents an example of a facet (highlighted by the red arrow) that undergoes a change in orientation and movement. Moreover, it is exposed to two splitting events, making it an unstable

facet with significant perturbations over time. In Figure 4.24, its experimental data is marked by the red circle, with a measured growth velocity equal to 2 µm/s and an uncertainty of 1 µm/s.

Finally, at 2.5 µm/s the experimental data points align more closely the theoretical curve, exhibiting minimal scatter compared to other velocities. This can be explained either by the fact that facets velocities are lower, reducing measurement uncertainty and thus bringing the values closer to the theoretical curve, or by a physical interpretation: as velocity increases, kinetic effects become more pronounced, leading to deviations from the theoretical velocity. The non-stationary behavior of the interface in this experiment, where various defects such as splitting, nucleation, and facets competition are observed, can also explain the deviations between experimental and theoretical results. Figure 4.26 showcases an example of a facet (highlighted by the red arrow) that is eliminated by a neighboring facet. The facet growth velocity is measured at 1 µm/s with an uncertainty of 0.5 µm/s (experimental data point marked by the red circle), different from the theoretical value.

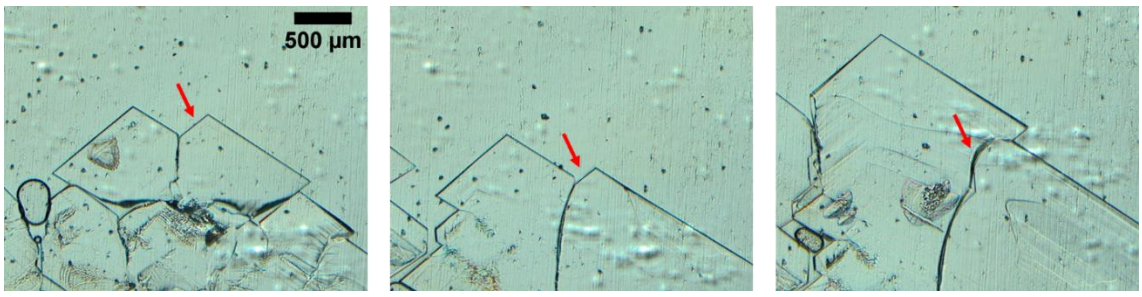


Figure 4.26 – Images showing cases where a facet exhibiting a significant difference between experimental and theoretical values. (SAL_G3_3, V_p = 2.5 µm/s, G = 1.2 K/mm)

These findings indicate that the facet velocities generally agree with theoretical predictions based solely on pulling velocity, with some exceptions due to experimental perturbations.

4.6 Relationship between facet velocity and undercooling

In this section, we aim to establish a relationship between the facet undercooling ΔT_f and facet velocity V_f. After characterizing the crystallographic orientation of facets, we found that the observed facets correspond to {111} crystallographic planes. We measured their growth velocities and undercooling, with the undercooling being measured at the center of the facet

(Table 4.5). The undercooling is found to range between 4 and 7 K, depending on the experimental conditions.

Dey and Sekhar [7, 15] found that during the solidification of salol, the facet growth is influenced by the pulling velocity, thermal gradient and undercooling. When the undercooling is low (ranging from 3 to 7 K), the facets are well-defined and stable. Moreover, numerous researchers [11, 19-27] have contributed to establishing the kinetic laws of salol by investigating the relationship between facet velocity and undercooling. These studies led to the development of laws that describe this relation, which can also provide insights into the type of facet growth.

Figure 4. 27 illustrates various kinetic laws linking facet velocity to undercooling, highlighting different types of facet growth corresponding to different crystallographic planes. Is also includes our experimental findings, represented by the black points.

We observe significant variability among the theoretical kinetic laws. As a function of undercooling, these laws exhibit similar orders of magnitude, making it challenging to precisely identify the growth type of our facets. Upon examining the curves, we find that the growth by screw dislocations closely matches our results [22, 23, 27], with a two-dimensional law [19, 20] also showing comparability. Based on our qualitative analysis, the trends in experimental curves suggest that the facet growth is governed either by screw dislocations (pink curve) or by two-dimensional nucleation (blue curve).

To delve deeper, we suggest that in our case there is a transition between different growth regimes, specifically from two-dimensional nucleation to growth enhanced by the presence of screw dislocations. Cahn et al. [21] explain that the growth kinetics are characterized by two-dimensional nucleation, which has a parabolic limit that corresponds to the screw dislocation regime under conditions where heat flow is negligible, leading to lateral growth. Based on our results, we propose that the growth regime transitions to continuous growth, as also discussed in the literature [21].

If we assume that the facets are growing via two-dimensional nucleation, we can establish the following exponential law linking the facet velocity and undercooling in our experiments:

$$V_f = 111\, exp(-17/\Delta T)\ \mu m/s \qquad \textit{Eq. 4. 2}$$

Alternatively, if growth is governed by screw dislocations, the law can be expressed as:

$$V_f = 0.1\, \Delta T^{1.9}\ \mu m/s \qquad \textit{Eq. 4. 3}$$

Several laws corresponding to growth enhanced by screw dislocations better agree with our measurements. Moreover, it is highly probable that dislocations are present in our experiments. In addition, Chadwick *et al.* [28] and Dürig *et al.* [29] have shown that at low velocities, salol grows through the screw dislocations mechanism.

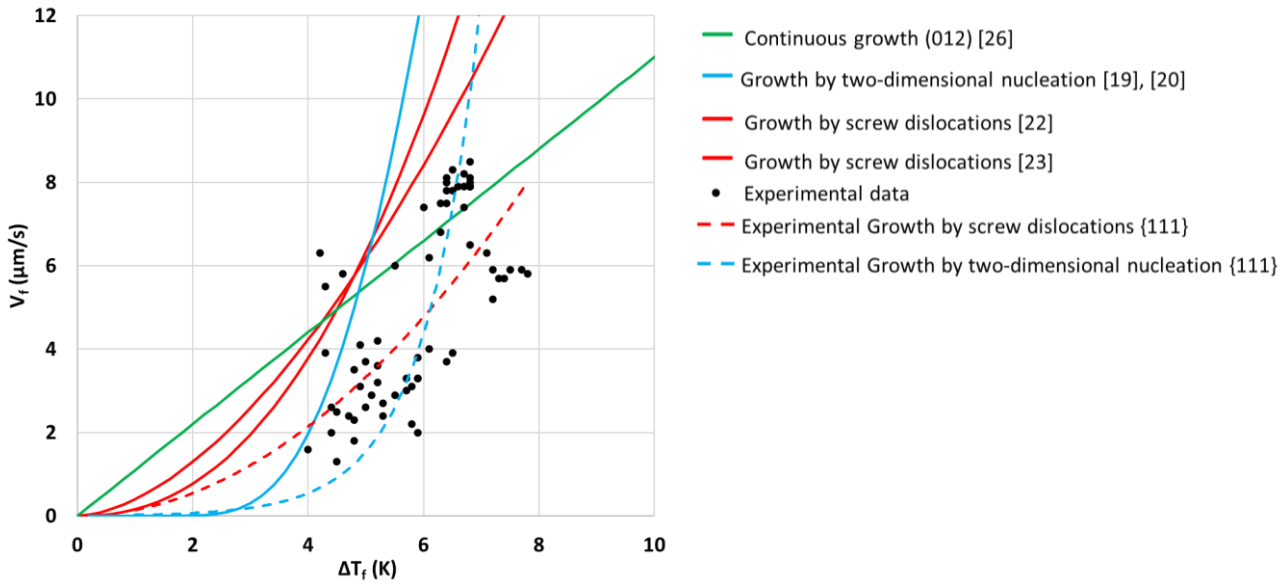


Figure 4. 27 – Theoretical curves of facet velocity as a function of undercooling in salol and experimental data points (black pints).

Further investigations are needed, including studies of additional experimental conditions. Simulation models of the systems could also be useful for drawing correlations between facet velocity and undercooling.

4.7 Conclusions

This chapter presents an in-depth quantitative investigation of the dynamic growth of the salol interface during directional solidification. Through numerous experiments, we explore the factors influencing facet behavior, growth, and orientation. We focus on several characteristics, including interface movement, facet size, interplanar angles, facet velocity, and their relationship with undercooling.

We find that increasing the pulling velocity or reducing the thermal gradient results in smaller facet sizes. Notable variations in facet size are observed in specific cases, such as when defects

cause facet splitting, altering facet growth. Our results align well with existing literature, demonstrating a clear relationship between pulling velocity, thermal gradient and facet size.

The interplanar angles are measured to identify the observed facets as specific crystallographic planes. Most facets correspond to {111} planes, with a few exceptions. The experimental observations are consistent with theoretical predictions of interplanar angles for the orthorhombic structure of salol.

Facet tip velocities generally remain consistent with the pulling velocity, except in rare cases where defects influence facet growth dynamics. In contrast, facet normal growth velocities exhibit more complex behavior, particularly in the presence of defects such as bubbles, splitting, distortions, or during competitive growth between neighboring facets. This can lead to deviations between the measured facet growth velocity and the theoretical projection of the pulling velocity. The study confirms that, in ideal cases, two facets exhibit the same measured velocities, and the grain boundary aligns with the bisector between them. Exceptions occur when deviations are attributed to events such as facet competition and defects.

Finally, the relationship between facet velocity and undercooling suggests that {111} facets grow via screw dislocations or two-dimensional nucleation, with a potent transition to continuous growth at higher undercoolings. Further analysis is needed to confirm these growth regimes.

4.8 Bibliography

[1] F. L. Mota, N. Bergeon, D. Tourret, A. Karma, R. Trivedi, and B. Billia, « Initial transient behavior in directional solidification of a bulk transparent model alloy in a cylinder », Acta Mater., vol. 85, p. 362-377, 2015.

[2] M. C. Flemings, « Solidification processing », New-York: McGraw-Hill, 1974.

[3] V. V. Podolinski, « Investigation of structural formation and growth kinetics of organic crystals », Journal of Crystal Growth, vo. 46, p. 511-522, 1979.

[4] V. Stamelou, M. G. Tsoutsouva, T. Riberi-Beridot, G. Reinhart, G. Regula, J. Baruchel, and N. Mangelinck-Noel, « {111} facet growth laws and grain competition during silicon crystallization », J. Cryst. Growth, vol. 479, p. 1-8, 2017.

[5] C. W. Lan, and C. Y. Tu, « Three-dimensional simulation of facet formation and the coupled heat flow and segregation in Bridgman growth of oxide crystals », J. Cryst. Growth, vol. 233, p. 523-536, 2001.

[6] D. K. Shangguan, and J. D. Hunt, « In situ observation of faceted cellular array growth », Metall. Trans. A, vol. 22, no 4, p. 941-945, 1991.

[7] N. Dey, and J. A. Sekhar, « Interface configurations during the directional growth of Salol—I. Morphology », Acta Metall. Mater., vol. 41, p. 409-424, 1993.

[8] L. M. Fabietti, and R. Trivedi, « In situ observations of stress-induced defect formation at the solid—liquid interface », J. Cryst. Growth, vol. 173, p. 503-512, 1997.

[9] C. Malgrange, C. Ricolleau, and F. Lefaucheux, « Symétrie et propriétés physiques des cristaux », EDP sciences, 2011.

[10] N. Millot, and J.-C. Nièpce, « Cristallographie géométrique: Cours, exercices et problèmes corrigés », Lavoisier, 2014.

[11] H. G. Riveros, « Growth of salol crystals », J. Cryst. Growth, vol. 2, p. 173-177, 1968.

[12] G. Neuroth, and H. Klapper, « Dislocation reactions in Czochralski-grown salol crystals », Z. Für Krist., vol. 209, p. 216-220, 1994.

[13] VESTA, Visualization for Electronic and STructural Analysis. https://jp-minerals.org/vesta/en/).

[14] K. Momma, and F. Izumi, « For three-dimensional visualization of crystal, volumetric and morphology data », Journal of Applied Crystallography, vol. 44, p. 1272-1276, 2011.

[15] N. Dey, and J. A. Sekhar, « Interface configurations during the directional growth of salol—II. Thermal stress cracking », Acta Metall. Mater., vol. 41, p. 425-439, 1993.

[16] K. A. Jackson, « Kinetic processes: crystal growth, diffusion, and phase transitions in materials », John Wiley & Sons, 2010.

[17] J. G. Dash, V. A. Hodgkin, and J. S. Wettlaufer, « Dynamics of Faceted Grain Boundary Grooves », Journal of Statistical Physics, vol. 95, p. 1311-1322, 1999.

[18] T. Duffar, and A. Nadri, « The grain–grain–liquid triple phase line during solidification of multi-crystalline silicon », Comptes Rendus Phys., vol. 14, p. 185-191, 2013.

[19] V. I. Danilov and V. I. Malkin, « Experimental Verification of the Theory of Crystal Growth and the Relation between the Equilibrium Forms and the Growth Forms », Z. Fiz. Khim, vol. 27, p. 1837, 1954.

[20] V. I. Malkin, « On the Rate of Crystal Growth of Salol in the Glassy State », Z. Fiz. Khim, vol. 28, p. 1966-1968, 1954.

[21] J. W. Cahn, W. B. Hillig, and G. W. Sears, « The molecular mechanism of solidification ». Acta Metallurgica, vol. 12, p.1421 -1439, 1964.

[22] H. Pollatschek, « The Determination of the Temperature at the Solid-Liquid Boundary During the Crystallization of Undercooled Melts », Z. Phys. Chem. A, vol. 142, p. 289, 1929.

[23] K. Neumann, and G. Micus, « The Linear Crystallization Rate of Salol in Thin Layers », Z. Phys. Chem. vol. 2, p. 25-39, 1954.

[24] J. W. Cahn, « Theory of crystal growth and interface motion in crystalline materials », Acta Metall, vol.8, p. 554-562, 1960.

[25] K. A. Jackson, D. R. Uhlmann, and J. D. Hunt, « On the nature of crystal growth from the melt », J. Cryst. Growth, vol. 1, p. 1 - 36, 1967.

[26] W. Q. Jin, J. Lin, and H. Komatsu, « Experimental studies on growth kinetics of salol crystals from the melt », J. Cryst. growth, vol. 99, p. 128- 133, 1990.

[27] T. H. Ie, and R. F. Strickland-Constable, « Mechanism of growth from the melt based on experiments with salol », J. Cryst. Growth, vol. 21, p.243-253, 1974.

[28] G. A. Chadwick, « Crystal Growth from the Melt », J. SHEFFIELD UNIV. MET SOC, vol. 9, p. 15-22, 1970.

[29] U. Dürig, J. H. Bilgram, and W. Känzig, « Properties of the solid-liquid interface of growing salol crystals: a dynamic light scattering investigation », Physical Review A, vol. 30, p. 946-959,1984.

CONCLUSIONS

The study of the solid-liquid interface during solidification from the melt is of utmost importance in the design and processing of new materials, and directional solidification has proven to be a powerful technique in its study, since the growth parameters can be accurately controlled. Faceted interfaces at the macroscopic scale are a typical interface morphology generated during solidification of many materials like semiconductors, quasicrystals, or proteins. Understanding faceted growth mechanisms is of major interest in materials science, as this is encountered during the formation of most semiconductors and oxides. The main aim of this thesis is to investigate and explore the dynamics of faceted solid-liquid interface under various experimental conditions (thermal gradient and pulling velocity). To better understand the mechanisms that control the faceted crystal growth, we integrate a systematic approach combining experimental observations and quantitative measurements.

A large part of my work concerned the establishment of an experimental framework to achieve directional solidification in organic materials presenting faceted interfaces. Materials were pre-selected before the thesis beginning, respecting the criteria of melting point lower than 100°C and optical transparency that allows *in situ* and in real time observations. I established experimental protocols for the material purification using different methods. I also prepared the samples and crucibles, and conducted the solidification experiments. These were performed using the ECODIS device, a setup dedicated to the study of rectangular samples that includes the temperature gradient stage, the motor stage and the optical system (camera mounted on an optical microscope). The temperature gradient stage is composed by a cold and a hot chamber, separated by an adjustable gap. The thermal gradient measurement procedure is carefully detailed. The sample is moved across the thermal gradient using an ultra-precision linear motor stage. It is preferable to start a solidification experiment with an interface, as much as possible, flat and free from defects at rest to be able to study the facetted interface dynamics in the best conditions. Therefore, two different procedures to prepare the initial solid seed are described.

Despite the different materials pre-selected, this thesis focuses solely on the experiments performed using salol. A series of experiments were carried out with different thermal gradients and pulling velocities, which all displayed a highly faceted solid-liquid interface. All experiments qualitatively follow the same process. The effect of the pulling velocity and thermal gradient on the interface morphology and stability are studied. Additionally, the complex dynamics of the interface reveals the occurrence of several defects during growth. It

is essential to study their formation and dynamics, as they play a critical role in first, the dynamics of the faceted interface and second, in the final material properties. Bubbles, which are common volume defect, are systematically observed in the experiments and their occurrence has no direct relationship with the facet velocity. Their origin is most likely due to nitrogen inclusion in the melt during sample filling. Growth striations, parallel lines in the crystal structure, are observed mainly on facets indexed as {111} crystallographic planes, which is in favor with the hypothesis of dislocations that can slip along the gliding planes. Indeed in salol, the densest planes are found to be the {111}. Facet splitting is another commonly observed defect and, in the majority of the cases, it is linked to stress accumulation. The increase in the facet size is found to favor the splitting instability. Crystal distortions, microscopic defect where the regular atomic arrangement in a crystal lattice is disrupted, and possibly cracks can arise because of thermal stresses and grain interactions. Finally, we observe the formation of twin boundaries. They are a specific type of grain boundary where two crystals have a specific orientation relationship. In the few observed examples, the twining plane is of type {111} with a relative rotation of 180 ° between both grains which indicates that the twin boundary is a Σ3 twin. These twins are more easily formed during growth as they correspond to a low energy cost.

The quantitative analyses of the performed experiments also reveal key factors of the growth of the faceted interface of salol. The study of the interface movement during solidification allow us to quantify the interface undercooling. Even if the facet size is highly conditioned by the rich dynamics and competition with neighbor grains, it increases when increasing the pulling velocity and reducing the thermal gradient. In order to index the facets observed experimentally, we measure the angle between two tipped facets and we compare it to the theoretical interplanar angles considering the orthorhombic structure of salol and the main crystal faces. We find that most of them correspond to {111} planes. Tip and facet velocities are measured: both can display local fluctuations, which is systematic in the experiments carried out and is associated to the rich and complex dynamics of the salol growth (e.g., facet competition, facet split, bubble nucleation). Finally, we explore the relationship between facet velocity and its undercooling suggesting that the facets grow with regimes corresponding to growth enhanced by the presence of screw dislocations or by two-dimensional nucleation regime, with a potential shifting to continuous growth at high undercoolings.

To summarize, this work enhances our understanding on faceted solid-liquid interface in organic transparent materials notably salol. These findings highlight the complex interplay

between solidification parameters and the evolution of the crystal and its morphology, providing valuable comprehensions in the field of crystal growth. The methodologies treated in this work can present a robust framework for further investigations of salol and hold good potential to work on other organic transparent systems.

FUTURE WORK

This thesis has addressed several problematics, that opens the way for further investigations. Future work can expand from our study in the following directions:

- Broader investigations on the dynamics of the faceted solid-liquid interface of salol. For instance, in Figure A, we observe the formation of a grain boundary with a particular shape resulting from two facets growing in competition. This can be attributed to the crystallographic misorientation between the grains. This kind of phenomena happens several times during our experiments and should be further explored. Therefore, a deep analysis of such behavior, but also more generally of dynamics of grain boundaries, would be needed to better understand how the competition influences the final crystal structure.

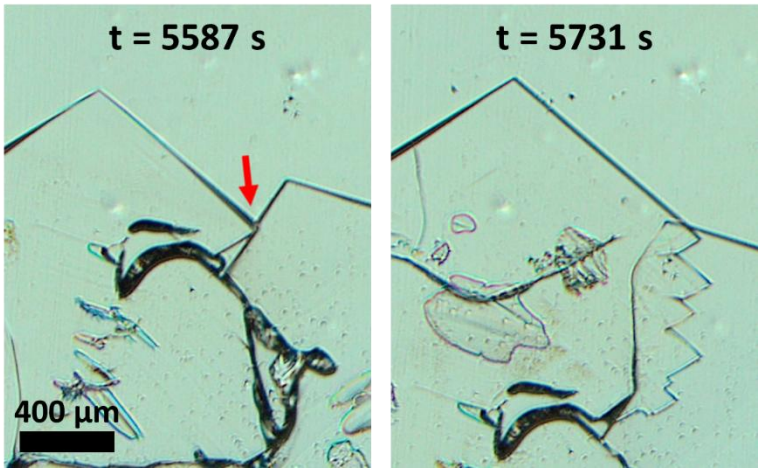
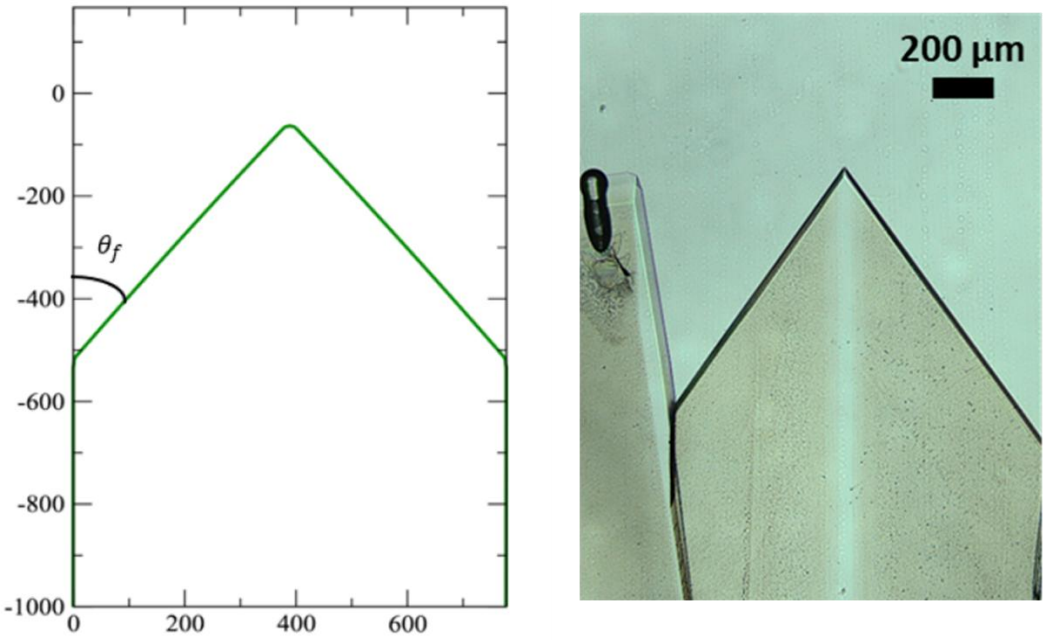


Figure A – Images showing the formation of a grain boundary with a particular shape between two facets. (SAL_G1_4, V_p = 5 µm/s, G = 1.2 K/mm)

- The experimental results from this thesis provide a benchmark database fundamental for developing and validating predictive simulation tools for the elaboration processes of strategic materials. The models can simulate the behavior of the solid-liquid interface, the effect of the variation the thermal and the kinetic parameters during solidification. On the framework of a

master internships (B. G. MANGOUBI), phase-field simulations were done to follow qualitatively the morphology of salol solid-liquid interface over several length and time scales. Anisotropy functions for surface energy and kinetic attachments are re-calibrated to simulate {111} facet formation in two different crystallographic orientations. Overall, the results provided valuable information and strong support for experimental studies (Figure B). The agreement reached between the experimental results, phase-field simulations based on anisotropic functions, and theoretical calculations opens up new perspectives for performing simulations in the other crystal directions <111> and also <110>. The numerical code was originally developed for silicon growth, and the anisotropy function and the code itself were adapted to salol.



(a) (b)

Figure B – (a) Representation of the converged solid-liquid interface of salol by phase-field simulations (V_p = 10 µm/s, G = 1.1 K/mm). (b) Experimental image of the solid-liquid interface of salol (SAL_E4_2, V_p = 10 µm/s, G = 2.4 K/mm).

- Our work represents a significant insight to understand the directional solidification process of salol, organic transparent material, exhibiting a highly faceted solid-liquid interface. Exploring the faceted interface for other transparent organic systems is required, such as for the succinonitrile-borneol and succinonitrile-vanillin alloys that we have presented in Chapter 2. At the beginning of my thesis, I performed some preliminary experiments using these systems.

These studies were followed up in the framework of a master internship (A. AFAILAL) aiming at *in situ* and in real time study of the evolution of the succinonitrile-borneol interface. This alloy is supposed to present a faceted solid-liquid interface, for a concentration of borneol between 3.3 and 11 wt%. During this experiment, faceted dendritic structured are observed, including needle-like shapes and polygonal facets (Figure C). The interface appears to be complex indicating of facets destabilization and growth blocking. These observations suggest the need for further investigations. Future studied are needed, varying the solute concentration, the thermal gradient and the pulling velocity, as well as the control or characterization of the orientation of the initial solid seed.

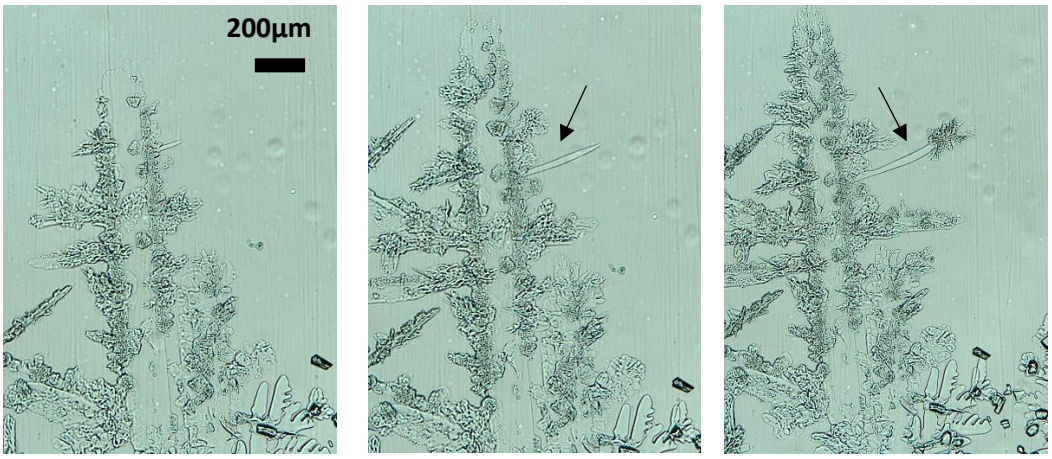


Figure C – Images of the solid-liquid interface of succinonitrile-9.6 wt% borneol alloy showing the evolution of the facet highlighted by the black arrow over time (V_p = 10 µm/s, G = 2 K/mm).

- Finally, integrating and using advanced imaging techniques such as X-Ray imaging and high-resolution imaging methods, such as diffraction or topography, is important. They could provide complementary information concerning the defects and crystallographic information.